

SMALL-SIGNAL MODELLING AND ANALYSIS OF DOUBLY-FED INDUCTION GENERATORS IN WIND POWER APPLICATIONS

by
FRANCOISE MEI

A report submitted in fulfilment of requirements for PhD examination.

Control and Power Group
Dept of Electrical and Electronic Engineering
Imperial College London
University of London

Abstract

The worldwide demand for more diverse and greener energy supply has had a significant impact on the development of wind energy in the last decades. From 2 GW in 1990, the global installed capacity has now reached about 100 GW and is estimated to grow to 1000 GW by 2025. As wind power penetration increases, it is important to investigate its effect on the power system. Among the various technologies available for wind energy conversion, the doubly-fed induction generator (DFIG) is one of the preferred solutions because it offers the advantages of reduced mechanical stress and optimised power capture thanks to variable speed operation. This work presents the small-signal modelling and analysis of the DFIG for power system stability studies.

This thesis starts by reviewing the mathematical models of wind turbines with DFIG convenient for power system studies. Different approaches proposed in the literature for the modelling of the turbine, drive-train, generator, rotor converter and external power system are discussed. It is shown that the flexibility of the drive train should be represented by a two-mass model in the presence of a gearbox.

In the analysis part, the steady-state behaviour of the DFIG is examined. Comparison is made with the conventional synchronous generators (SG) and squirrel-cage induction generators to highlight the differences between the machines. The initialisation of the DFIG dynamic variables and other operating quantities is then discussed. Various methods are briefly reviewed and a step-by-step procedure is suggested to avoid the iterative computations in initial condition mentioned in the literature.

The dynamical behaviour of the DFIG is studied with eigenvalue analysis. Modal analysis is performed for both open-loop and closed-loop situations. The effect of parameters and operating point variations on small signal stability is observed. For the open-loop DFIG, conditions on machine parameters are obtained to ensure stability of the system. For the closed-loop DFIG, it is shown that the generator electrical transients may be neglected once the converter controls are properly tuned. A tuning procedure is proposed and conditions on proportional gains are obtained for stable electrical dynamics.

Finally, small-signal analysis of a multi-machine system with both SG and DFIG is performed. It is shown that there is no common mode to the two types of generators. The result confirms that the DFIG does not introduce negative damping to the system, however it is also shown that the overall effect of the DFIG on the power system stability depends on several structural factors and a general statement as to whether it improves or deteriorates the oscillatory stability of a system can not be made.

Contents

List of figures	3
List of tables	7
List of abbreviations	9
List of symbols	11
Acknowledgements	13
List of publications	14
1 Wind energy background	15
1.1 Background 1: Topics on wind energy	15
1.1.1 Wind power worldwide and in the UK	15
1.1.2 Capacity factor and generation cost	18
1.1.3 Wind energy conversion systems	20
1.1.4 Components	23
1.1.5 Aerodynamic torque control	24
1.1.6 Generator concepts	26
1.1.7 Operating regimes	28
1.1.8 Grid integration issues	29
1.2 Background 2: Topics on DFIG	31
1.2.1 Modelling	31
1.2.2 Control	40
1.2.3 Dynamical behaviour in power systems	47
1.3 Present thesis	48
1.3.1 Objectives	48
1.3.2 Motivation	49
1.3.3 Approach	50
1.3.4 Contributions	50
1.3.5 Layout of the thesis	52
2 Modelling	53
2.1 Turbine	53
2.1.1 Modelling approaches	54

2.1.2	Theoretical modelling methods	54
2.1.3	Model for power system studies	56
2.1.4	Parameters data	58
2.2	Drive train	62
2.2.1	Terminology	62
2.2.2	Modelling alternatives	63
2.2.3	Model for power system studies	67
2.2.4	Parameters data	71
2.3	Induction generator	73
2.3.1	Model in abc-frame	73
2.3.2	Model in dq-frame	76
2.3.3	Per unit conversion	80
2.3.4	Model for power system studies	84
2.3.5	Parameters data	86
2.4	Converter	87
2.4.1	Rotor-side converter	89
2.4.2	Grid-side converter and dc-link	92
2.4.3	Alignment of the dq-frame	93
2.5	Blade pitching	93
2.5.1	Mechanism and control	94
2.5.2	Model equations	95
2.5.3	Parameters data	95
2.6	External network	96
2.6.1	Admittance matrix	96
2.6.2	Interfacing between the DFIG and network	97
2.7	Dynamic model equations	97
2.8	Summary	99
3	Analysis: Steady-state behaviour	101
3.1	Steady-state equations	101
3.2	Squirrel cage induction generator	103
3.3	Doubly-fed induction generator	105
3.3.1	Steady-state characteristics	106
3.3.2	Effect of d-axis control setpoint	115
3.3.3	Effect of q-axis control setpoint	118
3.4	Initialisation	120
3.5	Summary	124
4	Analysis: Open-loop behaviour	126
4.1	Modal analysis	127
4.2	Base case eigenvalues	129
4.3	Sensitivity to operating point	132
4.3.1	Rotor speed and active power	132
4.3.2	Terminal voltage and reactive power	136
4.3.3	Comparison with SCIG	137

4.4	Sensitivity to machine parameters	138
4.4.1	Inductances	138
4.4.2	Resistances	141
4.4.3	Mechanical parameters	143
4.5	Sensitivity to grid strength	144
4.6	Summary	146
5	Analysis: Closed-loop behaviour	149
5.1	Closed-loop DFIG eigenvalues	149
5.2	Tuning issues of rotor-side converter	152
5.2.1	Inappropriate tuning with simplified DFIG model	153
5.2.2	Steady-state behaviour: Sign of the P-gains	154
5.2.3	Stator modes location: Limit value of the P-gains	155
5.2.4	Rotor electrical mode location: Magnitude of the P-gains	157
5.3	Proposed tuning procedure	159
5.4	Robustness verification	162
5.4.1	Robustness to operating point	162
5.4.2	Robustness to machine parameters	164
5.4.3	Robustness to disturbance severity	165
5.5	Pitch control tuning	167
5.5.1	Choosing PI-gains	167
5.5.2	Activation and deactivation conditions	177
5.5.3	Coordination of torque control	180
5.6	Summary	185
6	Analysis: Multi-machine power system	186
6.1	Small-signal properties of the study system	187
6.2	Impact of power generation dispatch	194
6.3	Impact of power transfer	197
6.4	Summary	203
7	Conclusion and future work	204
7.1	Conclusion	204
7.2	Future work	206
	Appendix 1: DFIG parameters	208
	Appendix 2: Gershgorin theorem	210
	Appendix 3: Two-area power system parameters	212
	Bibliography	217

List of Figures

1.1	Worldwide installed wind power capacity in GW from 1990 to 2007 . . .	16
1.2	Installed wind power capacity per region in GW by end 2007	16
1.3	Present and future UK wind farm connections by end 2007	18
1.4	Examples of horizontal and vertical axis wind turbines	21
1.5	Main components of a wind turbine generator	23
1.6	Definition of aerodynamical angles, forces, and wind speeds	24
1.7	Laminar flow (left) and stalled flow (right)	25
1.8	Electrical generator used in commercial wind turbines	26
1.9	Power curve of GE 3.6 MW and Vestas 3MW turbines	29
1.10	Components of the back-to-back converter	37
1.11	Two common layouts for the rotor-side and grid converter control	41
1.12	Common layout for the pitch angle control	42
2.1	C_p curves as function of tip speed ratio with pitch angle (β) as parameter .	60
2.2	Schematic representation of the drive train	64
2.3	Two-mass two-spring system (left) and equivalent one-mass one-spring system. θ_e, k_e = electrical twist angle and stiffness (external network); θ_{tw}, k_{sh} = me- chanical twist angle and stiffness (drive train); ω_r, H_g = generator speed and inertia; ω_t, H_t = turbine speed and inertia.	66
2.4	Force-current analogy between rotational and electrical systems.	69
2.5	Typical drive train parameters for different power generation schemes (H in [s], k in [pu/el.rad])	72
2.6	Convention for direction of positive current.	74
2.7	Induction machine stator and rotor circuits.	74
2.8	Rotating dq-axis with respect to stationary stator three-axis frame.	77
2.9	Generators as voltage source behind transient impedance: SG and SCIG (left); DFIG (right)	84
2.10	DFIG stator and rotor equivalent circuits	86
2.11	Ac-dc-ac converter in the rotor circuit with back-to-back PWM convert- ers. RSC = rotor side converter; GSC = grid side converter.	87
2.12	Generic control loops of the rotor side converter. T_e = electrical torque, Q_s = stator reactive power, i_{qr} and i_{dr} = quadrature and direct component of the rotor, subscript ' $_{ref}$ ' = setpoints, K_x = proportional gains, T_x = integral times.	89
2.13	Typical reference electromagnetic torque as function of the rotor speed. .	90

2.14	Pitch controller and actuator.	94
3.1	Power flows of grid connected doubly-fed induction generator (top) and squirrel cage induction generator (bottom).	102
3.2	SCIG steady-state operating points as function of rotor speed under nominal terminal voltage: torque and powers (left), current magnitudes (right).	103
3.3	Zoomed view of Fig. 3.2.	103
3.4	SCIG steady-state operating points at different wind speeds v_w [m/s] and gearbox ratios n_{gb}	105
3.5	DFIG electrical torque and power as function of rotor speed under nominal terminal voltage and unity power factor for different rated rotor speeds.	107
3.6	DFIG steady-state power flows in the stator and rotor: active power (left), reactive power (right).	109
3.7	Zoomed view of Fig. 3.6.	110
3.8	DFIG active power flows.	111
3.9	Required rotor currents to achieve the steady-state characteristics in Fig. 3.5: d- and q-axis components (left), magnitudes (right).	112
3.10	Required rotor voltages to achieve the steady-state characteristics in Fig. 3.5: d- and q-axis components (left), magnitudes (right).	113
3.11	Zoomed view of Fig. 3.10.	114
3.12	Effect of $Q_{s,ref}$ on DFIG rotor active and reactive power.	115
3.13	Effect of $Q_{s,ref}$ on DFIG rotor d- and q-axis currents and voltages.	117
3.14	Effect of $Q_{s,ref}$ on DFIG rotor voltage and current magnitudes.	117
3.15	Effect of $T_{e,ref}$ on DFIG rotor active and reactive power.	118
3.16	Effect of $T_{e,ref}$ on DFIG rotor d- and q-axis currents and voltages.	119
3.17	Effect of $T_{e,ref}$ on DFIG rotor voltage and current magnitudes.	120
3.18	DFIG initialisation procedure alternatives	122
3.19	DFIG initialisation procedure used in this work.	123
4.1	Active power response of open-loop DFIG to 100ms-50% voltage drop at base case operating point. Thin light line = stator transient included; thick dark line = stator transients neglected.	131
4.2	Electrical torque and rotor speed response of open-loop DFIG response to 100 ms-50% voltage drop at base case operating point. Thin light line = stator transient included; thick dark line = stator transients neglected.	132
4.3	Investigated initial operating points for rotor speed and active power.	133
4.4	Eigenvalues loci for operating points in Fig. 4.3 (DR = damping ratio).	134
4.5	Open-loop DFIG response to 50% voltage drop during 100 ms with sub- and supersynchronous initial rotor speed. Thin light line = stator transients represented; thick dark line = stator transients neglected.	135
4.6	Eigenvalues loci for different terminal voltage, power factor and rotor speed. Triangles, stars, circles are used for $Q_{tot} = +0.5, 0, -0.5$ respectively.	136

4.7	Open-loop DFIG response to 50% voltage drop during 100 ms with $L_m = 1$ and 10 pu. Thin light line / thick dark line = stator transients included / neglected.	141
4.8	Open-loop DFIG response to 50% voltage drop during 100 ms with $R_s = 0.1$ and 0.0001 pu. Thin light / thick dark line = stator transients included / neglected.	143
4.9	Root loci of open-loop DFIG at zero slip for different values of X_e and R_e ($X_t = 0.005$ pu = transfo reactance, DR = damping ratio).	145
4.10	Root loci of open-loop DFIG at zero slip for different values of X_e and B_e ($X_t = 0.005$ pu = transfo reactance).	147
5.1	Max/min values of K_{Te} as function of K_{iq} for $T_1 = 10000$. Continuous: $v_{qs}=1, \omega_r=0.7$; dotted: $v_{qs}=0.5, \omega_r=0.7$; dash-dotted: $v_{qs}=1, \omega_r=1.1$. Shaded area = values that satisfy (5.3).	157
5.2	Max/min values of K_{Qs} as function of K_{id} for $T_2 = 10000$. Continuous: $v_{qs}=1, \omega_r=0.7$; dotted: $v_{qs}=0.5, \omega_r=0.7$; dash-dotted: $v_{qs}=1, \omega_r=1.1$. Shaded area = values that satisfy (5.5).	157
5.3	Root-loci of rotor electrical mode for FOM and 5 th OM. Parameters varied are: d-axis gains (I, II, III); q-axis gains: $K_{Te}=-1 \sim -20$ (arrows), $K_{iq}=-0.5, -1, -2, -10$ (a, b, c, d). Operating point: $V_s=1, P_{tot}=0.5, \omega_r=0.955$	158
5.4	DFIG response to network disturbance (0.5 pu voltage drop at infinite bus) with the control parameters of Table 5.5 and constant wind speed. . .	167
5.5	DFIG response to random wind speed variation with the control parameters of Table 5.5 and constant infinite bus voltage.	168
5.6	Zoomed view of Fig. 5.4	169
5.7	Root loci of turbine-pitch modes for different values of pitch control parameters K_{ω_r} and T_{ω_r}	171
5.8	Root loci of turbine-pitch modes for different values of wind speed v_w and pitch angle β	172
5.9	Closed-loop DFIG response to wind speed step increase from $v_w = 15$ to 16 m/s at $t = 5$ s for different values of K_{ω_r}	174
5.10	Closed-loop DFIG response to wind speed step increase from $v_w = 15$ to 16 m/s at $t = 5$ s for different values of T_{ω_r}	175
5.11	Closed-loop DFIG response (with deadzone) to randomly varying wind speed for different values of proportional gain K_{ω_r}	176
5.12	Closed-loop DFIG response (with deadzone) to randomly varying wind speed for different values of integral time constant T_{ω_r}	177
5.13	Closed-loop DFIG response to wind speed decrease in rated regime with/without condition on β_{up}	179
5.14	Closed-loop DFIG response to varying wind speed around rated value with $\beta_{up} = 0.1, 0.3, 0.5$	181
5.15	Deactivation of pitch control with final wind speed below rated value for $\beta_{th, Teref} = 0.01, 0.001, 0.0001$	182

5.16	Deactivation of pitch control with final wind speed around rated value for $\beta_{th,T_{eref}} = 0.01, 0.001, 0.0001$	183
5.17	Activation and deactivation conditions for the pitch controller.	184
5.18	Coordinated objective of the electrical torque controller.	184
6.1	Two-area power system model	187
6.2	Base case inter-area mode damping ratio and frequency	189
6.3	Effect of power generation sharing with low power transfer	195
6.4	Effect of power generation sharing with high power transfer	196
6.5	Effect of power transfer with low sharing of Gen2	199
6.6	Effect of power transfer with high sharing of Gen2	200
6.7	Effect of power transfer with constant Gen1 output	201
6.8	Effect of power transfer with constant Gen2 output	202
7.1	Gershgorin disks of the 2x2 matrix $B = T^{-1}AT$	211
7.2	Slow exciter: DC-type exciter model	214
7.3	Fast exciter: Static-type exciter model	216

List of Tables

1.1	Installed capacity and penetration level of top ten countries	17
1.2	Capacity factor of wind plants in Europe in 2005	19
1.3	Estimated generation cost in the UK	20
1.4	Typical control strategies used for fixed speed and variable speed systems	29
1.5	Common reactive power sharing schemes between the DFIG stator and GSC	45
2.1	Turbine modelling approaches and methods	54
2.2	Aerodynamic sources contributing to turbine airloads	55
2.3	Theoretical turbine modelling alternatives and validation status	56
2.4	C_p curves parameters from different references.	59
2.5	Maximum C_p and corresponding optimal λ	59
2.6	Turbine parameters obtained for different C_p curves	61
2.7	Drive train model alternatives	64
2.8	Oscillation frequencies of the mass-spring systems in Fig. 2.3	67
2.9	Force-current analogy between rotational and electrical systems	69
2.10	Typical range for drive train parameters	72
2.11	Gearbox ratio for different rated generator speed	73
2.12	Chosen and deduced base quantities for three-phase variables and parameters.	81
2.13	Choice of base voltage for three phase variables and parameters	82
2.14	Choice of base voltage for dq-variables and parameters	82
2.15	Chosen and deduced base quantities for the dq-variables and parameters	82
2.16	DFIG parameters from references	87
2.17	Pitching mechanism model parameters	95
3.1	DFIG initialisation in subrated condition	123
3.2	DFIG initialisation in rated condition	124
4.1	Two cases of open-loop DFIG	129
4.2	Base case eigenvalues and participation factors of open-loop DFIG	130
4.3	Effect of rotor speed on open-loop DFIG eigenvalues and participation factors	135
4.4	Eigenvalues and participation factors of SCIG	137
4.5	Effect of stator and rotor inductances on the modes of the open-loop DFIG at zero slip	139

4.6	Effect of mutual inductance on the modes of the open-loop DFIG at zero slip	140
4.7	Effect of stator and rotor resistance on the modes of the open-loop DFIG at zero slip	141
4.8	Participation factors of open-loop DFIG at zero slip for different resistances	142
4.9	Effect of drive train parameters on the modes of the open-loop DFIG at zero slip	143
4.10	Eigenvalues of open-loop DFIG at zero slip connected to a weak grid . . .	146
5.1	DAE variables and functions for the closed-loop DFIG	150
5.2	Eigenvalues of the DFIG with closed controls	150
5.3	Example of inadequate PI-gains and corresponding eigenvalues	153
5.4	Oscillatory coupling between d- and q-axis dynamics	160
5.5	Example of Adequate PI-Gains and Corresponding Eigenvalues	161
5.6	Effect of Integral Times on DFIG Modes	161
5.7	Effect of rotor speed on the closed-loop DFIG Modes	162
5.8	Effect of terminal voltage on closed-loop DFIG modes	163
5.9	Effect of reactive power level on the closed-loop DFIG modes	163
5.10	Effect of inductances on the closed-loop DFIG modes	164
5.11	Effect of resistances on the closed-loop DFIG modes	165
5.12	Effect of inertias on the closed-loop DFIG modes	166
5.13	Example of closed-loop DFIG eigenvalues in rated regime	170
5.14	Participation factors of the turbine-pitch modes for different operating points	170
5.15	Turbine-pitch modes for different values of K_{ω_r}	173
5.16	Turbine-pitch modes for different values of T_{ω_r}	173
6.1	Base case loadflow solution	188
6.2	Base case complex modes: SG with DC1A self exciter	190
6.3	Base case complex modes: SG with DC1A separate exciter	191
6.4	Base case complex modes: SG with DC2A exciter	192
6.5	Base case complex modes: SG with ST1A static exciter	193
6.6	Active power generation, load and transfer for Fig. 6.3	195
6.7	Active power generation, load and transfer for Fig. 6.4	196
6.8	Active power generation, load and transfer for Fig. 6.5	199
6.9	Active power generation, load and transfer for Fig. 6.6	200
6.10	Active power generation, load and transfer for Fig. 6.7	201
6.11	Active power generation, load and transfer for Fig. 6.8	202

List of abbreviations

CCT	critical clearing time
DAE	differential algebraic equation
DFIG	doubly-fed induction generator
FRT	fault ride-through
GSC	grid side converter
IAM	inter-area mode
MPT	maximum power tracking
PCC	point of common coupling
RSC	rotor side converter
SCIG	squirrel cage induction generator
SG	synchronous generator
UPS	uninterruptible power supply
VRT	voltage ride-through
WECS	wind energy conversion system
WT	wind turbine

List of symbols

$C_p(\lambda, \beta)$	performance coefficient
c_{sh}	drive train damping coefficient
e'_{ds}	direct component of equiv. volt. source behind trans. impedance
e'_{qs}	quadrature component of equiv. volt. source behind trans. impedance
H_t	turbine inertia
H_g	generator inertia
i_{dr}	direct component of rotor current
i_{ds}	direct component of stator current
i_{qr}	quadrature component of rotor current
i_{qs}	quadrature component of stator current
k_{sh}	drive train shaft stiffness
K_{mrr}	$= L_m / L_{rr}$
K_{opt}	$= 0.5 \rho \pi R^5 C_{pmax} \omega_{trated}^3 / (\lambda_{opt}^3 P_{rated})$
L_m	mutual inductance
L_{ss}	stator inductance
L_{rr}	rotor inductance
L'_s	$= L_{ss} - L_m K_{mrr}$
n_{gb}	gearbox ratio $= \omega_{rrated} / \omega_{trated}$
n_{pp}	generator pole pairs number
P_{rated}	turbine rated power
P_r	rotor active power
P_s	stator active power
P_{tot}	total active power
Q_r	rotor reactive power
Q_s	stator reactive power
Q_{tot}	total reactive power
R	blade length
R_s	stator resistance
R_r	rotor resistance
R_1	$= R_s + R_2$
R_2	$= K_{mrr}^2 R_r$
T_e	electrical torque

T_m	mechanical torque
T_r	$= L_{rr}/R_r$
T_{mB}	turbine base torque $= n_{gb}P_{rated}/\omega_{rrated}$
v_{dr}	direct component of rotor voltage
v_{ds}	direct component of stator voltage
v_{qr}	quadrature component of rotor voltage
v_{qs}	quadrature component of stator voltage
$V_{r,ang}$	angle of rotor voltage
$V_{r,mag}$	magnitude of rotor voltage
$V_{s,ang}$	angle of stator voltage
$V_{s,mag}$	magnitude of stator voltage
V_i, V_k	voltage magnitude at bus i and k
v_w	wind speed
v_{wrated}	rated wind speed
Y_{ik}, α_{ik}	mag., ang. of element (i,k) of bus admittance matrix
β	blade pitch angle
λ	tip speed ratio
ρ	air density
Φ_{id}	current controller state variable in the direct axis
Φ_{iq}	current controller state variable in the quadrature axis
Φ_{Te}	electrical torque controller state variable
Φ_{Vs}	stator voltage controller state variable
ψ_{dr}	direct component of rotor flux
ψ_{ds}	direct component of stator flux
ψ_{qr}	quadrature component of rotor flux
ψ_{qs}	quadrature component of stator flux
$\Psi_{r,ang}$	angle of rotor voltage
$\Psi_{r,mag}$	magnitude of rotor voltage
$\Psi_{s,ang}$	angle of stator voltage
$\Psi_{s,mag}$	magnitude of stator voltage
θ_i, θ_k	voltage angle at bus i and k
θ_{tw}	equiv. twist angle of drive train shaft
ω_r	rotor speed
ω_s	synchronous speed
ω_t	turbine speed
ω_{rrated}	generator rated speed (mechanical) $= \omega_{el}/n_{pp}$
ω_{trated}	turbine rated speed $= v_{wrated}\lambda_{opt}/R$

Acknowledgements

I would like to thank my supervisor Dr B.C. Pal for giving me the opportunity and guiding me through the PhD. His serious but cheerful personality made our regular discussions enjoyable and fruitful. I would also like to thank my parents for their support and encouragement. Finally I thank my fellow PhD colleagues who made this study period lively and colorful.

List of publications

The following publications have been written during the course of this work:

- F. Mei, B.C. Pal, “Modelling and small-signal analysis of a grid connected doubly-fed induction generator”, in *Proc. 2005 IEEE Power Engineering Society General Meeting*, June 2005, pp 1503-1510.
- F. Mei, B.C. Pal, “Modal Analysis of a Grid Connected Doubly-Fed Induction Generator,” in *Proc. of Power Electronics, Machines and Drives Int. Conf.*, April 2006, pp 611-615.
- F. Mei, B.C. Pal, “Modelling and dynamic behavior of wind generation as it relates to power system control and dynamic performance,” in *Cigre Technical Report Working Group 601 of Study Committee C4*, CIGRE-WG-601.C4, Chapter contribution, January 2007.
- F. Mei, B.C. Pal, “Modal analysis of grid connected doubly-fed induction generators,” in *IEEE trans. on Energy Conversion*, vol 22, nb 3, September 2007, pp 728-736.
- F. Mei, B.C. Pal, “On the modelling adequacy of the DFIG in power system stability studies,” in *IET Journal of Renewable Power Generation*, vol 2, nb 3, September 2008, pp 181-190.

Chapter 1

Wind energy background

The present thesis investigates the small-signal modelling and behaviour of the doubly-fed induction generator (DFIG) in grid connected wind energy conversion systems.

To place the work into context, this chapter starts by giving general background on wind energy and the DFIG. In the first section, relevant concepts and common terminologies are introduced. In the second section, studies on the dynamical behaviour of the DFIG and its impact on the power system are reviewed. A summary is given on the modelling alternatives, control approaches and study methods reported in the literature. The third section concludes the chapter by presenting the objectives, motivations and contributions of the present work.

1.1 Background 1: Topics on wind energy

1.1.1 Wind power worldwide and in the UK

The growing demand for more secure and greener energy supply has had a significant impact on the development of wind energy in the last decades. From about 2 GW in 1990, the global installed capacity has now reached nearly 100 GW (Fig. 1.1 [1,2]). For the last ten years, the sector has been growing exponentially at about 30% annually with Europe leading the market (Fig. 1.2 [1]). Predictions for the future give the same order of growth figure and it is estimated that global installed capacity may reach up to 1000 GW by 2025 [3]. Denmark, Germany and Spain have presently the highest wind penetration in terms of wind capacity to peak demand (Table 1.1 [1,4,5]). In terms of production, in 2006, wind power plants generated 100 TWh in Europe, representing 3.3% of the EU

electricity consumption [1].

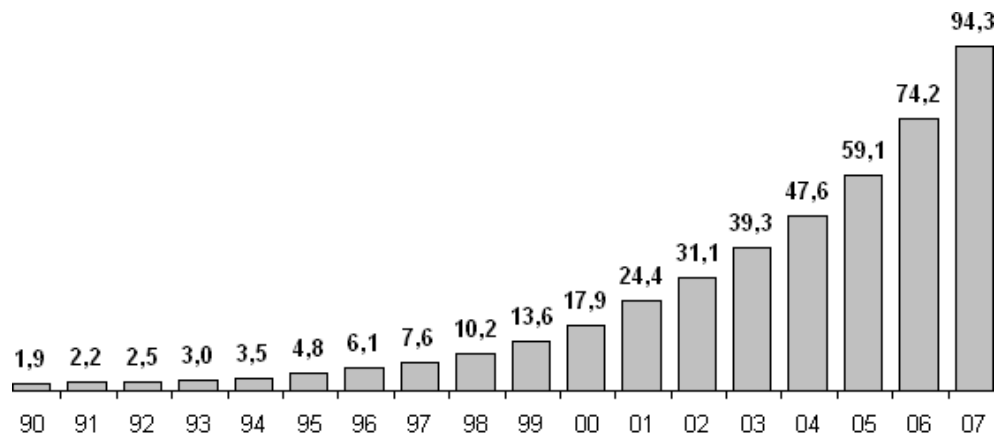


Figure 1.1: Worldwide installed wind power capacity in GW from 1990 to 2007

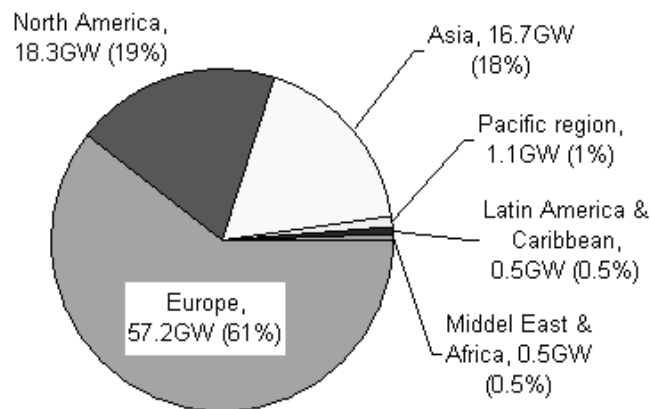


Figure 1.2: Installed wind power capacity per region in GW by end 2007

Two critical aspects that have a direct impact on the growth of wind energy are the policy frameworks and the manufacturing capabilities. A well-known example of policies impact is the Production Tax Credit (PTC) in the US. Under this scheme, wind farm developers receive a tax credit (1.9 cent/kWh) over the first 10 years of a project operations. In 2003 the PTC expired without being renewed, and new installations amounted to 389 MW in 2004. By the end of that year the PTC was finally extended, and more than 2400 MW were installed in each of the following years [1]. The other aspect is the ability of the supply chain to keep up with the strong demand. Wind farms developers have now (2006-2007) to wait 12 months for the manufacturing of the turbines and the growing de-

Table 1.1: Installed capacity and penetration level of top ten countries

	Top 10 capacity = 81.1 GW	wind capacity* [GW]	peak demand** [GW]	penetration [%] (wind cap/peak dem)
1	Germany	22.2	76.6	29.0
2	US	16.8	na	na
3	Spain	15.1	43.2	35.0
4	India	8.0	na	na
5	China	6.1	na	na
6	Denmark	3.1	4.7	66.7
7	Italy	2.7	53.4	5.1
8	France	2.5	86.1	2.9
9	UK	2.4	na	na
10	Portugal	2.2	8.9	24.7

*end 2007 , **Jan 07

mand suggests that this waiting period is likely to increase to 18-24 months [1]. Industry experts predict that the current bottleneck issues will be overcome by 2009 [1].

In the UK, recognising the role of renewables in reducing carbon emissions, the government introduced the Renewables Obligation (RO) in 2002 requiring all electricity suppliers to provide 10% of their supply from renewables by 2010 (the exact figure is different for England & Wales, Scotland and Northern Ireland, but the idea behind the scheme is the same) [6, 7]. In 2003, the Energy White Paper was published and stated a goal of 60% reduction in carbon emission by 2050. In response to the ambitious programme, the RO target was increased to 15% of electricity supply by 2015 [7].

To comply with the RO, suppliers can either buy Renewable Obligation Certificates (ROCs) which are issued to renewable generators for each MWh of electricity produced, or they can pay a buy-out fund (30£/MWh in 2002) [6]. The RO does not specify which particular technology is preferred and ROCs are issued to all types of renewables. However, it is expected that three-quarter of the 10% by 2010 target (about 8 GW of capacity) will be supplied by wind power as it is relatively more mature and economical [7].

The location of potential future wind farms in the UK is shown in Fig. 1.3 [8–10]. In Scotland, most interest has been expressed for onshore sites [8]. In England and Wales, most development is expected to come from offshore [8] due to the less favorable wind conditions onshore. To accommodate this, the Crown Estate has made available areas of

seabeds through two rounds of competitive tenders. Wind farms sited in the leased areas of Round one and two are estimated to provide 1.3 and 7.1 GW respectively [8].

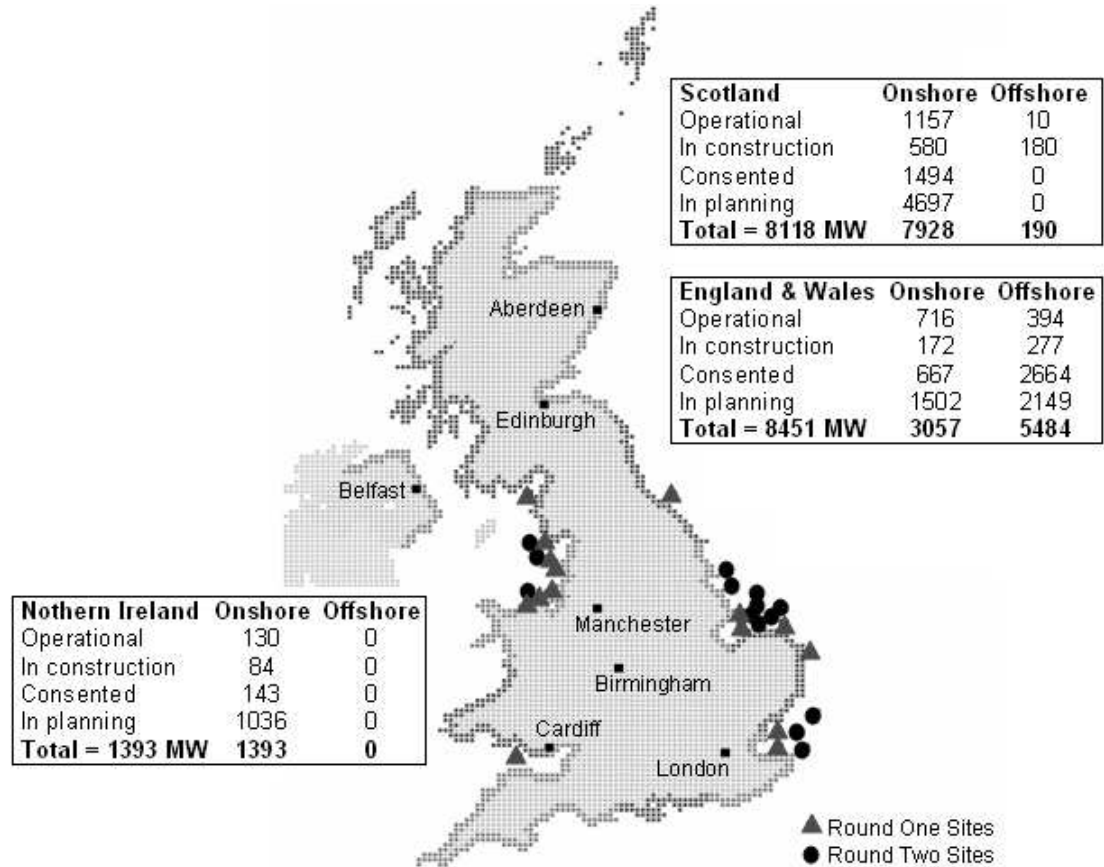


Figure 1.3: Present and future UK wind farm connections by end 2007

In February 2007, the UK achieved a new milestone in the wind energy sector as it reached 2 GW of total installed capacity (onshore and offshore) [11]. By end 2007, operational capacity increased to 2.4 GW with in addition 1.3 GW of wind farms under construction, 5.2 GW of consented projects, and 9.2 GW of planning projects [10]. The present 2.4 GW represents 1.5% of UK electricity supply (1.1 million homes) and places the UK in the top 10 countries worldwide (Table 1.1).

1.1.2 Capacity factor and generation cost

The term capacity factor of a wind power plant refers to the ratio of actual electricity production over the total production if the plant was running continuously at full capacity

[6]. It is equivalent to the term load factor of conventional plants. Since wind turbines are operating most of the time at less than full capacity, the capacity factor of wind plants are typically lower than conventional plants [6]. For wind units, a capacity factor of 0.25-0.3 can be considered as reasonable and a capacity factor of 0.4 as very good [12]. These values can be compared to average load factor of conventional plants ranging from 0.5 to 1 [13] (developed countries with more excess capacity tend to operate at the lower end of the range, developing countries with more pressing demand tend to operate at the higher end of the range).

The capacity factor depends on the location and technology of the wind farm. In the UK, typical values of onshore plants are between 0.20-0.40 [6]. The industry standard is to assume a value of 0.30 [6]. For the near future, it is expected that this figure will increase (up to 0.35-0.40 [6]) as windier sites and offshore wind farms are developed. Table 1.2 [13] shows average capacity factors of other European countries. It is seen that the UK has indeed better wind resources.

Table 1.2: Capacity factor of wind plants in Europe in 2005

UK	0.28
Spain	0.25
Denmark	0.24
Germany	0.16
Sweden	0.19

There are various ways to evaluate the economics of a wind farm (generation cost, integration cost, wind farm cost, etc). In the following, a brief discussion on generation cost is given, as it is often used to compare different types of generation.

Generation cost is expressed in £/kWh, hence both total cost and total production of a wind farm over its lifetime influence the estimated figure. The total production depends mainly on the average wind speed and is site specific (the higher the wind speed, the higher the output, and hence the lower the generation cost). The total cost can be split into investment capital (planning, construction, transport, material, grid connection, etc), operational expenses (maintenance, repair, administration, etc) and integration costs (reserve, emissions, network reinforcement, subsidies).

Due to the high level of initial investment, the total cost is very sensitive to the interest charged on the capital and the repayment period. These two parameters differ from country to country, which explains partly the wide range of reported cost figures. For example, Danish wind farms are typically cheaper because utilities use public sector interest rate and repayment periods (about 5% over life time of the plant). In UK, where the industry is liberalised and undertaken by the private sector, interest rates are higher and repayment period shorter (about 8-10% over 15-20 years) [6]. The integration costs are still subject to debates and it is unclear whether to include them.

Depending on the assumptions, estimated generation costs can be very different, as shown in Table 1.3 [6, 7, 14] for the UK. The most notable differences are for nuclear and

Table 1.3: Estimated generation cost in the UK

	RAE [p/kWh] Mar 04	BWEA [p/kWh] Nov 04	SDC [p/kWh] May 05
CCGT	2.0-2.5 + 1.5 for CO ₂	2.6-3.0 + 0.2 for CO ₂	2.3-3.0
Coal	2.2-3.4 + 2.0 for CO ₂	2.6-3.2 + 0.6 for CO ₂	3.0-3.5
Nuclear	2.2-2.4	3.0-4.3	3.0-4.0
Onshore wind	3.7-5.4	2.6-3.9	3.2
Offshore wind	5.5-7.2	3.7-5.0	5.5

RAE = Royal Academy of Engineering [14], BWEA = British Wind Energy Assoc. [7],
SDC = Sustainable Development Commission [6]

wind. For nuclear generation, the RAE assumes simpler and cheaper modern technology. For wind, it assumes cost of back up eight times larger than those of the BWEA [15]. The estimates show nevertheless that present wind generation cost is higher than CCGT, and offshore generation is more expensive than onshore due to the higher capital cost. It is forecast that by 2020 the cost may drop to 1.5-2.5 p/kWh for onshore and 2.0-3.0 p/kWh for offshore due to economies of scale and exploitation of windier sites [6].

1.1.3 Wind energy conversion systems

Horizontal and vertical axis wind turbines

From the physical setup viewpoint, there are horizontal axis wind turbines (HAWT) and vertical axis wind turbines (VAWT) [16]. For HAWT, the blade rotate about an axis parallel to the ground and windflow. Common examples are the old-style Dutch windmill

and modern wind turbine. For the VAWT the blades rotate about an axis perpendicular to the ground. The most common design are the Darrieus (curved blades), Giromill (straight blades) and Savonius (scoop blades), as shown in Fig. 1.4.

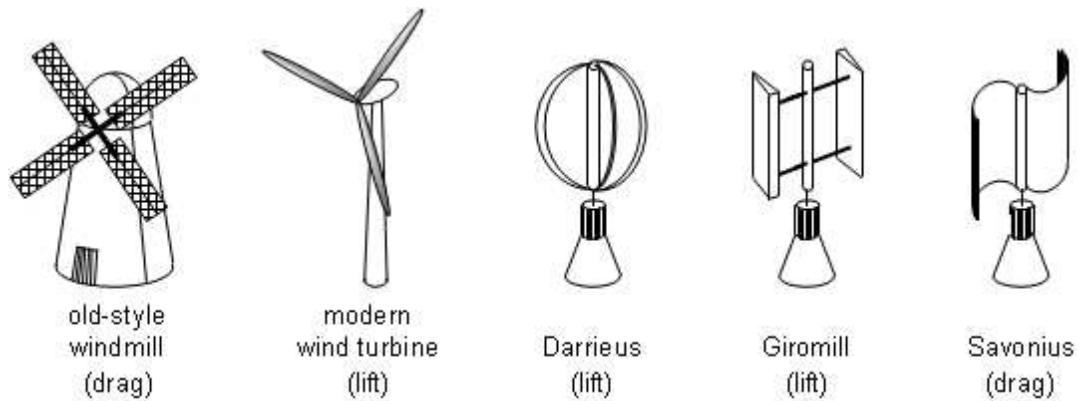


Figure 1.4: Examples of horizontal and vertical axis wind turbines

Nearly all the larger turbines employed in modern wind farms are HAWT [17]. One reason is that they are more suitable for harnessing the higher and smoother wind speed at higher altitude. In terms of blade loading and fatigue, HAWT are subject to reversing gravitational loads (structural load is reversed when the blade goes from upwards to downwards position) which imposes a limit on the size of such turbine [16]. In terms of material, VAWT have greater solidity (fraction of swept area that is solid) and hence are more heavy [16]. Presently, HAWT are the most commercially viable.

Drag and lift powered motion

The rotation of both HAWT and VAWT can be powered predominantly by lift or drag force depending on the design of the blade. In drag design, the wind pushes the blade out of the way. The rotational speed is typically slower. Due to their high torque capabilities, drag powered turbines are suitable for pumping, sawing or grinding [17]. The typical example of such design is the old style Dutch windmill. In lift design, the blade cross section has an airfoil shape so that when the wind passes by the blade, the pressure on the lower surface is higher and hence lifts the blade. The same principle allows airplanes and birds to fly. Lift powered turbines have much higher rotational speed than drag-powered turbine and are well suited for electricity generation [17]. In general, lift machines are

more efficient than their drag counterpart [18].

Number of blades

In order to extract a maximum amount of wind power, each blade should interact as much as possible with the wind passing through the swept area. Hence the lesser the blades the higher the rotational speed of the turbine, as the blades have to move faster to ‘fill up’ the swept area [16]. In theory, the more blades a turbine has, the more efficient it should be. However for larger number of blades there is more interference and a blade is more likely to pass in the disturbed weaker flow of the previous blade. In practice, low-solidity turbines tend to have a higher efficiency [16].

From a structural stability viewpoint, the number of blades of lift powered HAWT should be odd and greater or equal to 3, in which case the dynamic properties of the turbine rotor are similar to those of a disc [19]. For an even number of blades, the structure is subject to more important bending forces because when a blade is in the uppermost position receiving most wind power, another blade is in the lowermost position in the shadow of the tower. The majority of commercialized modern wind turbines are three bladed. Sometimes two bladed or even single bladed design are used to save the cost of blades. However these turbines require more complex structural design to avoid heavy shocks (two-bladed turbines require a teetering hub, one bladed turbines require a counterweight on the hub) and are visually more intrusive due to their higher rotational speed [19].

Betz limit

An important operational characteristic of wind turbines is the Betz limit. It indicates the theoretical maximum amount of wind energy that can be extracted by a turbine. If turbines were 100% efficient all the airflow energy would be extracted and the flow speed after passing through the turbine would be zero, which is impossible. In 1928, Betz showed that under ideal assumptions (uniform rotor disk with infinite number of blades) the maximum efficiency of a turbine is $16/27$ (59.3%) [16]. In practice, this coefficient is less due to non-idealities (wake rotation behind the rotor, finite number of blades, blade-tip losses, frictional drag, etc). Present turbines have efficiency around 30-40% [16, 18].

1.1.4 Components

The main components of a wind turbine generator is shown in Fig. 1.5 (drawing not in scale). The *turbine* is formed by the blades, the hub and the connecting components (bearings, pitching actuators). It transforms wind kinetic energy into mechanical energy. For multi-megawatt turbines, dimensions are large with blade length ranging from 35-60 meters [20].

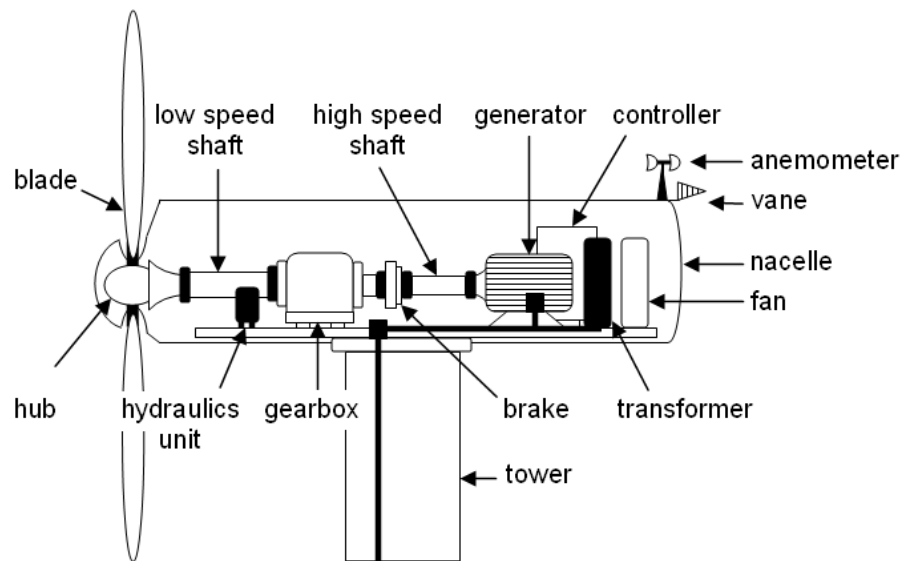


Figure 1.5: Main components of a wind turbine generator

The *drive train* is formed by the turbine rotating mass, low-speed shaft, gearbox, high-speed shaft and generator rotating mass. It transfers input power (turbine mechanical power) to the point where useful power (generator mechanical power) is used. In most cases, a gearbox is required because the rotating speed of the turbine is much lower than that of the generator. For multi-MW units the gearbox ratio is about 50-100 as the typical speed range of the turbine is 10-20 rpm while for the generator it is about 1000-2000 rpm [20]. For smaller wind turbines, the turbine speed is higher, hence the gearbox ratio may be less than 50 [19]. The low speed shaft contains pipes for the hydraulics system that operates the aerodynamic brake [19]. The high speed shaft is equipped with an emergency mechanical brake that is used in case of failure of the aerodynamic brake [19].

The *generator* converts mechanical power into electrical power. For variable speed

generators, an ac-dc-ac converter is required. Usually the generator produces power at 690 V and a transformer steps up this voltage to 33 kV for underground cable transmission [21]. The transformer may be placed at the bottom of the tower [19] or in the nacelle for losses consideration [6]. The power is then transmitted to the wind farm substation where a further voltage step-up may be done to 110~765 kV for long distance transmission [18].

Other components include the anemometer and vane which measure the wind speed and direction respectively. Wind speed measurement is used to start and stop the turbine. Wind direction measurement is used by the yaw-control mechanism (see next subsection). Devices such as electric fans and oil coolers are used to cool the gearbox and generator.

1.1.5 Aerodynamic torque control

The mechanical input torque can be controlled in many ways. Fig. 1.6 [16, 18] shows the tower yaw angle γ and blade pitch angle β , which can be actively controlled for aerodynamic torque regulation.

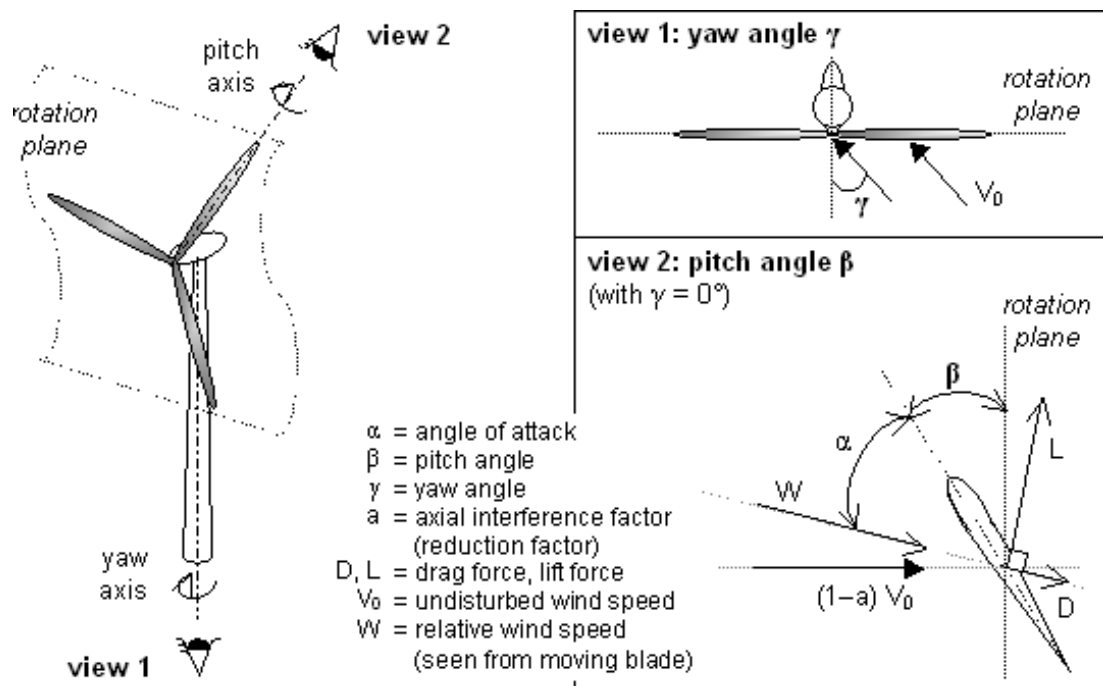


Figure 1.6: Definition of aerodynamical angles, forces, and wind speeds

The yaw angle is usually controlled to make sure that the turbine is facing the wind

($\gamma = 0^\circ$). It is done by rotating the nacelle about the yaw axis (tower axis) [19]. In theory, it can also be used to reduce the captured power by turning the turbine out of the wind. However this is only possible for very small turbines (≤ 1 kW) because operation with yaw error increases fatigue loads (cyclical varying stresses, bending torques) which damage the structure [19].

Reduction of input mechanical power is usually done with the blades. In stall-controlled turbines, the aerofoil shape (blade cross-section) is designed so that above a certain speed the blade goes into stalling mode (Fig. 1.7 [22]) [18]. When the blade is stalled, the wind flow is partly detached on the upper surface, reducing the lift and hence performance. Stall-regulated turbine can be passive- or active-stall controlled. In the former case, the blades are bolted on the hub at fix angle [19]. In the latter case, a pitching mechanism pitches the blade to stall (increases the angle of attack) when required.

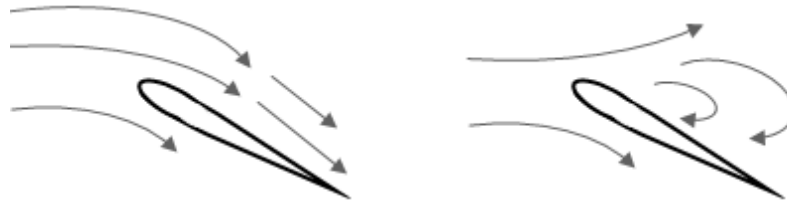


Figure 1.7: Laminar flow (left) and stalled flow (right)

The counterpart of stall-controlled turbines are pitch-controlled turbines. In these configurations, the windflow is always laminar and the aerodynamic torque is regulated by pitching the blade to feather (by reducing the angle of attack). Pitch regulated turbines can also be active- or passive-pitch controlled. In the former case, a pitching mechanism (usually hydraulics system) is in place. In the latter case, the blades are mounted on the hub so that the thrust force pitches the blade (i.e. the blades are “self-pitched”) [18].

Rotation to feather (smaller angle of attack) gives quieter operation and easier control [18]. Rotation to stall (larger angle of attack) is faster but gives more noise, bending loads, and less exact control due to the unsteady nature of stalled flow [18]. The advantage of stall-regulation is that complex control for blade pitching is not required. The aerodynamic and structural design of the turbine are however more complex. In the early days, most wind turbines were fixed speed stall regulated [22], nowadays the trend is the

use of variable speed pitch regulated turbines because of increased performance (notable but not the main reason) and less mechanical loads (main reason) [18, 23].

1.1.6 Generator concepts

There are mainly four types of electrical generator used commercially (Fig. 1.8 [24]) [24–26]. Depending on the generator type, the turbine is referred to as fixed or variable speed.

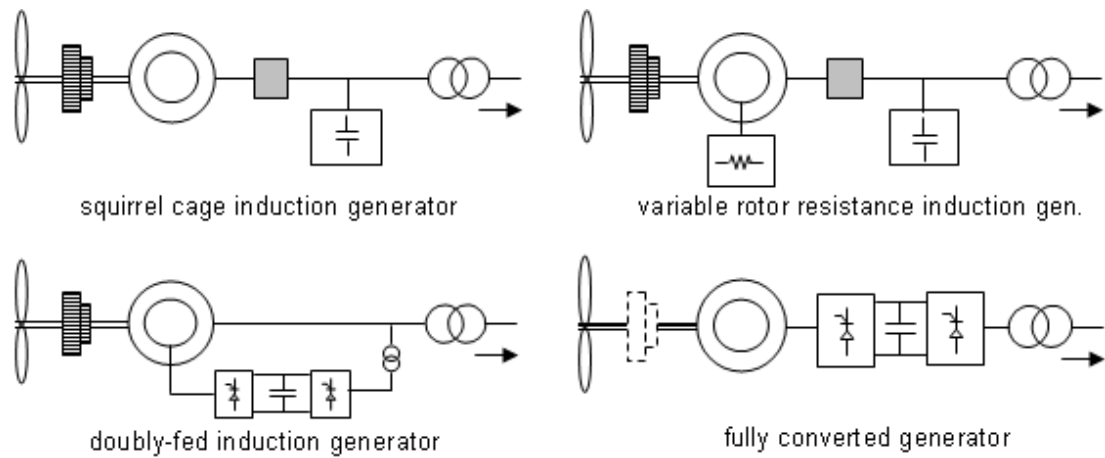


Figure 1.8: Electrical generator used in commercial wind turbines

The simplest type is the fixed speed squirrel cage induction generator (SCIG) which makes up the biggest share of the smaller wind turbines already installed and scattered on the network [22]. The rotor consists in short circuited bars i.e. the rotor voltage is zero. The speed varies within a very narrow range (practically constant) and the mechanical torque is usually controlled by stalling the blades actively or passively [18, 22]. The advantages of the SCIG are its simplicity and robustness [22]. For small size turbines in a strong grid, this is arguably the most economical solution as the grid is able to provide reactive power and maintain a satisfactory voltage profile. Capacitor banks are installed to complement the reactive power consumption. The capacitors must be carefully sized to avoid self excitation [18]. Soft-starter are used to mitigate the high starting currents [18].

The second type of generator is a wound rotor induction generator with variable rotor resistance (best known under the commercial brand name “opti-slip” from Vestas).

It is essentially a fixed-speed machine, where the speed range is increased to typically 2-10% [24] by inserting an adjustable resistor bank in the rotor. The mechanical input is controlled by pitch regulation for optimal wind power capture. The advantage of this generator type is its larger slip range compared to the conventional SCIG and simpler control structure compared to the following two generator types. It has however the same problems as the SCIG. Reactive compensation and soft-starters are required and voltage quality is easily deteriorated in weak networks. Compared to the SCIG it has increased losses due to the larger rotor resistance.

The third type of generator is the doubly-fed induction generator. It is a variable speed asynchronous generator where the rotor consists in conductors with slip-rings fed by an ac-dc-ac converter connected to the grid. The provision of non-zero rotor voltage at slip frequency results in speed variability. Modern transistor based back-to-back converters allow bi-directional rotor power flows and hence operation at both sub- and super-synchronous speed [27]. Typically the slip range is $\pm 30\%$ (determined by the size of the converters). The advantages of the DFIG are the speed variability which reduces mechanical stress [28, 29], the possibility to optimise the power capture by regulating the electrical torque and control reactive power independently [27, 30]. Recent studies investigated further potential advantages such as frequency control and power system stabilizer capabilities [31, 32]. Both acquired and potential capabilities of the DFIG are achieved by appropriate control of the rotor voltage.

The last type of generator is the fully-converted SG or fully-converted SCIG. Synchronous generators are suitable for large rating applications as they operate at unity power factor. Induction generators need reactive power compensation from the generator side converter or additional capacitor banks, hence are more suitable for small rating applications [19]. For the SG which can be excited externally or with permanent magnet, using a multi-pole design removes the need of the gearbox [25]. As the converter rating is the full rating of the generator, the slip range is not limited to $\pm 30\%$. The main advantage of the fully converted generator is the complete decoupling of the generator from the grid which can facilitate the control of the system under severe disturbances from the wind or network. The main disadvantage is the higher cost of the large converter.

The present trend in the industry is to use variable speed generators [33]. Initially, the main reasons were the reduced mechanical stress (longer life time), better wind capture, smoother power output (due to both variable speed and controllable electrical torque), and ability to operate at unity power factor. Nowadays, tighter grid connection requirements (see Subsection 1.1.8) and advances in semi-conductors make converters economically justifiable. It is not yet clear which of the DFIG or fully converted generator will be the preferred choice in the future. It has been suggested that experienced manufacturers tend to propose the fully-converted design for new wind farm development [34]. In the last decade, a significant share of the wind farms installed was DFIG based [33].

1.1.7 Operating regimes

The operating regimes of wind machines can be illustrated by their power curve, which gives the estimated power output as function of wind speed. Examples from two leading manufacturers are shown in Fig. 1.9 [35, 36]. The power curve gives three important values:

- (1) Cut-in wind speed: wind speed at which usable power is generated.
- (2) Rated wind speed: wind speed at which the turbine generate a designated rated power, which is often but not always the maximum power [18].
- (3) Cut-out wind speed: wind speed at which the turbine is shut down (with automatic brakes and/or blade pitching) to protect the turbine from mechanical damage [18].

Below rated wind speed the wind turbine is said to be in sub-rated regime. Above rated wind speed, it is said to be in rated regime. In each region the turbine can be controlled in various ways to achieve specific objectives. Table 1.4 [18] gives an overview of typical control strategies used for fixed speed and variable speed systems [18]. The primary goals are to optimize the power capture in subrated regime, and reduce power capture in rated regime [18]. It is noted that the pitch angle is usually kept constant in subrated regime to limit the mechanical wear of the pitching mechanism [18].

A remark on power curves is that in practice they are obtained by field measurements [19]. Though, they may also be obtained by computation using blade element methods

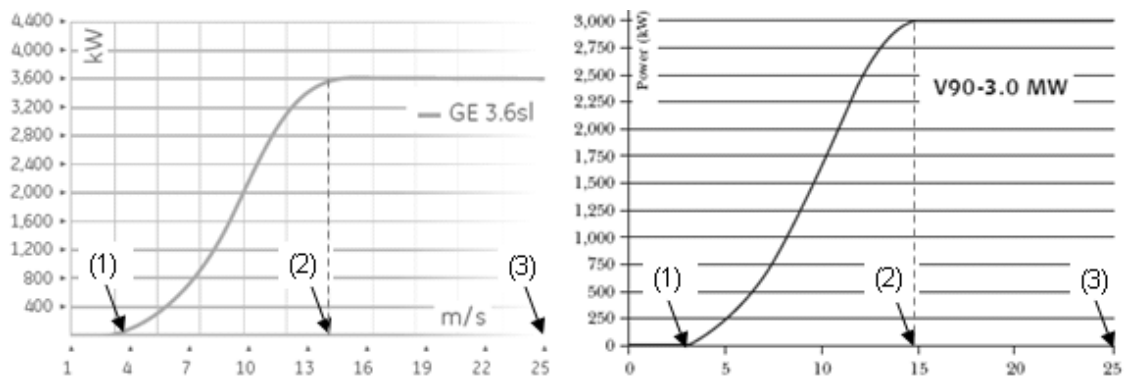


Figure 1.9: Power curve of GE 3.6 MW and Vestas 3MW turbines

Table 1.4: Typical control strategies used for fixed speed and variable speed systems

		Below rated speed Optimized performance	Above rated speed Reduced performance
Fixed speed	Stall controlled	Design aerofoil for laminar flow	Design aerofoil for stall with/without pitching (active/passive stall)
	Pitch controlled	Use fixed pitch and constant speed	Control pitch (difficult as fast pitching is required due to constant speed)
Variable speed	Stall controlled	Control generator torque	Control generator torque
	Pitch controlled	Use fixed pitch and control generator torque	Coordinate pitch and generator torque control

[18, 37]. Due to the difficulty of measuring accurately the wind speed (the anemometer must be able to measure the undisturbed wind flow speed, which is virtually impossible for the feasible positioning of the device [19]) and due to the sensitivity of power output to wind speed (power is related the cubic power of wind speed), measurements are made of a collection of scattered points and the power curve is fitted through the data. Because of the uncertainty in measurements, power curves may not be used to evaluate the exact power output at a certain wind speed [19]. They do however give a good estimation.

1.1.8 Grid integration issues

Grid connected wind generators raise a series of issues due to their fluctuating active power output, demand in reactive power (fixed speed systems), and injection of harmonics by converters (variable speed systems). The difficulty of integration depends, among other

things, on the grid strength¹. In weak grids, penetration of wind energy is often limited because the issues listed below can not be addressed economically.

In the early days, utilities were faced with small SCIGs scattered over the distribution system. The main integration issues were mainly related to voltage and power quality problems such as [18, 38]:

- Steady-state voltage change
- Voltage flicker
- Harmonics (for fully converted IG)

Steady-state voltage changes with the wind farm average production. It depends largely on the system X/R ratio and generator characteristics [18]. For X/R of about 2 (typical range is 0.5-10), voltage fluctuation of the SCIG is the lowest [39]. Voltage flicker refers to fast and small variations caused by switching operations (connection, disconnection) and torque fluctuations (tower shadow, pitch change, turbulence). Various standards are in place, such as the IEC 1000-3-7 and 61000-4-15 (International Electrotechnical Commission), which give guidelines for emission limits and measurement [38]. Harmonics relate to the distortion of the grid voltage fundamental sinewave and are typically caused by inverters. Older inverters (mostly grid commutated, thyristor based) produce integer harmonics in the range of hundreds Hz. Modern inverters (mostly self-commutated, transistor based) have harmonics in the range of kHz which are easier to filter out [38].

The shift towards the DFIG during the last decade has alleviated some of the above integration issues since such generators have smoother power output, are able to control power factor, and use modern power electronics. However, new integration issues are raised because of the increasing size and geographic concentration of modern wind farms. In the recent years, most countries have enforced new grid codes requiring larger wind farms to behave more as conventional plants [8]. Examples of new requirements are:

- Power factor control at point of common coupling (PCC)
- Voltage control
- Frequency control
- Ride through capabilities

¹A wind farm is said to be connected to a strong grid if the short circuit ratio (short circuit level at the connection point over rated capacity of the wind plant) is above 20-25, and weak if it is below 8-10 [38]

The challenge of the above issues are more related to their cost rather than their technical feasibility. Recent studies have shown how the various control capabilities can be achieved by modifying the control algorithm (see Subsection 1.2.2). There are usually requirements for performance sacrifice (operation at less than optimal power capture) [40] and larger or additional compensation devices such as uninterruptible power supplies [41]. It can be argued that when addressing these new integration issues the economics and easiness of implementation put the DFIG and fully converted SG on the same foot. This probably explains the recent shift towards the latter scheme by large manufacturers.

1.2 Background 2: Topics on DFIG

Following the introduction on general topics of wind energy, the present section reviews the main studies related to the dynamical behaviour of the DFIG and its impact on the power system stability. The research results that are relevant to the present thesis can be broadly classified into three areas:

- Modelling
- Control
- Dynamical behaviour in power systems

Before reviewing each of these areas, it is noted that the present work studies modern DFIG with back-to-back transistor based converters. The older configurations, such as slip energy recovery drives (SERD) with diode rectifiers (unidirectional rotor power flow) are not discussed. Details on SERD, DFIG with cycloconverters or thyristor based converters, and history of variable speed wind turbines can be found in [27, 30, 42–44]. Similarly, hardware implementation issues are not in the scope of the present work. Experimental settings and ways of practical realisation of various control schemes (e.g. without rotor speed measurement encoder) can be found in [27, 45–47].

1.2.1 Modelling

Depending on the purpose of the study (power quality, steady-state stability, dynamical stability, protection) different modelling details may be pursued. Clearly, the component subject to or causing the dynamics of interest should be modelled in greater detail, e.g.:

- Mechanical engineers will pay more attention to the turbine and its aerodynamics to ensure structural stability and performance (fatigue, vibration, soundness, efficiency), while electrical engineers will be more concentrated on the generator and its controllers to ensure stable and compliant electrical power production [39].
- For power system stability studies, the interest is in low frequency dynamics over a time frame of 0.1-10 seconds after a fault, hence fast dynamics that are damped out very quickly are ignored [48,49]. For fault current and protection studies, the focus is on the first few cycles after a fault, requiring consideration of subtransients and non-linear phenomena such as magnetic saturation and iron losses [39].

In dynamical studies of wind energy conversion systems (WECS) with DFIG, the modelling is mostly done in a modular fashion [18,22,48,50–52]. This approach allows the testing of different models for a particular module (component) to determine which degree of complexity or simplicity should be used. Below, an overview of the common modelling alternatives for the main components of the wind driven DFIG is given. The specific models used in this work are detailed in Chapter 2.

Turbine

For the turbine, a non-linear algebraic model (i.e. without dynamical equations) is used in power system studies [48,51–53]. The model gives the mechanical torque as function of wind speed, turbine rotational speed and blade pitch angle. Since it is algebraic, it assumes that the torque changes instantaneously with its input variables. In contrast, dynamical models require the modelling of wind power capture dynamics (aerodynamics of windflow around the turbine) with advanced fluid theory and methods. In the context of power system studies, the additional accuracy gained with detailed dynamical turbine models does not justify the extra computational cost [54]. To address the issue, different modelling methods have been proposed to represent the impact of aerodynamics in power system studies.

In these approaches, the focus is essentially on refining the wind speed model. The windflow dynamics are approximated by replacing the incoming wind speed with an equivalent signal that generates an input torque containing the disturbances of interest,

such as dynamic stall and inflow (also known as induction lag, which is the dynamical effect of wake adjustment after wind speed or blade pitch angle change), evening out of wind speed variations over the rotor surface, and tower shadow (dynamical effect of blade passing in front of the tower) [25, 39, 53, 55, 56]. The equivalent wind speed signal is obtained by passing the average wind speed through different functions which can be approximated by first order filters [39] and/or second-order rational functions [53, 56]. With the simpler filters, the accuracy in response is only possible for low frequencies up to 2Hz [39], restricting the applicability of such models.

Apart from the dynamical phenomena accounted with the filtered signals, the stochastic nature of the wind (mean, ramp, gust, turbulence) can be represented by models based on Kaimal spectrum (common stochastic model used for wind speed signal to predict wind turbulence) [48, 53] or alternatively one can use recorded wind speed data [53, 57].

When investigating the impact of the SCIG on the network voltage, detailed model of the wind input is important because for fixed speed generators the wind disturbances are directly translated into electrical torque disturbances [39]. For power system stability studies of the DFIG, it has been observed that the pulsating torque does not seem to have significant impact [57] and it is common to simply assume a constant wind speed [51, 58, 59]. In such case it is argued that the effect of aerodynamics and stochasticity are negligible over the time frame of network disturbance studies (5-30 seconds [59]).

Pitching

Blade pitching is a slow process (in the order of seconds) due to the heaviness of the blades and limited capability of the actuators [48, 60]. This sluggish behaviour must be represented as it can have a significant impact on the required coordination with the electrical torque control (rotor-side converter) [60] and on power system dynamics [51].

The pitching behaviour is usually represented by a first order actuator [50, 53, 58, 61–64] or second order with delay [65]. The simpler model (first order) is used for power system studies, the more detailed model for pitch control design. In few cases, actuators dynamics have been neglected by only considering the controller dynamics with a saturation constraint on the controller output and its rate of change [52]. This approach should however be avoided because it assumes that the pitch angle reaches its setpoint instantaneously.

neously ($\beta = \beta_{ref}$) when the rate limit is not exceeded, or that the outputs of a rate limiter and first order system are identical (which is not the case) when the rate limit is exceeded.

The finite bandwidth (response speed) of the actuators are represented by inserting limiters on the rate of change and actual value of the pitch angle within the first order model [58, 61–63]. A deadzone can also be included for avoidance of too frequent small pitch angle changes which cause unwanted wearing of the components [50, 62, 63].

Drive train

For the drive-train, the common discussion is whether to use the single or two-mass model. The lumped mass model is often suggested simply to follow the modelling approach of conventional power plants [29, 51, 61, 66–70]. On the other hand, the two-mass model has been recommended to reflect the fact that the shaft stiffness in wind applications is typically lower (due to the gearbox) than that of conventional power plants [71–73]. Obviously, soft and stiff drive trains behave differently. One difference is that a softer shaft damps the high frequency input variations [39]. There is however not yet an agreement on whether the lower shaft stiffness has a significant impact on power system stability [51] and recent large scale studies have been performed with both lumped-mass model [37, 59, 67] and two-mass models [44, 58, 74].

By taking a closer look at the research findings, it may be argued that the two-mass model should be preferred. On one hand, for the fixed speed SCIG, it has been shown that the response to large voltage disturbances with the lumped mass model may be over-optimistic [72]. This can be explained by the fact that for a larger inertia (such as the lumped-mass model), the pull-out torque of the SCIG is reached more slowly and hence the stability margin may be overestimated. On the other hand, for the variable speed DFIG, it has been suggested that the one-mass model could be used because the converter control decouples the electrical frequency and generator rotor speed (whose mechanical oscillations can be damped by well-designed controllers) [48]. In other words, since the electrical torque is controlled, assuming different shaft flexibility affects the particular frequency and damping of the mechanical oscillations, but does not change the final steady-state. This is reasonable if the interest is in the final steady-state. However, as rotor speed is the controlled variable, the way it varies (which depends on the shaft model), has

significant impact on the control performance and coordination of the electrical torque (rotor-side converter) and mechanical torque (pitch) control. When assessing novel control schemes such as frequency support capabilities with exploitation of the kinetic energy [31, 40, 67], it may be important to have an accurate estimation of the available and feasible acceleration or deceleration. In such cases, the two-mass model should be used for a more accurate evaluation.

Generator

For the generator model, the practice is to express the machine equations in a rotating two-axis frame so that decoupled control of active and reactive variables can be formulated. Derivation of the model from three-phase to two axis frame (abc-to-dq) are found in [29, 49, 75] and will be recalled in detail in Chapter 2. In such framework, it is assumed that the system is balanced (so that the zero sequence component can be neglected). The exact expression of the induction generator equations given in the literature, may differ according to:

- the choice of state variables: flux [27, 45, 61, 67, 68], current [76], or equivalent voltage behind transient impedance [29, 37, 44, 57, 69, 70, 75, 77],
- whether the dq-frame is rotating at synchronous (most ref.) or rotor speed [47, 75],
- the alignment of the rotating frame: d-axis along stator flux ($\Psi_{qs} = 0$) [27, 37, 57, 61, 69, 76, 77], d-axis along airgap flux [45], q-axis along terminal voltage ($v_{ds} = 0$) [28, 29, 31, 68], or d-axis along terminal voltage ($v_{qs} = 0$) [44],
- whether the q-axis (most ref.) or d-axis [75] is leading,
- whether the abc-dq transformation is power invariant (most ref.) or not [27, 45, 76],
- whether the direction of positive current is defined according to the motor [27, 29, 44, 45, 67, 68, 75, 76] or generator convention [25, 37, 57, 61, 69, 70, 77],
- whether equations are in per unit (most ref.) or actual units [27, 45, 61, 70, 76].

These choices give different arbitrary constant and/or sign, however when the same dynamics are modelled, results on stability and performance are evidently unchanged.

For power system studies, the different generator models relate to whether stator and rotor electrical dynamics are represented. In all the reviewed references, stator transients are neglected for transients studies. The justification put forward is always identical to that given for conventional synchronous generator, namely that stator transients are associated with 50 Hz oscillations [48, 78]. This was shown to be the case for the open-loop DFIG (rotor voltage maintained at a fixed value) [24, 46], for the DFIG with open outer-loop control (no outer-loop feedback, see Subsection 1.2.2) [29, 52], and for the SCIG (zero rotor voltage) [79]. In addition, it has also been suggested that rotor electrical transients can be neglected due to the fast acting of the converter controls [25, 51, 61]. This is because when rotor currents are instantaneously equal to their setpoints (infinitely fast current control), rotor voltage equations are not needed for finding the operating point [30].

Saturation, skin effect, and iron losses (hysteresis and eddy currents) are neglected in power system stability studies because they are mainly important during the first few cycles after a fault, and because they mainly influence the current transients. In other words, these phenomena are more important for loss-performance, sub-transient and transient fault studies. For faults occurring close to the generator, including magnetic saturation in the machine model gives a larger current transient during the first peak period (10 % larger during the first 20 ms [80]) but does not change the dynamical characteristics of the response. Hence, when the interest is in low frequency oscillations, these phenomena are ignored [25, 39, 79].

For the sake of completeness, the different modelling approaches that are commonly used to represent the sub-transient and transient phenomena are briefly mentioned. For example, saturation of the main flux can be modelled by varying the magnetising inductance (instead of assuming it constant) according to the level of flux with an algebraic or differential relationship [79]. For the cage induction machine, observing particular transfer functions showed that saturation influences mainly the amplitude of the response but not its frequency [79]. Iron losses may be represented as equivalent resistance in parallel with the magnetising inductance [79] or finite element methods (FEM) may be used to analyse

their effect [47]. Skin effect can be considered by using a double-cage model [68, 79]. In such models, the current subtransient displacement effects in the rotor are represented with two or more parallel RL-ladder circuits [64]. These models were originally proposed for fault current studies of induction motors. It is noted that the accuracy of these detailed models depend largely on the accuracy of the additional parameters that are required [79].

Converter

For the converter modelling in power system studies, the discussion is often about whether they should be represented as voltage or current sources and whether the dc-link dynamics should be considered (Fig. 1.10). Switchings are not discussed because modern converters with self commutated transistor based design have dynamics in the range of kHz that can be easily filtered out [38, 68, 81]. From the power system stability perspective, the concern is less in the dynamics and filtering of switching effects but more in the control algorithm i.e. the way in which the values of the voltage or current sources are produced.

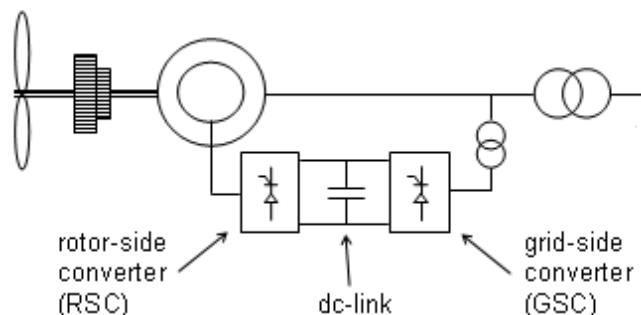


Figure 1.10: Components of the back-to-back converter

The choice between voltage or current source model depends on the assumption made regarding the current-controllers (inner-loop controllers of the converters). If they are assumed to be infinitely fast (infinite bandwidth), the converters are modelled as current sources. This means that controlled currents are instantaneously equal to their setpoint (given by the outer-loop controllers). This approach is often adopted [30, 46, 48, 51, 52, 61, 76] because the typical time constant of the current controllers is in the order of 10 ms [48, 52]. One modelling advantage of the current source model (though not a rigorous argument) is that there are less control parameters that need to be specified since the inner-loop control is simply ignored.

If the limited bandwidth or design of the current controller is considered (e.g. to evaluate the effect of over-current protection), the converters are modelled as voltage sources. In this case, the controlled voltages can be assumed to be equal to their setpoint (given by the inner-loop controllers) [29,37,68] or a delayed version of their setpoint [44].

In most of the reviewed references, the grid-side converter (GSC) is represented as a current source. For the rotor-side converter (RSC), both voltage and current source models have been employed. A comparative study showed that from the power system transient stability viewpoint (defined as the rotor angle stability of synchronous generators on the network) the voltage and current source models give similar response for faults that are electrically far from the DFIG [37]. For faults close to the DFIG however, it is suggested that assuming ideal current controllers may not be suitable [64, 82, 83].

For the dc-capacitor, its dynamics are represented when testing the ability of the GSC to maintain instantaneous active power transfer between the DFIG rotor and terminal (i.e. its ability to maintain constant dc-voltage) [27, 52, 82]. For power system stability studies, if it is assumed that an appropriate control acting sufficiently fast is in place, the dynamics of the dc-link can be neglected and the dc-voltage assumed constant [29,68,77]. It has been suggested that when studying the fault-ride through behaviour of the DFIG, where controller saturation and converter protection are of interest, the dc-capacitor model should be incorporated [82,83] otherwise the triggering of protection devices may not be observed accurately.

Another modelling ‘paradigm’ is to assume the whole converter control as ideal (instantaneous) and consider the DFIG as a controlled electrical torque and reactive power source [48,51]. The value of the electrical torque is determined from the measured rotor speed according to an optimal torque-speed characteristic. The reactive power can be obtained from the voltage error through a PI-control [51] or P-control [48] and a first order lag whose time constant depends on the external network [48]. This model is generic in the sense that no particular control scheme is considered for the torque control, and it is attractive because only few control parameters (voltage loop) need to be specified.

Protection

The modelling of the DFIG protection consists mainly in specifying the sequence of protective actions that is followed when converter current or voltage limits are reached or when the grid frequency is out of the permitted range. Although large frequency deviations are not necessarily fatal for the DFIG, they indicate problems on the external system such as islanding in which case the generator should be disconnected [38]. Over-current situation happens typically when the DFIG terminal voltage is depressed.

In general, the first step is to switch to an open-loop control mode and to prioritize a particular control channel, e.g. by limiting more restrictively the active rotor current thereby prioritizing the reactive power control [51]. If the disturbance is such that the converters are still driven to their limits the next step involves disconnection of the rotor converters and short circuiting the DFIG rotor with crowbars [68, 84]. At this stage if emergency components are provided such as uninterruptible power supply, they may be switched on [41]. For persistent or even larger disturbance the switchgear at the DFIG terminal disconnect the unit [37, 51]. Nowadays with the fault-ride through requirements of revised grid codes, intensive research activities are going on in order to devise innovative ride-through capabilities, e.g. with robust control techniques [85], non-linear methods [86], storage systems [41, 87], or alternative control loops during the fault [88, 89].

Wind farm aggregate model

In power system stability studies, it is common to represent a wind farm with several turbines by one equivalent machine with suitable scaling and adjustment of the transformer and line between the generator and PCC (to account for the wind farm internal cabling) [37, 76, 90]. Alternatively, semi-aggregate models may be used where the electrical part of the wind farm (generator) is aggregated but not the aerodynamical part (wind speed and turbine) and/or mechanical part (drive train) [64]. For stability studies of the electrical transmission system, the single equivalent model is acceptable [51, 64, 91]. Individual representation along with detailed wind speed model taking into account the geographic spread of the wind farm is more important when evaluating the wind farm internal dynamics, such as anti-phase oscillations between turbines (not excited by the electrical network [71]), partial disconnection in some area of the wind farm, etc [64].

1.2.2 Control

As for any controlled system, the behaviour of the DFIG is largely determined by its controllers [24, 39, 68, 92]. These are located in three entities: the rotor side converter, the grid side converter, and the pitch angle controller [48, 50, 53]. The RSC controls the rotor speed and electrical torque (for maximum power capture in subrated regime and for rated power production rated regime), and the power factor or terminal voltage. The GSC controls the dc-link voltage and may participate to power factor control by sharing reactive power production with the DFIG stator [58]. The pitch angle controller is activated in rated regime, where speed control is achieved by both the pitch controller (mechanical torque control) and the RSC (electrical torque control). Electrical control of the converter is very fast in the order of 100 ms [60, 93]. Mechanical control is typically slower [62] due to heavy blades and limited bandwidth of the pitch actuator.

The distinctiveness of the DFIG control resides in the fact that decoupled and simultaneous regulation can be done for active variables (speed, active power or torque) and reactive variables (voltage, reactive power or power factor) [28]. This is achieved by formulating the control algorithm in a synchronously rotating two axis reference frame, with each axis taking care of either the active or reactive control [28]. When the rotor power flow is allowed to flow in both direction, the control can be done over a wide range of rotor speed covering both sub- and super-synchronous speed [27, 28, 30].

In wind driven DFIG, the primary control objectives are to maximise power capture in subrated condition, limit the rotor speed in rated regime and control power factor at all times. Additional control objectives in modern large scale wind farms are to provide frequency control and voltage-ride through (VRT) capabilities. Numerous control schemes have been proposed to realize these objectives. They can be distinguished according to their controller layout, controlled variables, and manipulated variables.

Controller layout

Fig. 1.11 shows two layouts that are often proposed for the controllers of the converter. In the reported literature, the inner-loop current control is always done in a closed-loop fashion with PI-controllers. For the outer-loop control, various solutions have been tested.

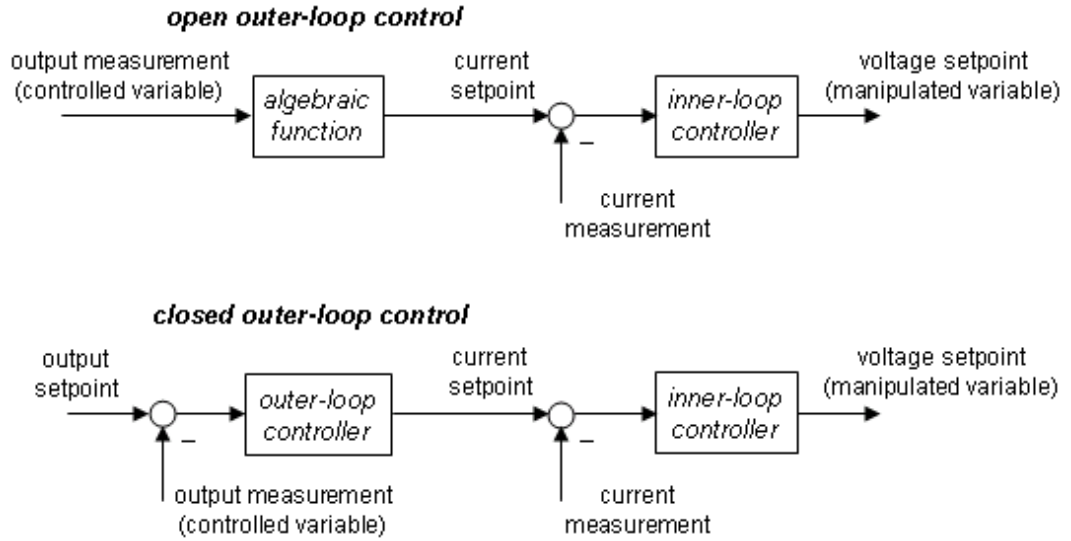


Figure 1.11: Two common layouts for the rotor-side and grid converter control

When the outer-loop control is not closed, the rotor current setpoints are obtained from output measurements processed through some algebraic functions (look-up tables). This scheme has been used for both the reactive power (or voltage) control [45] and speed (or electrical torque) control [29, 46, 61, 68, 69]. This simple approach is generic in the sense that the functions used to obtain the setpoints are derived from the machine equations directly and there is no control parameters to be tuned for the outer-loop. However, the control performance relies on accurate machine parameter values (needed in the algebraic function). In most cases, a steady-state error will be present.

When the outer-loop control is closed, the rotor current setpoint is obtained from an error signal processed by some controller. The controller can be made of a simple proportional gain [29, 48, 69], a PI-controller [30, 50, 53, 58, 67, 76], or a PID-controller [37]. Steady-state errors are eliminated when integral controllers are employed. To ensure tighter tracking, feedforward voltage decoupling terms may be added [27, 69, 76]. To improve stability margins, lead-lag compensators may be inserted [31]. Clearly, the stability and control performance relies on the adequate tuning of the controllers and compensators. Apart from these classical controllers (P, PI or PID), more innovative solutions have been proposed such as fuzzy logic based controllers [30, 70] and non-linear controllers [86]. Although these may offer better performance, their adoption in the industry

is often hindered by the more complex theory and required training.

It is noted that when the converters are modelled as controlled current sources, the inner-loop control is simply ignored as it is assumed that the current controllers have infinite bandwidth (are infinitely fast). In such case, the machine rotor currents are equal to their setpoints ($i_{qr} = i_{qr,ref}$, $i_{dr} = i_{dr,ref}$).

For the pitch controller, a common layout is shown in Fig. 1.12. In most cases, a PI controller corrects the error in the output [53]. Alternatively, it has been suggested that due to wind speed variation, the DFIG is never at steady-state and hence a simple proportional controller is sufficient [48]. Other types of controller such as the PD or PID have also been proposed for better performance [50, 63]. Filters and/or additional control signals may be added to attenuate tower resonance and displacement [94]. However as for any controlled system, there is a trade-off between control action (pitching activity) and number of additional control capabilities [94]. Non-linear control methods have been applied to the pitch controller to consider conflicting objectives in an optimal way [94].

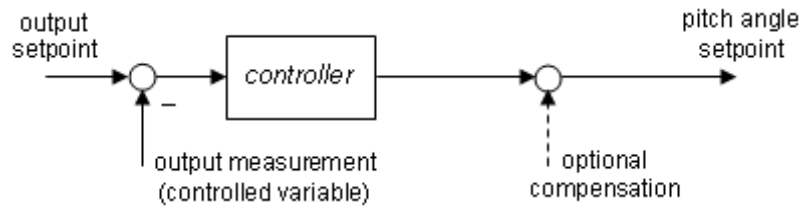


Figure 1.12: Common layout for the pitch angle control

It is recalled that due to the slowness of the pitching mechanism, the pitch angle is not equal to its setpoint, but to a delayed version (typically first order) of it. As a remark, differential pitch control (independent pitch control of each blade) as opposed to collective pitch control has also been suggested [94]. The benefit is a better reduction of the structural loading (fatigue loads). However the effectiveness of such method relies on the availability of measurement of asymmetrical loads over the turbine [94].

Controlled variables

For the *inner-loop control of the RSC and GSC*, the controlled variables are usually the rotor currents. In a few instances, the rotor flux [31] and equivalent internal voltage [84]

have been chosen instead. From an implementation viewpoint, rotor current control (and measurement) is easier. From a theoretical viewpoint, the different options are all valid and should give similar performance because the DFIG torque can be derived as being proportional to each of the considered variables.

For the *active outer-loop control of the RSC*, the controlled variable can be:

- the electromagnetic torque [30, 95],
- the stator active power [50, 76],
- the total active power output (stator and rotor active power) [32, 58, 62, 64, 67],
- the airgap power (electromagnetic torque multiplied by rotor speed) [31, 84],
- the rotor speed [27, 45, 57, 70, 77, 96].

The latter choice (rotor speed control) is claimed to give better tracking performance (maximum power tracking) [27], however it is difficult to realize in practice because the computation of the setpoint requires either reliable online wind speed measurements (not easily obtained) [18], or a mechanical torque observer (not easily designed) [27]. When torque or airgap power is controlled, the setpoint is obtained conveniently as function of the measured rotor speed according to the optimal torque-speed characteristic [27, 48, 68]. Controlling the stator or total active power will give slightly less than optimal operation because the reference power setpoint is obtained from the mechanical input which is the total power plus friction and copper losses. Controlling the electromagnetic torque or the airgap power gives better result as only friction losses are neglected.

For the *active outer-loop control of the GSC*, the controlled variable is the dc-link voltage [27]. Keeping it constant ensures that the rotor power flow is transmitted completely to or from the grid without being stored in the dc-link capacitor.

For the *reactive outer-loop control of the RSC*, the controlled variable can be:

- the stator reactive power [28, 44, 53],
- the power factor [47],
- the terminal voltage [37, 48, 51, 61, 67–69].

When the stator reactive power is controlled, the setpoint can be obtained in different ways and depends on the sharing strategy with the GSC. In theory, any arbitrary reactive power sharing scheme (between the DFIG stator and the GSC) can be chosen as long as

the total reactive power matches the requirement of the network ($Q_{tot} = Q_s + Q_{GSC}$). In practice some choices make more sense depending on the objective being pursued. E.g.:

- One possibility is to impose the magnetisation current (calculated as function of the terminal voltage) as the setpoint of the reactive rotor current [61,68,69]. This makes the DFIG rotor provide the magnetization of the machine. It results in some level of stator reactive power and the GSC has to provide the remaining compensation required for terminal voltage or power factor control.
- Another possibility is to impose zero reactive rotor current [27] with as consequence the reactive power required by the machine flowing completely via the stator. In this case, the rotor current is solely used for speed control thereby minimizing the rotor-side converter losses. However it is done at the expense of the GSC as the latter has to take care of the terminal voltage or power factor control.
- A third possibility is to impose the stator reactive power at a value that minimizes the machine losses [30]. In such scheme the GSC is also operated at non-unity power factor as it has to complement the reactive power production.
- A fourth option is to impose the stator reactive power as the total reactive power required by the network so that the GSC is operated at unity factor [37,48,68,81]. This alternative was shown to be very effective as reactive power injection through the RSC is amplified with a factor $1/s$ where s is the slip [68,97].

Table 1.5 summarises the above sharing schemes.

When the terminal voltage control is done, the reactive rotor current setpoint can be obtained in different ways as well. It can be the output of a PI-controller acting on the terminal voltage error [48, 51, 67]. Alternatively, it can be determined as the sum of a magnetising component (calculated from the measured terminal voltage) and a voltage control component (obtained by amplifying the terminal voltage error) [37,61,68,69].

For the *reactive outer-loop* control of the GSC, coordination is required with that of the RSC so that the reactive demand of the network is met. When the RSC does not control explicitly the terminal voltage or power factor, the task has to be done by the

Table 1.5: Common reactive power sharing schemes between the DFIG stator and GSC

	Stator reactive power Q_s	GSC reactive power Q_{GSC}
1	Q_s so that $Q_r = Q_{r,magn}$	$Q_{GSC} = Q_{tot,ref} - Q_s \neq 0$
2	Q_s so that $Q_r = 0$	$Q_{GSC} = Q_{tot,ref} - Q_s \neq 0$
3	Q_s so that copper losses are min.	$Q_{GSC} = Q_{tot,ref} - Q_s \neq 0$
4	$Q_s = Q_{tot,ref}$	$Q_{GSC} = 0$

Q_r is the rotor reactive power, $Q_{r,magn}$ is the magnetizing reactive power,
 $Q_{tot,ref}$ is the reactive power required by the network, or determined by
an outer voltage control loop

GSC. In such case, the controlled variable can be either terminal voltage or the terminal power factor. When the DFIG controls directly the terminal voltage or power factor, the GSC operates at unity power factor.

For the *pitch controller*, the controlled variable can be either the rotor speed [32, 50, 53, 61, 63–65, 67], or the total active power output [28, 62, 94]. When rotor speed is the controlled variable, the active power may be used to provide a compensation signal [51]. Speed control does not differentiate between shaft acceleration due to increase in wind speed or system faults. In either case, the response (increase in pitch angle setpoint) is appropriate [74]. For power control, a fault in the network or an increase in wind speed give output error of opposite signs, which is less desirable.

Manipulated variables

For the rotor-side converter as a voltage source, the manipulated variables are in most cases the cartesian components (real and imaginary parts) of the rotor voltage (v_{qr} and v_{dr}). It has been shown that polar components (magnitude and angle) of the rotor voltage ($V_{r,mag}$ and $V_{r,ang}$) [98], rotor flux ($\Psi_{r,mag}$ and $\Psi_{r,ang}$) [31], or equivalent voltage behind impedance (E'_{mag} and E'_{ang}) [84] can also be used. Such scheme has been referred to as flux-magnitude and angle controller (FMAC) [31, 84] and was proposed to interpret the control of the DFIG like that of conventional synchronous machines.

Using cartesian or polar components of the rotor voltage or flux results in different control formulation and layout. However, the physics of the DFIG are the same i.e. two control inputs must be specified to the rotor to determine an operating point. The choice of one scheme over the other is more likely to be decided by the practicality and feasibility

of the required measurements. It is not yet clear if one framework performs significantly better or worse, though it was shown that the FMAC has difficulty around synchronous speed [84].

Control for large wind farms

As mentioned in Subsection 1.1.8, frequency control is presently required for larger wind farms. This dynamical capability can be achieved in two ways. For short term support (duration for the SG governors action to take place), the kinetic energy of the DFIG rotor and turbine may be used by extracting/storing power out of/into it. This can be done by imposing additional control signal in the active control loop of the RSC [31, 67, 95]. One issue with this method is that input torque (mechanical torque) changes with rotor speed, hence the turbine may be driven inadvertently into stalling mode when extracting kinetic energy. This would reduce the output power and as a consequence inhibit the frequency control. Another issue is that sufficient kinetic energy must be available, hence the performance of this frequency support method depends on the initial rotor speed (how far away from minimum or maximum). More quantitative investigations are needed to address these issues.

The second way of providing frequency control is to operate the turbine with partial deloading [32, 40, 67, 99]. This is feasible on large scale and over a realistically longer period. The drawback however is extraction of less than optimal wind power, which is more of an economical issue rather than a technical one. Depending on the required degree of control flexibility, partial deloading may require the pitch control to be active at all time [32]. In such case, pitching activity would be increased and more important wearing of the components would be expected.

To conclude, other innovative control schemes for large wind farms have been explored, such as coordination with external system components and hierarchical control within the windfarm. By sending the DFIG status to on-load tap changers on the network (which requires additional communication links) better voltage control can be achieved in a particular area [97]. By formulating the wind farm control in a hierarchical structure, individual command for active and reactive power of the turbines can be computed in order to provide the requested output at the point of common coupling and simultaneously

minimise losses within the wind farm [32, 40].

1.2.3 Dynamical behaviour in power systems

In the reported literature, the impact of the DFIG on the power system stability has been assessed primarily by comparing it to the SG and SCIG. The study approaches have consisted in both time domain and eigenvalue analysis. Time domain studies have been used to investigate the voltage recovery profile of the DFIG following severe network faults [57, 59, 67], and the critical clearing time (CCT) of synchronous machines on the network [37, 58, 72, 77]. Eigenvalue analysis has been used to see how the low-frequency oscillating modes of the synchronous machines are affected [59, 74, 84, 100, 101].

One salient characteristic of the DFIG with respect to its synchronous and fixed speed counterparts, is the decoupling between the grid frequency (electrical) and the rotor speed (mechanical) due to the converter controls [25, 48]. As the electrical torque is explicitly controlled, variation in mechanical input torque (due to wind speed variation, shaft torsion, tower shadow) translates into speed variation dictated by the torque unbalance rather than electrical torque variation as in fixed speed generators. Because of the high inertia, rotor speed change is small and hence the output power variation is limited. This is also why variable speed generators are said to act as buffer of wind speed variations [25, 48].

A second notable difference of the DFIG with respect to both the SG and SCIG is its better controllability. For the SCIG any dynamical control has to be provided by additional components (e.g. dynamic voltage compensator). For the SG since all the control is done by regulating the field voltage magnitude, additional control such as power system stabilizer capability is realized at the expense of voltage control performance [84]. For the DFIG, the control flexibility is greater since two independent variables (rotor voltage direct and quadrature components) are used to control output variables.

From the time domain studies, it has been shown as expected that, compared to the SCIG, the voltage recovery profile of the DFIG is much better [57, 67]. One obvious reason is that unlike the SCIG where the uncontrolled reactive power demand is very sensitive to voltage level and rotor speed, the DFIG can control its reactive power or terminal voltage independently of rotor speed. The voltage behaviour of the SCIG is

typically poor because at fault clearing the machine has accelerated, resulting in higher currents (along with higher active and reactive power magnitude) and more important longer lasting voltage drop in the network lines [57]. If the SCIG has exceeded its pull-out torque the machine accelerates further and may be tripped by overspeed protection logic [57]. Compared to the synchronous generator, the DFIG with power factor and VRT control has a slower voltage recovery profile [58]. With voltage and VRT control, the DFIG voltage recovers better than that of the SG [59, 67].

For the CCT criteria, the DFIG gives also better result compared to both the SCIG [37] and SG [58] (i.e. when replacing the SCIG or SG by a DFIG), which can again be explained by the better controllability of the DFIG.

From the eigenvalue studies, it has been shown that the DFIG does not introduce problematic oscillatory modes [100]. Replacing an SG by a DFIG gives better damping of the network lower oscillation frequency modes (inter-area modes) [59, 74, 84, 100, 101] because in such scenario, the size of the total synchronous inertia that participate into system oscillations is reduced [100]. Mode shape analysis has shown that indeed the DFIG does not contribute (neither positively or negatively) to inter-area mode [74]. In fact with suitable control design, the DFIG can even actively improve the network oscillation damping [84]. This requires that the DFIG output power is injected into the grid so that it produces an electrical torque component in the SGs that is in phase with their rotor speed [84]. The design of such compensator for the DFIG may not be a trivial task depending on the network and SG location.

1.3 Present thesis

1.3.1 Objectives

The objectives of the present thesis is to study the small-signal behaviour of the DFIG in view of building a better understanding of its inherent dynamics and effect on the external system. The research questions of interest can be summarised as follows:

- *Inherent dynamics of the DFIG*: Which variables are coupled or decoupled? What are the typical oscillations frequencies and damping? What are they caused by?

- *Influence of machine parameters and operating condition:* How sensitive are the DFIG dynamics to machine parameters and operating point? Is there any case for which the system is unstable? When is it more stable and when is it closer to instability?
- *Role of the controllers:* What is the difference between open-loop and closed-loop operation? How do the control settings change or determine the behaviour of the DFIG?
- *Effect on the external network:* What distinguishes the DFIG from the SG and SCIG? What are the consequences in terms of behaviour in the power system?

1.3.2 Motivation

As reviewed in Section 1.1, the DFIG is one of the preferred option for variable speed wind energy conversion systems. The advantages are its wide range of feasible rotor speed, reduced mechanical stress, reduced power electronics rating and optimized power capture. These technical and economical characteristics have motivated the introduction of the technology in modern wind farms. To facilitate its further integration into the power system, it is therefore important to assess its dynamical behaviour, performance and impact on the network. The present work aims at contributing the understanding of the DFIG in that respect.

The review of Section 1.2 helped identify the above research questions. Some of these have been addressed in the reported literature and Section 1.2 provided a summary of the main results. It was shown that the dynamics of the DFIG has been mostly assessed with time domain studies and modelling practice has followed essentially that adopted for conventional synchronous machines (neglecting stator transients, one mass drive train, etc). The present work takes an alternative approach (eigenvalue analysis) in order to provide analytical justifications and additional observations.

The results and conclusions made in this thesis are obtained from theoretical studies, as opposed to experimental ones. Since assumptions have a significant impact on this type of study, a considerable part is dedicated to the derivation of the mathematical models.

In addition, as the dynamical behaviour of the DFIG is determined by its controllers, the tuning of the control settings is also examined. The importance of the controllers and the non-triviality of their tuning have been recognized [70, 81], hence the details of how the control parameters are obtained in this work is provided. Understanding how the DFIG dynamics are influenced and modified by the controllers helps in the tuning process; hence this was identified as one of the research questions.

1.3.3 Approach

The research questions of Section 1.3.1 can be answered by experimental studies, simulation studies, or analytical analysis. The present work considers the latter approach. In first instance, the DFIG is considered in normal operating conditions and under small disturbances so that linear system theory such as eigenvalue analysis can be applied.

The eigenvalues of a system contain a whole spectrum of information. They indicate for example the stability of the system and they can be used to determine the coupling between the system's variables or to tune the system's controllers. In power system studies, it has been typically used to assess the oscillatory behaviour of synchronous machines. In this work it used to analyze the doubly-fed induction generator itself.

Also, eigenvalue analysis is a convenient tool that can be automated to examine the problem in a systematic way. It offers an alternative interpretation of the system behaviour and can reinforce the results obtained with simulation studies. It also allows the justification of certain modelling practice such as two-mass drive train and neglect of both stator and rotor electrical transients after appropriate control design.

1.3.4 Contributions

The contributions of the present work can be summarised as follows:

- *Improving the understanding of the DFIG modelling:* Usual practice and purpose of the different modelling alternatives are reviewed for the building blocks of the DFIG wind turbine. The relevant models are derived and typical parameters that are available in the literature are compared. Recommendation is made for selecting the appropriate model for the purpose of this work.

- *Improving the understanding of the DFIG dynamics:* Steady-state, open-loop and closed-loop behaviour are examined in detail. From the steady-state analysis, the sign of the process gains are determined and the impact on DFIG control design is explained. From the modal analysis of the open and closed-loop system, the typical time frame and characteristics of the different dynamical parts are determined and the effects of closing the control loops are identified.
- *Investigating further the distinction of the DFIG with respect to the SG and SCIG:* It is well known that unlike the SG the DFIG is an asynchronous machine and that unlike the SCIG the DFIG is fed with non-zero rotor voltage. Additionally, variability of the speed and controllability of the electrical torque result in decoupling of electrical and mechanical dynamics. The impact of this feature on the modelling adequacy is examined.
- *Proposing a tuning procedure for generic PI-controllers:* The effect of the control parameters on the location of the eigenvalues are identified. The result allows a pole placement process which considers the poles of both DFIG and controllers. The range of parameters value that can not be used for stability and resonance reasons are determined. A step-by-step method is formulated and the robustness of the resulting controller is verified.
- *Explaining the observations made in previous research:* Among other points, it is shown that the poorly damped mode near line frequency observed in [46] as being the stator mode, is indeed the stator mode but for the open-loop DFIG. For the closed-loop DFIG, the situation is different because of the rotor-side converter control actions. It is also shown why voltage control parameters should not be too high as stated in [51]. The answer is obtained by examining the sensitivity of the DFIG electrical dynamics to these particular control parameters.
- *Implementing an automated routine for eigenvalue analysis of a grid connected DFIG:* The grid can consist of a simple infinite bus or it can consist of a network with multiple synchronous machines and other DFIGs. The routine performs a full

initialization of the DFIG for specified load flow configuration. Different model assumptions such as omission of the DFIG electrical transients can be tested. Root-loci are obtained conveniently so that the effect of control parameters, machine parameters or operating point can be assessed in a systematic fashion.

1.3.5 Layout of the thesis

The present thesis can be divided in two main parts: *Modelling* and *analysis*.

The next chapter describes the modelling of a wind turbine with doubly-fed induction generator. The models that are suitable in the context of this work, namely eigenvalue analysis of the DFIG from the power system viewpoint, are reviewed in detail.

In the analysis part, the study begins with the steady-state behaviour in Chapter 3. Comparison is made with the conventional SCIG and differences are highlighted. In Chapter 4, the open-loop system is examined. The inherent dynamics are identified and similarities with the SCIG are observed. Chapter 5 presents the behaviour of the closed-loop system and proposes a tuning procedure for generic PI-controllers. Finally in Chapter 6 a multi-machine network with both SG and DFIG is analysed.

Conclusions and discussions are summarized in Chapter 7. Future work is also discussed.

Chapter 2

Modelling

Eigenvalue analysis requires a set of equations representing the system dynamics. The first part of this work consists therefore in determining a suitable mathematical model that can be used to answer the research questions listed in Subsection 1.3.1. As reviewed in the previous chapter, many modelling alternatives have been proposed (Subsection 1.2). The models chosen for the purpose of this work are described in the following. For each component, the different modelling approaches proposed in the literature are briefly explained, the justification for selecting a particular model is given, and the model equations are presented.

2.1 Turbine

For the turbine modelling, it is important to understand the airflow dynamics around the structure because the resulting unsteady forces determine the turbine performance (energy yield), structural loads and acoustic noise. Inaccurate predictions may lead to non-optimal design, larger capital investments and larger operation/maintenance costs.

From a mechanical aspect, the turbine converts power by withstanding various kinds of stresses due to the air movement surrounding the turbine. Hence the detailed airflow dynamics are of interest to the turbine designer because they determine the soundness and fatigue life of the structure.

From an electrical viewpoint, the turbine applies an input torque on the drive train. Any unbalance with respect to the load torque applied by the generator translates into acceleration or deceleration of the shaft and associated variation of electrical variables.

Hence for the electrical engineer, the interest is mainly in the dynamics of the input torque, while the complex airflow dynamics and associated mechanical vibrations and deformations may be ignored.

2.1.1 Modelling approaches

Broadly speaking, there are two approaches to calculate the turbine input torque. In the first approach, referred to as ‘theoretical approach’ in this work, airflows surrounding the turbine are modelled so that forces on the blades and hence torque on the shaft can be calculated. In the second approach, referred to as ‘empirical approach’ in this work, the input torque is expressed as an algebraic function of selected input variables (wind speed, pitch angle, turbine speed). Table 2.1 shows the main turbine modelling methods that are used presently. The different methods are described in the following subsections.

Table 2.1: Turbine modelling approaches and methods

Theoretical approach	Empirical approach
- Blade element theory methods	- Constant input power or torque
- Engineering models	- Algebraic C_p curves
- Wake methods	- Dynamical C_p curves
- Computational fluid dynamics methods	

Theoretical models are extremely computational intensive and mostly used for turbine design. Empirical models are satisfactory for power system studies and give a right balance between accuracy and complexity. Although theoretical methods are not used in this work, they are briefly reviewed for a better understanding of wind turbine modelling issues.

2.1.2 Theoretical modelling methods

The aerodynamics of a wind turbine are quite complex because the flow field surrounding the structure results from many types of interacting sources, as shown in Table 2.2, making both measurements and calculations difficult [102]. Some sources are mostly periodic such as the wind flow itself, the yawing system related oscillations (oscillation of the nacelle about the tower axis), and the tower shadow effect (passage of the blades in front

of the tower which modifies the free wind flow). Other sources are mostly aperiodic such as turbulence (gusts), wake behaviour (disturbed fluid movement further behind the turbine), and blade-wake interactions.

Table 2.2: Aerodynamic sources contributing to turbine airloads

Mostly periodic	Mostly aperiodic
- Wind inflow	- Wind turbulence
- Yaw dynamics	- Wake dynamics
- Tower shadow	- Blade-wake interactions

The theoretical description of fluid flows are given by the so-called Navier-Stokes equations (equations of motion for viscous fluids) [103]. Analytical solutions are only known for few special cases and numerical solutions present stability difficulties and require prohibitive computational time. In non-academic environment, simpler modelling strategies are used [18].

The theoretical modelling strategies used in practice can be roughly classified into three types: blade element (BE) theory based methods, wake model based methods and computational fluid dynamic (CFD) methods [18, 103]. In BE methods also known as strip theory methods, the blades are divided in small sections and the forces on each of them are calculated. These are then converted into accelerations and integrated into velocities and positions. In wake methods also known as vortex methods, a more complex model is considered for the actual flow field. The wake behaviour further upfront and further behind the turbine is considered. It usually predicts fluctuating torques that are not forecast by BE methods. In CFD methods, the solution of the Navier-Stokes equations are approximated numerically. Table 2.3 summarises the main modelling alternatives and their validation status; more details can be found in [54].

A fourth type of theoretical modelling approach consists in the so-called ‘engineering models’, which were formulated to address slow unsteady flow phenomena [104]. In terms of complexity, engineering models lay between the BE and wake methods. Slow unsteady flow phenomena (5~10 s) relate to the ‘dynamical inflow’. They account for the influence of the time-varying wake vorticity (rate of rotational spin in a fluid) on the inflow velocity in the rotor plane. Dynamical inflow may have some effect during events

Table 2.3: Theoretical turbine modelling alternatives and validation status

BE methods	Wake methods	CFD methods
- BE theory only (experimental data needed a priori)	- Prescribed wake (geometry fixed or limited)	- Euler (non-viscous form of N-S equations)
- BE + momentum theory	- Free wake	- Navier-Stokes
- Acceptable predictions under simplified conditions	- Predictions with mixed performance	- Consistent and realistic simulations of flow field
- Implemented in aeroelastic design codes	- Simplest versions implemented in design codes	- Not yet validated enough for design purpose
→ → Increasing complexity → →		

happening on the same time scale, such as windgusts (few seconds), blade pitching actions (0.5~2 s) and yawing operations (1~2 s). In [104] it is argued that the pitching transients and overshoots in shaft torque measured on the Tjaereborg 2 MW turbine (Oye, Technical University of Denmark) are due to dynamical inflow; models are proposed to represent the effects.

A comparative study of various aerodynamic models can be found in [105]. The study involved 30 experts from 18 organisations and models were generated from 19 different turbine modelling tools. Predictions were made for precise conditions and measurements were carried out in the same conditions (Nasa-Ames wind tunnel test). In order to avoid reluctant participation, results were not identified by modeller and were compared anonymously. The results clearly showed that there were significant differences between the various predictions and also significant deviations from measurements. For example, turbine power predictions ranged from 25 to 175% of measured. This unfavourable conclusion reflected the complexity of the subject and need for improvement.

2.1.3 Model for power system studies

The theoretical methods reviewed in the previous subsection are mostly used for wind turbine design and wind farm economic evaluation. In these cases detailed modelling is desired because the design and economic value are very specific to the site and turbine considered. In power system studies it is more desirable to use generic models representing a whole class of wind turbine (e.g. megawatt variable speed wind turbines). Hence

simple models that are less computational intensive and yet capture turbine power conversion process are preferred.

The simplest turbine model is to assume a constant input power or torque, which is the same as assuming constant wind speed, rotor speed and pitch angle. This model can be used in small network disturbance studies with constant wind speed because in such cases, the variation in rotor speed and hence pitch angle is small. Obviously, for studies with changing wind speed or significant rotor speed variation, this model can not be used.

A more realistic assumption is to use the algebraic relationship $P_t = C_p P_w$ where P_t is the turbine power, P_w is the wind power and C_p is performance coefficient representing the portion of wind power that is extracted by the turbine. The expression for P_w is obtained as follows [16]. The kinetic energy of a mass of air m moving at an average speed v_w is $E_k = 0.5 m v_w^2$. The associated power is equal to the rate of change of E_k , i.e. $P_w = d(E_k)/dt = 0.5(dm/dt)v_w^2$ where dm/dt is the mass of air transferred per unit time. If the air is passing through an area A then $(dm/dt) = \rho A v_w$ where ρ is the air density. Hence the power of the air passing through that area is $P_w = 0.5\rho A v_w^3$ and the extracted turbine power is $P_t = C_p P_w = 0.5 \rho A C_p v_w^3$.

In BE methods, C_p is determined analytically by integrating the force and torque of each blade section over the blade length for all the blades. For generic power system studies, numerical approximations expressing C_p as function of tip-speed ratio λ and pitch angle β may be used [50, 61]. Hence if R is the blade length, the turbine model is:

$$P_t = 0.5 \rho \pi R^2 C_p(\lambda, \beta) v_w^3 \quad (2.1)$$

Examples of expressions for $C_p(\lambda, \beta)$ are given in the next subsection. The model in (2.1) is a non-linear expression relating turbine input power to wind speed, pitch angle and turbine speed. It is an algebraic model where airflow dynamics are ignored, hence turbine power changes instantaneously from one operating point to another when there is a change in wind speed, tip-speed ratio, or blade pitch angle.

Dynamical C_p models have been proposed to represent aerodynamics related transients such as dynamic stall [106] and dynamical inflow [107]. Dynamic stall happens during rapid aerodynamic changes. It can result in high transient forces when the wind speed increases and it usually delays the static stall behaviour (stall by design) [18]. The

associated time constant is in the order of the time for the relative wind to traverse the blade chord. For large wind turbines, the associated time scale is about 0.2 sec at the blade root to 0.01 sec at the blade tip. Dynamical inflow relates to the flow field dynamics due to turbulence or changes in the turbine operation (rotational speed or blade pitch angle). It can result in larger transients turbine loads [18]. The associated time constant is in the order of $2R/v_{w,av}$. E.g. for a large wind turbine with blade length $R = 40$ [m] and average wind speed $v_{w,av} = 15$ [m/s], the time constant is in the order of 5.33 [s]. It has been suggested in [104] that dynamic inflow transients occur ‘in the good direction’, e.g. when the pitch angle increases the turbine torque first decreases excessively before stabilising to its new operating value and vice versa.

Dynamical C_p models are not considered in this work because dynamic stall and dynamical inflow are more relevant for turbine efficiency or fatigue studies. For power system stability studies, dynamical stall is a relatively fast phenomenon. Neglecting it means that overshoots may be underestimated, however the overall dynamical behaviour of the turbine-generator would not change significantly. For the dynamical inflow phenomenon, the result in [104] suggests it is more conservative not to consider it. More detailed validation is needed for the relevance and suitability of the proposed dynamical models for power system stability studies, however this is out of the scope of the present work.

2.1.4 Parameters data

In general, C_p curves are provided by manufacturers from field testing [18]. For academic purpose, numerical approximations can be used [22]. An example of generic expression for the performance coefficient is [22, 108]:

$$C_p(\lambda, \beta) = c_1 \left(\frac{c_2}{\lambda + c_8\beta} - \frac{c_2 c_9}{\beta^3 + 1} - c_3\beta - c_4\beta^{c_5} - c_6 \right) \exp\left(\frac{-c_7}{\lambda + c_8\beta} + \frac{c_7 c_9}{\beta^3 + 1} \right) + c_{10}\lambda \quad (2.2)$$

where β [deg] is the pitch angle and λ the tip speed ratio (ratio between the speed at the tip of the blade and average wind speed):

$$\lambda = \frac{\omega_t R}{v_w} \quad (2.3)$$

In (2.3) ω_t [rad/s] is the turbine speed, R [m] is the blade length, and v_w [m/s] is the average wind speed. Parameters from different references are given in Table 2.4.

Table 2.4: C_p curves parameters from different references.

	c_1	c_2	c_3	c_4	c_5	c_6	c_7	c_8	c_9	c_{10}
Heier [22]	0.5	116	0.4	0	0	5	21	0.08	0.035	0
Matlab [108]	0.5176	116	0.4	0	0	5	21	0.08	0.035	0.0068
SI01 [61]	0.22	116	0.4	0	0	5	12.5	0.08	0.035	0
SI03-CS [48]	0.44	125	0	0	0	6.94	16.5	0	-0.002	0
SI03-VS [48]	0.73	151	0.58	0.002	2.14	13.2	18.4	-0.02	-0.003	0

CS = constant speed, VS = variable speed

The typical shape of C_p curves can be observed in Fig. 2.1, which shows the curves for the parameters of Table 2.4. Heier [22], Matlab [108] and Sloodweg01 [61] give similar C_p curves, while SI03-CS and SI03-VS [48] describe different types of turbine. The latter curve approximates the performance of the GE 1.5 and 3.6 MW DFIG [48, 51].

The maximum performance C_{pmax} is reached when the blade pitch angle β is zero. The tip-speed ratio at which this occurs is the optimal tip-speed ratio λ_{opt} . Table 2.5 gives C_{pmax} and λ_{opt} for the C_p curves of Table 2.4. In subrated conditions (when power produced is less than rated power), variable speed wind turbines are controlled so that their operating point on the C_p curve stays around C_{pmax} . This is achieved by maintaining the tip speed ratio at λ_{opt} by adjusting the rotor speed appropriately as the wind speed changes.

Table 2.5: Maximum C_p and corresponding optimal λ

	C_{pmax}	λ_{opt}
Heier [22]	0.411	7.954
Matlab [108]	0.48	8.1
SI01 [61]	0.4382	6.325
SI03-CS [48]	0.4906	8.7622
SI03-VS [48]	0.4412	7.2064

For a DFIG operating initially at C_{pmax} at a given rotor speed, if the wind speed increases suddenly (wind gust), the tip speed ratio decreases and the operating point on the C_p curve falls in the positive slope region. Similarly for a DFIG operating initially at C_{pmax} at a given wind speed, if the rotor speed increases suddenly (e.g. due to a fault on

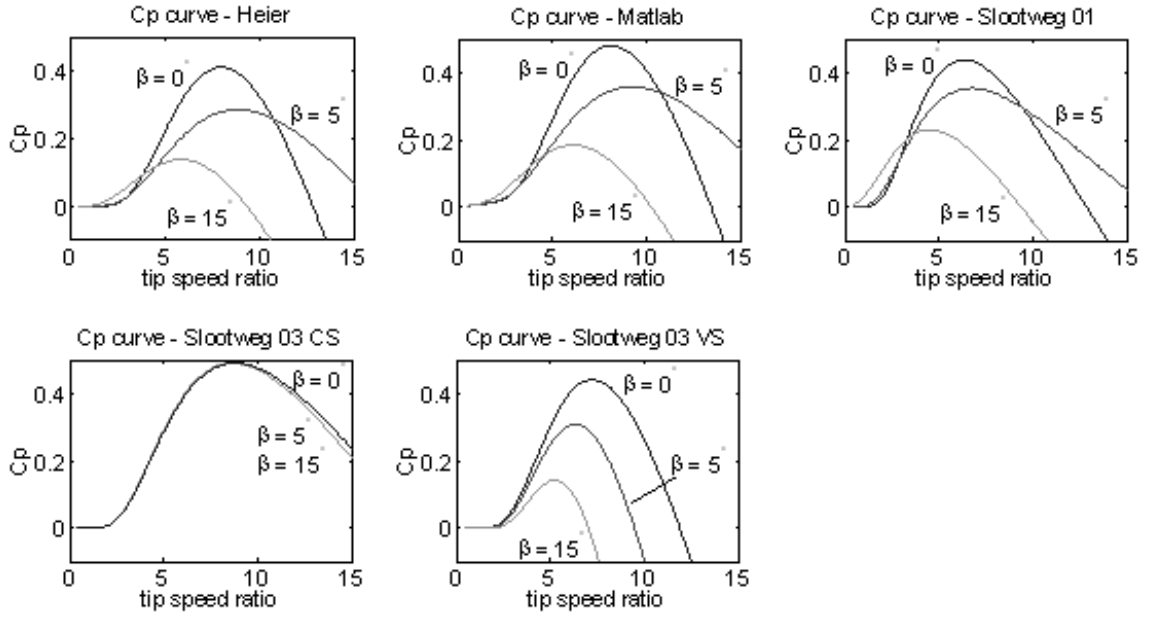


Figure 2.1: C_p curves as function of tip speed ratio with pitch angle (β) as parameter

the network), the tip speed ratio increases and the operating point on the C_p curve falls in the negative slope region. In both cases, the performance coefficient and hence the captured and produced power by the DFIG is less than optimal right after a disturbance.

In rated regime, speed control can be done by stall regulation or by variable pitch regulation. In stall control, the operating point goes on the ‘left’ of the C_p curve, where the blade is in stalling mode [63] the wind flow becomes partially detached from the blade surface. In pitch regulation the operating point stays on the ‘right’ portion of C_p curve where the wind flow is laminar i.e. stays attached to the blade surface. Stall control does not require pitching mechanism however requires better overtorque capability and corresponding rating adjustment of the generator [27].

In practice, dimensions of the turbine are also given by the manufacturer. For generic studies where numerical approximations of C_p curves are used, the parameters of the turbine can be computed from (2.1). This is done by considering the operating point where the turbine goes from subrated to rated conditions. At this operating point the turbine produces rated power P_{rated} , the wind speed is the rated wind speed $v_{w,rated}$ and

the coefficient performance is at its maximum $C_{p,max}$, hence:

$$R = \sqrt{P_{rated}[W]/(0.5\rho\pi C_{p,max}v_{w,rated}^3)} \quad (2.4)$$

From (2.4), for a given P_{rated} and $v_{w,rated}$, the higher $C_{p,max}$ the lower R . This is as expected since the higher the performance, the more efficient the turbine and hence the smaller the required swiped area to capture a given level of wind power. Table 2.6 shows indeed that for a given P_{rated} and $v_{w,rated}$ the rotor radius R obtained with the ‘Matlab’ C_p curve ($C_{p,max} = 0.48$) is the smallest.

At rated wind speed, the tip speed ratio relationship in (2.3) gives the turbine rated speed $\omega_{t,rated}$ [rad/s] and the blade rated tip speed $\omega_{t,tip}$ [m/s] as:

$$\omega_{t,rated} = (v_{w,rated}\lambda_{opt})/R \quad (2.5)$$

$$\omega_{tip,rated} = \omega_{t,rated}R = v_{w,rated}\lambda_{opt} \quad (2.6)$$

From (2.6), the blade rated tip speed depends only on λ_{opt} for a given $v_{w,rated}$. To avoid excessive rotational blade tip speed, the blade design should ensure that the optimal tip speed ratio λ_{opt} is not too high. This is shown in Table 2.6, where the blade rated tip speed is the lowest for the ‘SI01’ C_p curve ($\lambda_{opt} = 6.325$).

Table 2.6: Turbine parameters obtained for different C_p curves

C_p curve	P_{rated} [MW]	$v_{w,rated}$ [m/s]	$C_{p,max}$	R [m]	λ_{opt}	$\omega_{tip,rated}$ [m/s]	$\omega_{t,rated}$ [rad/s]	$n_{t,rated}$ [rpm]
SI01 [61]	3	12	0.4382	45.38	6.325	75.90	1.67	15.97
	5	12	0.4382	58.58	6.325	75.90	1.30	12.37
Heier [22]	3	12	0.411	46.86	7.954	95.45	2.04	19.45
	5	12	0.411	60.49	7.954	95.45	1.58	15.07
Matlab [108]	3	12	0.48	43.36	8.1	97.20	2.24	21.41
	5	12	0.48	55.97	8.1	97.20	1.74	16.58

To summarize the above observations, $C_{p,max}$ should be made as high as possible to keep the rotor blade length within reasonable limit, and λ_{opt} (λ at which $C_{p,max}$ is reached) should be made as low as possible so that the blade tip speed stays within acceptable limit. $C_{p,max}$ and λ_{opt} are design parameters (they depend on the airfoil shape, material, etc).

In the above procedure, turbine dimensions are calculated from a theoretical C_p curve. In practice, the process is reversed. The rated wind speed $v_{w,rated}$ is decided from statistics

collected at the wind farm site. Turbine dimensions P_{rated} and R are determined from design criteria and technology. The C_p curve is subsequently obtained by field testing. Due to confidentiality reasons, these parameters are rarely fully disclosed. In this work, where the focus is on generic modelling, the parameters are calculated as in (2.4).

2.2 Drive train

The drive train of the wind turbine can be represented as a series of rotating disks connected by shafts [18]. If the disks are rigid and the shafts are massless the system differential equations are obtained by writing Newton's motion equation for each disk angular speed. If the disks have some elasticity and the shafts have some distributed mass, wave equations with their continuity boundary conditions have to be established for each body [109].

From a mechanical viewpoint, drive train shafts are subject to twisting stresses. Hence, for the drive train designer a detailed model is needed in order to evaluate these stresses and determine the shaft strength required. From an electrical aspect, reduced order models can be used as long as electrical variable variations caused by drive-train dynamics are correctly represented.

In power system stability studies, it is reasonable to consider the turbine, gearbox and generator as rigid disks and shafts as massless torsional springs [18]. These assumptions are acceptable when comparing the components relatively. The turbine, generator and gearbox have negligible twisting compared to the shafts. The shafts have negligible mass compared to the turbine and generator.

2.2.1 Terminology

For easier discussion, some concepts that are used in the description of rotating mechanical systems are briefly defined here, for more details see [109].

Area moment of inertia J_a : Also known as the second moment of area, J_a is a property of shape indicating its resistance to bending and deflection. It is defined as $J_a = \int r^2 dA$ [m⁴] where r is the perpendicular distance of the area dA from the rotation axis.

Mass moment of inertia J : Also known as angular mass, J describes the mass distribution of a rigid body rotating about an axis. It is defined as $J = \int r^2 dm$ [kg m²] where r is the perpendicular distance of the mass dm from the rotation axis.

Torsional Stiffness k : For torsional systems represented by equivalent spring-mass models, the constant k called stiffness or spring constant relates torque to angular displacement. It has units of [Nm/rad] and is defined as $k = T_{sh}/\theta_{tw} = GJ_a/l$ where T_{sh} [Nm] is the shaft torque, θ_{tw} [rad] the twist angle, G [N/m²] the shaft material modulus of rigidity (material constant), l [m] the shaft length, and J_a [m⁴] the area moment of inertia. The stiffness of a shaft is its resistance to twisting when experiencing a torque, i.e. the amount of torque T_{sh} required to twist the shaft by an angle θ_{tw} . It depends on the material and is lower for shafts that are longer with smaller cross-section.

A parallel or series connection of n springs with stiffness k_1, k_2, \dots, k_n can be reduced to an equivalent spring with stiffness $k_{eq,par} = k_1 + k_2 + \dots + k_n$ or $k_{eq,ser}^{-1} = k_1^{-1} + k_2^{-1} + \dots + k_n^{-1}$ respectively. In a parallel connection the equivalent stiffness is larger than the initial largest stiffness. Conversely, in a series connection the equivalent stiffness is smaller than the initial smallest stiffness.

Gearred systems: For geared system, the low speed angular mass J_{LS} and stiffness k_{LS} can be referred to the high speed side by establishing kinetic and potential energy balance respectively [109]. The result gives $J'_{LS} = J_{LS}/n_{gb}^2$ and $k'_{LS} = k_{LS}/n_{gb}^2$ where J'_{LS} and k'_{LS} are the low speed parameters referred to the high speed side, n_{gb} is the gearbox ratio.

From the above definitions, it is seen that stiffness depends on material and geometry of the shaft. For geared system the impact of the parameter n_{gb} (gear ratio) is the highest. A large n_{gb} gives a low (inversely proportional to n_{gb} squared) equivalent stiffness when viewed from the high speed side (referred value). This is the reason why WECS drive train with gearbox is much more flexible than conventional drive trains.

2.2.2 Modelling alternatives

Fig. 2.2 shows a schematic representation of the DFIG drive train. A natural translation of the physical system into mathematical equations would be a 5th order model with three masses (turbine, gearbox and generator) and two shafts (low-speed and high-speed).

Depending on the point of interest and system characteristics, simplified models may be used as shown in Table 2.7.

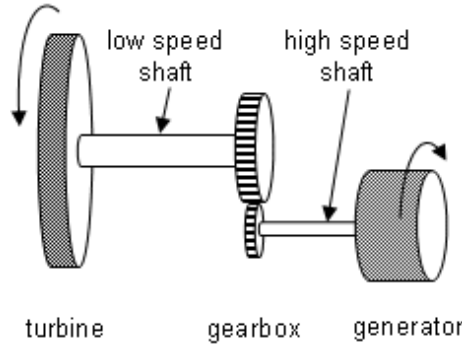


Figure 2.2: Schematic representation of the drive train

Table 2.7: Drive train model alternatives

3-mass 2-shaft (5 th order)	- LS and HS shaft are flexible (2 DE) - $d\omega/dt$ is different for each mass (3 DE)
2-mass 1-shaft (3 rd order)	- Equivalent shaft is flexible (1 DE) - $d\omega/dt$ is different for each mass (2 DE)
1-mass no-shaft (1 st order)	- All shafts are rigid - $d\omega/dt$ is same for each mass (1 DE)

DE = differential equation, ω = rotational speed

LS = low-speed, HS = high-speed

In Fig. 2.2 the turbine inertia represents the lumped-mass of blades and hub. For power system studies this is satisfactory (i.e. there is no need to represent the blades and hub with additional rotating masses and shafts) because the modes associated with the blades and hub are either well damped or out of the frequency range of interest [71].

In Table 2.7 the 3rd order model can be obtained from the 5th order model in two ways. In the first way, the gearbox inertia is ignored with respect to turbine and generator inertia, and the two shafts in series are replaced by an equivalent shaft [20]. In the second way, the HS shaft is considered as rigid compared to the LS shaft, hence the gearbox and generator inertia are lumped together and the equivalent shaft is the LS shaft [106].

The first approach can be justified by the definition of the moment of inertia. If the gearbox dimension and mass are much smaller than those of the turbine and generator,

it can be considered as having negligible area and mass moment of inertia. The second approach can be justified by comparing LS and HS shaft stiffness k_{LS} and k_{HS} . For consistent comparison they have to be referred to the same speed side. For example k_{LS} referred to the high speed side is $k'_{LS} = k_{LS}/n_{gb}^2$. As the gearbox ratio n_{gb} is at least 50, the HS shaft can be considered as relatively rigid compared to the LS shaft.

Whichever approach, the two-mass model accounts for the fact that turbine and generator may oscillate with respect to each other. In both approaches the equivalent stiffness is mainly determined by the low speed shaft since the first approximation gives $k_{eq} = 1/(k'^{-1}_{LS} + k^{-1}_{HS}) \approx k'_{LS}$ and the second $k_{eq} = k'_{LS}$.

In power system stability studies, the two most common models for the drive train are the lumped-mass and two-mass models. The two-mass model is recommended because it correctly represents the elasticity (or flexibility, or softness) of the shafts [50, 72]. However as reviewed in the previous chapter, the lumped mass-mass model is still frequently used.

The discrepancy between the two models has been observed experimentally and with simulation studies. From the experimental study (islanding of a wind farm in West Denmark), it was concluded that the lumped-mass model may be too optimistic for short-term voltage stability studies [20]. Measurements showed that the lumped-mass model underpredicted the reactive power requirement; and overpredicted the speed of voltage restoration. Similar results were obtained with simulation studies, which showed that for the SCIG, the lumped mass model can be over-optimistic as it can stand a much longer fault (critical clearing time) [72, 73].

The reason of the better behaviour of the lumped-mass model for the SCIG is its slower acceleration. The slower acceleration is due to two facts: higher mass and no shaft potential energy. For the two-mass model, during fault as the electrical torque drops the stored potential energy of the shaft is released further accelerating the generator [72, 73]. Hence the SCIG goes beyond its pull-out torque more quickly. For the DFIG, although there is no problem of pull-out torque for a well defined torque-speed control characteristic (see Subsection 2.4.1), the two-mass model is still important for control tuning and coordination. For the DFIG, the electrical torque setpoint is determined from the ro-

tor speed, hence the way in which it accelerates should be correctly represented for an accurate evaluation of the control performance.

Below, a simple illustration is given to show that for wind generators with gearbox, the rotating bodies do not behave as a single equivalent mass as opposed to the situation of conventional synchronous machines. The observation is made by comparing the two-mass two-spring system and its equivalent one-mass one-spring system in Fig. 2.3.

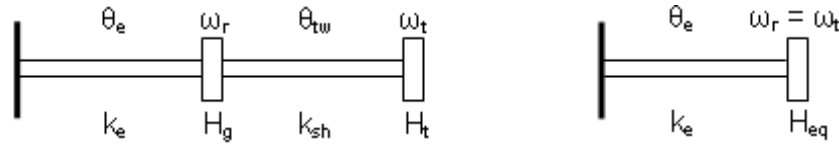


Figure 2.3: Two-mass two-spring system (left) and equivalent one-mass one-spring system. θ_e , k_e = electrical twist angle and stiffness (external network); θ_{tw} , k_{sh} = mechanical twist angle and stiffness (drive train); ω_r , H_g = generator speed and inertia; ω_t , H_t = turbine speed and inertia.

The fixed end in the figure represents the infinite bus, k_e the equivalent stiffness of the electrical network and k_{sh} the equivalent stiffness of the generator drive train. The dynamics of the two-mass system with no damping are given by:

$$d\theta_e/dt = \omega_r \quad (2.7)$$

$$d\omega_r/dt = (0.5/H_g)(k_{sh}\theta_{tw} - k_e\theta_e) \quad (2.8)$$

$$d\theta_{tw}/dt = \omega_t - \omega_r \quad (2.9)$$

$$d\omega_t/dt = (0.5/H_t)(-k_{sh}\theta_{tw}) \quad (2.10)$$

The dynamics of the lumped-mass model with no damping are described by:

$$d\theta_e/dt = \omega_r \quad (2.11)$$

$$d\omega_r/dt = (0.5/H_{eq})(-k_e\theta_e) \quad (2.12)$$

where H_{eq} is the equivalent inertia. Substituting (2.11) in (2.12) gives $\ddot{\theta}_e + (k_e/(2H_{eq}))\theta_e = 0$ which has as solution $\theta = C \sin((2\pi f)t + \Phi)$ where C is the oscillation amplitude, $f = (1/(2\pi))\sqrt{k_e/(2H_{eq})}$ the oscillation frequency, and Φ the phase angle [109]. Table 2.8 shows the oscillation frequencies for different values of stiffness and inertia.

Table 2.8: Oscillation frequencies of the mass-spring systems in Fig. 2.3

2-mass model: $H_g = 0.5$, $H_t = 5$ [s]			
k_e	k_{sh}	f_1 [Hz]	f_2 [Hz]
20	200	0.206	2.46
20	20	0.157	1.02
20	0.2	0.022	0.715
1-mass model with $H_{eq} = H_g + H_t$			
$k_e = 20$		$f = 0.215$	

When $k_e \ll k_{sh}$ the lower frequency mode (f_1) can be approximated by the one-mass model with $H_{eq} = H_t + H_g$. When $k_e \approx k_{sh}$ or $k_e \gg k_{sh}$, the oscillatory dynamics of the two models are completely different.

For conventional power plants with synchronous generators the equivalent electrical stiffness k_e (between the generator and infinite bus) is much lower than the mechanical stiffness k_{sh} (between the generator and turbine) [71]. Hence the drive-train can be approximated by the equivalent lumped-mass model. For wind power plants with a gearbox in the drive-train, the shaft is much slender, resulting in a mechanical stiffness k_{sh} of same order or lower than the equivalent electrical stiffness k_e [71, 73]. Hence the two-mass model should be used to preserve correctly the oscillatory behaviour.

2.2.3 Model for power system studies

In the previous subsection the reasons for preferring the two-mass model for the drive train instead of the lumped-mass model were given. In this subsection the mathematical model is presented and an interpretation is given by means of an electro-mechanical analogy.

The dynamical equations of the two-mass model are obtained from Newton's equation of motion for each mass (rotational speed) and shaft (torsion or twist angle) [109]. In actual units, variables and parameters have to be referred to a same speed side. For power system studies, a convenient choice is the high speed side (generator) since one is interested in the electrical variables. With turbine side variables referred to the generator

side, the drive-train dynamical equations are:

$$J'_t \frac{d}{dt} \omega'_t = T'_t - T_{sh} \quad (2.13)$$

$$J_g \frac{d}{dt} \omega_r = T_{sh} - T_e \quad (2.14)$$

$$T_{sh} = k_{eq} \theta_{tw,eq} + c_{eq} \frac{d}{dt} \theta_{tw,eq} \quad (2.15)$$

$$\frac{d}{dt} \theta_{tw,eq} = \omega'_t - \omega_r \quad (2.16)$$

where the apostrophe indicates referred variables; J'_t , J_g are the turbine and generator inertia; ω'_t , ω_r the turbine and generator speed; k_{eq} , c_{eq} the stiffness and damping coefficient of the equivalent shaft; $\theta_{tw,eq}$ the shaft torsional angle; T'_t , T_e the turbine and generator torque.

The understanding of the above model may be facilitated with an electromechanical analogy. Electromechanical analogies were used before the development of digital computers to simulate mechanical systems [109] (p. 413). Presently, they can also be useful for implementing the drive train model in software packages like EMTP [72].

In such framework, complex mechanical systems such as gear trains or automobile suspensions are reduced to a spring-mass-damper equivalent circuit, and their dynamical behaviour are analysed by implementing the equivalent electrical circuit. There are two types of analogy. If the mechanical force is set analogous to electrical voltage (hence velocity analogous to electrical current), the analogy is referred to as ‘force-voltage’ analogy. If the mechanical force is set analogous to electrical current (hence velocity analogous to electrical voltage) the analogy is referred to as ‘force-current’ analogy. The force-current analogy is often preferred because the equivalent electrical structure ‘looks’ like the original mechanical system [109].

Figure 2.4 and Table 2.9 show the force-current equivalence between a two-speed rotational system and two-voltage electrical circuit. It is seen that speed change is determined by torque unbalance in a similar way as voltage change is determined by current unbalance. Dampers and resistances dissipate energy, while inertia, springs and capacitances, inductances store it.

In power system studies, it is often more convenient to express all variables and parameters in per unit (per unit values are normalised values with respect to some chosen

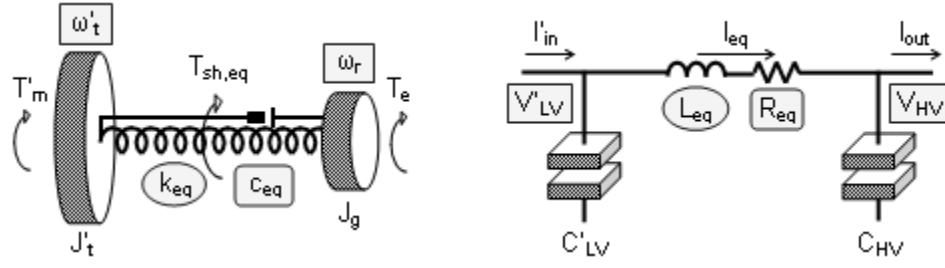


Figure 2.4: Force-current analogy between rotational and electrical systems.

Table 2.9: Force-current analogy between rotational and electrical systems

Rotational variables		Electrical variables	
ω	rotational speed [rad/s]	V	voltage [V]
T	torque [Nm]	I	current [A]
c^{-1}	damping ⁻¹ [Nm.s/el.rad] ⁻¹	R	resistance [Ω]
k^{-1}	stiffness ⁻¹ [Nm/el.rad] ⁻¹	L	inductance [H]
J	angular mass [kg m ²]	C	capacitance [F]
θ_{tw}	twist angle [el.rad]	ψ	flux [wb-turns]
LS referred to HS		LV referred to HV	
ω'_t	$= n_{gb} \omega_t$	V'_{LV}	$= n V_{LV}$
T'_m	$= T_m / n_{gb}$	I'_{in}	$= I_{in} / n$
c'^{-1}_{LS}	$= n_{gb}^2 c'^{-1}_{LS}$	R'_{LV}	$= n^2 R_{LV}$
k'^{-1}_{LS}	$= n_{gb}^2 k'^{-1}_{LS}$	L'_{LV}	$= n^2 L_{LV}$
J'_t	$= J_t / n_{gb}^2$	C'_{LV}	$= C_{LV} / n^2$
θ'_{twLS}	$= n_{gb} \theta_{twLS}$	ψ'_{LV}	$= n \psi_{LV}$
c'^{-1}_{eq}	$= c'^{-1}_{LS} + c'^{-1}_{HS}$	R_{eq}	$= R'_1 + R_2$
k'^{-1}_{eq}	$= k'^{-1}_{LS} + k'^{-1}_{HS}$	L_{eq}	$= L'_1 + L_2$
$J'_t \frac{d}{dt} \omega'_t$	$= T'_m - T_{eq}$	$C'_{LV} \frac{d}{dt} V'_{LV}$	$= I'_{in} - I_{eq}$
$J_g \frac{d}{dt} \omega_r$	$= T_{eq} - T_e$	$C_{HV} \frac{d}{dt} V_{HV}$	$= I_{eq} - I_{out}$
T_{eq}	$= k_{eq} \theta_{tw,eq} + c_{eq} \frac{d}{dt} \theta_{tw,eq}$	I_{eq}	$= \frac{1}{L_{eq}} \psi_{eq} + \frac{1}{R_{eq}} \frac{d}{dt} \psi_{eq}$
$\frac{d}{dt} \theta_{tw,eq}$	$= \omega'_t - \omega_r$	$\frac{d}{dt} \psi_{eq}$	$= V'_1 - V_2$
LS = low speed, HS = high speed		LV = low voltage, HV = high voltage	

base). The conversion of the drive train equations into per unit can be done in two steps: (1) each variable in actual unit is replaced by $x_{act} = x_{pu} x_B$ (actual value = per unit value times base value); (2) common variables are simplified on the left and right hand sides of

the equations. The turbine base speed and base torque are:

$$\omega_{tB} = \omega_{rB}/n_{gb} \quad (2.17)$$

$$T_{tB} = T_{eB}n_{gb} \quad (2.18)$$

where n_{gb} is the gearbox ratio, $\omega_{rB} = \omega_{el}/n_{pp}$ and $T_{eB} = P_{rated}/\omega_{rB}$ are the generator mechanical base speed and generator electrical base torque ($\omega_{el} = 2\pi 50$ is the electrical speed, n_{pp} is the generator pole pairs number). Using the definitions in Table 2.9, the differential equation (2.13) for ω'_t can be rewritten as:

$$\left\{ \frac{J_t}{n_{gb}^2} \right\} \frac{d}{dt} \{ \omega_t n_{gb} \} = \left\{ \frac{T_t}{n_{gb}} \right\} - T_{sh} \quad (2.19)$$

$$\frac{J_t}{n_{gb}^2} \frac{d}{dt} \{ \omega_{t,pu} \omega_{tB} \} n_{gb} = \frac{\{ T_{t,pu} T_{tB} \}}{n_{gb}} - \{ T_{sh,pu} T_{eB} \} \quad (2.20)$$

$$\frac{J_t}{n_{gb}^2} \omega_{rB} \frac{d}{dt} \omega_{t,pu} = T_{eB} (T_{t,pu} - T_{sh,pu}) \quad (2.21)$$

If the turbine inertia constant is defined as:

$$H_t = \frac{1}{2} \frac{J_t}{n_{gb}^2} \frac{\omega_{rB}}{T_{eB}} \quad (2.22)$$

the differential equation of the turbine speed in per unit becomes:

$$2H_t \frac{d}{dt} \omega_{t,pu} = T_{t,pu} - T_{sh,pu} \quad (2.23)$$

If the generator rated power is chosen as the generator base power i.e. $S_B = P_{rated}$, the electrical base torque is $T_{eB} = S_B/\omega_{rB}$ and other equivalent definitions of H_t are:

$$2H_t = \frac{J_t}{n_{gb}^2} \frac{\omega_{rB}}{T_{eB}} = J'_t \frac{\omega_{rB}}{T_{eB}} = J'_t \frac{\omega_{rB}^2}{S_B} = \frac{J_t}{n_{gb}^2} \frac{\omega_{rB}^2}{S_B} = J_t \frac{\omega_{tB}^2}{S_B} \quad (2.24)$$

Similarly the differential equation (2.14) for the rotor speed ω_r and the equivalent definitions of the generator inertia H_g are:

$$2H_g \frac{d}{dt} \omega_{r,pu} = T_{sh,pu} - T_{e,pu} \quad (2.25)$$

$$2H_g = J_g \frac{\omega_{rB}}{T_{eB}} = J_g \frac{\omega_{rB}^2}{S_B} \quad (2.26)$$

From the units of J [kg m²], ω_r [rad/s] and S [VA], it is seen that H is in [s].

Equation (2.15) for the shaft torque T_{sh} can be written as:

$$\{T_{sh,pu}T_{eB}\} = \{k_{eq,pu}k_{eqB}\} \theta_{tw,eq} + \{c_{eq,pu}c_{eqB}\} \frac{d}{dt} \theta_{tw,eq} \quad (2.27)$$

If the base stiffness is defined as $k_{eqB} = T_{eB}/(1 \text{ el.rad})$ i.e. base torque per electrical radian, and the base damping coefficient as $c_{eqB} = T_{eB}/(1 \text{ el.rad} / 1 \text{ sec})$ i.e. base torque per electrical radian per second, (2.27) becomes:

$$T_{e,pu} = k_{eq,pu}^* \theta_{tw,eq} + c_{eq,pu}^* \frac{d}{dt} \theta_{tw,eq} \quad (2.28)$$

where $k_{eq,pu}^* = k_{eq,pu}/(1 \text{ el.rad})$ is the the per unit stiffness per electrical radian and $c_{eq,pu}^* = c_{eq,pu}/(1 \text{ el.rad} / 1 \text{ sec})$ is the per unit damping per electrical radian per second. It is noted that in (2.28) the equivalent twist angle $\theta_{tw,eq}$ is not converted in per unit as the interpretation of angles is easier in actual units (radians).

In the remainder of this text, equations are expressed in per unit unless otherwise specified. Hence the subscript ‘*pu*’ and ‘*eq*’ and superscript ‘*’ are dropped, and the drive train equations can be summarized as:

$$\frac{d}{dt} \omega_t = \frac{1}{2H_t} (T_t - T_{sh}) \quad (2.29)$$

$$\frac{d}{dt} \omega_r = \frac{1}{2H_g} (T_{sh} - T_e) \quad (2.30)$$

$$T_{sh} = k\theta_{tw} + c\frac{d}{dt} \theta_{tw} \quad (2.31)$$

$$\frac{d}{dt} \theta_{tw} = \omega_{elB} (\omega_t - \omega_r) \quad (2.32)$$

with k in [pu/el.rad], c in [pu.s/el.rad]; H_g, H_t, t are in [s]; ω_{elB} in [el.rad/s], θ_{tw} in [rad].

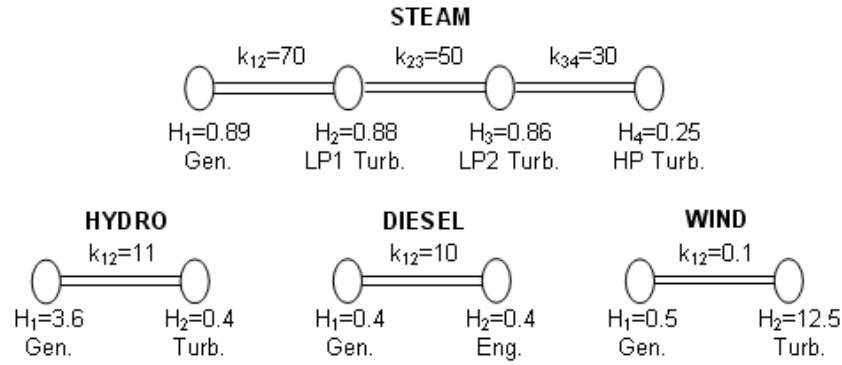
2.2.4 Parameters data

Table 2.10 gives typical values of stiffness and inertia for modern wind plants [20]. Fig. 2.5 [71] shows a comparison of typical drive train parameters for different generation schemes.

Although the data in Fig. 2.5 may be outdated for wind plants (1982), parameters for conventional plants can still be consulted as the technology has changed to a lesser extent. Considering the updated values of Table 2.10, it is seen that wind farms have indeed more flexible drive trains.

Table 2.10: Typical range for drive train parameters

Parameter	Typical range
Generator inertia H_g [s]	0.4~0.8
Wind turbine inertia H_t [s]	2~6
High speed shaft stiffness k_{HS} [pu/el.rad]	2~4
Low speed shaft stiffness k_{LS} [pu/el.rad]	0.35~0.7
Equivalent shaft stiffness k_{eq} [pu/el.rad]	0.3~0.6

Figure 2.5: Typical drive train parameters for different power generation schemes (H in [s], k in [pu/el.rad])

An additional parameter that needs to be specified is the gearbox ratio. Although it does not appear in the model (2.29)-(2.32), it is required for per unit conversion as shown in (2.17)-(2.18). The gearbox ratio n_{gb} is obtained as the rotor rated speed divided by the turbine rated speed:

$$n_{gb} = \frac{\omega_{r, rated}}{\omega_{t, rated}} \quad (2.33)$$

The turbine rated speed $\omega_{t, rated}$ is given in (2.5). The generator rated mechanical speed $\omega_{r, rated}$ can be chosen arbitrarily [27]. The higher $\omega_{r, rated}$, the higher the gearbox ratio, as shown in Table 2.11.

Choosing a higher rated rotor speed $\omega_{r, rated}$ may be desirable as power optimization is done over a wider range of rotor speed. The effect of different $\omega_{r, rated}$ on the DFIG steady-state characteristics is discussed later in Chapter 3.

From Table 2.11, the gearbox ratio depends also on the number of generator pole pairs n_{pp} . The higher the number of generator poles, the lower the gearbox ratio since the generator mechanical speed is lower.

Table 2.11: Gearbox ratio for different rated generator speed

C_p curve	P_{rated} [MW]	$v_{w,rated}$ [m/s]	R [m]	$\omega_{t,rated}$ [rad/s]	$\omega_{r,rated}$ [rad/s]	n_{gb}
SI01 [61]	3	12	45.38	1.67	$1.0 (\omega_{el}/n_{pp})$	93.91
	3	12	45.38	1.67	$1.2 (\omega_{el}/n_{pp})$	112.67
	5	12	58.58	1.30	$1.0 (\omega_{el}/n_{pp})$	121.23
	5	12	58.58	1.30	$1.2 (\omega_{el}/n_{pp})$	145.48

ω_{el} = electrical base speed = $2\pi 50$ [rad/s], n_{pp} = gen. pole pair nb = 2

2.3 Induction generator

As explained in the literature review of the previous chapter, the modelling of the induction generator consists in expressing the machine equations in a two axis synchronously rotating frame, referred to as the dq-frame. The dq-model is obtained from the three-phase voltage equations. The derivation is presented in detail below so that parameters, conventions and variables used in this work are unambiguously defined.

Magnetic saturation, iron losses (hysteresis and eddy currents), slot effects, and unbalanced conditions are not considered (see Subsection 1.2.1). These assumptions keep the model simple (only positive sequence components are simulated) and are appropriate for power system dynamic studies with three-phase disturbances.

2.3.1 Model in abc-frame

The three-phase differential equations for the electrical dynamics of the induction generator are obtained by applying Kirchoff voltage law to the stator and rotor circuits of the machine. The direction for positive current and induced voltage polarity used in this text, is shown in Fig. 2.6. The generator convention is used as positive current flows out of the coil. The voltage balance equation for the circuit in Fig. 2.6 is $v = -p\psi - Ri$ where $p = \frac{d}{dt}$. The minus sign of the derivative term is due to Lenz's law, which states that the polarity of the voltage induced by a changing flux is so that it results in a current that opposes the change [110]. It is noted that for induction motors, the direction for positive current in Fig. 2.6 is reversed and the voltage equation is $v = p\psi + Ri$.

For the induction generator, whose stator and rotor circuits are shown in Fig. 2.7, the

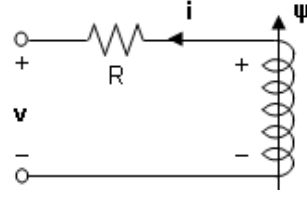


Figure 2.6: Convention for direction of positive current.

voltage equations are:

$$\begin{pmatrix} v_{as} \\ v_{bs} \\ v_{cs} \end{pmatrix} = -p \begin{pmatrix} \psi_{as} \\ \psi_{bs} \\ \psi_{cs} \end{pmatrix} - R_s \begin{pmatrix} i_{as} \\ i_{bs} \\ i_{cs} \end{pmatrix}, \quad \begin{pmatrix} v_{ar} \\ v_{br} \\ v_{cr} \end{pmatrix} = -p \begin{pmatrix} \psi_{ar} \\ \psi_{br} \\ \psi_{cr} \end{pmatrix} - R_r \begin{pmatrix} i_{ar} \\ i_{br} \\ i_{cr} \end{pmatrix} \quad (2.34)$$

where v_{as} , v_{bs} , v_{cs} are the stator phase voltages; i_{as} , i_{bs} , i_{cs} the stator phase currents; ψ_{as} , ψ_{bs} , ψ_{cs} the flux linkages; R_s the stator resistance. Similar definitions are used for the

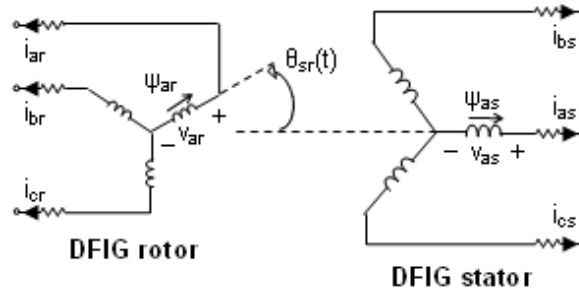


Figure 2.7: Induction machine stator and rotor circuits.

rotor. Flux linkages result from currents flowing through winding inductances:

$$\begin{pmatrix} \psi_{as} \\ \psi_{bs} \\ \psi_{cs} \end{pmatrix} = \begin{pmatrix} L_{aas} & L_{abs} & L_{acs} \\ L_{bas} & L_{bbs} & L_{bcs} \\ L_{cas} & L_{cbs} & L_{ccs} \end{pmatrix} \begin{pmatrix} i_{as} \\ i_{bs} \\ i_{cs} \end{pmatrix} + \begin{pmatrix} \mathcal{L}_{asar} & \mathcal{L}_{asbr} & \mathcal{L}_{ascr} \\ \mathcal{L}_{bsar} & \mathcal{L}_{bsbr} & \mathcal{L}_{bscr} \\ \mathcal{L}_{csar} & \mathcal{L}_{csbr} & \mathcal{L}_{cscr} \end{pmatrix} \begin{pmatrix} i_{ar} \\ i_{br} \\ i_{cr} \end{pmatrix} \quad (2.35)$$

$$\begin{pmatrix} \psi_{ar} \\ \psi_{br} \\ \psi_{cr} \end{pmatrix} = \begin{pmatrix} L_{aar} & L_{abr} & L_{acr} \\ L_{bar} & L_{bbr} & L_{bcr} \\ L_{car} & L_{cbr} & L_{ccr} \end{pmatrix} \begin{pmatrix} i_{ar} \\ i_{br} \\ i_{cr} \end{pmatrix} + \begin{pmatrix} \mathcal{L}_{aras} & \mathcal{L}_{arbs} & \mathcal{L}_{arcs} \\ \mathcal{L}_{bras} & \mathcal{L}_{brbs} & \mathcal{L}_{brcs} \\ \mathcal{L}_{cras} & \mathcal{L}_{crbs} & \mathcal{L}_{crCs} \end{pmatrix} \begin{pmatrix} i_{as} \\ i_{bs} \\ i_{cs} \end{pmatrix} \quad (2.36)$$

where L_{aas} , L_{bbs} , L_{ccs} are stator winding self inductances; L_{abs} , L_{acs} , L_{bas} , L_{bcs} , etc are mutual inductances between stator windings; \mathcal{L}_{asar} , \mathcal{L}_{asbr} , \mathcal{L}_{ascr} , \mathcal{L}_{bsar} , etc are mutual inductances between stator and rotor windings. Similar definitions are used for the rotor.

Assuming identical stator windings for the three phases and identical rotor windings for the three phases:

$$L_{aas} = L_{bbs} = L_{ccs} = L_{self,s} , \quad L_{aar} = L_{bbr} = L_{ccr} = L_{self,r} \quad (2.37)$$

$$L_{abs} = L_{bas} = L_{acs} = L_{cas} = L_{bcs} = L_{cbs} = L_{mut,s} \quad (2.38)$$

$$L_{abr} = L_{bar} = L_{acr} = L_{car} = L_{bcr} = L_{cbr} = L_{mut,r} \quad (2.39)$$

In the ideal case, the self inductance of a stator or rotor winding is [111]:

$$L_{self,s}^{ideal} = \mu_0 N_s^2 \frac{rl}{g} \frac{\pi}{4} , \quad L_{self,r}^{ideal} = \mu_0 N_r^2 \frac{rl}{g} \frac{\pi}{4} \quad (2.40)$$

where μ_0 is the free space permeability, N_s and N_r the stator and rotor effective number of turns, r the radius of the machine cross-section, l the length of the machine, and g the airgap radial length. In practice there is also some leakage flux around a coil. Hence the total self inductance of a winding can be written as the sum of an ideal magnetizing inductance and a leakage inductance:

$$L_{self,s} = L_{self,s}^{ideal} + L_{ls} , \quad L_{self,r} = L_{self,r}^{ideal} + L_{lr} \quad (2.41)$$

The mutual inductance between two stator or between two rotor windings depends on the angle between the windings as [111]:

$$L_{mut,s} = \mu_0 N_s^2 \frac{rl}{g} \frac{\pi}{4} \cos \theta_{ss} , \quad L_{mut,r} = \mu_0 N_r^2 \frac{rl}{g} \frac{\pi}{4} \cos \theta_{rr} \quad (2.42)$$

where θ_{ss} is the angle between two stator windings and θ_{rr} the angle between two rotor windings. Since $\theta_{ss} = \theta_{rr} = 120^\circ$:

$$L_{mut,s} = -0.5 L_{self,s}^{ideal} , \quad L_{mut,r} = -0.5 L_{self,r}^{ideal} \quad (2.43)$$

The mutual inductance between stator and rotor windings depends also on the angle between the two windings. As the rotor rotates, the angle is time dependent and the stator-rotor mutual inductance is not constant. E.g. for the stator and rotor phase a windings:

$$\mathcal{L}_{asar} = \left\{ \mu_0 N_s N_r \frac{rl}{g} \frac{\pi}{4} \right\} \cos \theta_{sr} = L_{sr} \cos \theta_{sr} \quad (2.44)$$

where L_{sr} is the peak value of the stator-rotor mutual inductance and $\theta_{sr} = \theta_{sr}(t)$ is the time dependent angle between the stator and rotor phase a windings as shown in Fig.

2.7. Similar expressions are obtained for \mathcal{L}_{asbr} , \mathcal{L}_{ascr} , \mathcal{L}_{bsar} , etc. Considering the above definitions and assuming that the system is balanced ($i_{as} + i_{bs} + i_{cs} = 0$), the stator flux linkage of phase a is:

$$\begin{aligned}\psi_{as} &= L_{self,s}i_{as} + L_{mut,s}i_{bs} + L_{mut,s}i_{cs} + \mathcal{L}_{asar}i_{ar} + \mathcal{L}_{asbr}i_{br} + \mathcal{L}_{ascr}i_{cr} \\ &= (L_{self,s} - L_{mut,s})i_{as} + L_{mut,s}(i_{as} + i_{bs} + i_{cs}) + \mathcal{L}_{asar}i_{ar} + \mathcal{L}_{asbr}i_{br} + \mathcal{L}_{ascr}i_{cr} \\ &= (L_{self,s} - L_{mut,s})i_{as} + \mathcal{L}_{asar}i_{ar} + \mathcal{L}_{asbr}i_{br} + \mathcal{L}_{ascr}i_{cr}\end{aligned}\quad (2.45)$$

Similar expressions are obtained for the other stator and rotor phases.

In matrix form, (2.34)-(2.36) are rewritten as:

$$\mathbf{v}_{abc,s} = -p\mathbf{\Psi}_{abc,s} - R_s\mathbf{i}_{abc,s}\quad (2.46)$$

$$\mathbf{v}_{abc,r} = -p\mathbf{\Psi}_{abc,r} - R_r\mathbf{i}_{abc,r}\quad (2.47)$$

$$\mathbf{\Psi}_{abc,s} = L_{ss}\mathbf{i}_{abc,s} + \mathcal{L}_{sr}\mathbf{i}_{abc,r}\quad (2.48)$$

$$\mathbf{\Psi}_{abc,r} = L_{rr}\mathbf{i}_{abc,r} + \mathcal{L}_{rs}\mathbf{i}_{abc,s}\quad (2.49)$$

where L_{ss} and L_{rr} referred to as ‘stator inductance’ and ‘rotor inductance’ are:

$$L_{ss} = L_{self,s} - L_{mut,s} = L_{self,s}^{ideal} + L_{ls} - L_{mut,s} = 1.5 L_{self,s}^{ideal} + L_{ls}\quad (2.50)$$

$$L_{rr} = L_{self,r} - L_{mut,r} = L_{self,r}^{ideal} + L_{lr} - L_{mut,r} = 1.5 L_{self,r}^{ideal} + L_{lr}\quad (2.51)$$

and the matrices \mathcal{L}_{sr} and $\mathcal{L}_{rs} = \mathcal{L}_{sr}^t$ are:

$$\mathcal{L}_{sr} = L_{sr} \begin{pmatrix} \cos \theta_{sr} & \cos(\theta_{sr} + \frac{2\pi}{3}) & \cos(\theta_{sr} - \frac{2\pi}{3}) \\ \cos(\theta_{sr} - \frac{2\pi}{3}) & \cos \theta_{sr} & \cos(\theta_{sr} + \frac{2\pi}{3}) \\ \cos(\theta_{sr} + \frac{2\pi}{3}) & \cos(\theta_{sr} - \frac{2\pi}{3}) & \cos \theta_{sr} \end{pmatrix}\quad (2.52)$$

2.3.2 Model in dq-frame

In (2.48)-(2.49), the variables L_{ss} and L_{rr} are constant while the matrices \mathcal{L}_{sr} and \mathcal{L}_{rs} are time dependent. Hence, in the three phase axis frame (abc-frame) the coupling between stator and rotor circuits is time-varying. The coupling can be made time invariant by transforming stator and rotor three-phase variables into a common rotating two-axis frame [111] with the transformation:

$$\mathbf{x}_{qd0} = \mathbf{T}_\theta \mathbf{x}_{abc}\quad (2.53)$$

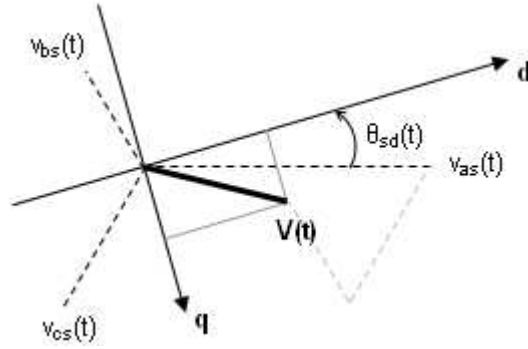


Figure 2.8: Rotating dq-axis with respect to stationary stator three-axis frame.

$$\mathbf{T}_\theta = \sqrt{\frac{2}{3}} \begin{pmatrix} \sin \theta & \sin(\theta - \frac{2\pi}{3}) & \sin(\theta + \frac{2\pi}{3}) \\ \cos \theta & \cos(\theta - \frac{2\pi}{3}) & \cos(\theta + \frac{2\pi}{3}) \\ 1/\sqrt{2} & 1/\sqrt{2} & 1/\sqrt{2} \end{pmatrix} \quad (2.54)$$

where $\mathbf{x}_{qd0} = [x_q \ x_d \ x_0]'$, $\mathbf{x}_{abc} = [x_a \ x_b \ x_c]'$, and θ is an arbitrary rotation angle. The factor $\sqrt{2/3}$ makes the transformation orthogonal i.e. $\mathbf{T}_\theta^{-1} = \mathbf{T}_\theta'$, which results in a power invariant transformation (see below). The third component x_0 is a dummy variable added for complete degree of freedom (transformation of three variables into three variables) [49].

The stator abc-variables are transformed into dq-variables with $\theta = \theta_{sd}(t)$ where θ_{sd} is the angle between the d-axis and stator a-axis as shown in Fig. 2.8. For rotor variables, a relative rotational angle must be used because of the rotor rotation i.e. $\theta = \theta_{rd}(t) = \theta_{sd}(t) - \theta_{sr}(t)$ where θ_{sr} is the angle between the stator and rotor a-axis as shown in Fig. 2.7. For a synchronously rotating dq-frame:

$$d\theta_{sd}/dt = \omega_s, \quad d\theta_{rd}/dt = \omega_s - \omega_r = s\omega_s \quad (2.55)$$

where s is the rotor slip. Fig. 2.8 shows the dq-axis with respect to the stator three-axis frame. In this work the convention of [110] is followed i.e. the d-axis is leading the q-axis. Applying transformations (2.54) with (2.55) to the stator voltage equations (2.46) gives:

$$\begin{aligned} \mathbf{T}_{\theta_{sd}} \mathbf{V}_{abc,s} &= -\mathbf{T}_{\theta_{sd}} p \mathbf{\Psi}_{abc,s} - R_s \mathbf{T}_{\theta_{sd}} \mathbf{i}_{abc,s} \\ \mathbf{v}_{qd0,s} &= -(p \{ \mathbf{T}_{\theta_{sd}} \mathbf{\Psi}_{abc,s} \} - \{ p \mathbf{T}_{\theta_{sd}} \} \mathbf{\Psi}_{abc,s}) - R_s \mathbf{i}_{qd0,s} \\ \mathbf{v}_{qd0,s} &= -(p \mathbf{\Psi}_{qd0,s} - \{ p \mathbf{T}_{\theta_{sd}} \} \mathbf{\Psi}_{abc,s}) - R_s \mathbf{i}_{qd0,s} \end{aligned} \quad (2.56)$$

where the term in brackets follows the product derivative rule and:

$$\begin{aligned} \{p\mathbf{T}_{\theta_{sd}}\}\Psi_{\text{abc},s} &= \sqrt{\frac{2}{3}}\omega_s \begin{pmatrix} -\sin\theta_{sd} & -\sin(\theta_{sd} - \frac{2\pi}{3}) & -\sin(\theta_{sd} + \frac{2\pi}{3}) \\ -\cos\theta_{sd} & -\cos(\theta_{sd} - \frac{2\pi}{3}) & -\cos(\theta_{sd} + \frac{2\pi}{3}) \\ 0 & 0 & 0 \end{pmatrix} \begin{pmatrix} \psi_{as} \\ \psi_{bs} \\ \psi_{cs} \end{pmatrix} \\ &= \omega_s \begin{pmatrix} -\psi_{ds} \\ +\psi_{qs} \\ 0 \end{pmatrix} = \begin{pmatrix} 0 & -\omega_s & 0 \\ \omega_s & 0 & 0 \\ 0 & 0 & 0 \end{pmatrix} \begin{pmatrix} \psi_{qs} \\ \psi_{ds} \\ \psi_{0s} \end{pmatrix} = \mathbf{M}_{\omega_s} \Psi_{\text{qd0},s} \end{aligned} \quad (2.57)$$

Since \mathbf{M}_{ω_s} has only off-diagonal non-zero elements, (2.57) represents the cross-coupling between the stator dq-variables. The same procedure is applied to the rotor voltage equations in (2.47). For the stator flux linkages in (2.48) the abc-dq transformation gives:

$$\begin{aligned} \mathbf{T}_{\theta_{sd}} \Psi_{\text{abc},s} &= L_{ss} \mathbf{T}_{\theta_{sd}} \mathbf{i}_{\text{abc},s} + \mathbf{T}_{\theta_{sd}} \mathcal{L}_{sr} \mathbf{i}_{\text{abc},r} \\ \Psi_{\text{qd0},s} &= L_{ss} \mathbf{i}_{\text{qd0},s} + \{\mathbf{T}_{\theta_{sd}} \mathcal{L}_{sr}\} \mathbf{i}_{\text{abc},r} \\ \Psi_{\text{qd0},s} &= L_{ss} \mathbf{i}_{\text{qd0},s} + \{(3/2)L_{sr} \mathbf{T}_{\theta_{rd}}\} \mathbf{i}_{\text{abc},r} \end{aligned} \quad (2.58)$$

The same procedure is applied to the rotor flux linkage voltage in (2.49). To sum up, the two-axis model of the induction generator is in matrix form:

$$\mathbf{v}_{\text{qd0},s} = -p\Psi_{\text{qd0},s} + \mathbf{M}_{\omega_s} \Psi_{\text{qd0},s} - R_s \mathbf{i}_{\text{qd0},s} \quad (2.59)$$

$$\mathbf{v}_{\text{qd0},r} = -p\Psi_{\text{qd0},r} + \mathbf{M}_{s\omega_s} \Psi_{\text{qd0},r} - R_r \mathbf{i}_{\text{qd0},r} \quad (2.60)$$

$$\Psi_{\text{qd0},s} = L_{ss} \mathbf{i}_{\text{qd0},s} + (3/2)L_{sr} \mathbf{i}_{\text{qd0},r} \quad (2.61)$$

$$\Psi_{\text{qd0},r} = L_{rr} \mathbf{i}_{\text{qd0},r} + (3/2)L_{sr} \mathbf{i}_{\text{qd0},s} \quad (2.62)$$

Taking the d- and q-components of (2.59)-(2.62) gives:

$$v_{qs} = -R_s i_{qs} - p\psi_{qs} + \omega_s \psi_{ds} \quad (2.63)$$

$$v_{ds} = -R_s i_{ds} - p\psi_{ds} - \omega_s \psi_{qs} \quad (2.64)$$

$$v_{qr} = -R_r i_{qr} - p\psi_{qr} + s\omega_s \psi_{dr} \quad (2.65)$$

$$v_{dr} = -R_r i_{dr} - p\psi_{dr} - s\omega_s \psi_{qr} \quad (2.66)$$

$$\psi_{qs} = L_{ss} i_{qs} + L_m i_{qr} \quad (2.67)$$

$$\psi_{ds} = L_{ss} i_{ds} + L_m i_{dr} \quad (2.68)$$

$$\psi_{qr} = L_{rr} i_{qr} + L_m i_{qs} \quad (2.69)$$

$$\psi_{dr} = L_{rr} i_{dr} + L_m i_{ds} \quad (2.70)$$

where L_{ss} , L_{rr} are defined in (2.50), (2.51); and L_m referred to as ‘mutual inductance’ is defined as $L_m = (3/2)L_{sr}$.

From the above equations, the active power and electromagnetic torque of the induction generator can be obtained in terms of dq-components. The total power output is:

$$\begin{aligned}
 P_{tot} &= \mathbf{v}'_{abc,s} \mathbf{i}_{abc,s} + \mathbf{v}'_{abc,r} \mathbf{i}_{abc,r} \\
 &= \mathbf{v}'_{abc,s} \mathbf{T}'_{\theta_{sd}} \mathbf{T}_{\theta_{sd}} \mathbf{i}_{abc,s} + \mathbf{v}'_{abc,r} \mathbf{T}'_{\theta_{rd}} \mathbf{T}_{\theta_{rd}} \mathbf{i}_{abc,r} \\
 &= \mathbf{v}'_{qd0,s} \mathbf{i}_{qd0,s} + \mathbf{v}'_{qd0,r} \mathbf{i}_{qd0,r} \\
 &= v_{qs} i_{qs} + v_{ds} i_{ds} + v_{qr} i_{qr} + v_{dr} i_{dr}
 \end{aligned} \tag{2.71}$$

Substituting (2.63)-(2.66) in (2.71) gives:

$$\begin{aligned}
 P_{tot} &= -R_s(i_{qs}^2 + i_{ds}^2) - R_r(i_{qr}^2 + i_{dr}^2) \\
 &\quad - i_{qs} \frac{d}{dt} \psi_{qs} - i_{ds} \frac{d}{dt} \psi_{ds} - i_{qr} \frac{d}{dt} \psi_{qr} - i_{dr} \frac{d}{dt} \psi_{dr} \\
 &\quad + \omega_s \psi_{ds} i_{qs} - \omega_s \psi_{qs} i_{ds} + s \omega_s \psi_{dr} i_{qr} - s \omega_s \psi_{qr} i_{dr}
 \end{aligned} \tag{2.72}$$

The first two terms correspond to the machine losses, the second four terms to the power associated with flux variation, and the last four terms to the airgap power, i.e. the power converted from mechanical to electrical form:

$$P_{ag} = \omega_s \psi_{ds} i_{qs} - \omega_s \psi_{qs} i_{ds} + s \omega_s \psi_{dr} i_{qr} - s \omega_s \psi_{qr} i_{dr} \tag{2.73}$$

The electromagnetic torque T_e is the airgap power divided by the mechanical speed:

$$\omega_{r,mech} = \frac{\omega_{r,el}}{n_{pp}} = \frac{(1-s)\omega_s}{n_{pp}} \tag{2.74}$$

where n_{pp} is the number of pole pairs. Hence substituting (2.67)-(2.70) in $T_e = P_{ag}/\omega_{r,mech}$ gives:

$$T_e = n_{pp} L_m (i_{qs} i_{dr} - i_{ds} i_{qr}) \tag{2.75}$$

Other equivalent expressions for the electrical torque may be obtained, e.g. by adding and subtracting the term $L_{rr} i_{dr} i_{qr}$ in (2.75) and using (2.69)-(2.70) gives:

$$T_e = n_{pp} (\psi_{qr} i_{dr} - \psi_{dr} i_{qr}) \tag{2.76}$$

Adding and subtracting $L_{ss}i_{qs}i_{ds}$ in (2.75) and using (2.67)-(2.68) gives:

$$T_e = n_{pp}(\psi_{qs}i_{ds} - \psi_{ds}i_{qs}) \quad (2.77)$$

Adding and subtracting $(L_{ss}/L_{ss})L_m i_{qr}i_{dr}$ in (2.75) and using (2.67)-(2.68) gives:

$$T_e = n_{pp}(L_m/L_{ss})(\psi_{qs}i_{dr} - \psi_{ds}i_{qr}) \quad (2.78)$$

Adding and subtracting $(L_{rr}/L_{rr})L_m i_{qs}i_{ds}$ in (2.75) and using (2.69)-(2.70) gives:

$$T_e = n_{pp}(L_m/L_{rr})(i_{qs}\psi_{dr} - i_{ds}\psi_{qr}) \quad (2.79)$$

Multiplying (2.75) by $(L_{ss}L_{rr} - L_m^2)/(L_{ss}L_{rr} - L_m^2)$ and using (2.67)-(2.70) gives:

$$T_e = n_{pp}L_m/(L_{ss}L_{rr} - L_m^2)(\psi_{qs}\psi_{dr} - \psi_{ds}\psi_{qr}) \quad (2.80)$$

The factor n_{pp} is due to the fact that (2.75)-(2.80) are expressed in actual units [Nm]. In per unit this factor does not appear in the equation.

2.3.3 Per unit conversion

As mentioned in the previous section, a common practice for power system studies is to express all variables and parameters in per unit (normalised value with respect to a base value). The per unit system conveniently simplifies the computations and understanding of the system as it allows comparison between systems with different ratings and removes arbitrary constants [49, 112]. Examples of arbitrary constants are transformation turn ratio, gearbox ratio, generator number of pole pairs, etc. The main task when converting equations in per unit is to define appropriate base quantities. The procedure consists in choosing three base quantities (usually power, voltage and some variable involving time), then deducing the other base quantities [49, 112]. Base quantities are normally chosen so that variables of interest are equal to one per unit under rated condition.

In wind applications, it is convenient to take the generator rated power, nominal voltage, and electrical synchronous speed as the chosen base values. The different base voltages (on the low and high voltage sides of transformers) are related to each other with the appropriate turn ratio. The different base speeds (on the low and high speed sides of gearboxes) are related to each other with the gearbox ratio. The base speeds for mechanical

and electrical rotation are related to each other with the generator pole pair number. Table 2.12 gives the chosen and deduced base quantities for the DFIG. The quantities refer to three-phase variables and parameters.

Table 2.12: Chosen and deduced base quantities for three-phase variables and parameters.

Chosen electrical base quantities			
S_B	$= S_{3ph, rated}$	3-phase generator rated power	[VA rms]
V_B	$= V_{LL, rated}$	stator rated line-to-line rms voltage	[V rms]
ω_{elB}	$= \omega_{el} = 2\pi 50$	electrical base speed	[el.rad/s]
Deduced electrical base quantities			
I_B	$= S_B / (\sqrt{3} V_B)$	base current	[A rms]
Z_B	$= V_B / (\sqrt{3} I_B) = V_B^2 / S_B$	base impedance	[Ω]
R_B, X_B	$= Z_B$	base resistance and reactance	[Ω]
L_B	$= X_B / \omega_{elB} = Z_B / \omega_{elB}$	base inductance	[H]
ψ_B	$= L_B I_B = V_B / (\sqrt{3} \omega_{elB})$	base flux	[wb-turns]
P_B, Q_B	$= S_B$	base active and reactive power	[W], [VAr]
Deduced mechanical base quantities			
ω_{rB}	$= \omega_{elB} / n_{pp}$	base generator mechanical speed	[mech.rad/s]
ω_{tB}	$= \omega_{rB} / n_{gb}$	base turbine speed	[mech.rad/s]
Deduced electro-mechanical base quantities			
T_{eB}	$= S_B / \omega_{rB} = 3 n_{pp} \psi_B I_B$	base electromagnetic torque	[Nm]
T_{tB}	$= S_B / \omega_{tB} = n_{gb} T_{eB}$	base turbine torque	[Nm]

For dq-variables and parameters the choice of the base voltage is not straightforward as the abc-dq transformation does not correspond to a physical transformer transformation. In [112], the base voltage of the 3-phase variables is also used as the base voltage for the dq-variables. In this work, the dq-base voltage is chosen so that the dq-base current is the rated line current. This choice follows the situation for the three-phase quantities where the deduced base current is the actual rated line current, as shown in Table 2.13, for both cases where the line-to-line and line-to-neutral voltage is chosen as the base voltage. Table 2.14 shows the chosen dq-base voltage for both cases where a power invariant and ‘power variant’ (no factor $\sqrt{2/3}$ in (2.54)) abc-dq transformation is used. Table 2.15 shows the chosen and deduced base quantities for the DFIG dq-variables and parameters. Their relationship with the three-phase base quantities is also given.

Table 2.13: Choice of base voltage for three phase variables and parameters

	$V_B = \text{LL voltage}$	$V_B = \text{LN voltage}$
Chosen base power	$S_B = S_{3ph, rated}$	$S_B = S_{3ph, rated}$
Chosen base voltage	$V_B = V_{LL, rated}$	$V_B = V_{LN, rated}$
Since total power is	$S_{tot} = \sqrt{3}V_{LL}I_{LL}$	$S_{tot} = 3V_{LN}I_{LN}$
→ Deduced base current is	$I_B = S_B/(\sqrt{3}V_B) = I_{line}$	$I_B = S_B/(3V_B) = I_{line}$

LL = line-to-line, LN = line to neutral

Table 2.14: Choice of base voltage for dq-variables and parameters

	$T_\theta = \text{power invariant}$	$T_\theta = \text{not power invariant}$
Chosen base power	$S_B = S_{3ph, rated}$	$S_B = S_{3ph, rated}$
Chosen base voltage	$V_{Bdq} = \sqrt{3}V_{LL, rated}$	$V_{Bdq} = (2/3)\sqrt{3}V_{LL, rated}$
Since total power is	$S_{tot} = V_{dq}I_{dq}$	$S_{dq} = (3/2)V_{dq}I_{dq}$
→ Deduced base current is	$I_{Bdq} = S_B/(V_{Bdq}) = I_{line}$	$I_{Bdq} = S_B/((3/2)V_{Bdq}) = I_{line}$

Table 2.15: Chosen and deduced base quantities for the dq-variables and parameters

Chosen dq-base quantities			
S_{Bdq}	$= S_B$	base power	[VA]
V_{Bdq}	$= \sqrt{3}V_{LL, rated} = \sqrt{3}V_B$	base voltage	[V]
Deduced dq-base quantities			
I_{Bdq}	$= S_B/V_{Bdq} = I_B$	base current	[A]
Z_{Bdq}	$= V_{Bdq}/I_{Bdq} = 3Z_B$	base impedance	[Ω]
R_{Bdq}, X_{Bdq}	$= Z_{Bdq} = 3Z_B$	base resistance and reactance	
L_{Bdq}	$= Z_{Bdq}/\omega_{elB} = 3L_B$	base inductance	[H]
ψ_{Bdq}	$= L_{Bdq}I_{Bdq} = 3\psi_B$	base flux	[wb-turns]
P_{Bdq}, Q_{Bdq}	$= S_{Bdq} = S_B$	base active and reactive power	[W], [VA]
Deduced mechanical dq-base quantities			
ω_{rBdq}	$= \omega_{rB}$	base generator mechanical speed	[mech.rad/s]
ω_{tBdq}	$= \omega_{tB}$	base turbine speed	[mech.rad/s]
Deduced dq-electro-mechanical quantities			
T_{eBdq}	$= T_{eB} = n_{pp}\psi_{Bdq}I_{Bdq}$	base electromagnetic torque	[Nm]
T_{tBdq}	$= T_{tB}$	base turbine torque	[Nm]

With the defined base quantities, the conversion of the IG equations in per unit is done by using the relationship $x_{act} = x_{pu}x_B$ (actual value = per unit value times base value). E.g. the torque T_e in (2.75) is rewritten as:

$$\begin{aligned} \{T_{e,pu}T_{eBdq}\} &= n_{pp}\{L_{m,pu}L_{Bdq}\}\left(\{i_{qs,pu}I_{Bdq}\}\{i_{dr,pu}I_{Bdq}\} - \dots \right. \\ &\quad \left. \dots \{i_{ds,pu}I_{Bdq}\}\{i_{qr,pu}I_{Bdq}\}\right) \\ T_{e,pu} n_{pp}L_{Bdq}I_{Bdq}^2 &= n_{pp} L_{m,pu}L_{Bdq}I_{Bdq}^2 \left(i_{qs,pu} i_{dr,pu} - i_{ds,pu} i_{qr,pu}\right) \\ T_{e,pu} &= L_{m,pu}(i_{qs,pu} i_{dr,pu} - i_{ds,pu} i_{qr,pu}) \end{aligned} \quad (2.81)$$

It is seen that in per unit the pole pair number does not appear in the torque equation. Similarly, the voltage equation in (2.63) can be written as:

$$\begin{aligned} \{v_{qs,pu}V_{Bdq}\} &= -\{R_{s,pu}R_{Bdq}\} \{i_{qs,pu}I_{Bdq}\} - p\{\psi_{qs,pu}\psi_{Bdq}\} + \dots \\ &\quad \dots \{\omega_{s,pu}\omega_{elB}\}\{\psi_{ds,pu}\psi_{Bdq}\} \\ v_{qs,pu}\sqrt{3}V_B &= -R_{s,pu} i_{qs,pu} \sqrt{3}V_B - p\psi_{qs,pu} (\sqrt{3}V_B/\omega_{elB}) + \dots \\ &\quad \dots \omega_{s,pu}\omega_{elB}\psi_{ds,pu} (\sqrt{3}V_B/\omega_{elB}) \\ v_{qs,pu} &= -R_{s,pu} i_{qs,pu} - p\psi_{qs,pu} (1/\omega_{elB}) + \omega_{s,pu}\psi_{ds,pu} \end{aligned} \quad (2.82)$$

It is seen that in per unit, there is a factor $(1/\omega_{elB})$ in the derivative term. This is because the time t is in [s]. Time is not converted in per unit as the interpretation is easier in [s].

In the remainder of this text, the induction generator variables and parameters are expressed in per unit, unless otherwise specified. Hence the subscript ‘ pu ’ is dropped, and the DFIG voltage equations in per unit are summarised as:

$$v_{qs} = -R_s i_{qs} - \frac{1}{\omega_{el}} \frac{d}{dt} \psi_{qs} + \omega_s \psi_{ds} \quad (2.83)$$

$$v_{ds} = -R_s i_{ds} - \frac{1}{\omega_{el}} \frac{d}{dt} \psi_{ds} - \omega_s \psi_{qs} \quad (2.84)$$

$$v_{qr} = -R_r i_{qr} - \frac{1}{\omega_{el}} \frac{d}{dt} \psi_{qr} + s\omega_s \psi_{dr} \quad (2.85)$$

$$v_{dr} = -R_r i_{dr} - \frac{1}{\omega_{el}} \frac{d}{dt} \psi_{dr} - s\omega_s \psi_{qr} \quad (2.86)$$

$$\psi_{qs} = L_{ss}i_{qs} + L_m i_{qr} \quad (2.87)$$

$$\psi_{ds} = L_{ss}i_{ds} + L_m i_{dr} \quad (2.88)$$

$$\psi_{qr} = L_{rr}i_{qr} + L_m i_{qs} \quad (2.89)$$

$$\psi_{dr} = L_{rr}i_{dr} + L_m i_{ds} \quad (2.90)$$

$$T_e = L_m(i_{qs}i_{dr} - i_{ds}i_{qr}) \quad (2.91)$$

$$T_e = (\psi_{qr}i_{dr} - \psi_{dr}i_{qr}) \quad (2.92)$$

$$T_e = (\psi_{qs}i_{ds} - \psi_{ds}i_{qs}) \quad (2.93)$$

$$T_e = (L_m/L_{ss})(\psi_{qs}i_{dr} - \psi_{ds}i_{qr}) \quad (2.94)$$

$$T_e = (L_m/L_{rr})(i_{qs}\psi_{dr} - i_{ds}\psi_{qr}) \quad (2.95)$$

$$T_e = L_m/(L_{ss}L_{rr} - L_m^2)(\psi_{qs}\psi_{dr} - \psi_{ds}\psi_{qr}) \quad (2.96)$$

2.3.4 Model for power system studies

For power system studies it is common to represent generators with a simple equivalent model whereby the machine is represented as a voltage source behind transient impedance as shown in Fig. 2.9. For the synchronous generator (SG) and squirrel cage induction generator (SCIG), the current injected to the grid is the stator current \bar{I}_s . For the DFIG, the current injected to the grid is the sum of the stator current \bar{I}_s and grid-side converter ac-current \bar{I}_{GSC} (to be more accurate, the current \bar{I}_{GSC} in Fig. 2.9 is in fact the grid side converter output current passed through some filter and/or transformer).

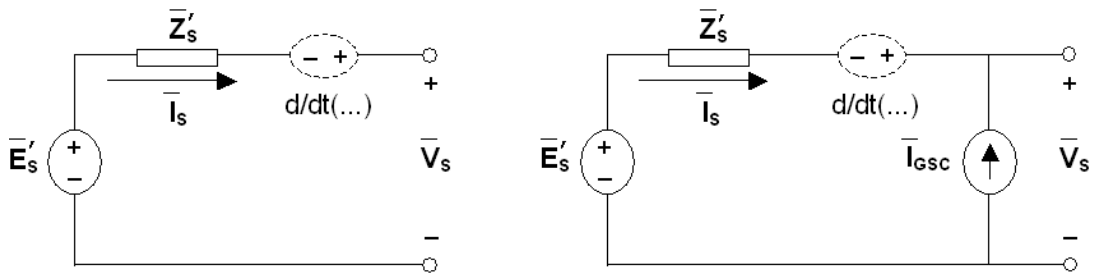


Figure 2.9: Generators as voltage source behind transient impedance: SG and SCIG (left); DFIG (right)

The DFIG model equations (2.63)-(2.70) can be written in terms of the variables

shown in Fig. 2.9 with the following definitions:

$$e'_{qs} = K_{mrr}\omega_s\psi_{dr} \quad (2.97)$$

$$e'_{ds} = -K_{mrr}\omega_s\psi_{qr} \quad (2.98)$$

$$L'_s = L_{ss} - (L_m^2/L_{rr}) \quad (2.99)$$

$$T_r = L_{rr}/R_r \quad (2.100)$$

where $K_{mrr} = L_m/L_{rr}$ (the parameters $\sigma_r = 1/K_{mrr}$, $\sigma_s = L_m/L_{ss}$ and $\sigma = L'_s/L_{ss}$ are also known as leakage factors [93]). The variables e'_{qs} and e'_{ds} are proportional to the rotor flux ψ_{dr} and ψ_{qr} respectively. Substituting (2.97)-(2.98) in (2.83)-(2.90) gives:

$$\frac{L'_s}{\omega_{elB}} \frac{d}{dt} i_{qs} = -R_1 i_{qs} + \omega_s L'_s i_{ds} + \frac{\omega_r e'_{qs}}{\omega_s} - \frac{e'_{ds}}{\omega_s T_r} - v_{qs} + K_{mrr} v_{qr} \quad (2.101)$$

$$\frac{L'_s}{\omega_{elB}} \frac{d}{dt} i_{ds} = -\omega_s L'_s i_{qs} - R_1 i_{ds} + \frac{e'_{qs}}{\omega_s T_r} + \frac{\omega_r e'_{ds}}{\omega_s} - v_{ds} + K_{mrr} v_{dr} \quad (2.102)$$

$$\frac{1}{\omega_s \omega_{elB}} \frac{d}{dt} e'_{qs} = R_2 i_{ds} - \frac{e'_{qs}}{\omega_s T_r} + (1 - \frac{\omega_r}{\omega_s}) e'_{ds} - K_{mrr} v_{dr} \quad (2.103)$$

$$\frac{1}{\omega_s \omega_{elB}} \frac{d}{dt} e'_{ds} = -R_2 i_{qs} - (1 - \frac{\omega_r}{\omega_s}) e'_{qs} - \frac{e'_{ds}}{\omega_s T_r} + K_{mrr} v_{qr} \quad (2.104)$$

$$i_{qr} = -(e'_{ds}/X_m) - K_{mrr} i_{qs} \quad (2.105)$$

$$i_{dr} = (e'_{qs}/X_m) - K_{mrr} i_{ds} \quad (2.106)$$

$$\psi_{qs} = -(1/\omega_s) e'_{ds} + L'_s i_{qs} \quad (2.107)$$

$$\psi_{ds} = (1/\omega_s) e'_{qs} + L'_s i_{ds} \quad (2.108)$$

where $R_1 = R_s + R_2$ and $R_2 = K_{mrr}^2 R_r$. To show that (2.101)-(2.108) can be represented by the equivalent model shown in Fig. 2.9, the dq-variables are interpreted as real and imaginary parts of complex variables, e.g. $\overline{E}'_s = e'_{qs} + j e'_{ds}$. Grouping $\{(2.101)-(2.104)\} + j\{(2.102)+(2.103)\}$ and $\{(2.101)+(2.104)\} + j\{(2.102)-(2.103)\}$ and writing complex variables with an overline, gives:

$$\overline{V}_s = \overline{E}'_s - \overline{Z}'_s \overline{I}_s - \frac{1}{\omega_{elB}} \frac{d}{dt} (L'_s \overline{I}_s + j \frac{\overline{E}'_s}{\omega_s}) \quad (2.109)$$

$$\overline{V}_r = \overline{E}'_r - R_r \overline{I}_r - \frac{1}{\omega_{elB}} \frac{d}{dt} (j \frac{\overline{E}'_s}{\omega_s K_{mrr}}) \quad (2.110)$$

where $\bar{E}'_r = (s/K_{mrr})\bar{E}'_s$ and $\bar{Z}'_s = R_s + jX'_s$. For both stator and rotor circuits, the voltage is equal to a voltage source minus a voltage drop across an impedance, minus a term that is non-zero only during transients. Grouping $\{(2.105)+j(2.106)\}$ and $\{(2.107)+j(2.108)\}$ gives:

$$\bar{I}_r = j \frac{\bar{E}'_s}{X_m} - K_{mrr} \bar{I}_s \quad (2.111)$$

$$\bar{\Psi}_s = j \frac{\bar{E}'_s}{\omega_s} + L'_s \bar{I}_s \quad (2.112)$$

The DFIG stator and rotor equivalent circuit in terms of complex variables (2.109)-(2.112) are shown in Fig. 2.10. The rotor voltage \bar{V}_r is a controlled voltage source,

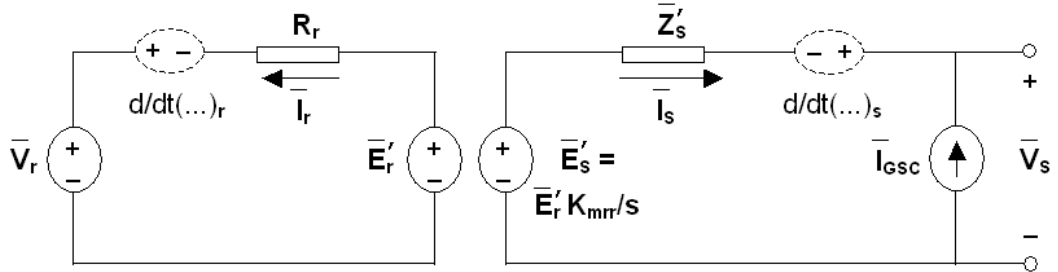


Figure 2.10: DFIG stator and rotor equivalent circuits

which is determined by the rotor-side converter controls (see next section). The converter current \bar{I}_{GSC} is a controlled current source, which is determined by the grid-side converter controls (see next section). The coupling between stator and rotor circuit is defined by the relationship $\bar{E}'_s = \bar{E}'_r (K_{mrr}/s)$. The latter expression shows the amplification factor $1/s$ ($K_{mrr} = L_m/L_{rr} \approx 1$) when going from rotor to stator circuit. This explains why reactive power control is more economical to do from the rotor-side converter rather than from the grid-side converter, as reviewed in the previous chapter (Subsection 1.2.2).

2.3.5 Parameters data

DFIG parameters are not readily available and differ between references. Table 2.16 shows a comparison in terms of ratios (it is noted that parameters of ‘Akh03’ [113] are given for a SCIG). Parametric studies with small-signal analysis can be done to assess the effect of parameters variation on DFIG dynamics and stability. Such investigations are performed in the following chapters.

Table 2.16: DFIG parameters from references

	P_{rated}, V_{sLL}	R_s [pu]	R_r/R_s	L_m [pu]	L_s/L_m	L_r/L_s	H_g [s]	H_t [s]
Pen96 [27]	7.5kW, 415V	.0462	0.755	$X_s/R_s = 61.2$	1.134	1	$H_{tot} = 5.48$	-
Pap97 [42]	90kW, 380V	.0326	0.616	1.57	1.05	1	1.11	-
Les99 [114]	660kW, NA	.0078	1.053	4.1	1.019	1.077	0.1	4.05
Slo01 [61]	2MW, NA	.01	1	3	1.033	0.994	$H_{tot} = 3.64$	-
Ak03 [113]*	2MW, 690V	.048	0.375	3.8	1.02	1.012	0.5	2.5
Hol03 [69]	2MW, 690V	.0049	1.125	3.95	1.023	1.002	$H_{tot} = 3.5$	-
vMe03 [115]	2MW, 690V	.0069	1.307	3.3	1.025	1.006	$H_{tot} = 3.52$	-

* parameters given for SCIG; $H_{tot} = H_t + H_g$.

2.4 Converter

The ac-dc-ac converter in the rotor circuit (Fig. 2.11) is required to produce rotor voltage at slip frequency. Modern design use two pulse-width modulated (PWM) inverters connected back-to-back via a dc-link. This configuration allows bidirectional power flows in the rotor circuit and hence operation at both sub- and super-synchronous speed.

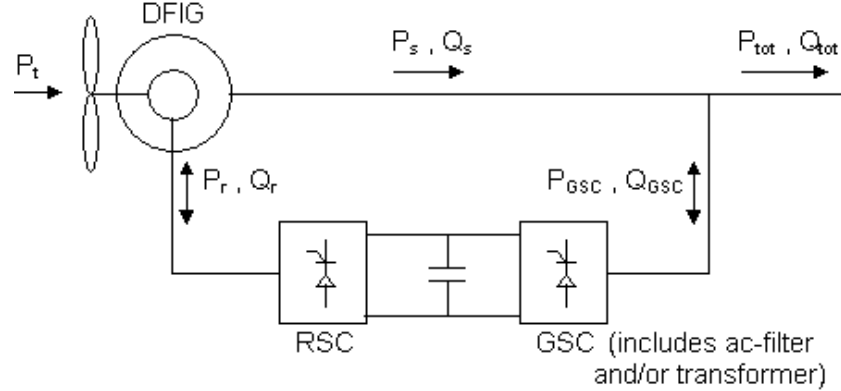


Figure 2.11: Ac-dc-ac converter in the rotor circuit with back-to-back PWM converters. RSC = rotor side converter; GSC = grid side converter.

As reviewed in the previous chapter, there are several ways to control the ac-dc-ac converter. Usually the control algorithm of the converters are formulated in a synchronously rotating two-axis frame so that decoupled control can be achieved for real and reactive power in each converter. The control objectives of the RSC and GSC have to be coordinated so that the system is stable.

For the *active* power flow control, the RSC is controlled so that maximum wind power is extracted in subrated regime and constant torque is tracked in rated regime (the coordinated action of the pitch control in rated regime achieves the overall speed control, see Section 2.5), and the GSC is controlled so that the dc-link voltage is constant.

For the *reactive* power flow control, different operating strategies may be pursued depending on the sharing of reactive power production between the DFIG stator and GSC. For a desired level of total reactive power output (imposed by the grid), the RSC can be controlled so that the DFIG stator produces an arbitrary portion (subject to machine limits) while the GSC produces the rest of it. For minimum converter rating, the GSC is operated at unity power factor and the DFIG stator delivers the total reactive power.

As described in Subsection 1.2.1, the converters can be represented as controlled voltage or current sources. In Fig. 2.10 showing the generator equivalent model used in this work, the rotor-side converter is modelled as a controlled voltage source and injects an ac-voltage at slip frequency to the DFIG rotor; the grid-side converter is modelled as a controlled current source and injects an ac current at grid frequency to the network. This representation of the ac-dc-ac converter follows the choice to consider in more detail the controls of the RSC, while the dynamics of the dc-link GSC controls are assumed as ideal.

The GSC controls are not considered because they are not specific to wind driven DFIG applications and because they influence mainly the dc-link dynamics. The latter may be more important for fault-ride through studies, which are not in the scope of the present work. The ways in which the GSC maintains the dc-link voltage constant and controls the power factor of its ac-output have been treated in other applications of back-to-back converters, see e.g. [116–119].

The RSC controls, on the other hand, are considered because they are specific to wind driven DFIG applications (optimization of wind power capture) and because they have a direct effect on the dynamics of the generator (since generator speed/torque and power factor/voltage are directly controlled) and hence on the system stability.

It is also assumed that the ac-dc-ac converter is made of lossless components and the switching dynamics are not considered (not in the frequency range of interest).

2.4.1 Rotor-side converter

There are various ways to implement the RSC controls, as reviewed in Subsection 1.2.2. In this work, generic PI-controllers are considered. The converter controls consist in two decoupled loops, with each loop made of PI-controllers in cascade. The slower outer loop achieves electrical torque or reactive power control and produces the setpoint for the faster inner current control loop. Fig. 2.12 shows the generic control loops of the RSC. Feedforward decoupling terms can also be included, however as shown in Chapter 5, adequate tuning of the PI-controllers removes the need of such terms.

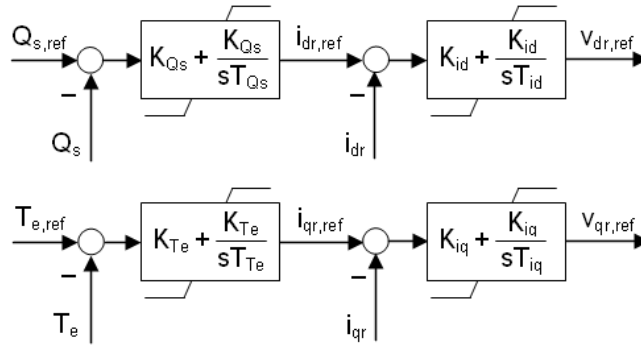


Figure 2.12: Generic control loops of the rotor side converter. T_e = electrical torque, Q_s = stator reactive power, i_{qr} and i_{dr} = quadrature and direct component of the rotor, subscript ‘ $_{ref}$ ’ = setpoints, K_x = proportional gains, T_x = integral times.

If terminal voltage instead of reactive power control is desired, the variables $Q_{s,ref}$ and Q_s in Fig. 2.12 are replaced by $V_{s,ref}$ and V_s respectively. Similarly if active power instead of electromagnetic torque control is desired, the variables $T_{e,ref}$ and T_e are replaced by $P_{tot,ref} = T_{e,ref}\omega_r$ and P_{tot} . In Fig. 2.12, the ac-voltage of the RSC is determined by imposing a constraint on the electrical torque control and another on reactive power, i.e.:

$$\bar{V}_r = \bar{V}_{r,ref} \quad \text{so that} \quad 1) T_e = T_{e,ref}, \quad 2) Q_s = Q_{s,ref} \quad (2.113)$$

Since this work studies grid-connected DFIG applications, preference is given to the control of reactive power directly (or voltage or power factor) in the d-axis. The magnetization current is not explicitly controlled (see Subsection 1.2.2) as such approach makes more sense for drive applications where voltage is provided by the network. In the q-axis, preference is given to torque (or power) control rather than speed control. This is because

the latter scheme requires either a mechanical torque observer or accurate measurements of undisturbed wind speed, which are difficult to realize (see Subsection 1.2.2).

In Fig. 2.12, the reference reactive power $Q_{s,ref}$ is determined by the wind farm control centre, or it can be given by an outer voltage control loop. The reference electromagnetic torque $T_{e,ref}$ depends on the operating regime. In subrated conditions, the electrical torque is determined so that the resulting tip speed ratio is optimal (i.e. maximum power is extracted from the wind). In rated condition, the torque control operates in conjunction with the pitch control to maintain the generator speed and power at their designated level (often the rated level). Fig. 2.13 shows examples of typical electrical torque reference as function of rotor speed for different chosen values of rated rotor speed.

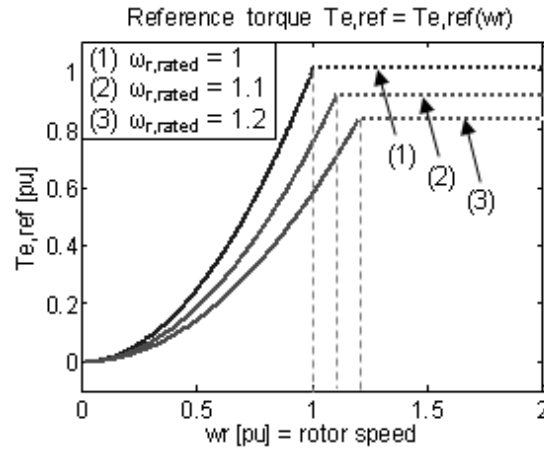


Figure 2.13: Typical reference electromagnetic torque as function of the rotor speed.

It is noted that the torque-speed curve in Fig. 2.13 is not the same as the power curves shown in Subsection 1.1.7. The optimal torque-speed curve gives the electrical torque as function of *rotor* speed. The power curve gives output power as function of *wind* speed.

To achieve maximum power tracking (MPT) in subrated regime and rated torque tracking in rated regime, as shown in Fig. 2.13, the following reference torque is used:

$$T_{e,ref} = K_{opt} \omega_r^2 \quad \text{in subrated regime } (\omega_r < \omega_{r,rated}) \quad (2.114)$$

$$T_{e,ref} = T_{e,rated} \quad \text{in rated regime } (\omega_r \geq \omega_{r,rated}) \quad (2.115)$$

where K_{opt} is a constant determined from (2.1) and (2.3) with $C_p = C_{p,max}$ and $\lambda = \lambda_{opt}$.

In actual unit and in per unit, K_{opt} is obtained as:

$$K_{opt,act} = 0.5\rho\pi R^5 C_{pmax} / \lambda_{opt}^3 \quad (2.116)$$

$$K_{opt,pu} = 0.5\rho\pi R^5 C_{pmax} \omega_{tB}^3 / (\lambda_{opt}^3 S_B) \quad (2.117)$$

where ω_{tB} and S_B are the turbine base speed and power (see Table 2.12).

In rated conditions, the RSC keeps the electrical torque constant at its rated level $T_{e,rated}$ while the pitch control regulates the rotor speed. Hence constant power tracking in rated regime is achieved by the action of both RSC and pitch controllers. In Fig. 2.13, the torque reference in rated regime is shown in dotted line because it is not a steady-state condition. For any point on the dotted part, the pitch control will act until the speed comes back to rated level.

One may be tempted to replace the reference torque in rated regime given in (2.115) by $T_{e,ref} = P_{ag,rated}/\omega_r$ so that power is constant. However, this would make the load torque T_e decrease for increasing rotor speed, which would further decrease the load torque and hence increase the rotor speed, etc. As pitch control is much slower (due to the blade inertias), it may not be able to bring the speed back to its rated value leading to unstable operation. In other words, if the RSC does constant power tracking instead of constant torque tracking in rated regime, the DFIG has a pull-out torque problem as in the SCIG and stability performance would be deteriorated. To avoid this, it is better for the RSC to do constant torque tracking while pitch control does rated speed tracking, so that the combined effect is rated power tracking.

The DAE of the controllers shown in Fig. 2.12 can be written as:

$$\frac{d\Phi_{Te}}{dt} = T_{e,err} \quad (2.118)$$

$$\frac{d\Phi_{iq}}{dt} = K_{Te} T_{e,err} + \frac{K_{Te}}{T_{Te}} \Phi_{Te} - i_{qr} \quad (2.119)$$

$$v_{qr} = K_{iq} K_{Te} T_{e,err} + K_{iq} \frac{K_{Te}}{T_{Te}} \Phi_{Te} - K_{iq} i_{qr} + \frac{K_{iq}}{T_{iq}} \Phi_{iq} \quad (2.120)$$

$$\frac{d\Phi_{Qs}}{dt} = Q_{s,err} \quad (2.121)$$

$$\frac{d\Phi_{id}}{dt} = K_{Qs} Q_{s,err} + \frac{K_{Qs}}{T_{Qs}} \Phi_{Qs} - i_{dr} \quad (2.122)$$

$$v_{dr} = K_{id} K_{Qs} Q_{s,err} + K_{id} \frac{K_{Qs}}{T_{Qs}} \Phi_{Qs} - K_{id} i_{dr} + \frac{K_{id}}{T_{id}} \Phi_{id} \quad (2.123)$$

Equations (2.118)-(2.120) represent the q-axis control loop; $T_{e,err} = T_{e,ref} - T_e$ is the torque error; Φ_{Te} is the state variable of the outer controller; Φ_{iq} is the state variable of the inner controller. Similarly, (2.121)-(2.123) represent the d-axis control loop; Φ_{Qs} and Φ_{id} are the state variables of the outer and inner controllers; $Q_{s,err} = Q_{s,ref} - Q_s$ is the reactive power error. The parameters K_{iq} , K_{id} , K_{Te} , K_{Qs} are the controller proportional gains (P-gains). They may be positive or negative depending on the steady state relationship between input and output [92] (which also depends on the definition of positive current direction). From Fig. 2.12, K_{iq} and K_{id} have units of impedance, K_{Te} has units of speed over voltage, and K_{Qs} has units of voltage inversed. In the following, their values are given in per unit on machine base. The parameters T_{iq} , T_{id} , T_{Te} , T_{Qs} are the controller reset times or integral times (I-times) [92]. As they are time parameters, they are positive and have units of second.

2.4.2 Grid-side converter and dc-link

As explained above, the GSC and dc-link dynamics are not considered in the present work. The dc-voltage is assumed constant and the GSC is represented as a current source. It is also assumed that the GSC is operated at unity power factor. Since the GSC controls are done instantaneously, the grid-side converter ac-current is such that the active power injected to the mains matches that of the rotor-side converter at unity power factor, i.e.:

$$\bar{I}_{GSC} = \bar{I}_{GSC,ref} \quad \text{so that} \quad 1) P_{GSC} = P_r, \quad 2) Q_{GSC} = 0 \quad (2.124)$$

The dc-link voltage error is used to measure the imbalance. Hence by assuming instantaneous rotor active power transfer, the dc-link voltage is constant and no dynamical model is required for the dc-link capacitor. The role of the dc-link capacitor is to act as a voltage source to the converters. For drive applications using a diode rectifier on the rotor-side, the dynamics of the dc-link components may not be ignored because of the dc-energy storage mechanism, bulkier dc-components, and lesser control capability [118]. For back-to-back converters however, an adequate control eliminates the need of storage in the dc-link and ensures a practically constant dc-voltage [116–119].

When the dc-link dynamics are neglected, the model of the GSC is simply:

$$P_{GSC} = P_r \quad (2.125)$$

$$Q_{GSC} = \alpha Q_{tot} \quad (2.126)$$

where α defines the reactive power sharing between stator and GSC. For minimum converter rating, as assumed in this text, no sharing is done and $\alpha = 0$, $Q_{GSC} = 0$, $Q_s = (1 - \alpha)Q_{tot} = Q_{tot}$. The injected current grid-side converter current is therefore $\bar{I}_{GSC} = (P_{GSC} + jQ_{GSC})/\bar{V}_s = P_r/\bar{V}_s$.

2.4.3 Alignment of the dq-frame

Decoupled control of the generator speed (or active power) and terminal voltage (or reactive power) is achieved by formulating the control algorithm of the converter in a synchronously rotating two-axis frame. The rotating frame can be aligned with any synchronously rotating variable such as the terminal voltage or stator flux (see Subsection 1.2.1). In the latter case, the control algorithm is similar to that of the vector control used in variable speed drive applications (induction motors). The preference of an alignment over another is not discussed as it is not the objective of this work. The choice of a particular alignment may have some effect on implementation issues but will not modify the dynamical properties of the system. In this work, the q-axis is aligned with stator voltage and the d-axis is leading the q-axis; hence $\bar{V}_s = v_{qs} + jv_{ds}$ and $v_{qs} = |\bar{V}_s|$, $v_{ds} = 0$.

2.5 Blade pitching

In variable pitch wind turbines, the mechanical input power can be limited by increasing the blade pitch angle. As mentioned in Subsection 1.1.7, the pitch control is activated in rated condition (i.e. when the wind speed is sufficiently high so that the maximum power extractable from the wind is larger than the rated power of the generator).

Coordination between the RSC and pitch controller is done whereby the rotor side converter regulates the load torque (electrical torque) by maintaining it constant at its rated value (defined as rated power over rated speed), while the pitch controller regulates the

input torque (mechanical torque) by adjusting the blade pitch angle so that the mechanical torque matches the electrical torque at desired rotor speed (the rated speed).

2.5.1 Mechanism and control

The pitching mechanism consists in the pitch controller, the actuators and the blades (inertia). As reviewed in Subsection 1.2.2, the pitch controller produces the pitch angle setpoint from the rotor speed error or power output error. When the pitch mechanism is actuated there is a lag between the reference (setpoint) and actual value of the blade pitch angle due to the dynamics of the actuators and blade inertias. The former are very fast (< 5 ms [65]) while the latter are relatively slow (~ 0.5 s [63]).

Fig. 2.14 shows a generic pitch controller and actuator model [63]. The PI-controller,

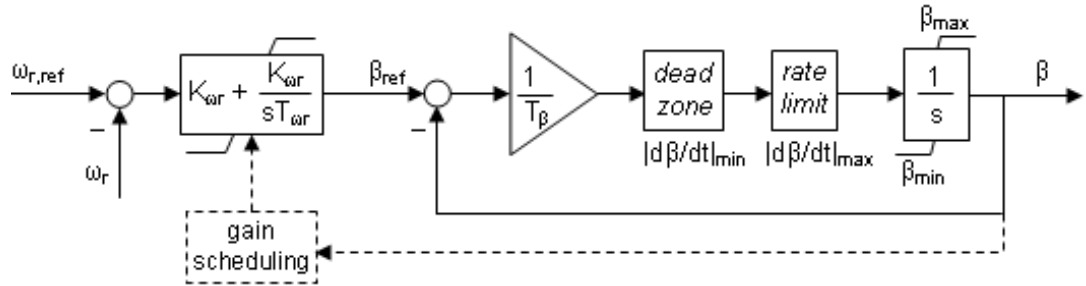


Figure 2.14: Pitch controller and actuator.

with proportional gain K_{ω_r} and integral time T_{ω_r} , computes the reference pitch angle that is required so that the rotor rotates at desired speed. The actuator is modelled as a first order system with time constant T_β which represents the lag due to the blade inertias. In this simple model, the lag associated with the actuators are not represented as they are relatively small. To limit the actuator motions and noise in command signal, a pitch rate limiter ($|d\beta/dt|_{max}$) and dead zone ($|d\beta/dt|_{min}$) are included.

If a more detailed model is deemed necessary (e.g. for turbine design or for detailed control algorithm development) the model proposed in [65] can be used, where the actuators dynamics are modelled with a delay (represented by a Pade approximation) and the blades dynamics with a second order system. In this work the generic model in Fig. 2.14 is used as the focus is on the overall effect of the wind generator on the power system rather than the study of a particular control algorithm.

In some cases, gain scheduling (non-linear control) is provided to express nonlinearities amplification of the system (at large pitch angle, a unit change in pitch angle gives larger decrease in input power) [55]. When linear control gives instability in high wind speed, the gain scheduling block adjusts the total gain of the system so that it remains stable. Details of the gain scheduling design and implementation are in [55].

2.5.2 Model equations

The differential algebraic equations for the model in Fig. 2.14 are obtained as:

$$\frac{d\Phi_{\omega_r}}{dt} = -\frac{1}{T_{\omega_r}}\Phi_{\omega_r} + \frac{1}{K_{\omega_r}}\beta_{ref} \quad (2.127)$$

$$\frac{d\beta}{dt} = \frac{1}{T_\beta}(\beta_{ref} - \beta) \quad (2.128)$$

$$\beta_{ref} = (\omega_{r,ref} - \omega_r)K_{\omega_r} + \Phi_{\omega_r} \frac{K_{\omega_r}}{T_{\omega_r}} \quad (2.129)$$

where Φ_{ω_r} , K_{ω_r} , T_{ω_r} are respectively the state variable, proportional gain, and integral time constant of the PI-controller (hence $K_{\omega_r}/T_{\omega_r}$ is the integral gain); T_β is the time constant of the actuators; β_{ref} and $\omega_{r,ref}$ are the pitch angle and rotor speed setpoints.

2.5.3 Parameters data

Table 2.17 shows the typical parameter values of the pitching mechanism. Control parameters are given in Chapter 5 where the tuning of the controllers and pitch activation conditions are discussed.

Table 2.17: Pitching mechanism model parameters

	NREL99 [63]	Riso03 [55]	ECN03 [65]	Cigre06 [120]
T_β [s]	0.5	na	na	0.3~1
$ d\beta/dt _{max}$ [°/s]	10	8	4 (10 in emergency)	10
$ d\beta/dt _{min}$ [°/s]	0.1	0.5	0.5	na
$\beta_{min} \sim \beta_{max}$ [°]	3~60	na	-2.5~90	0~30

na = not available, $|d\beta/dt|_{max}$ = rate limit, $|d\beta/dt|_{min}$ = deadzone

2.6 External network

2.6.1 Admittance matrix

In power system stability studies, the electromagnetic transients (very fast dynamics) of the network are neglected [49] and an algebraic admittance matrix \bar{Y}_{bus} is used to represent the power system network:

$$\bar{Y}_{bus} = \begin{pmatrix} \bar{y}_{11} & \bar{y}_{12} & \bar{y}_{13} & \cdots \\ \vdots & \ddots & \vdots & \\ \bar{y}_{ij} & \cdots & \bar{y}_{ii} & \vdots \\ \vdots & & \cdots & \bar{y}_{nn} \end{pmatrix} \quad (2.130)$$

In (2.130), n is the number of busses, \bar{y}_{ii} is the sum of the admittances connected to bus i , \bar{y}_{ij} is -1 multiplied by the admittance between bus i and j [49].

In this work, transmission lines are represented by an equivalent pi-model, where the series resistance and reactance represent the active and reactive losses over the line and the shunt conductance and susceptance represent the line charging. Transformers are represented by a series reactance.

For time domain studies, the operating point of the power system is found by solving the equation:

$$\bar{V}_{bus} = \bar{Y}_{bus}^{-1} \bar{I}_{bus} \quad (2.131)$$

where \bar{I}_{bus} are the net injected current at each bus and depend on generators and loads.

For frequency domain studies (eigenvalues computation), the network is represented by the algebraic power flow equations:

$$0 = \sum_{k=1}^n V_i V_k Y_{ik} \cos(\theta_i - \theta_k - \alpha_{ik}) - P_{tot,i} \quad (2.132)$$

$$0 = \sum_{k=1}^n V_i V_k Y_{ik} \sin(\theta_i - \theta_k - \alpha_{ik}) - Q_{tot,i} \quad (2.133)$$

where $P_{tot,i}$ and $Q_{tot,i}$ are the active and reactive power injected at bus i , the parameters Y_{ik} , α_{ik} are the magnitude and angle of the element (i,k) of the bus admittance matrix [121]. The variables V_i , θ_i are the magnitude and angle of the voltage at bus i .

2.6.2 Interfacing between the DFIG and network

When studying the dynamics of a grid connected DFIG, all equations must be expressed on the same per unit base and in a same rotational frame (i.e. all rotation angles must be referred to a same reference angle). The base power of the DFIG and external system are often different hence suitable conversion factors must be included where appropriate.

Similarly, the common reference frame (e.g. that of the slack bus synchronous machine) here referred to as DQ-frame, is different from the DFIG dq-frame. Both DQ-axis and dq-axis frames rotate synchronously, thus the angle δ between the q- and Q-axis is constant and the relationship between dq- and DQ-variables is

$$\overline{X}_{dq} = \overline{X}_{DQ} \exp(-\delta) \quad (2.134)$$

where $\overline{X}_{dq} = x_q + jx_d$ and $\overline{X}_{DQ} = x_Q + jx_D$.

If the synchronous dq-frame is aligned with the stator voltage, as assumed in this work, the dq-components of the terminal voltage are $v_{qs} = |\overline{V}_s|$ [pu] and $v_{ds} = 0$, and the angle between the rotating frames is $\delta = \gamma_{V_s}$ where γ_{V_s} is the DFIG terminal voltage angle given by solving (2.131).

2.7 Dynamic model equations

The differential algebraic equations of the DFIG are summarized as follows:

$$\frac{L'_s}{\omega_{elB}} \frac{d}{dt} i_{qs} = -R_1 i_{qs} + \omega_s L'_s i_{ds} + \frac{\omega_r e'_{qs}}{\omega_s} - \frac{e'_{ds}}{\omega_s T_r} - v_{qs} + K_{mrr} v_{qr} \quad (2.135)$$

$$\frac{L'_s}{\omega_{elB}} \frac{d}{dt} i_{ds} = -\omega_s L'_s i_{qs} - R_1 i_{ds} + \frac{e'_{qs}}{\omega_s T_r} + \frac{\omega_r e'_{ds}}{\omega_s} - v_{ds} + K_{mrr} v_{dr} \quad (2.136)$$

$$\frac{1}{\omega_s \omega_{elB}} \frac{d}{dt} e'_{qs} = R_2 i_{ds} - \frac{e'_{qs}}{\omega_s T_r} + \left(1 - \frac{\omega_r}{\omega_s}\right) e'_{ds} - K_{mrr} v_{dr} \quad (2.137)$$

$$\frac{1}{\omega_s \omega_{elB}} \frac{d}{dt} e'_{ds} = -R_2 i_{qs} - \left(1 - \frac{\omega_r}{\omega_s}\right) e'_{qs} - \frac{e'_{ds}}{\omega_s T_r} + K_{mrr} v_{qr} \quad (2.138)$$

$$\frac{d}{dt} \omega_r = \frac{1}{2H_g} (k\theta_{tw} + c \frac{d}{dt} \theta_{tw} - T_e) \quad (2.139)$$

$$\frac{d}{dt} \theta_{tw} = \omega_{elB} (\omega_t - \omega_r) \quad (2.140)$$

$$\frac{d}{dt} \omega_t = \frac{1}{2H_t} (T_t - k\theta_{tw} - c \frac{d}{dt} \theta_{tw}) \quad (2.141)$$

$$0 = \sum_{k=1}^n V_i V_k Y_{ik} \cos(\theta_i - \theta_k - \alpha_{ik}) - P_{tot} \quad (2.142)$$

$$0 = \sum_{k=1}^n V_i V_k Y_{ik} \sin(\theta_i - \theta_k - \alpha_{ik}) - Q_{tot} \quad (2.143)$$

where (2.135)-(2.136) represent the stator electrical dynamics, (2.137)-(2.138) the rotor electrical dynamics, (2.139)-(2.141) the drive-train mechanical dynamics, (2.142)-(2.143) the interface with the external network.

In (2.135) and (2.138), the q-axis component of the rotor voltage v_{qr} is obtained from the DAE of the q-axis controller of the rotor side converter:

$$\frac{d\Phi_{Te}}{dt} = T_{e,err} \quad (2.144)$$

$$\frac{d\Phi_{iq}}{dt} = K_{Te} T_{e,err} + \frac{K_{Te}}{T_{Te}} \Phi_{Te} - i_{qr} \quad (2.145)$$

$$v_{qr} = K_{iq} K_{Te} T_{e,err} + K_{iq} \frac{K_{Te}}{T_{Te}} \Phi_{Te} - K_{iq} i_{qr} + \frac{K_{iq}}{T_{iq}} \Phi_{iq} \quad (2.146)$$

In (2.136) and (2.137), the d-axis component of the rotor voltage v_{dr} is obtained from the DAE of the d-axis controller of the rotor side converter:

$$\frac{d\Phi_{Qs}}{dt} = Q_{s,err} \quad (2.147)$$

$$\frac{d\Phi_{id}}{dt} = K_{Qs} Q_{s,err} + \frac{K_{Qs}}{T_{Qs}} \Phi_{Qs} - i_{dr} \quad (2.148)$$

$$v_{dr} = K_{id} K_{Qs} Q_{s,err} + K_{id} \frac{K_{Qs}}{T_{Qs}} \Phi_{Qs} - K_{id} i_{dr} + \frac{K_{id}}{T_{id}} \Phi_{id} \quad (2.149)$$

In (2.141) the turbine torque $T_t = P_t/\omega_t$ is obtained from the turbine algebraic model:

$$P_t = 0.5 \rho \pi R^2 C_p(\lambda, \beta) v_w^3 \quad (2.150)$$

where the pitch angle β is zero in subrated regime and is obtained from the pitch controller in rated regime:

$$\frac{d\Phi_{\omega_r}}{dt} = -\frac{1}{T_{\omega_r}} \Phi_{\omega_r} + \frac{1}{K_{\omega_r}} \beta_{ref} \quad (2.151)$$

$$\frac{d\beta}{dt} = \frac{1}{T_{\beta}} (\beta_{ref} - \beta) \quad (2.152)$$

$$\beta_{ref} = (\omega_{r,ref} - \omega_r) K_{\omega_r} + \Phi_{\omega_r} \frac{K_{\omega_r}}{T_{\omega_r}} \quad (2.153)$$

In (2.142)-(2.143), the output power of the DFIG are obtained by the algebraic equations:

$$P_{tot} = P_s + P_r = v_{qs}i_{qs} + v_{ds}i_{ds} + v_{qr}i_{qr} + v_{dr}i_{dr} \quad (2.154)$$

$$Q_{tot} = Q_s + Q_{GSC} = Q_s = -v_{qs}i_{ds} + v_{ds}i_{qs} \quad (2.155)$$

where the grid-side converter reactive power is zero since it is operated at unity power factor. The rotor currents are:

$$i_{qr} = -(e'_{ds}/X_m) - K_{mrr}i_{qs} \quad (2.156)$$

$$i_{dr} = (e'_{qs}/X_m) - K_{mrr}i_{ds} \quad (2.157)$$

Numerical values of the component parameters have been given at the end of each section. The control parameters are given in Chapter 5 where the tuning procedure of the controllers and specification of pitch activation are discussed.

2.8 Summary

In this chapter, the wind driven DFIG model was presented. Model equations were derived and parameters data of each component were provided.

For the turbine, dynamical models (aerodynamics of the airflow around the turbine) are used for turbine design or specific site-turbine evaluation. For power system stability studies, a non-linear algebraic model is used, where the mechanical input power is obtained from the wind speed, pitch angle and rotor speed. A procedure has been given for consistent dimension calculation when using numerical approximations of the C_p curve.

For the drive-train, the presence of a gearbox results in a mechanical stiffness of the same order as the electrical stiffness (equivalent stiffness of the external power network). In such case, the drive train does not behave as a single equivalent rotating mass. In addition to evaluate the control performance accurately, it is important to consider the change in rotor speed as realistically as possible. Hence the two mass-model is used.

For the induction generator, the derivation of the model equations has been presented to define unambiguously all parameters, variables and conventions used in the present work. For power system studies, the DFIG can be represented as a voltage source (proportional to rotor flux) behind transient impedance, with a shunt controlled current source

at the terminal representing the current from the grid-side converter. Detailed explanation for the per unit conversion and choice of the base values have been given.

For the ac-dc-ac converter, the grid side converter controls are assumed as ideal i.e. the dc-voltage is constant (hence dc-link dynamics are ignored) and the GSC transfers the rotor active power instantaneously to or from the grid. It is also assumed that the GSC is operated at unity power factor. The RSC on the other hand is modelled as a controlled voltage source. The rotor voltage setpoints are determined by two loops of PI-controllers in cascade regulating the electrical torque and reactive power. Switching transients are ignored and rotor voltages are instantaneously equal to their setpoints.

For the blade pitching mechanism, the slow response speed of the pitch angle to a change in its setpoint is represented by a first order system. The setpoint of the blade pitch angle is determined by a PI-controller regulating the rotor speed.

The ac-dc-ac converter and pitch control have to be coordinated. In subrated regime, the pitch control is inactive and the rotor side converter ensures maximum power tracking and constant reactive power (or power factor or terminal voltage). In rated conditions, the RSC maintains a constant electrical torque and reactive power, while the pitch control ensures that the rotor speed stays at its rated value. The combined effect keeps the power output at rated level. At each instant, the grid side converter maintains a constant dc-link voltage at unity power factor (for minimum converter rating).

Chapter 3

Analysis: Steady-state behaviour

In the present chapter, the analysis of the DFIG behaviour is started by looking at the steady-state operating characteristics of the machine. Comparison is made with the squirrel cage induction generator (SCIG) to show that the non-zero rotor voltage of the DFIG results in completely different steady-state characteristics with controllable output power (both active and reactive). The initialisation procedure, which is the first step in both linear small-signal and non-linear large disturbance studies, is also discussed.

3.1 Steady-state equations

The steady state operating points of the induction generator can be obtained from the machine voltage equations (2.83)-(2.90) with all time derivatives equal to zero:

$$v_{qs} = -R_s i_{qs} + \omega_s (L_{ss} i_{ds} + L_m i_{dr}) \quad (3.1)$$

$$v_{ds} = -R_s i_{ds} - \omega_s (L_{ss} i_{qs} + L_m i_{qr}) \quad (3.2)$$

$$v_{qr} = -R_r i_{qr} + s\omega_s (L_{rr} i_{dr} + L_m i_{ds}) \quad (3.3)$$

$$v_{dr} = -R_r i_{dr} - s\omega_s (L_{rr} i_{qr} + L_m i_{qs}) \quad (3.4)$$

For given stator voltage (v_{qs} , v_{ds}), rotor voltage (v_{qr} , v_{dr}) and slip (s), (3.1)-(3.4) is a system of four equations four unknowns and can be solved for the stator and rotor current (i_{qs} , i_{ds} , i_{qr} , i_{dr}). Hence, if stator and rotor voltage are known, the outputs such as torque

and power can be obtained as function of the slip s or rotor speed $\omega_r = (1 - s)\omega_s$ as:

$$T_e = L_m(i_{qs}i_{dr} - i_{ds}i_{qr}) \quad (3.5)$$

$$P_s = v_{qs}i_{qs} + v_{ds}i_{ds} \quad (3.6)$$

$$P_r = v_{qr}i_{qr} + v_{dr}i_{dr} \quad (3.7)$$

$$Q_s = -v_{qs}i_{ds} + v_{ds}i_{qs} \quad (3.8)$$

$$Q_r = -v_{qr}i_{dr} + v_{dr}i_{qr} \quad (3.9)$$

Fig. 3.1 shows the doubly-fed and squirrel cage induction generators along with their power flows. The outputs of interest for the present analysis are the total active power output P_{tot} and the stator reactive power output Q_s . P_{tot} indicates the total useful power production that can be expected in the steady-state. Q_s indicates the compensation required from the DFIG grid-side converter or from the SCIG compensation device to meet the requirements on Q_{tot} (e.g. the grid operator may impose Q_{tot} to be zero or within a certain range for acceptable power factor operation).

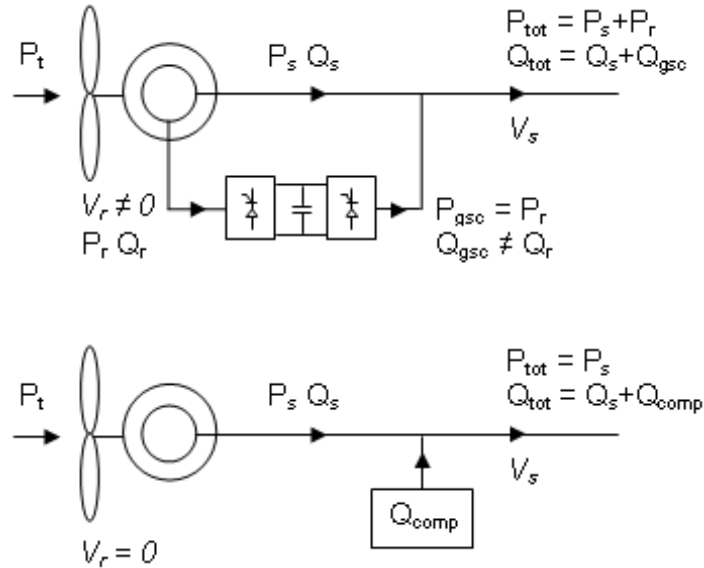


Figure 3.1: Power flows of grid connected doubly-fed induction generator (top) and squirrel cage induction generator (bottom).

In the following, the familiar steady-state characteristics of the SCIG are briefly recalled so that comparison can be made with the DFIG afterwards.

3.2 Squirrel cage induction generator

For the SCIG, the rotor voltage is zero ($v_{qr} = v_{dr} = 0$). Hence assuming that the terminal voltage is at nominal level ($v_{qs} = 1, v_{ds} = 0$), the system (3.1)-(3.4) can be solved for the machine currents over a chosen range of rotor speed (e.g. $\omega_r = 0$ to 2 pu, i.e. $s = +1$ to -1). The steady-state outputs can then be obtained with (3.5)-(3.9). The results¹ are shown in Fig. 3.2 and Fig. 3.3.

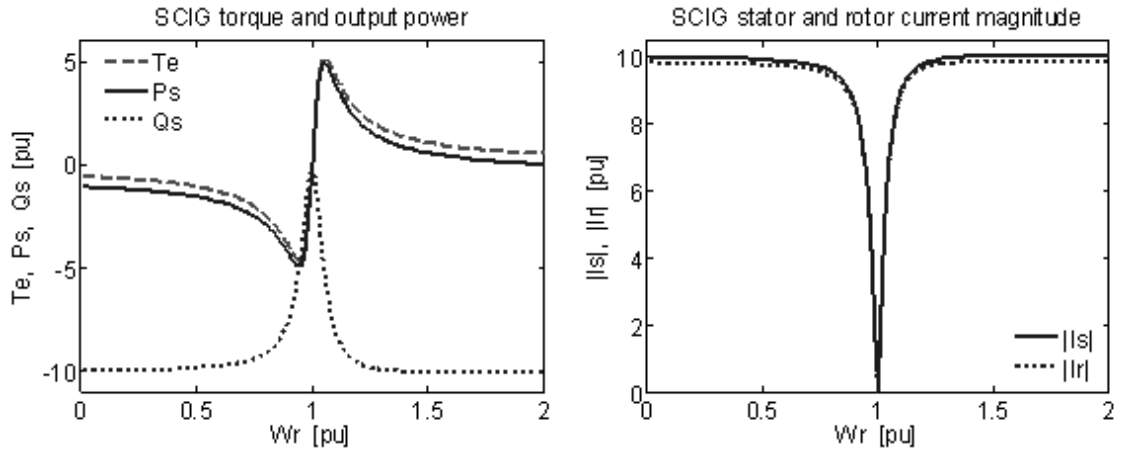


Figure 3.2: SCIG steady-state operating points as function of rotor speed under nominal terminal voltage: torque and powers (left), current magnitudes (right).

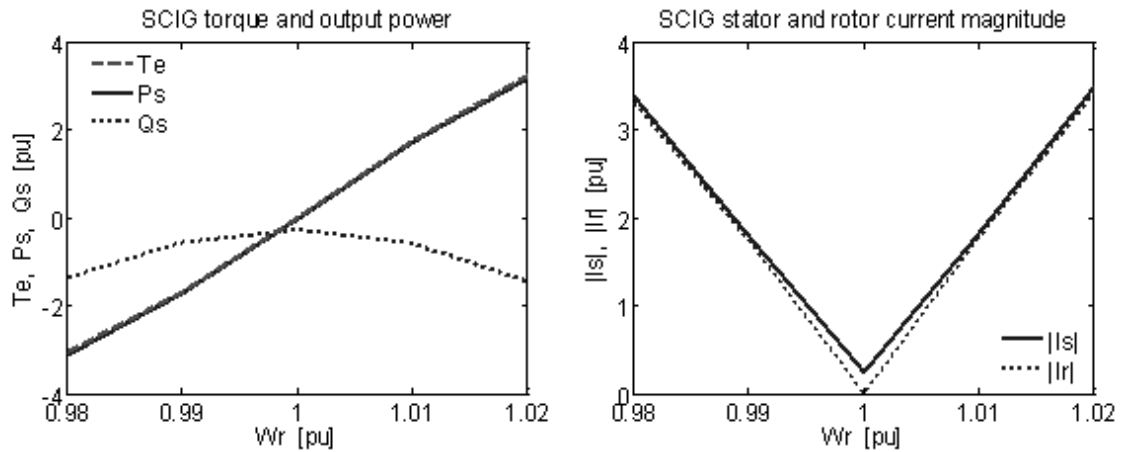


Figure 3.3: Zoomed view of Fig. 3.2.

¹The figures were obtained with the parameters of the DFIG given in the Appendix. It is noted that these parameters may not be used in practice for a real SCIG as it results in very large pull-out torque and stall current.

The SCIG is essentially a fixed speed device as it produces active power from 0 to 1 per unit within a very narrow slip range ($s = 0-1\%$ i.e. $\omega_r = 1-1.01$ pu) as can be seen in Fig. 3.3. The machine produces active power only in the super-synchronous speed region. In sub-synchronous speed, it operates as a motor. In both generator and motor mode, the stator reactive power is negative. Hence the machine absorbs reactive power and compensation must be provided to avoid voltage deterioration in weak systems.

An important trait of the SCIG behaviour is that torque, active power and reactive power demand are very sensitive to rotor speed. A small change in rotor speed gives a large change in power magnitude. Hence, if the input mechanical torque changes abruptly by a large amount (e.g. due to sudden large wind speed change) the rotor speed has just to change by a small amount for the electrical torque to match the mechanical torque i.e. for the generator to reach its new steady-state operating point. This explains the larger power fluctuations that are observed for SCIG based wind generators. As the rotor speed remain virtually constant, disturbances in wind speed appear on the electrical outputs. For the DFIG, as will be seen below, variability of the speed results in smoother behaviour.

The terminal voltage and mechanical power input of the SCIG can be controlled with suitable design and components. Terminal voltage can be maintained in a satisfactory range by using mechanically switched capacitor banks or more advanced reactive power compensators such as static var compensators (SVC) which can provide continuously variable susceptance [122]. Mechanical power input can be controlled by aerodynamic design of the blades and/or blade pitching. In high wind speed, the level of captured wind power can be limited by stalling or pitching the blades as discussed in Chapter 1. In lower wind speeds, since the SCIG is not controllable, the captured power can not be optimised.

The latter point is illustrated in Fig. 3.4 which shows the operating points² of the SCIG for different wind speeds and gearbox ratios. When the wind speed increases from $v_w = 8$ to 12 [m/s], the operating point goes from A to C . It can be seen that for a fixed gearbox ratio³, the power capture can be optimised only for one particular wind speed.

²Steady-state operating points are in fact given by the intersection of the input mechanical torque T_m and output electrical torque T_e characteristics. However, if machine resistances are small, losses are negligible under nominal voltage, and operating points can be approximated by the intersection of input and output power curves, P_m and P_s , as shown in Fig. 3.4.

³Changing the gearbox ratio translates the tip-speed ratio with respect to the rotor speed and hence

In the examples of Fig. 3.4, with the gearbox ratio $n_{gb} = 121.2$, the power capture is maximised for the wind speed $v_w = 12$ [m/s] (point C). With a $n_{gb} = 145.5$, the power capture is maximised for $v_w = 10$ [m/s] (point B). As will be shown below, the situation for the DFIG is different and maximum power tracking can be achieved over wide range of wind speed and rotor speed.

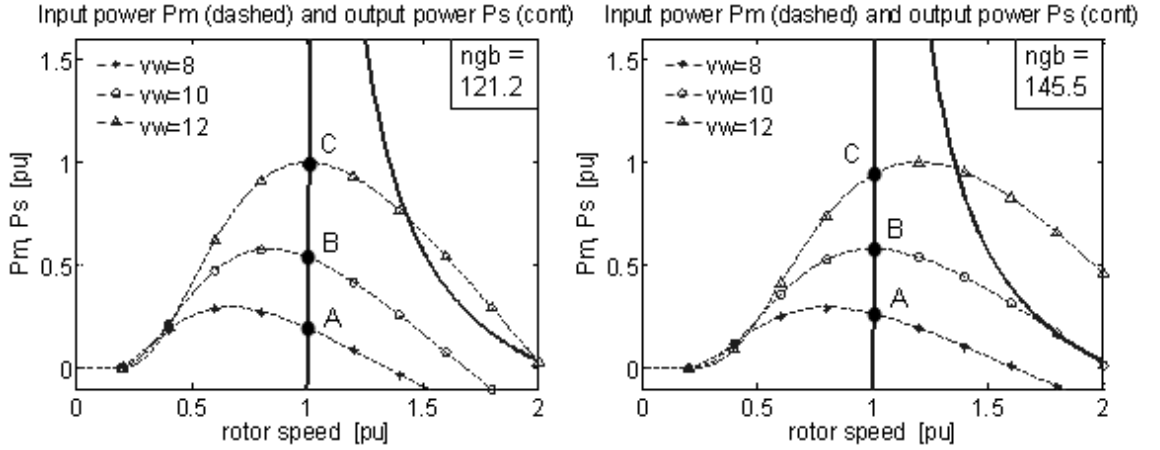


Figure 3.4: SCIG steady-state operating points at different wind speeds v_w [m/s] and gearbox ratios n_{gb} .

3.3 Doubly-fed induction generator

For the DFIG, the rotor voltage is non-zero ($v_{qr} \neq 0$, $v_{dr} \neq 0$). Hence, the steady-state equations (3.1)-(3.4) is a system of four equations and six unknowns for given terminal voltage and rotor speed. As a result, two constraints have to be specified so that an operating point can be determined. In wind applications, it is sensible to impose a constraint on the electrical torque (or rotor speed) for maximum power capture, and the other constraint on the reactive power (or power factor) for terminal voltage control. The two constraints can be written as:

$$T_{e,ref} = L_m(i_{qs}i_{dr} - i_{ds}i_{qr}) \quad (3.10)$$

$$Q_{s,ref} = -v_{qs}i_{ds} + v_{ds}i_{qs} \quad (3.11)$$

translates the input power curves P_m along the rotor speed axis.

As explained in Section 2.4, the constraints (3.10) and (3.11) are the control objectives of the rotor-side converter. The torque reference $T_{e,ref}$ is such that maximum power tracking is achieved in subrated condition and rated torque tracking is achieved in rated condition. The reference reactive power $Q_{s,ref}$ is determined by the desired power factor or terminal voltage and by the sharing policy with the GSC.

3.3.1 Steady-state characteristics

Fig. 3.5 shows the steady-state characteristics obtained by solving (3.1)-(3.4) and (3.10)-(3.11) with $T_{e,ref}$ given in (2.114)-(2.115), under the assumptions that the terminal voltage is at nominal level ($v_{qs} = 1, v_{ds} = 0$) and the DFIG at unity power factor ($Q_{s,ref} = 0$). The steady-state characteristics are shown for three examples of rated rotor speed ($\omega_{r,rated} = 1, 1.1$ or 1.2 pu). The figure shows also the input power P_m and operating point for different wind speeds. Unlike the SCIG which is in generator mode only at super-synchronous speed, the DFIG is able to produce active power ($P_{tot} > 0$) at unity power factor ($Q_s = 0$) regardless of the rotor speed. In addition, the DFIG is able to operate optimally in subrated regime by capturing maximum input power over a wide range of wind speed and rotor speed. It is seen that choosing a higher rated rotor speed gives lower electrical torque in rated regime since the rated torque is defined as the rated airgap power (rated output plus losses) divided by the rated rotor speed ($T_{e,rated} = P_{ag,rated}/\omega_{r,rated}$).

The fact that the DFIG can produce active power at both sub- and super-synchronous speed is due to the ability of the rotor active power to flow in both directions (into or out of the machine). Fig. 3.6 shows the DFIG active and reactive power flows in the stator and rotor. In sub-synchronous speed, the rotor power P_r is negative and hence the rotor absorbs active power. In super-synchronous speed, the opposite is true. For the rotor reactive power Q_r , it is seen that at unity power factor ($Q_s = 0$), the rotor absorbs and produces a moderate quantity of reactive power in sub- and super-synchronous speed respectively. Within the operating speed range ($\omega_r = 0.7$ to 1.3) the rotor reactive power magnitude is less than 0.1 pu. The effect of non unity power factor operation ($Q_s \neq 0$) on the DFIG steady-state characteristics is examined later.

The change in the direction of the rotor active power does not actually occur at exactly

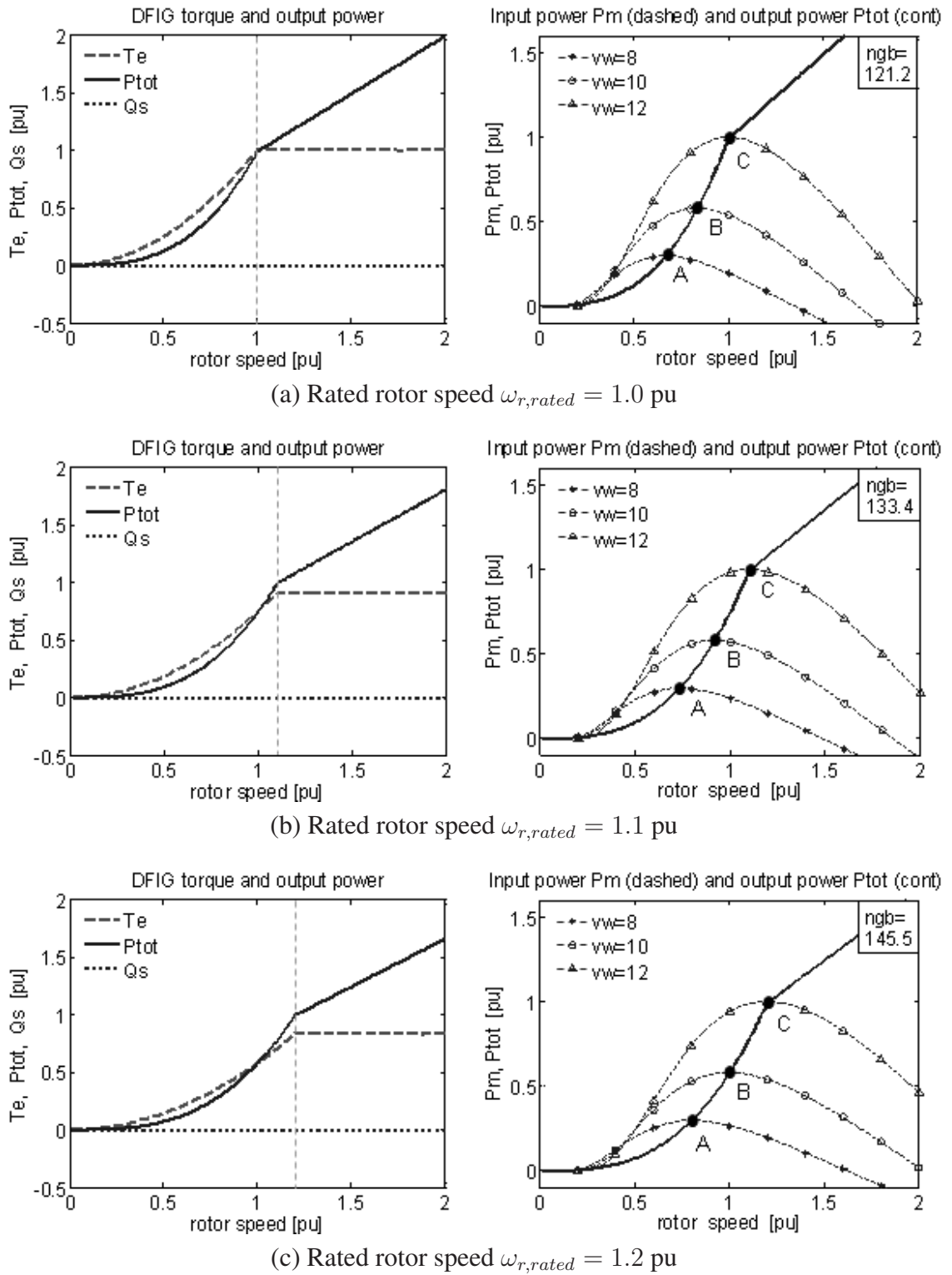


Figure 3.5: DFIG electrical torque and power as function of rotor speed under nominal terminal voltage and unity power factor for different rated rotor speeds.

the synchronous speed due to resistive losses. This is shown in Fig. 3.7 where it is seen that at synchronous speed P_r has a small negative value which corresponds to the active power required to cover the rotor copper losses. On the other hand, the rotor reactive power Q_r is indeed zero at synchronous speed, since in such case the rotor current is a dc-current.

The active power flows are obtained by substituting (3.1)-(3.4) into (3.6)-(3.7):

$$P_s = -R_s(i_{qs}^2 + i_{ds}^2) + \omega_s L_m(i_{qs}i_{dr} + i_{ds}i_{qr}) \quad (3.12)$$

$$P_r = -R_r(i_{qr}^2 + i_{dr}^2) - s\omega_s L_m(i_{qs}i_{dr} + i_{ds}i_{qr}) \quad (3.13)$$

$$P_{tot} = P_s + P_r = P_{ag} - P_{losses} \quad (3.14)$$

If winding losses are neglected, $P_r \approx -sP_s$ and $P_{ag} \approx (1 - s)P_s$. If mechanical losses are neglected, the airgap power is equal to the input power i.e. $P_{ag} \approx P_m$. Fig. 3.8 shows schematically the active power flows in the three rotor speed regions (sub-synchronous, synchronous, super-synchronous). At sub-synchronous speed ($\omega_r < 1$, $s > 0$), the rotor consumes active power ($P_r < 0$) that has to be produced by the stator ($P_s > P_{ag}$).

At synchronous speed ($\omega_r = 1$, $s = 0$), the rotor active power is nearly zero (rotor winding losses) and the airgap power is transferred to the grid via the stator ($P_r \approx 0$ and $P_s \approx P_{ag}$). At supersynchronous speed ($\omega_r > 1$, $s < 0$), the airgap power is transferred to the grid via both stator and rotor; the fraction $1/(1 - s)$ passes through the stator and the fraction $-s/(1 - s)$ through the rotor.

Fig. 3.9 shows the rotor currents that are required to achieve the control objectives in Fig. 3.5 (tracking of an optimal torque-speed curve at a desired power factor). The relationship between electrical torque and quadrature rotor current can be observed ($T_e \propto -i_{qr}$). It is seen that choosing a higher rated rotor speed $\omega_{r, rated}$ gives lower current magnitudes in rated regime.

Fig. 3.10 shows the rotor voltages that are required to achieve the control objectives in Fig. 3.5. The approximation $|V_r| \approx s|V_s|$ can be observed ($|V_r| = s|V_s|$ if losses and leakage inductances are neglected i.e. if $R_s = R_r = 0$ and $L_{ss} = L_{rr} = L_m$). It is noted that unlike the SCIG, the rotor voltage is always greater than zero. This can be seen on the zoomed view in Fig. 3.11.

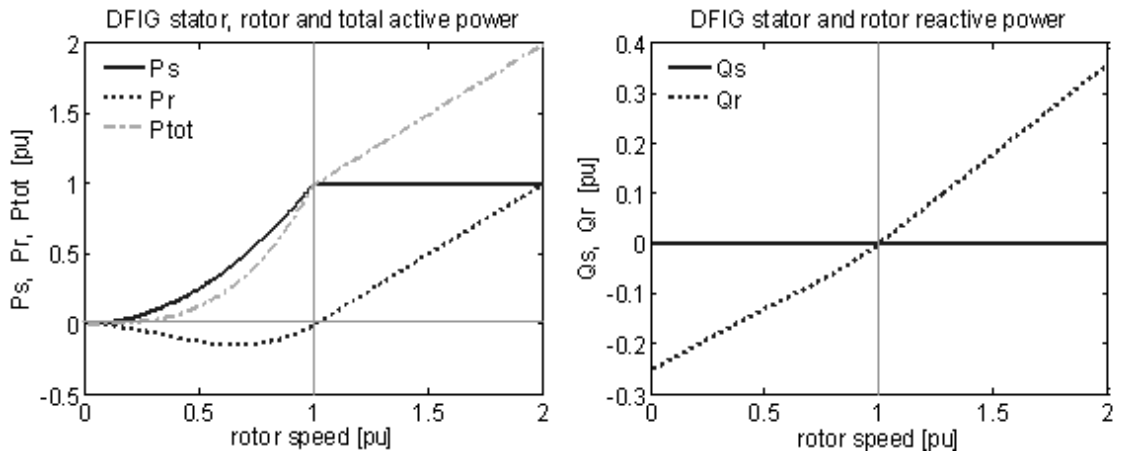
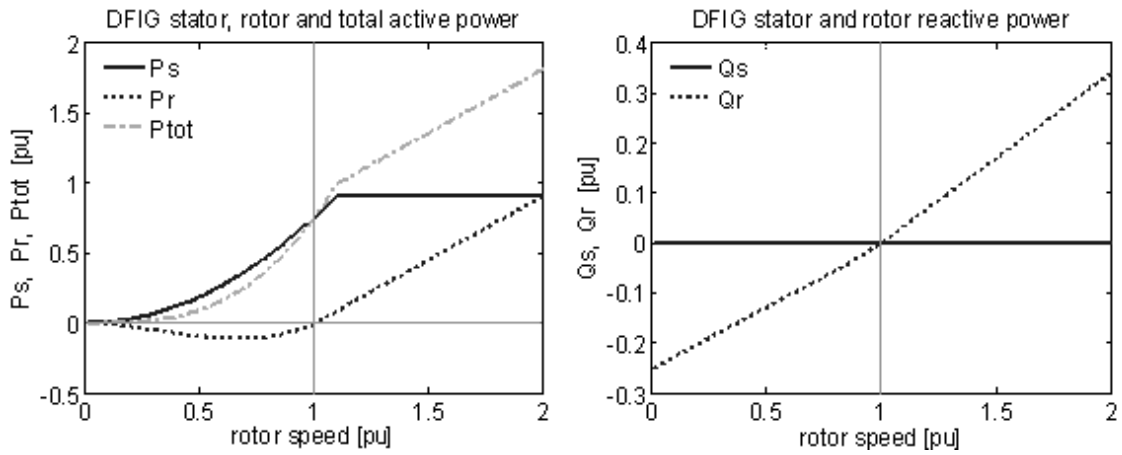
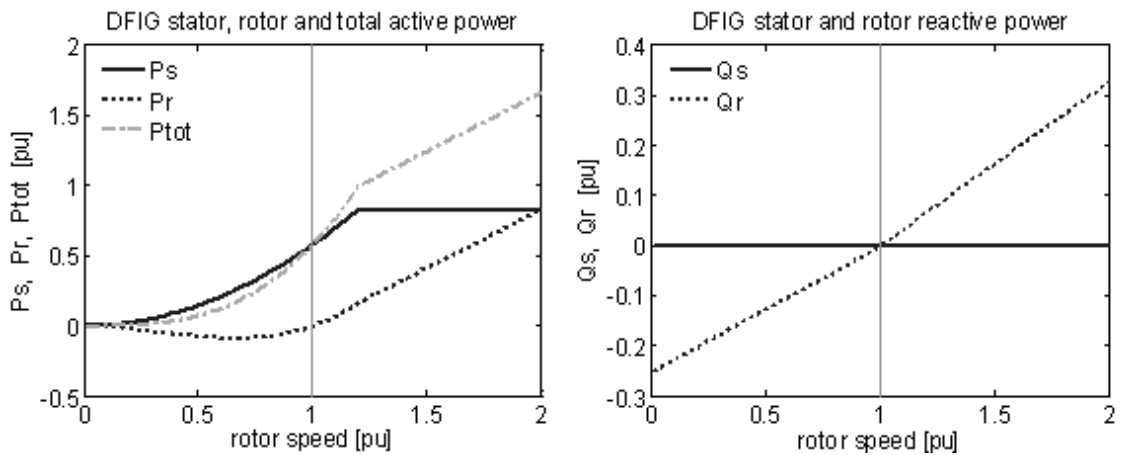
(a) Rated rotor speed $\omega_{r, \text{rated}} = 1.0$ pu(b) Rated rotor speed $\omega_{r, \text{rated}} = 1.1$ pu(c) Rated rotor speed $\omega_{r, \text{rated}} = 1.2$ pu

Figure 3.6: DFIG steady-state power flows in the stator and rotor: active power (left), reactive power (right).

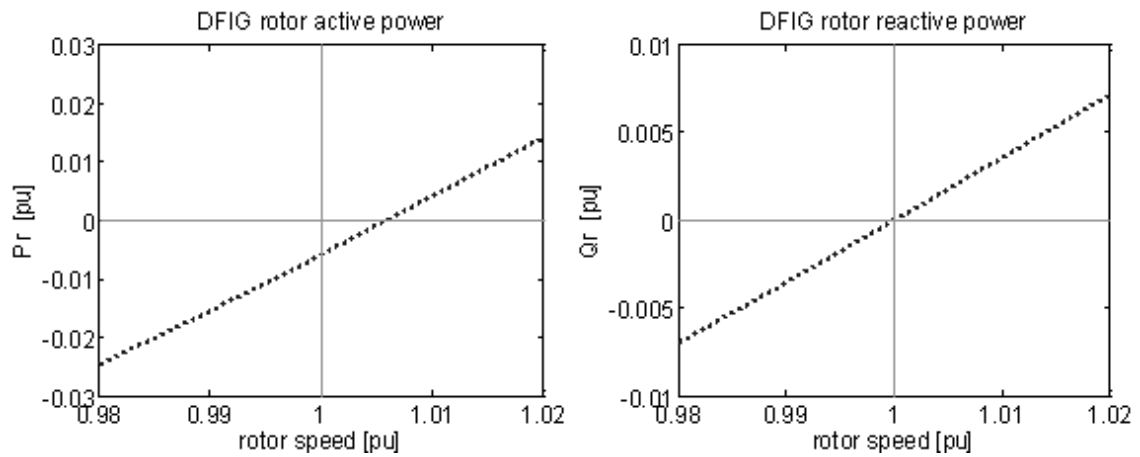
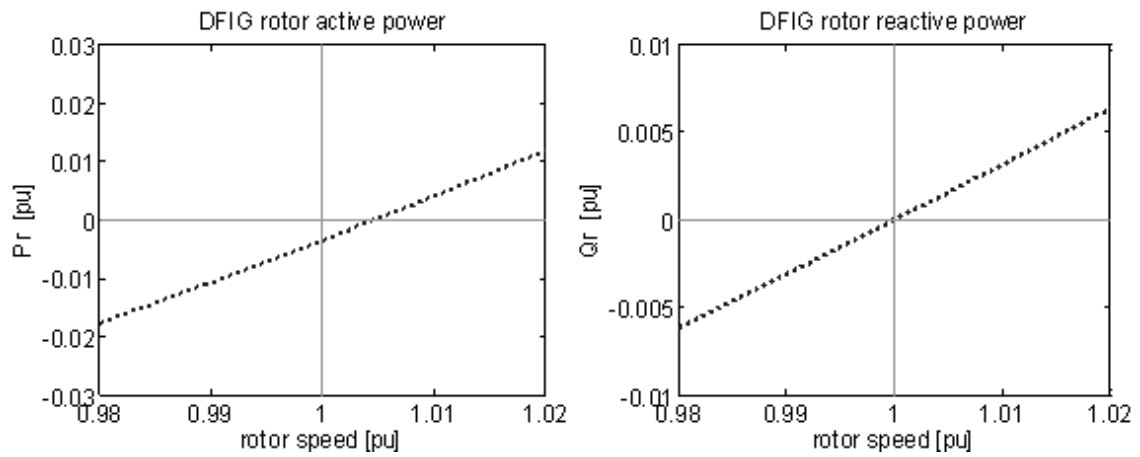
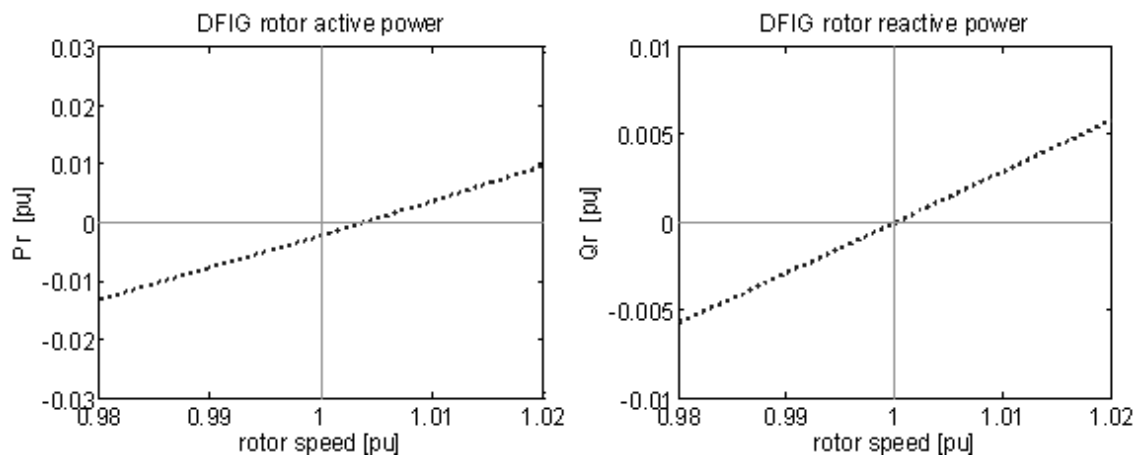
(a) Rated rotor speed $\omega_{r, rated} = 1.0$ pu(b) Rated rotor speed $\omega_{r, rated} = 1.1$ pu(c) Rated rotor speed $\omega_{r, rated} = 1.2$ pu

Figure 3.7: Zoomed view of Fig. 3.6.

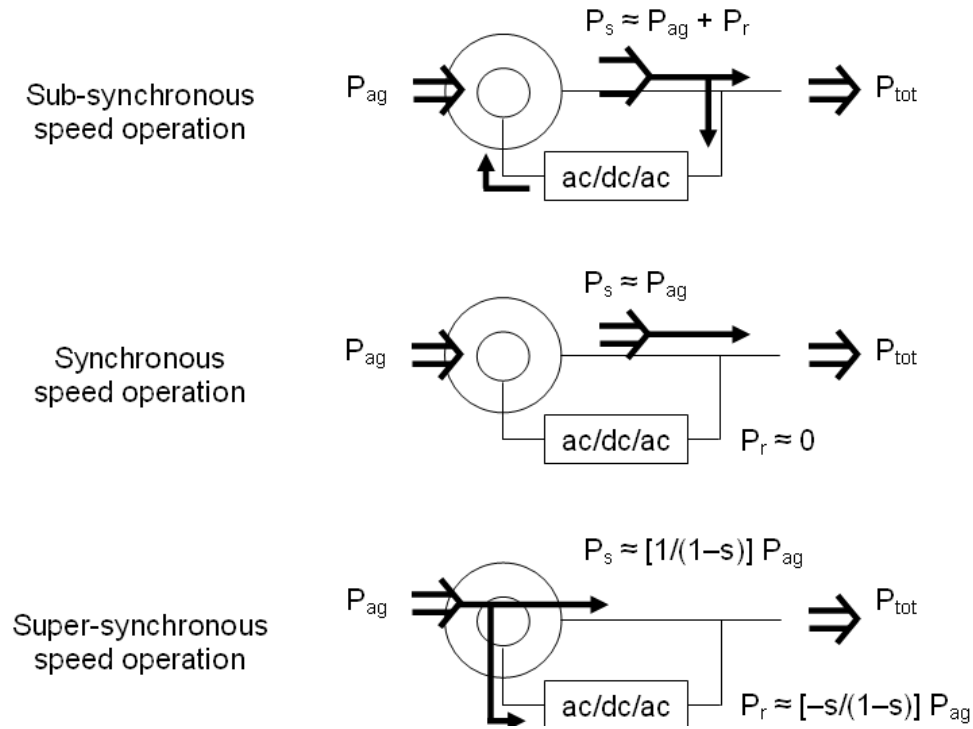


Figure 3.8: DFIG active power flows.

As mentioned in Subsection 2.2.4, the rated rotor speed can be chosen arbitrarily by adjusting the gearbox ratio. From Fig. 3.5 to 3.11, choosing different rated rotor speed has mainly influence on the electrical torque and machine currents. Power curves are translated along the rotor speed axis (for higher rated rotor speed a certain power output level is reached at a higher speed) but maximum magnitudes are not changed. For the rotor voltages, due to their small amplitudes the effect of different rated rotor speed is not significantly noticeable.

From the converter rating viewpoint, higher values of rated rotor speed are better since currents magnitudes in rated regime are lower. The rated rotor speed is usually chosen in the super-synchronous region at a value less than the maximum speed. The margin required between $\omega_{r, rated}$ and $\omega_{r, max}$ depends on the speed of the pitching mechanism and generator inertia. Lighter generators with slower pitching require a larger margin since they accelerate more quickly and the pitch control takes longer to limit the input torque.

In the remainder of this work the rated rotor speed will be assumed as $\omega_{r, rated} = 1.2$ pu, unless otherwise specified.

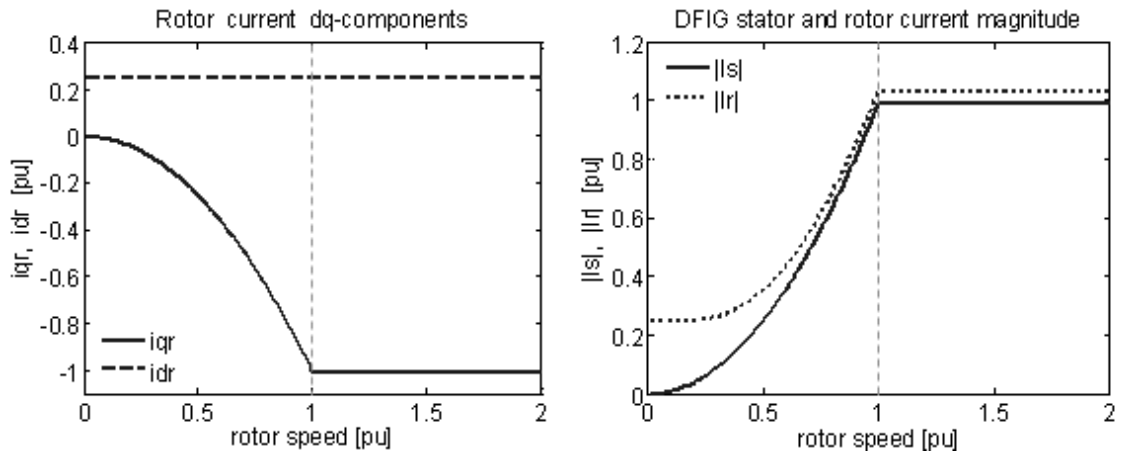
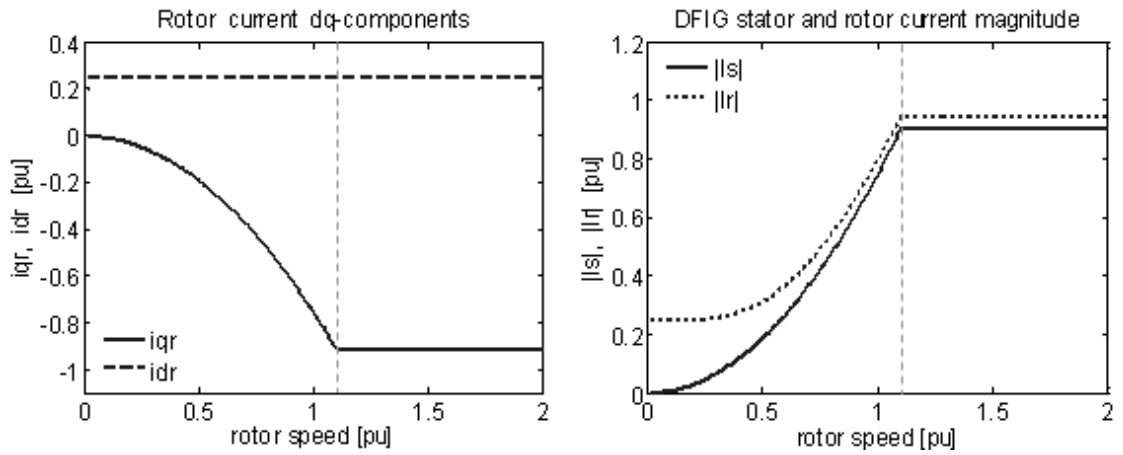
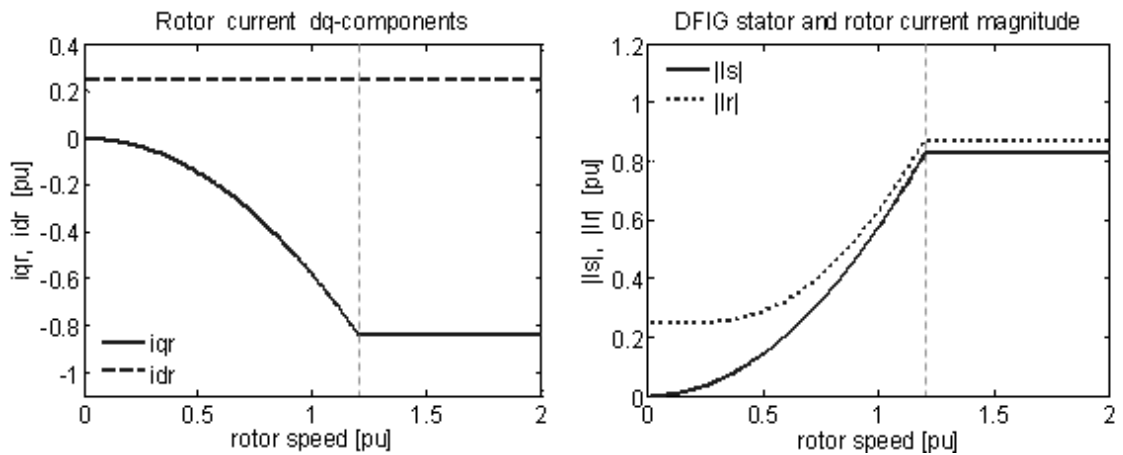
(a) Rated rotor speed $\omega_{r, \text{rated}} = 1.0$ pu(b) Rated rotor speed $\omega_{r, \text{rated}} = 1.1$ pu(c) Rated rotor speed $\omega_{r, \text{rated}} = 1.2$ pu

Figure 3.9: Required rotor currents to achieve the steady-state characteristics in Fig. 3.5: d- and q-axis components (left), magnitudes (right).

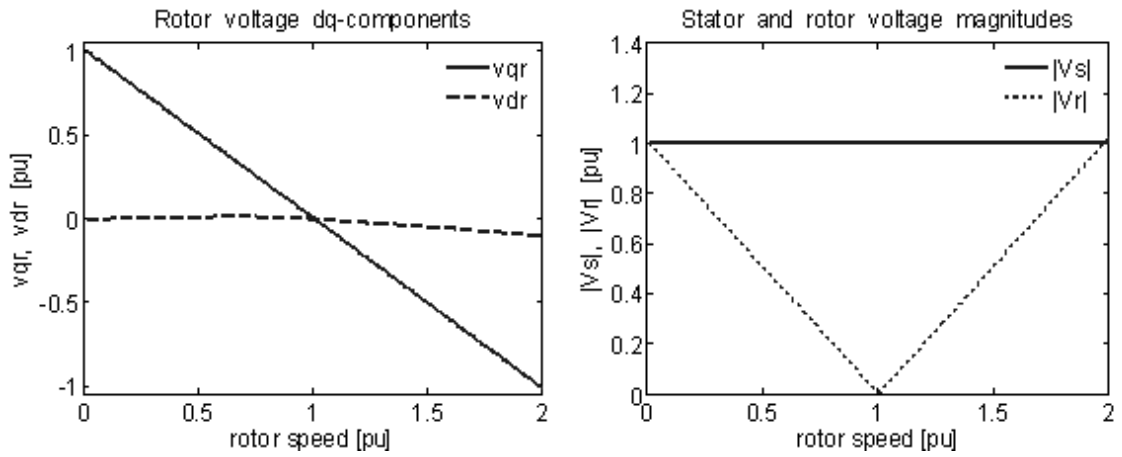
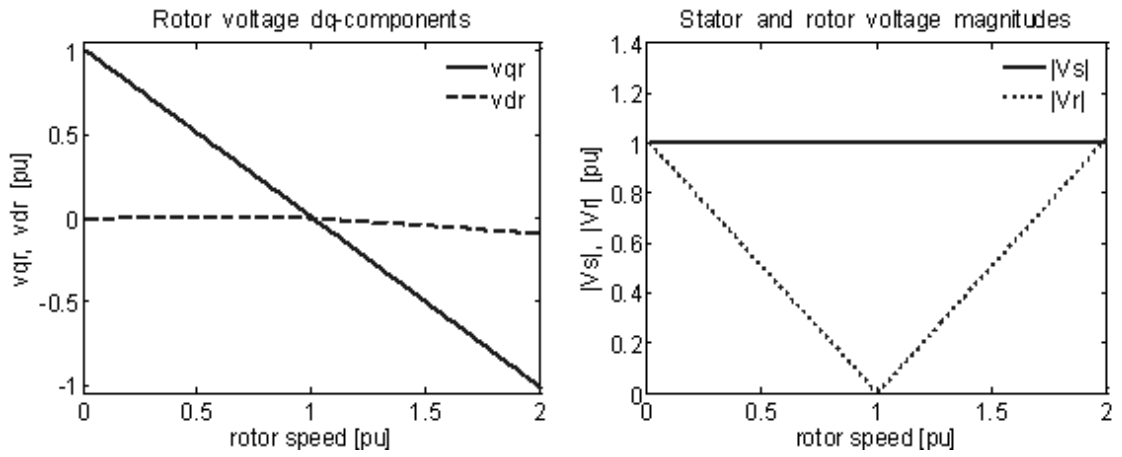
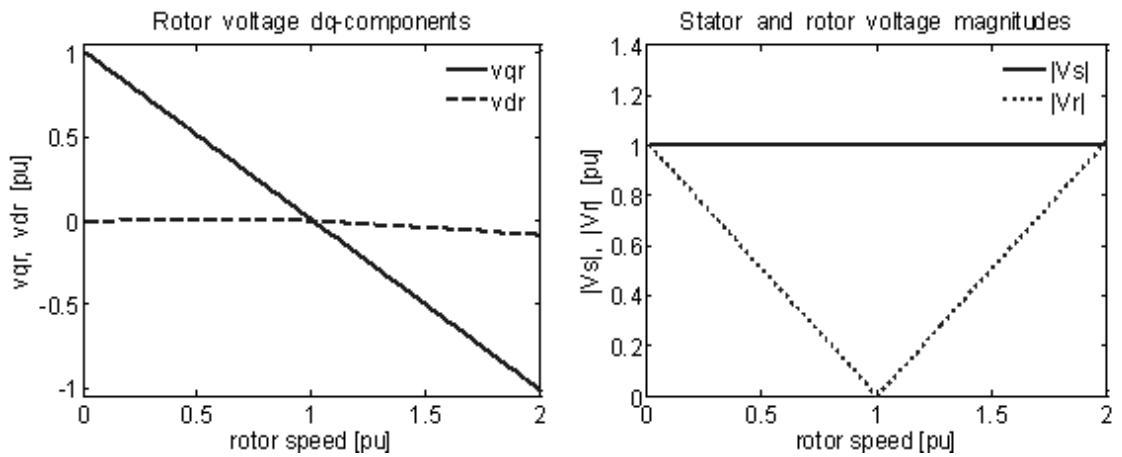
(a) Rated rotor speed $\omega_{r, rated} = 1.0$ pu(b) Rated rotor speed $\omega_{r, rated} = 1.1$ pu(c) Rated rotor speed $\omega_{r, rated} = 1.2$ pu

Figure 3.10: Required rotor voltages to achieve the steady-state characteristics in Fig. 3.5: d- and q-axis components (left), magnitudes (right).

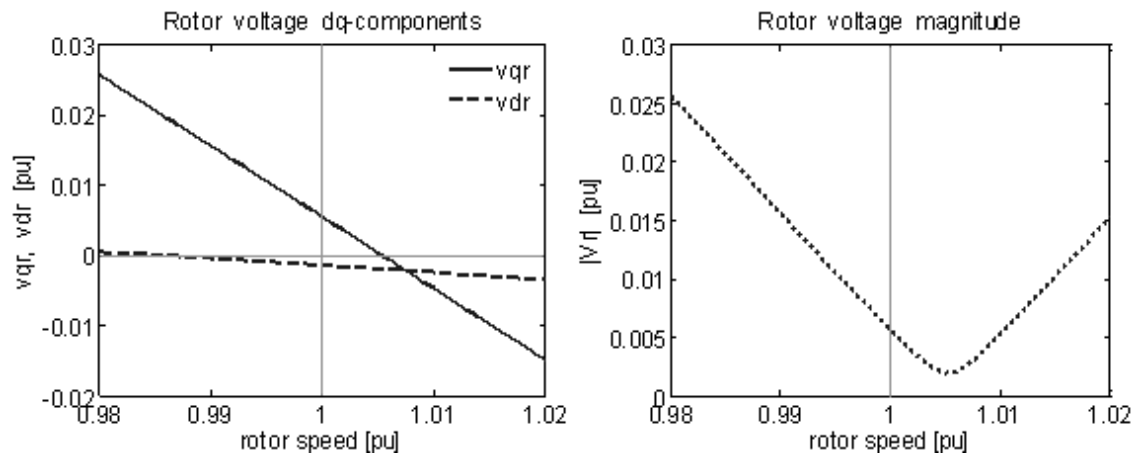
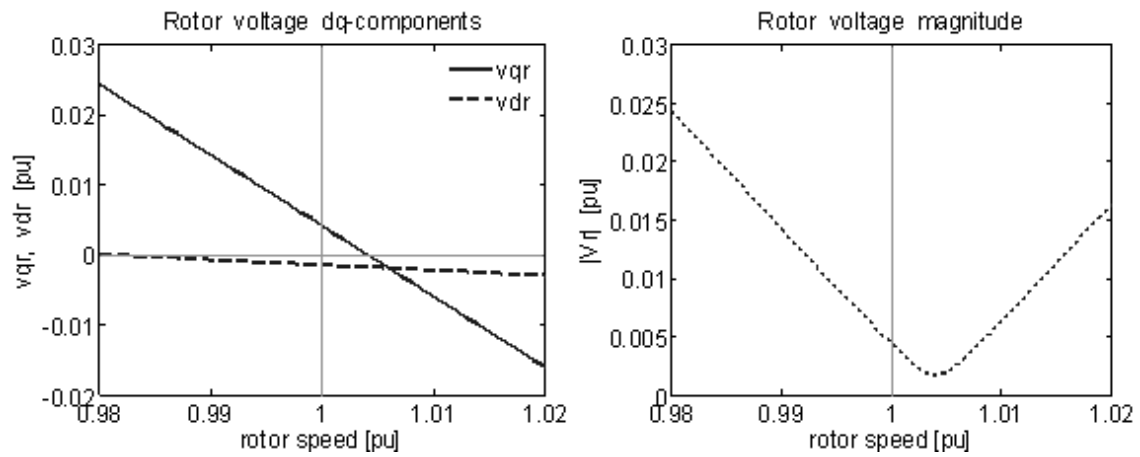
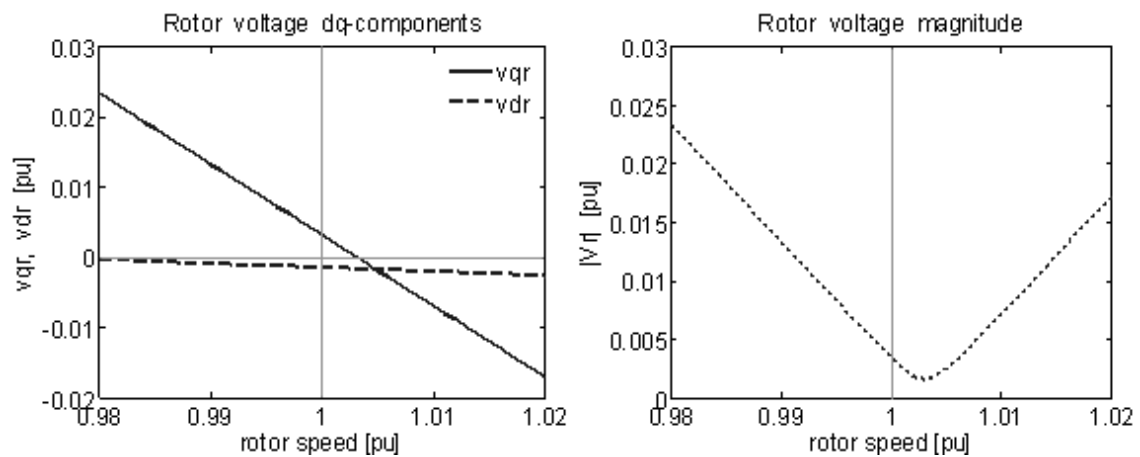
(a) Rated rotor speed $\omega_{r,rated} = 1.0$ pu(b) Rated rotor speed $\omega_{r,rated} = 1.1$ pu(c) Rated rotor speed $\omega_{r,rated} = 1.2$ pu

Figure 3.11: Zoomed view of Fig. 3.10.

In the next two subsections, the effects of imposing different levels of reactive power $Q_{s,ref}$ and electrical torque $T_{e,ref}$ are examined. The results are obtained for nominal terminal voltage ($v_{qs} = 1, v_{ds} = 0$).

3.3.2 Effect of d-axis control setpoint

Fig. 3.12 shows the effect of operating the DFIG at different levels of stator reactive power ($Q_{s,ref} = +0.5, 0, -0.5$) on the rotor active and reactive power. The rotor active power P_r is not affected by a change in reactive power setpoint. For the rotor reactive power Q_r , the flow direction (sign of Q_r) at a given rotor speed changes depending on the requested setpoint $Q_{s,ref}$.

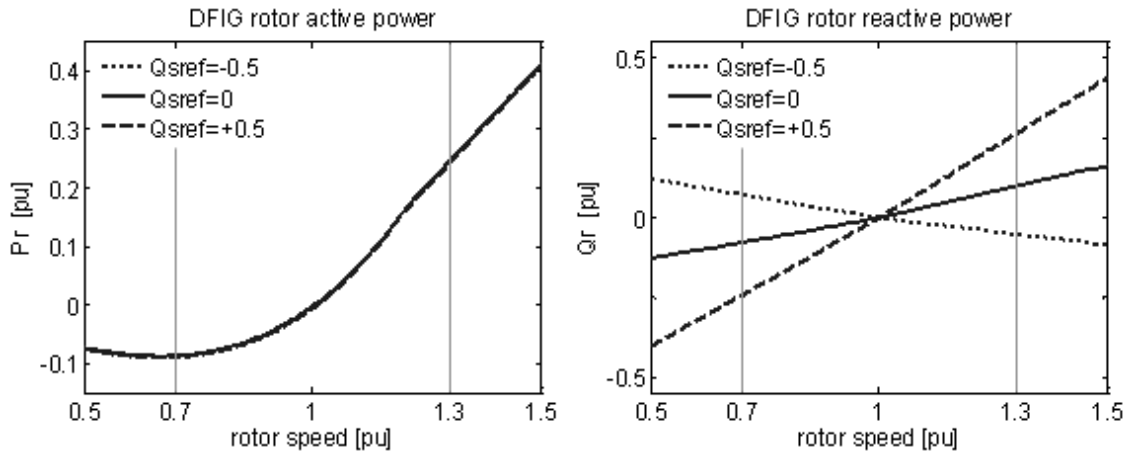


Figure 3.12: Effect of $Q_{s,ref}$ on DFIG rotor active and reactive power.

When the stator is requested to deliver 0.5 pu of reactive power, the maximum amplitude of Q_r is about 0.25 pu at the extreme values of the operating speed range ($\omega_r = 0.7$ to 1.3). Hence, in case the grid requires a reactive power output of $Q_{tot} = 0.5$ pu, the DFIG can produce that in the following ways:

- via the stator, in which case the rotor-side converter maximum reactive power amounts to about 0.25 pu and the grid-side converter operates at unity power factor, i.e. $Q_{s,ref} = Q_{tot} = 0.5$, $Q_{RSC,max} \approx 0.25$, $Q_{GSC} = 0$; or
- via the grid-side converter, in which case the DFIG stator operates at unity power factor and the rotor-side converter maximum reactive power amounts to about 0.1

pu, i.e. $Q_{s,ref} = 0$, $Q_{RSC,max} \approx 0.1pu$, $Q_{GSC} = Q_{tot} = 0.5$.

This shows that delivering reactive power via the stator rather than via the grid-side converter is more economical for the converter sizing.

Fig. 3.13 shows the effect of different $Q_{s,ref}$ levels on the direct and quadrature components of the rotor current and voltage. The figure shows the sign of the process gains i_{dr} -to- $Q_{s,ref}$ and v_{dr} -to- i_{dr} , which are important information for the tuning of the PI-controllers (discussed in more detail in Chapter 5). At a given rotor speed (e.g. $\omega_r = 0.7$), when the stator reactive power setpoint decreases (when $Q_{s,ref}$ goes from +0.5 to -0.5), the rotor d-axis current decreases (i_{dr} goes from 0.76 to -0.25). Hence the process gain i_{dr} -to- $Q_{s,ref}$ is positive and the process is referred to as direct acting. At a given rotor speed, when the rotor d-axis current decreases (when i_{dr} goes from 0.76 to -0.25), the rotor d-axis voltage increases (v_{dr} goes from 0.0036 to 0.0107). The process gain v_{dr} -to- i_{dr} is therefore negative and the process is referred to as reverse acting⁴.

The direct or reverse action of a process determines the sign of the controller gains. More explanations will be provided in Chapter 5.

Fig. 3.14 shows the effect of the reactive power setpoint $Q_{s,ref}$ on rotor voltage and current magnitudes. The curves of the rotor current magnitude for $Q_{s,ref} = 0$ or -0.5 are superposed because $|i_{qr}|$ and $|i_{dr}|$ are approximately equal for these two values of $Q_{s,ref}$ as shown in Fig. 3.13. For $Q_{s,ref}$ falling anywhere in between 0 and -0.5, the rotor current magnitude is lesser than for $Q_{s,ref} = 0$ or -0.5, because the direct axis rotor current magnitude is smaller in this range of reactive power setpoint as shown in Fig. 3.13 ($|i_{dr}| \leq 0.25$ when $-0.5 \leq Q_{s,ref} \leq 0$). This means that when the DFIG operates at unity power factor or when it absorbs reactive power from the grid up to 0.5 pu (with the grid-side converter at unity power factor), the maximum rotor current magnitude has the same value ($|I_r|_{max} \approx 0.9$ when $-0.5 \leq Q_{s,ref} \leq 0$). Hence if the generator and converters are rated for unity power factor operation, they will be able to absorb up to 0.5 pu of reactive power without exceeding their rating limits.

On the other hand, when the DFIG delivers reactive power ($Q_{s,ref} > 0$), the rotor

⁴It is noted that the directionality of the plant input-output process depends on the convention adopted for positive current. As shown in Fig. 2.6 and 2.7, the rotor current is defined in this work as positive when flowing out of the DFIG.

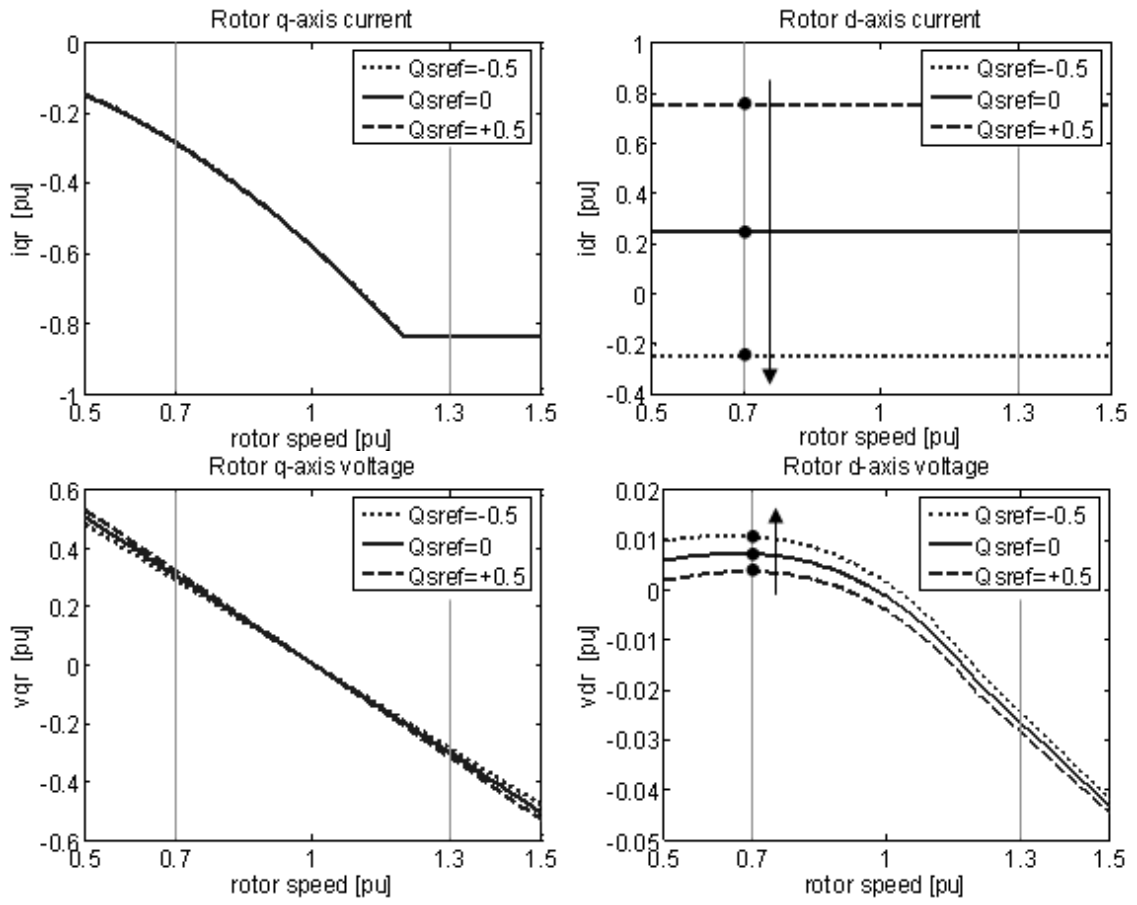


Figure 3.13: Effect of $Q_{s,ref}$ on DFIG rotor d- and q-axis currents and voltages.

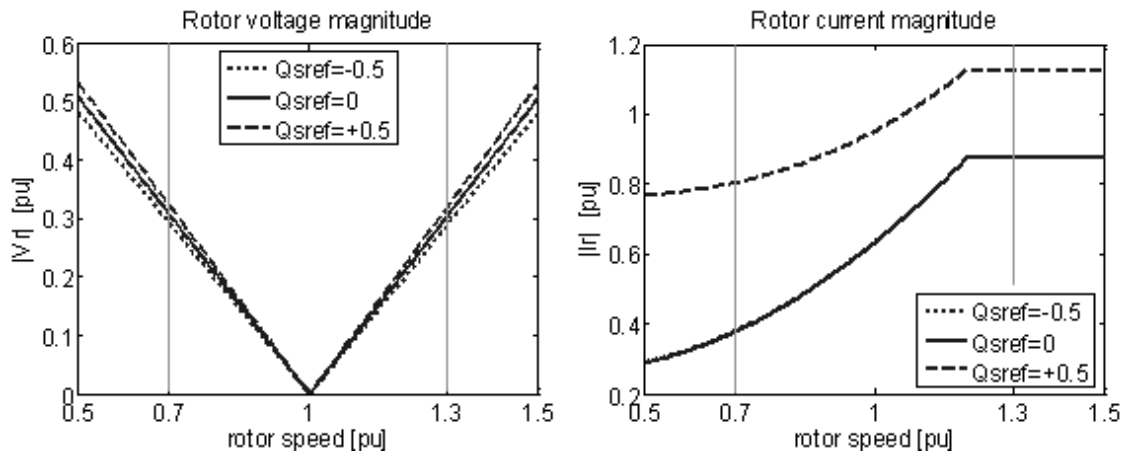


Figure 3.14: Effect of $Q_{s,ref}$ on DFIG rotor voltage and current magnitudes.

current magnitude is higher as expected. In Fig. 3.14, it is seen that for a reactive power production of 0.5 pu, the maximum rotor current magnitude is about 1.15 pu. This repre-

sents an increase in $|I_r|_{max}$ of nearly 30% with respect to zero reactive power production. The rating of the rotor-side converter decides the maximum rotor current magnitude that is permissible and hence the reactive power production capability of the DFIG.

3.3.3 Effect of q-axis control setpoint

To observe the effect of the electrical torque setpoint $T_{e,ref}$ at a given rotor speed, the following control characteristics are considered:

- $T_{e,ref1} = T_{e,ref} - 0.2$
- $T_{e,ref2} = T_{e,ref}$
- $T_{e,ref3} = T_{e,ref} + 0.2$

where $T_{e,ref}$ is given in (2.114)-(2.115). This is a purely academic exercise as in practice only $T_{e,ref2} = T_{e,ref}$ is used (the other two curves are non-optimal torque-speed curves). The analysis is however useful to verify the process gains of the q-axis variables.

Fig. 3.15 shows the effect of the electrical torque setpoint on the DFIG rotor active and reactive power (all figures in this subsection are obtained with $Q_{s,ref} = 0$).

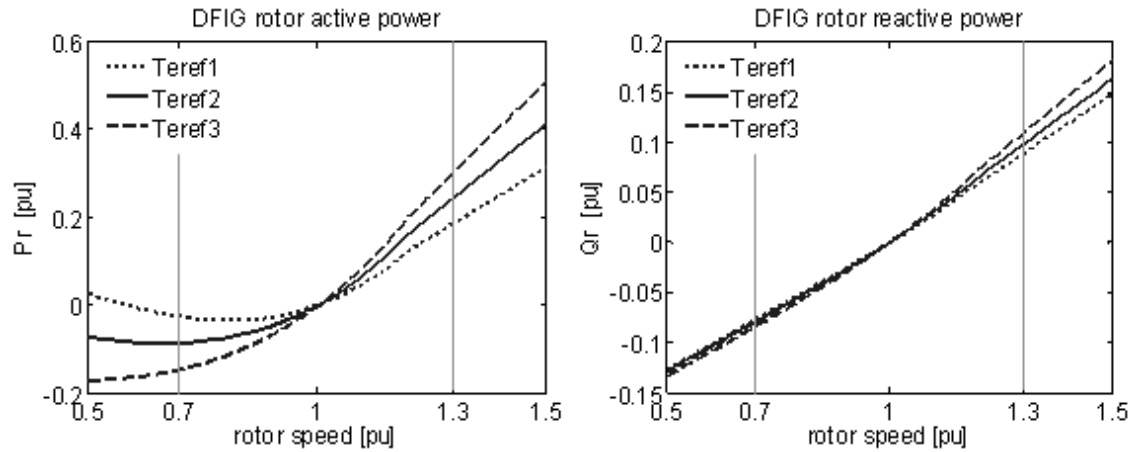


Figure 3.15: Effect of $T_{e,ref}$ on DFIG rotor active and reactive power.

As expected, when the electrical torque setpoint is higher ($T_{e,ref3}$) the rotor active and reactive power magnitudes are higher. Hence, if at a given rotor speed, the DFIG is required to extract more wind power, the rotor-side converter rating has to be larger.

Fig. 3.16 shows the effect of the torque setpoint $T_{e,ref}$ on the direct and quadrature components of the rotor current and voltage. The process gains of i_{qr} -to- T_e and v_{qr} -

to- i_{qr} can be observed by considering the operating points at a given rotor speed, e.g. $\omega_r = 0.7$. When the reference torque decreases from $T_{e,ref3}$ to $T_{e,ref1}$, the q-axis rotor current increases from -0.49 to -0.084 . Hence the process gain i_{qr} -to- T_e is negative and the process is reverse acting. Similarly, when the rotor current increases, the rotor voltage decreases. The process gain v_{qr} -to- i_{qr} is therefore negative and the process reverse acting.

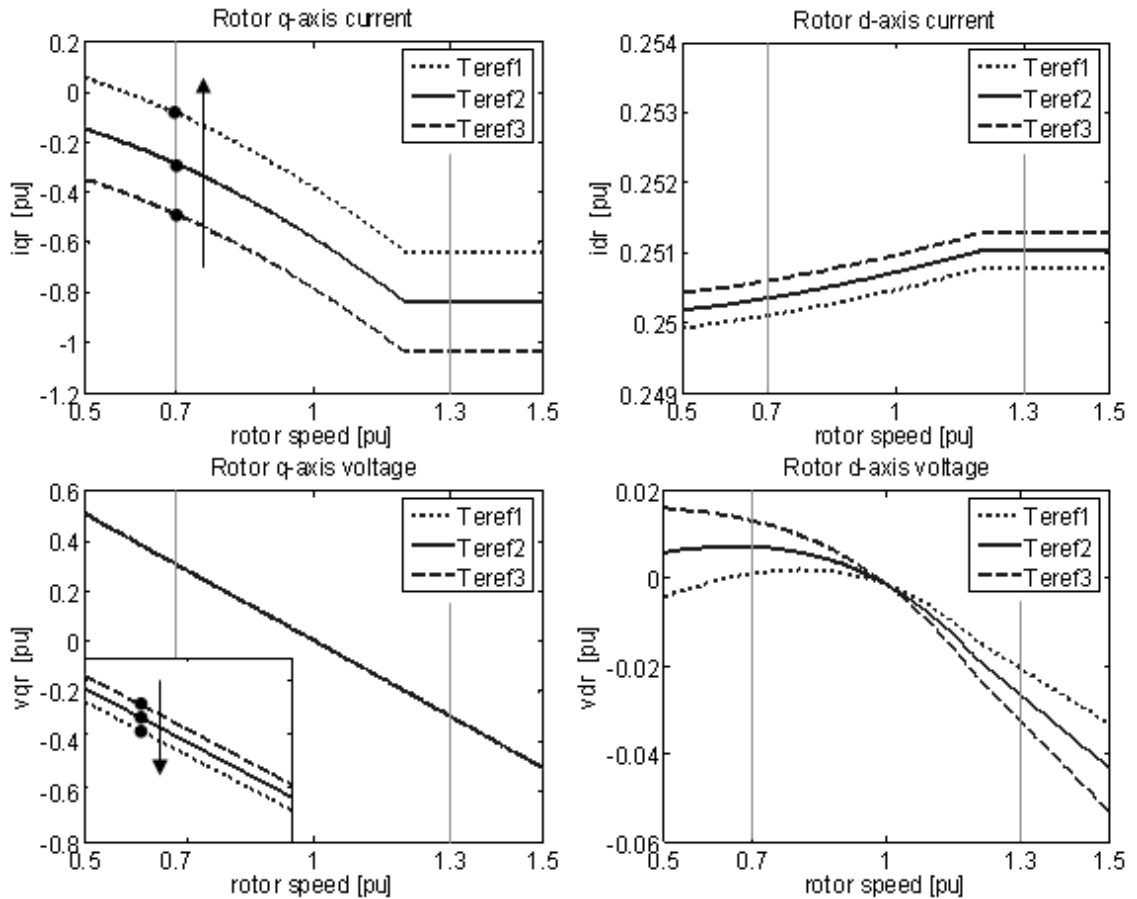


Figure 3.16: Effect of $T_{e,ref}$ on DFIG rotor d- and q-axis currents and voltages.

Fig. 3.17 shows the effect of the torque setpoint on the magnitude of the rotor current and voltage. The change in rotor voltage magnitude is very small. As expected, the rotor current magnitude is higher when the required torque is higher.

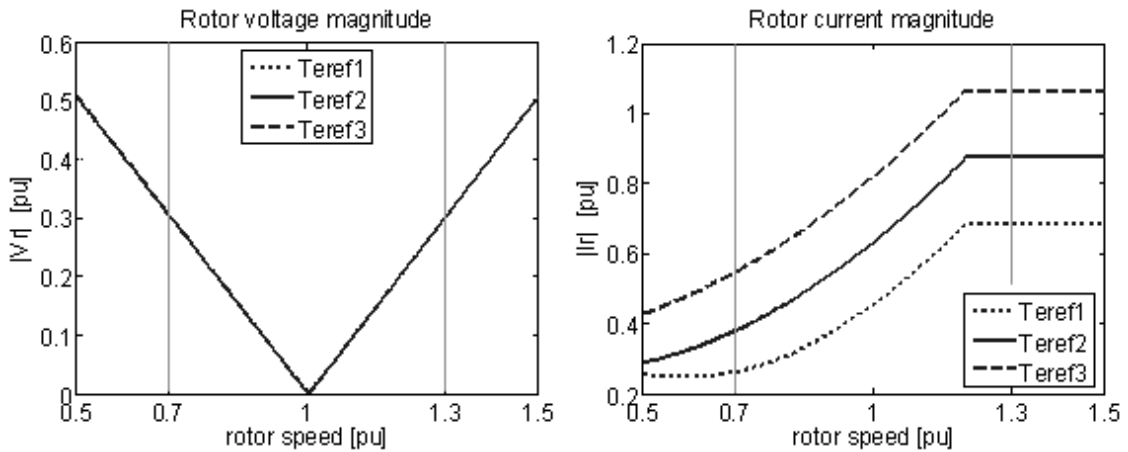


Figure 3.17: Effect of $T_{e,ref}$ on DFIG rotor voltage and current magnitudes.

3.4 Initialisation

Initialisation relates to determining the initial steady-state operating point of the dynamical system under consideration. It is the starting point for both non-linear time domain simulations and linear small-signal stability analysis. In power system studies, the procedure involves essentially two steps. In the first step, the network is initialised by a loadflow computation. The solution gives the DFIG terminal voltage (magnitude and angle) and power output (active and reactive). In the second step, the value of the DFIG state and algebraic variables are obtained by solving the steady-state equations (DAE with time derivatives equal to zero) so that the loadflow solution is satisfied.

For the conventional synchronous generator, the initialisation procedure is well known and is described in [121, 123]. For the DFIG, the fact that the rotor speed is not known in subrated regime and that there are two additional constraints for the rotor voltage has caused some confusion, resulting in different proposed methods [52, 106, 124, 125].

In [124], the equations to be solved and constraints to be considered during the initialisation are identified. However, the proposed method neglects the machine losses (i.e. it is assumed that $P_m = P_{tot}$) and considers only subrated regime when pitch angle is constant ($\beta = 0^\circ$). In [52, 106], the generator is initialised on one side from output to input and the turbine is initialised on the other side from input to output. Hence repetitive specification of initialisation starting point for both network and turbine are required

so that the variables at the interface between the turbine and generator match. In [125], the proposed method is also an iterative method as turbine and generator are initialised from input to output on one hand, while the network is initialised from output to input on the other hand. The interface where variables must match is between the generator and network. Fig. 3.18 illustrates schematically the above three methods (top figure [124], middle figure [52, 106], bottom figure [125]).

The motivation of using the methods in [52, 106, 125] is that the input wind speed can be specified. However to avoid repetitive loadflow computations (so that variables are matching between turbine and generator or between generator and network), the variables of the turbine should not be specified at the beginning but should be calculated by the initialisation procedure. Fig. 3.19 shows the procedure adopted in this work, where losses are considered. Although neglecting losses, as done in [124], does not cause large errors, including them is not be a problem since the equations are solved numerically.

The details of the three steps are as follows:

- Step 1: Compute the network loadflow solution which gives V_{mag} , V_{ang} , P_{tot} and Q_{tot} at the DFIG bus.
- Step 2: If in subrated condition, solve (3.1)-(3.8) with the loadflow solution ($v_{qs} = V_{mag}$, $v_{ds} = 0$, $P_{tot} = P_s + P_r$, $Q_{tot} = Q_s$) and with the electrical torque equal to its optimal value for maximum power tracking ($T_e = T_{e,ref} = K_{opt}\omega_r^2$), which is a system of 7 equations and 7 unknowns (i_{qs} , i_{ds} , i_{qr} , i_{dr} , v_{qr} , v_{dr} , ω_r). If in rated condition, solve (3.1)-(3.4) and (3.6)-(3.8) with the loadflow solution and with the rotor speed equal to its rated value ($\omega_r = \omega_{r,rated}$), which is a system of 6 equations and 6 unknowns (i_{qs} , i_{ds} , i_{qr} , i_{dr} , v_{qr} , v_{dr}).
- Step 3: If in subrated condition, solve the equation $P_m = 0.5\rho\pi R^2 C_p(\lambda, \beta) v_w^3$ for v_w with $P_m = T_m \omega_t$ and $\beta = 0^\circ$. If in rated condition, solve the equation $P_m = 0.5\rho\pi R^2 C_p(\lambda, \beta) v_w^3$ for β with $P_m = T_m \omega_t$ and v_w equal to a chosen wind speed above rated and below cut-out wind speed.

Table (3.1) and (3.2) give numerical examples of the DFIG initialisation in subrated and rated condition respectively. The parameters of the DFIG are in Appendix 1. It is seen

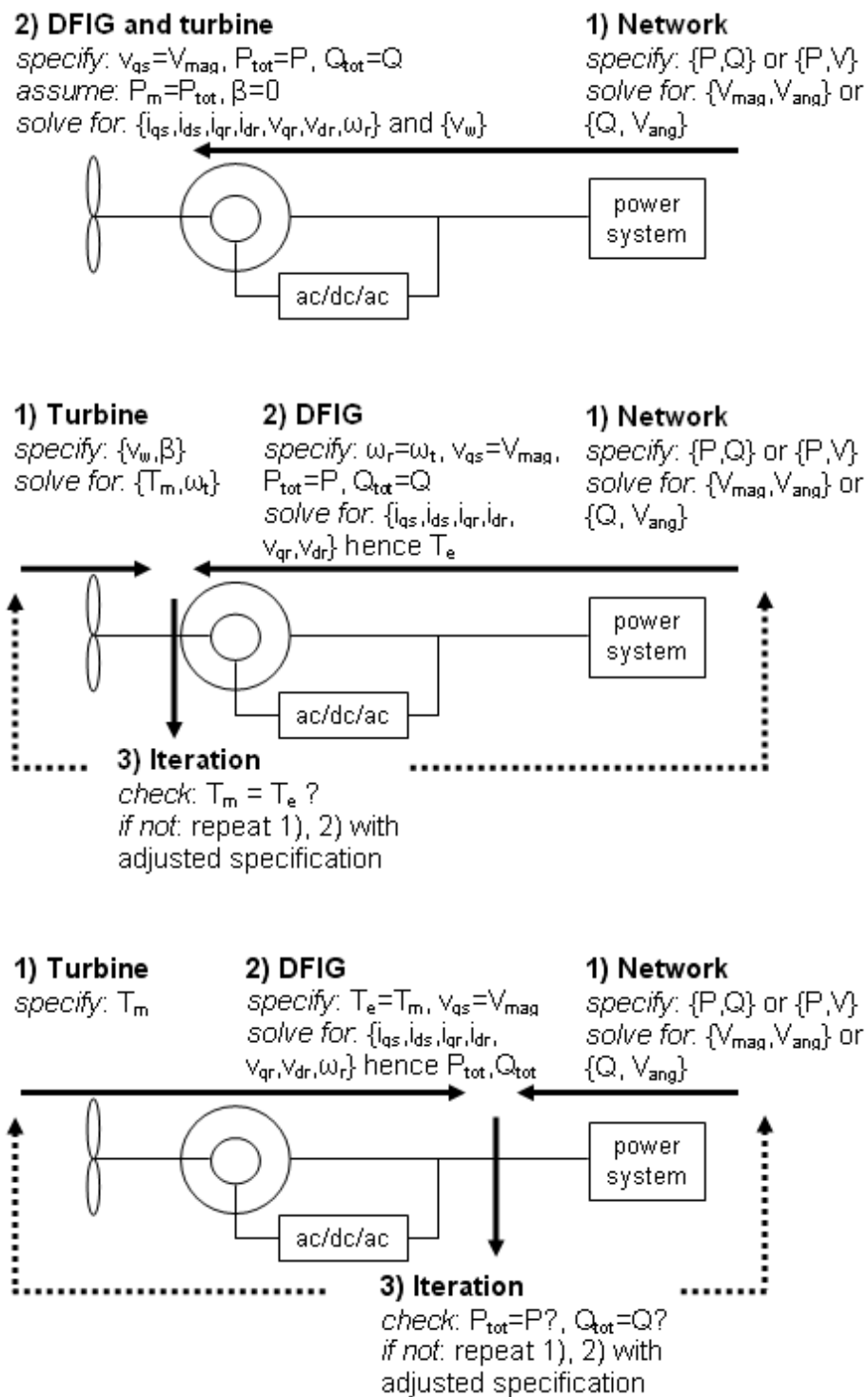


Figure 3.18: DFIG initialisation procedure alternatives

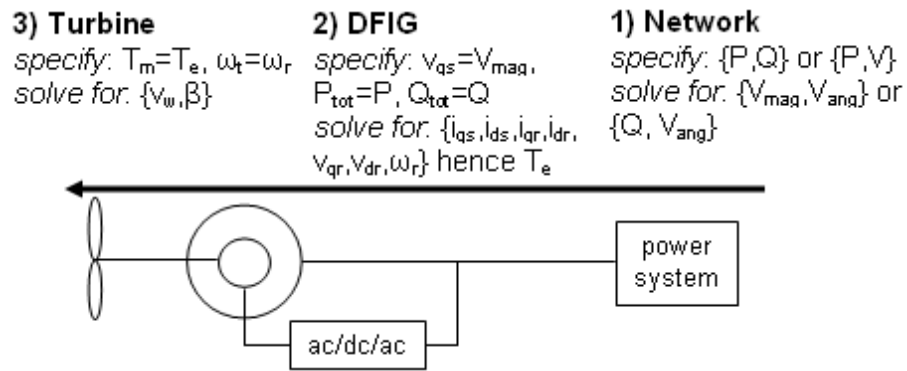


Figure 3.19: DFIG initialisation procedure used in this work.

that for same rotor speed (i.e. same active power output) the DFIG is able to operate at different power factors (i.e. different reactive power output) by adjusting the rotor voltage. The direct and reverse relationship between the d-axis variables can also be observed. In both Table (3.1) and (3.2) when Q_{tot} increases, i_{dr} increases and v_{dr} decreases. It is noted however that the relationship for the q-axis variables can not be observed in Table (3.1) and (3.2) because both torque and speed change from one table to the other. As shown in Fig. 3.16 the reverse relationship between i_{qr} - v_{dr} and T_e - i_{qr} is observed by varying the electrical torque for a same rotor speed.

Table 3.1: DFIG initialisation in subrated condition

Step 1: Network		
V_{mag}	P_{tot}	Q_{tot}
1	0.5	-0.25
1	0.5	0
1	0.5	0.25

Step 2: DFIG						
i_{qs}	i_{ds}	i_{qr}	i_{dr}	v_{qr}	v_{dr}	ω_r
0.526	0.250	-0.531	-0.002	0.0481	0.0025	0.955
0.526	0	-0.531	0.251	0.0492	0.0010	0.955
0.527	-0.250	-0.532	0.503	0.0495	-0.0005	0.955

Step 3: Turbine	
v_w [m/s]	β [°]
9.55	0
9.55	0
9.55	0

Table 3.2: DFIG initialisation in rated condition

Step 1: Network		
V_{mag}	P_{tot}	Q_{tot}
1	1	-0.25
1	1	0
1	1	0.25

Step 2: DFIG						
i_{qs}	i_{ds}	i_{qr}	i_{dr}	v_{qr}	v_{dr}	ω_r
1.006	0.250	-1.016	-0.001	0.006	-0.000	1.2
1.006	0	-1.016	0.251	0.006	-0.001	1.2
1.007	-0.250	-1.017	0.504	0.006	-0.002	1.2

Step 3: Turbine	
v_w [m/s]	β [°]
13 / 14	1.04 / 7.92
13 / 14	1.04 / 7.92
13 / 14	1.03 / 7.92

3.5 Summary

In this chapter, the operating characteristics of the SCIG and DFIG have been compared by analyzing the induction generator equations in the steady-state. For the SCIG, the rotor voltage is zero, the rotor speed is limited within a very narrow range and power capture can only be optimized for a particular wind speed. The machine absorbs reactive power at all times and electrical outputs are very sensitive to the rotor speed.

In case of the DFIG, the controllability of the rotor voltages results in controllable active and reactive output regardless of the rotor speed. This means that wind power capture can be optimised over a wide range of rotor speed and wind speed at desired power factor. The observation of the rotor active and reactive power for various terminal power factors showed that power factor control is more economical (for converter sizing) with the RSC rather than the GSC.

The steady-state analysis also showed the process gains between the inputs and outputs of the RSC control loops. The results are:

- i_{dr} -to- $Q_{s,ref}$ is direct acting,
- v_{dr} -to- i_{dr} is reverse acting,

- i_{qr} -to- $T_{e,ref}$ is reverse acting,
- v_{qr} -to- i_{qr} is reverse acting.

These observations are useful for the PI-tuning of the RSC controllers, as will be discussed in Chapter 5.

Various initialisation procedures proposed in the literature have been discussed briefly. A method has been proposed whereby no iteration in input specification is required.

Chapter 4

Analysis: Open-loop behaviour

In the previous chapter, the behaviour of the DFIG in the steady-state i.e. when all dynamics are settled, has been analysed. In this chapter, the dynamical behaviour of the open-loop DFIG in presence of small-disturbances is studied. The results will be compared in the next chapter to the closed-loop control case. The comparison will thus show the effect of the DFIG control from a dynamical behaviour viewpoint.

The system is referred to as open-loop as the rotor voltage produced by the rotor side converter is assumed constant at its initial value (pre-disturbance value), instead of being adjusted with output variations. Modal analysis (analysis of eigenvalue locations and participation factors) of the open-loop DFIG is done to gain a better understanding of the inherent strengths and weaknesses of the induction generator.

The open-loop analysis can be considered as a benchmark in the sense that the closed-loop system (discussed in the next chapter) is expected to present better dynamical characteristics. A weaker closed-loop dynamic performance would suggest an improper control design. Furthermore, it is shown that the small-signal dynamics of the conventional SCIG are similar to those of the open-loop DFIG at zero slip (synchronous speed). Hence, sensitivity results (effect of changing operating condition on the eigenvalues location) obtained for the open-loop DFIG at zero slip also hold for the SCIG.

This chapter begins with a brief review of the theoretical background for small-signal analysis and stability. A base case is then described and taken as a reference case. The effects of changing the operating point, machine parameters and grid strength on the small-signal dynamics are then discussed.

4.1 Modal analysis

The dynamical behaviour of a system, such as a grid connected DFIG, can be described by a set of differential algebraic equations (DAE) [49, 121, 126]:

$$\frac{d}{dt}x = f(x, z, u) \quad (4.1)$$

$$0 = g(x, z, u) \quad (4.2)$$

where x , z , and u are respectively the column-vectors of state variables, algebraic variables, and control inputs; f and g are respectively the column-vectors of differential and algebraic equations. In transient studies (time domain), (4.1)-(4.2) are solved simultaneously. The solution gives x , z and u as function of time, and allows calculation of the system outputs:

$$y = h(x, z, u) \quad (4.3)$$

where y is the column-vector of outputs and h the column-vector of output algebraic equations. In small-signal studies (frequency domain), (4.1)-(4.3) are linearized around an operation point and the eigenvalues of the state matrix A (defined below) allows assessment of the system small-signal stability.

Linearization of (4.1)-(4.3) is done by a Taylor series expansion around an operating point (x_0, z_0, u_0) computed by the system initialization procedure as described in the previous chapter. Neglecting terms of order two and above, the linear model is:

$$\Delta \dot{x} = \left[\frac{\partial f}{\partial x} \right]_0 \Delta x + \left[\frac{\partial f}{\partial z} \right]_0 \Delta z + \left[\frac{\partial f}{\partial u} \right]_0 \Delta u \quad (4.4)$$

$$0 = \left[\frac{\partial g}{\partial x} \right]_0 \Delta x + \left[\frac{\partial g}{\partial z} \right]_0 \Delta z + \left[\frac{\partial g}{\partial u} \right]_0 \Delta u \quad (4.5)$$

$$\Delta y = \left[\frac{\partial h}{\partial x} \right]_0 \Delta x + \left[\frac{\partial h}{\partial z} \right]_0 \Delta z + \left[\frac{\partial h}{\partial u} \right]_0 \Delta u \quad (4.6)$$

where $\Delta x = x - x_0$, $\Delta z = z - z_0$, $\Delta y = y - y_0$, and $[\cdot]_0$ indicates that the term in brackets is evaluated at the initial point (x_0, z_0, u_0) . Eliminating the algebraic variable z in (4.4)-(4.6) gives:

$$\Delta \dot{x} = A \Delta x + B \Delta u \quad (4.7)$$

$$\Delta y = C \Delta x + D \Delta u \quad (4.8)$$

where the matrices A , B , C and D are defined as:

$$A = \left[\frac{\partial f}{\partial x} - \frac{\partial f}{\partial z} \left(\frac{\partial g}{\partial z} \right)^{-1} \frac{\partial g}{\partial x} \right]_0 \quad (4.9)$$

$$B = \left[\frac{\partial f}{\partial u} - \frac{\partial f}{\partial z} \left(\frac{\partial g}{\partial z} \right)^{-1} \frac{\partial g}{\partial u} \right]_0 \quad (4.10)$$

$$C = \left[\frac{\partial h}{\partial x} - \frac{\partial h}{\partial z} \left(\frac{\partial g}{\partial z} \right)^{-1} \frac{\partial g}{\partial x} \right]_0 \quad (4.11)$$

$$D = \left[\frac{\partial h}{\partial u} - \frac{\partial h}{\partial z} \left(\frac{\partial g}{\partial z} \right)^{-1} \frac{\partial g}{\partial u} \right]_0 \quad (4.12)$$

The matrix A is the system state matrix. Its eigenvalues λ (real and/or complex) are the natural modes of the system and contain information on the small-signal stability and behaviour. If A is real, complex eigenvalues always appear in conjugate pairs.

For stable operation, all eigenvalues $\lambda = \sigma \pm j\omega$ must be in the left half plane (LHP) i.e. $\sigma < 0$. The time constant τ [s], damping ratio ζ and oscillation frequency f [Hz] of an eigenvalue are defined as:

$$\tau = 1/|\sigma| \quad (4.13)$$

$$\zeta = -\sigma/\sqrt{\sigma^2 + \omega^2} \quad (4.14)$$

$$f = \omega/(2\pi) \quad (4.15)$$

To determine the contributing dynamics (dominant states) of a particular mode (eigenvalue), participation factors are observed. The participation factors of the n state variables into mode i are obtained as:

$$\mathbf{p}_i = \begin{pmatrix} p_{1i} \\ p_{2i} \\ \dots \\ p_{ni} \end{pmatrix} \quad (4.16)$$

where p_{ki} is the normalized participation factor of the k^{th} state into the i^{th} mode:

$$p_{ki} = |\Psi_{ik}| |\Phi_{ki}| / \left(\sum_{k=1}^n |\Psi_{ik}| |\Phi_{ki}| \right) \quad (4.17)$$

In (4.17), Ψ_{ik} is the k^{th} element of the i^{th} mode left eigenvector, Φ_{ki} is the k^{th} element of the i^{th} mode right eigenvector [49, 121]. Participation factors are also known as the

sensitivity of an eigenvalue to the diagonal elements of the state matrix A . Hence a larger participation factor p_{ki} indicates that the location of eigenvalue λ_i is more sensitive to the state variable x_k . Conversely, if p_{ki} is zero, the eigenvalue λ_i is not affected by the value of state variable x_k .

The state matrix of the grid-connected DFIG is obtained by deriving (4.9) from the set of differential algebraic equations (2.135)-(2.155). In the present chapter, two cases of open-loop DFIG are considered:

- Case A: open-loop DFIG directly connected to the infinite bus,
- Case B: open-loop DFIG connected to the infinite bus via an external line.

Assuming the DFIG directly connected to the infinite bus means that the external grid is infinitely strong and hence the terminal voltage (magnitude and angle) is constant. If the DFIG is connected to the infinite bus via a line, the effect of grid strength can be investigated, with a larger line impedance representing a weaker network. The variables and functions for cases A and B are given in Table 4.1.

Table 4.1: Two cases of open-loop DFIG

	Case A	Case B
$f(x, z, u)$	(2.135)-(2.141)	(2.135)-(2.141)
$g(x, z, u)$	-	(2.154)-(2.155)
x	$[i_{qs} \ i_{ds} \ e'_{qs} \ e'_{ds} \ \omega_r \ \theta_{tw} \ \omega_t]'$	$[i_{qs} \ i_{ds} \ e'_{qs} \ e'_{ds} \ \omega_r \ \theta_{tw} \ \omega_t]'$
z	-	$[v_{qs} \ \gamma_{Vs}]'$
$u = u_0$	$[v_{qr} \ v_{dr} \ v_w \ \beta]' = [v_{qr0} \ v_{dr0} \ v_{w0} \ \beta_0]'$	$[v_{qr} \ v_{dr} \ v_w \ \beta]' = [v_{qr0} \ v_{dr0} \ v_{w0} \ \beta_0]'$
other constants	$v_{qs} = V_{s0}, \ \gamma_{Vs} = 0$	-

4.2 Base case eigenvalues

For easier discussion, a particular operating point is defined as the base case. In the base case, the terminal voltage magnitude is $|V_s| = 1$ pu, the rotor speed is equal to the synchronous speed $\omega_r = 1$ pu, the corresponding total active power is $P_{tot} = 0.575$ pu, and the total reactive power is $Q_{tot} = 0$ pu (unity power factor). The DFIG is directly connected to the infinite bus (Case A in Table 4.1), hence the terminal voltage is constant. The effect of finite grid strength is investigated subsequently in Subsection 4.5.

Table 4.2 shows the base case eigenvalues and corresponding participation factors (parameters are given in Appendix 1). The dynamics consist of four stable modes (negative real part), three of which are oscillating (complex eigenvalue). The participation factors indicate the dominant states for each mode. E.g. the high frequency eigenvalue λ_{HF} is mainly contributed by the dynamics of the stator currents i_{qs} and i_{ds} (48% and 46%) and negligibly by those of the internal voltages e'_{qs} and e'_{ds} (2% and 3%).

Table 4.2: Base case eigenvalues and participation factors of open-loop DFIG

Operating point: $V_s = 1$, $\omega_r = 1$, $P_{tot} = 0.575$, $Q_{tot} = 0$

Eigenvalue, frequency, damping ratio, time constant								
	$\lambda = \sigma \pm j\omega$	f_{osc} [Hz]	ζ	τ [s]				
λ_{HF}	$-16.15 \pm j313.30$	49.86	0.052	0.062				
λ_{MF}	$-10.01 \pm j63.67$	10.13	0.155	0.100				
λ_{LF}	$-0.47 \pm j3.33$	0.53	0.138	2.15				
λ_{NO}	-17.40	0	1	0.058				

Participation factors								
	i_{qs}	i_{ds}	e'_{qs}	e'_{ds}	ω_r	θ_{tw}	ω_t	
λ_{HF}	.48	.46	.02	.03	.00	.00	.00	E
λ_{MF}	.02	.01	.01	.47	.46	.01	.00	EM
λ_{LF}	.00	.00	.00	.01	.00	.49	.50	M
λ_{NO}	.00	.00	.98	.00	.00	.00	.00	E

HF , MF , LF = high, medium, low freq., NO = non-oscillating

E, M, EM = electrical, mechanical, electro-mechanical mode

In the base case, the high frequency mode λ_{HF} is an electrical mode associated with stator dynamics (i_{qs} , i_{ds}). The medium frequency mode λ_{MF} is an electro-mechanical mode associated with rotor electrical and rotor mechanical dynamics (q-axis flux $e'_{ds} \propto \psi_{qr}$ and generator speed ω_r). The low frequency mode λ_{LF} is a mechanical mode associated with shaft and turbine dynamics (torsion angle θ_{tw} and turbine speed ω_t). The non-oscillating mode λ_{NO} is a real eigenvalue associated with rotor electrical dynamics (d-axis flux $e'_{qs} \propto \psi_{dr}$). The modes are approximately decoupled since a particular state variable participates significantly in only one of the modes.

Fig. 4.1 shows the response of the DFIG active power to a 50% voltage drop from 1 to 0.5 pu at $t = 5$ s for a duration of 100 ms. It is seen that the time domain behaviour consists of a superposition of the characteristics given by the eigenvalues in Table 4.2.

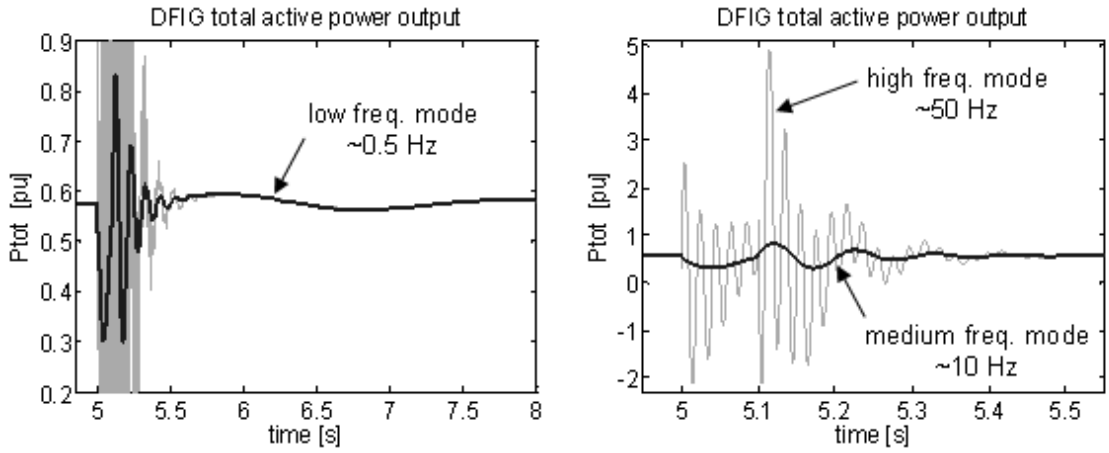


Figure 4.1: Active power response of open-loop DFIG to 100ms-50% voltage drop at base case operating point. Thin light line = stator transient included; thick dark line = stator transients neglected.

The low frequency mode λ_{LF} is the dominant mode (closest to the imaginary axis) and hence has largest time constant. It has a frequency of about 0.5 Hz with a reasonable damping ratio ($>10\%$). The medium frequency mode λ_{MF} oscillates around 10 Hz with a similar damping ratio. The high frequency mode λ_{HF} oscillates around 50 Hz and has the lowest damping ratio ($\sim 5\%$).

In Fig. 4.1, the responses are shown for both situations where stator transients are represented and neglected. It can be seen that the difference consists of only the 50 Hz mode and associated overshoot. Ignoring stator transients means that stator dynamics are assumed to change infinitely fast i.e. stator variables are assumed to be algebraic variables instead of state variables (derivatives terms in (2.135)-(2.136) are set to zero).

Oscillations due to stator transients can be omitted when they are: (a) stable (positive damping), (b) relatively faster (large real part magnitude), and (c) decoupled from the dynamics of interest. The latter condition requires that the stator mode is only contributed significantly by stator states and that stator states participate significantly only in the stator mode. Conditions (a)-(c) are satisfied for the base case as shown in Table 4.2. Hence if the interest is in the frequency range 0.1-10 Hz, stator dynamics can be ignored. It should however be kept in mind that oscillation amplitudes are underestimated during the few hundreds ms after a disturbance. This is shown in Fig. 4.2 where the underesti-

mated torque overshoot translates into underestimated speed deviation. Depending on the purpose of study, these approximations may or may not be acceptable.

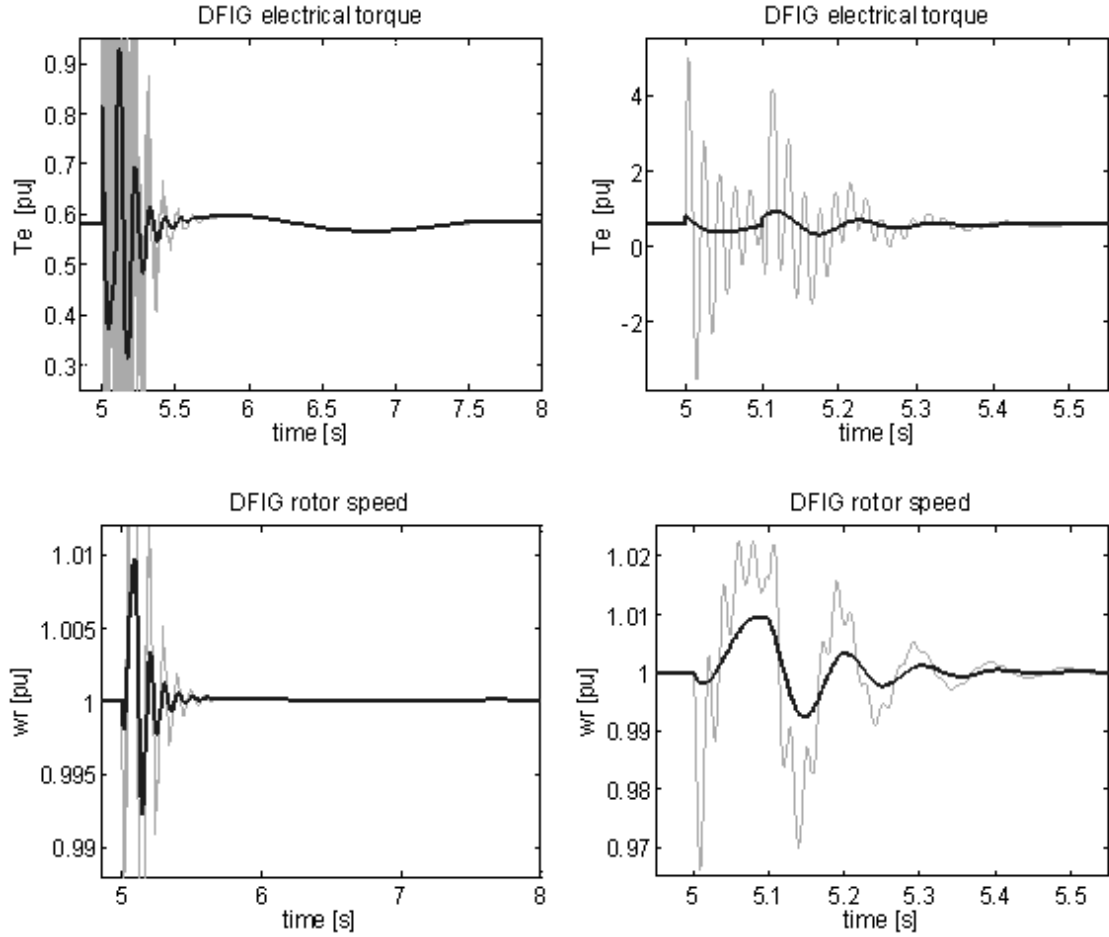


Figure 4.2: Electrical torque and rotor speed response of open-loop DFIG response to 100 ms-50% voltage drop at base case operating point. Thin light line = stator transient included; thick dark line = stator transients neglected.

4.3 Sensitivity to operating point

Since the DFIG may operate at large slip with different levels of active and reactive power output, it is important to study how its dynamic behaviour changes with these conditions.

4.3.1 Rotor speed and active power

To observe the sensitivity of the eigenvalue locations to the level of active power and rotor speed, the operating points in Fig. 4.3 are investigated. The rotor speed is varied from 0.7

to 1.3 pu (slip range of $\pm 30\%$). Two sets of active power output are considered. Set (1) represents the typical steady-state output power of the DFIG as function of rotor speed. Set (2) represents a hypothetical case where the output is constant at 0.5 pu at all speeds. Circle markers are used for operating points in the sub-synchronous speed region; triangle markers are used for the super-synchronous region.

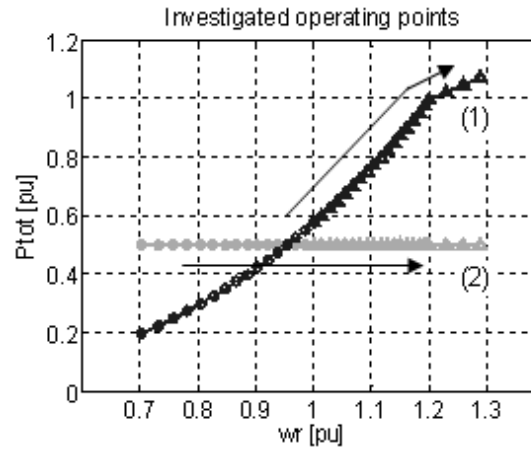


Figure 4.3: Investigated initial operating points for rotor speed and active power.

Fig. 4.4 shows the root-loci of the open-loop DFIG eigenvalues for the operating points in Fig. 4.3. It is observed that the eigenvalue locations for the two sets of operating points are not significantly different. In other words, small-signal dynamics are more sensitive to rotor speed and relatively less sensitive to active power level.

Considering the scaling of the axes, the effect of initial rotor speed on the high frequency mode (stator electrical dynamics) is not significant. For the medium frequency modes (rotor electrical and/or mechanical dynamics) small-slip speed gives oscillations with lower frequency (smaller imaginary part magnitude) and longer time constant (smaller real part magnitude). The low frequency mode (mechanical dynamics) is closer to the imaginary axis at zero and large negative slip i.e. at synchronous and large super-synchronous speed (points at the middle and end extremity of the root-loci), however the mode remains well damped ($\zeta > 10\%$). The non-oscillating mode (rotor electrical or mechanical dynamics) is closer to the imaginary axis at large slip (positive and negative). Since all eigenvalues remain in the left half plane, the open-loop DFIG remains stable within the operating slip range.

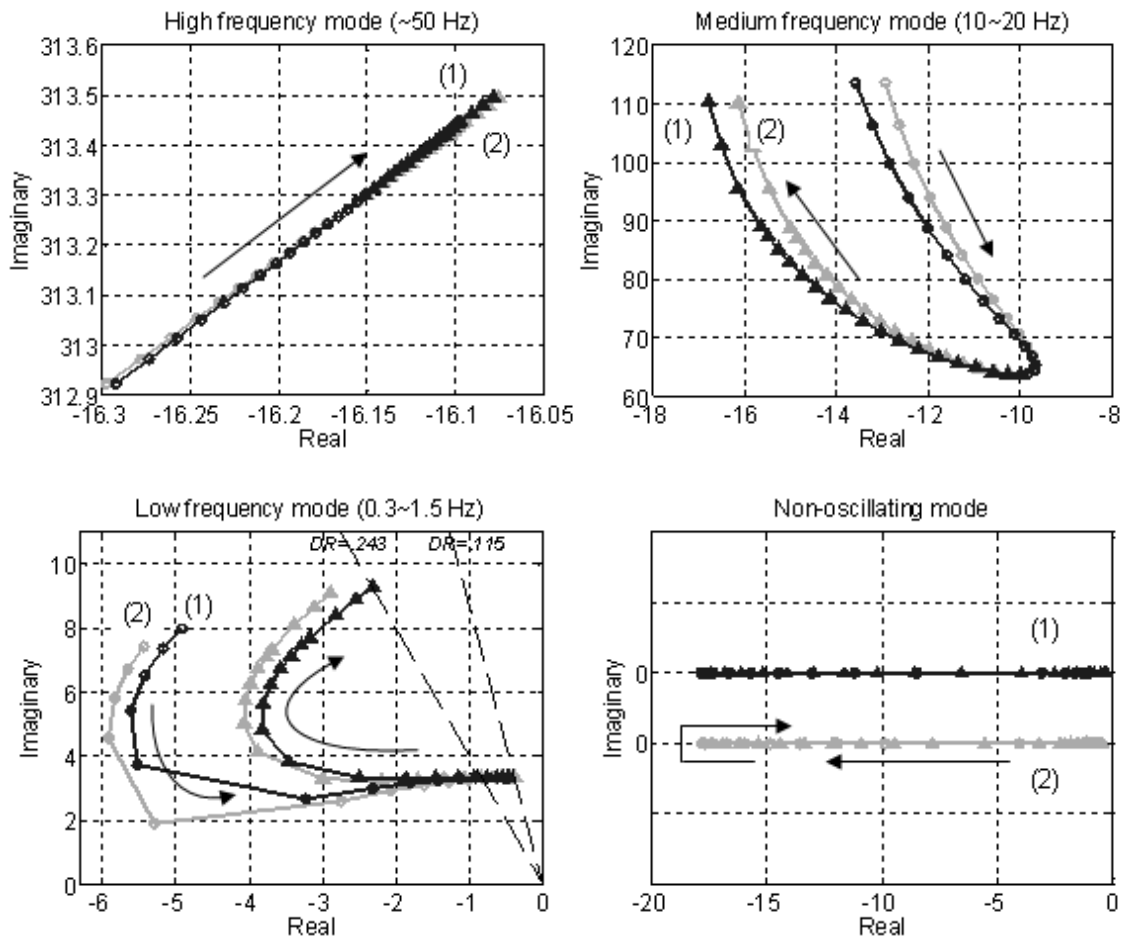


Figure 4.4: Eigenvalues loci for operating points in Fig. 4.3 (DR = damping ratio).

Table 4.3 shows the open-loop DFIG eigenvalues and participation factors for three particular operating points. As observed above, the rotor speed has significant effect on all the eigenvalues, except for the high frequency mode. Participation factors are also affected. At non-synchronous speed (sub- and super-), the electrical and mechanical dynamics tend to be decoupled. It will be seen in the next chapter that for the closed-loop system, the control actions decouple the electrical and mechanical dynamics at all speeds.

Fig. 4.5 shows the time domain response of the open-loop DFIG active power to a 100 ms-50% voltage drop with sub- and supersynchronous initial rotor speed. As expected from Fig. 4.4 and Table 4.3, in subsynchronous speed, the damping ratio of the medium frequency mode is lower. In supersynchronous speed, the damping ratio of the low frequency mode is lower.

Table 4.3: Effect of rotor speed on open-loop DFIG eigenvalues and participation factors

At sub-synchronous speed: $\omega_r = 0.70$ pu, $P_{tot} = 0.2$ pu

	$\lambda = \sigma \pm j\omega$	f_{osc}	ζ	i_{qs}	i_{ds}	e'_{qs}	e'_{ds}	ω_r	θ_{tw}	ω_t	
λ_{HF}	$-16.29 \pm j312.92$	49.80	.052	.47	.45	.03	.04	.00	.00	.00	E
λ_{MF}	$-13.58 \pm j113.50$	18.06	.119	.04	.05	.34	.44	.13	.00	.00	E
λ_{LF}	-4.91 ± 7.99	1.27	.524	.00	.04	.10	.00	.31	.49	.05	M
λ_{NO}	-1.06	0	1	.00	.01	.03	.00	.10	.07	.79	M

At synchronous speed: $\omega_r = 1$ pu, $P_{tot} = 0.575$ pu (base case)

	$\lambda = \sigma \pm j\omega$	f_{osc}	ζ	i_{qs}	i_{ds}	e'_{qs}	e'_{ds}	ω_r	θ_{tw}	ω_t	
λ_{HF}	$-16.15 \pm j313.30$	49.86	.052	.48	.46	.02	.03	.00	.00	.00	E
λ_{MF}	$-10.01 \pm j63.67$	10.13	.155	.02	.01	.00	.48	.47	.01	.00	EM
λ_{LF}	$-0.47 \pm j3.33$	0.53	.138	.00	.00	.00	.01	.00	.49	.50	M
λ_{NO}	-17.40	0	1	.00	.00	.99	.00	.00	.00	.00	E

At super-synchronous speed: $\omega_r = 1.29$ pu, $P_{tot} = 1.075$ pu

	$\lambda = \sigma \pm j\omega$	f_{osc}	ζ	i_{qs}	i_{ds}	e'_{qs}	e'_{ds}	ω_r	θ_{tw}	ω_t	
λ_{HF}	$-16.08 \pm j313.50$	49.90	.051	.49	.46	.02	.03	.00	.00	.00	E
λ_{MF}	$-16.79 \pm j110.27$	17.55	.151	.02	.05	.27	.50	.15	.00	.00	E
λ_{LF}	$-2.32 \pm j9.27$	1.48	.243	.00	.04	.17	.00	.27	.46	.06	M
λ_{NO}	-0.26	0	1	.00	.01	.05	.00	.09	.00	.85	M

 HF, MF, LF = high, medium, low freq., NO = non-oscillating

E, M, EM = electrical, mechanical, electro-mechanical mode

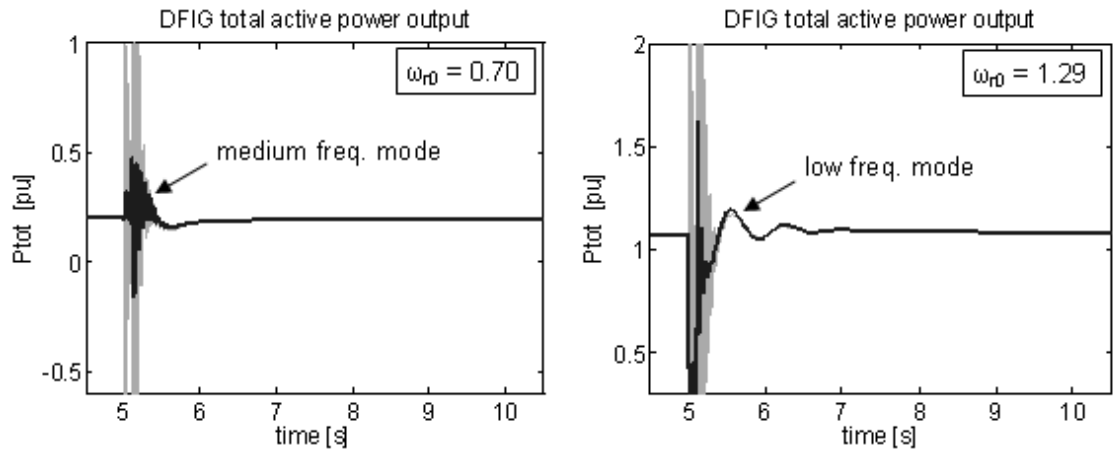


Figure 4.5: Open-loop DFIG response to 50% voltage drop during 100 ms with sub- and supersynchronous initial rotor speed. Thin light line = stator transients represented; thick dark line = stator transients neglected.

4.3.2 Terminal voltage and reactive power

Fig. 4.6 shows the root loci of the open-loop DFIG when the terminal voltage is varied from $V_s = 0.5 \sim 1.5$ pu at different rotor speeds ($\omega_r = 0.71, 1, 1.3$ pu).

Considering the scaling of the axis, the high frequency mode is not significantly sensitive to V_s . The medium frequency mode remains in the left half plane and well damped for the tested range of terminal voltage. At non-synchronous speed, the low frequency and non-oscillating modes are closer to the imaginary axis when the voltage level is lower. At supersynchronous speed, the non-oscillating mode is in the right half plane for lower voltage, hence the system is unstable.

Fig. 4.6 also shows the effect of reactive power. At each rotor speed, the root loci

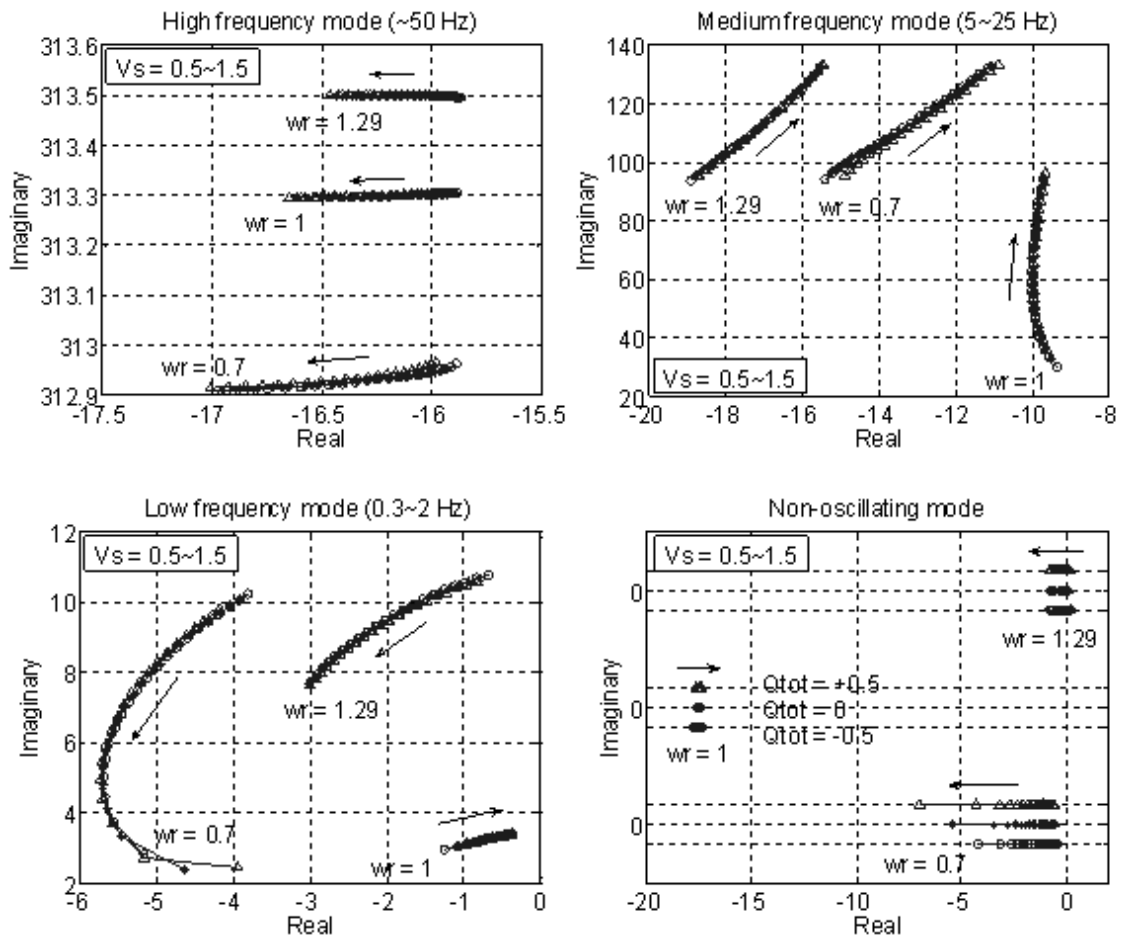


Figure 4.6: Eigenvalues loci for different terminal voltage, power factor and rotor speed. Triangles, stars, circles are used for $Q_{tot} = +0.5, 0, -0.5$ respectively.

are obtained for $Q_{tot} = +0.5, 0$ and -0.5 . It is seen that the influence on the eigenvalue location is not significant. This means that small-signal dynamics are more sensitive to terminal voltage and relatively less sensitive to reactive power level.

4.3.3 Comparison with SCIG

From the above analysis, the DFIG eigenvalue are mainly determined by the rotor speed and terminal voltage level. The change in eigenvalue location due to variations of active and reactive power is relatively less significant. As a consequence, the eigenvalues of the SCIG can be expected to be close to those of the open-loop DFIG at zero slip, assuming same terminal voltage conditions. The reason is that, although both machines have different active and reactive power outputs, their rotor speeds are nearly the same (the DFIG speed is synchronous, while for the SCIG the speed is near synchronous).

Tables 4.4 gives the eigenvalues and participation factors of the SCIG. It can be seen that they are indeed similar to those of the open-loop DFIG at synchronous speed given in Table 4.2.

Table 4.4: Eigenvalues and participation factors of SCIG

Operating point: $V_s = 1$, $\omega_r = 1.0056$, $P_s = 1$, $Q_s = -0.353$

Eigenvalues, frequency, damping ratio, time constant								
	$\lambda = \sigma \pm j\omega$				f_{osc} [Hz]	ζ	τ [s]	
λ_{HF}	$-16.13 \pm j313.31$				49.86	0.051	0.062	
λ_{MF}	$-10.13 \pm j62.69$				9.98	0.160	0.099	
λ_{LF}	$-0.44 \pm j3.33$				0.53	0.130	2.287	
λ_{NO}	-17.17				0	1	0.058	

Participation factors								
	i_{qs}	i_{ds}	e'_{qs}	e'_{ds}	ω_r	θ_{tw}	ω_t	
λ_{HF}	.48	.46	.02	.03	.00	.00	.00	E
λ_{MF}	.02	.01	.00	.47	.46	.01	.00	EM
λ_{LF}	.00	.00	.00	.02	.00	.48	.50	M
λ_{NO}	.00	.00	.99	.00	.00	.00	.00	E

HF, MF, LF = high, medium, low freq., NO = non-oscillating
E, M, EM = electrical, mechanical, electro-mechanical mode

It is important to note that the similarity between the conventional SCIG and open-loop DFIG at zero-slip is only from a modal behaviour viewpoint (eigenvalues location

i.e. oscillation and stability characteristics). The steady-state operating points (pre- and post-disturbance amplitudes) are indeed different for both cases as it was shown in the previous section.

4.4 Sensitivity to machine parameters

In this subsection the effect of machine inductances (L_{ss} , L_{rr} and L_m), resistances (R_s and R_r) and mechanical parameters (H_g , H_t and k) on the eigenvalues of the open-loop DFIG are observed. These parameters vary with the size of the machine, the design, the materials used, and the working conditions (e.g. higher temperature). From the data given in Chapter 2, the range of parameter values may be large. It is therefore worthwhile to examine how the dynamics are affected and whether some particular values lead to instability. In this subsection, all eigenvalues are obtained for the base case operating point, i.e. nominal terminal voltage and synchronous rotor speed ($V_s = 1$ pu, $\omega_r = 1$ pu). As explained above, conclusions drawn are also valid for the SCIG and do not depend on the level of active or reactive power output for both DFIG and SCIG.

4.4.1 Inductances

The machine inductances have significant effect on the stability of the open-loop DFIG. For some values, the open-loop DFIG at zero slip (and hence the SCIG) is unstable. For the discussion, it is useful to define the ratio of stator self to mutual inductance $a_{ss} = L_{ss}/L_m$, the ratio of rotor self to mutual inductance $a_{rr} = L_{rr}/L_m$, and the ‘transient stator inductance’ $L'_s = L_{ss} - L_m^2/L_{rr} = L_m(a_{ss} - 1/a_{rr})$. Table 4.5 shows the eigenvalues of the open-loop DFIG at zero slip for different ratios a_{ss} and a_{rr} with mutual inductance $L_m = 4$ pu.

The machine is stable (all eigenvalues with negative real part) for $L'_s \geq 0.01$. Alternatively, a more restrictive stability condition is that both $a_{ss} \geq 1$ and $a_{rr} \geq 1$ i.e. both $L_{ss} \geq L_m$ and $L_{rr} \geq L_m$, which means that leakage inductances are positive as explained below. When the magnitude of L'_s is small i.e. when $a_{ss}a_{rr} \approx 1$ ($L_{ss} \approx L_m$ and $L_{rr} \approx L_m$) the eigenvalue sensitivity is larger and there is more coupling between the modes (shown by participation factors).

Table 4.5: Effect of stator and rotor inductances on the modes of the open-loop DFIG at zero slip

$$a_{ss} = L_{ss}/L_m, a_{rr} = L_{rr}/L_m, L_m = 4 \text{ pu}, L'_s = L_m(a_{ss} - 1/a_{rr})$$

a_{ss}	a_{rr}	L'_s	λ_{HF}	λ_{MF} and/or λ_{NO}	λ_{LF}
1.01	1.130	+0.5	$-3.16 \pm j314.1$	$-3.33 \pm j30.2, -3.10$	$-0.41 \pm j3.17$
1.01	1.003	+0.05	$-32.8 \pm j310.7$	$-17.5 \pm j88.8, -35.3$	$-0.50 \pm j3.35$
1.01	0.991	+0.005	$-563.3 \pm j171.3$	$+3.11 \pm j186.3, -244.2$	$-0.51 \pm j3.38$
1.01	0.989	-0.005	$+695.5 \pm j110.6$	$+54.9 \pm j196.3, -142.4$	$-0.51 \pm j3.38$
1.01	0.978	-0.05	$+30.2 \pm j310.6$	$+36.4, +107.8, -73.7$	$-0.53 \pm j3.40$
1.01	0.881	-0.5	$+3.13 \pm j314.1$	$+3.99, +26.8, -25.9$	$-0.65 \pm j3.63$
0.99	1.156	+0.5	$-3.16 \pm j314.1$	$-3.28 \pm j30.2, -2.97$	$-0.40 \pm j3.17$
0.99	1.023	+0.05	$-32.9 \pm j310.8$	$-16.8 \pm j88.9, -34.0$	$-0.49 \pm j3.36$
0.99	1.011	+0.005	$-519.1 \pm j182.1$	$+2.65 \pm j184.6, -253.3$	$-0.50 \pm j3.38$
0.99	1.009	-0.005	$+651.7 \pm j110.9$	$+58.0 \pm j194.7, -143.6$	$-0.50 \pm j3.38$
0.99	0.998	-0.05	$+30.2 \pm j310.7$	$+34.9, +106.9, -74.2$	$-0.52 \pm j3.40$
0.99	0.897	-0.5	$+3.13 \pm j314.1$	$+3.84, +26.7, -26.0$	$-0.64 \pm j3.63$

The parameters $L_m = (3/2)L_{sr}$, L_{ss} and L_{rr} were defined in (2.44), (2.50), (2.51) as:

$$L_m = 1.5\mu_0 N_s N_r \frac{rl}{g} \frac{\pi}{4}$$

$$L_{ss} = 1.5\mu_0 N_s^2 \frac{rl}{g} \frac{\pi}{4} + L_{ls}$$

$$L_{rr} = 1.5\mu_0 N_r^2 \frac{rl}{g} \frac{\pi}{4} + L_{lr}$$

Hence, the parameters $a_{ss} = L_{ss}/L_m$ and $a_{rr} = L_{rr}/L_m$ depend on the design of the stator and rotor coils. In the simplest case where stator and rotor coils have same effective number of turns ($N_s = N_r$), one can conclude that the open-loop DFIG is stable if leakage inductances are positive ($L_{ls}, L_{lr} > 0$). If the design is such that $L'_s < 0.01$, stabilizing control must be added for stable operation.

The larger sensitivity of the eigenvalues with respect to L'_s when its magnitude is smaller can be explained from the differential equations of i_{qs} and i_{ds} in (2.101) and (2.102):

$$\frac{L'_s}{\omega_{elB}} \frac{d}{dt} i_{qs} = -R_1 i_{qs} + \omega_s L'_s i_{ds} + \frac{\omega_r e'_{qs}}{\omega_s} - \frac{e'_{ds}}{\omega_s T_r} - v_{qs} + K_{mrr} v_{qr}$$

$$\frac{L'_s}{\omega_{elB}} \frac{d}{dt} i_{ds} = -\omega_s L'_s i_{qs} - R_1 i_{ds} + \frac{e'_{qs}}{\omega_s T_r} + \frac{\omega_r e'_{ds}}{\omega_s} - v_{ds} + K_{mrr} v_{dr}$$

The parameter L'_s must be different from zero in order for i_{qs} and i_{ds} to be state variables (if $L'_s = 0$, the variable i_{qs} and i_{ds} are algebraic variables i.e. there is no stator transients). When $L'_s \neq 0$, the first two diagonal entries of the state matrix are $A_{sys}(1, 1) = A_{sys}(2, 2) = -R_1\omega_{el}/L'_s$. The diagonal elements of the state matrix are the centers of the Gershgorin disks which contain the eigenvalues of the matrix (see Appendix 2 for explanations on Gershgorin theorem). Hence for positive L'_s , the centers of the first two Gershgorin disks, are in the left half plane. For negative L'_s , the disk centers are in the right half plane. As L'_s is in the denominator, the displacement in the disk centers and hence the sensitivity of the eigenvalue location with respect to L'_s is larger for small amplitude of L'_s .

In the above discussion, the effect of varying the ratios a_{ss} and a_{rr} for a given value of mutual inductance L_m was examined. Table 4.6 shows the effect of varying L_m with constant ratio $a_{ss} = 1.01$ and $a_{rr} = 1.015$. The eigenvalues in which electrical state

Table 4.6: Effect of mutual inductance on the modes of the open-loop DFIG at zero slip

L_m in [pu], $a_{ss} = 1.01$, $a_{rr} = 1.015$, $L'_s = L_m(a_{ss} - 1/a_{rr})$					
L_m	L'_s	λ_{HF}	λ_{MF}	λ_{NO}	$\lambda_{LF\pm}$
10	0.2483	$-6.38 \pm j314.02$	$-5.14 \pm j41.37$	-6.96	$-0.468 \pm j3.27$
8	0.1986	$-7.99 \pm j313.95$	$-5.97 \pm j45.91$	-8.70	$-0.476 \pm j3.29$
6	0.1490	$-10.69 \pm j313.78$	$-7.33 \pm j52.58$	-11.61	$-0.483 \pm j3.31$
4	0.0993	$-16.16 \pm j313.30$	$-9.99 \pm j63.80$	-17.44	$-0.491 \pm j3.33$
2	0.0497	$-33.06 \pm j310.70$	$-17.36 \pm j89.07$	-35.12	$-0.499 \pm j3.36$
1	0.0248	$-70.11 \pm j300.16$	$-28.20 \pm j125.03$	-71.86	$-0.504 \pm j3.37$

variables participate (λ_{HF} , λ_{MF} , λ_{NO}) are mostly affected. For all modes, when L_m decreases, the real part magnitude increases while the imaginary part magnitude changes also but to a lesser extent. Since L_m is inversely related to the airgap length, this means that for larger airgap machine (smaller L_m), time constants decrease and damping ratios increase.

These observations can be seen in Fig. 4.7 which shows the active power response of the open-loop DFIG to a 100 ms-50% voltage drop with $L_m = 10$ and 1 pu. The duration of oscillations is shorter for $L_m = 1$ pu, though the overshoots have much larger magnitude.

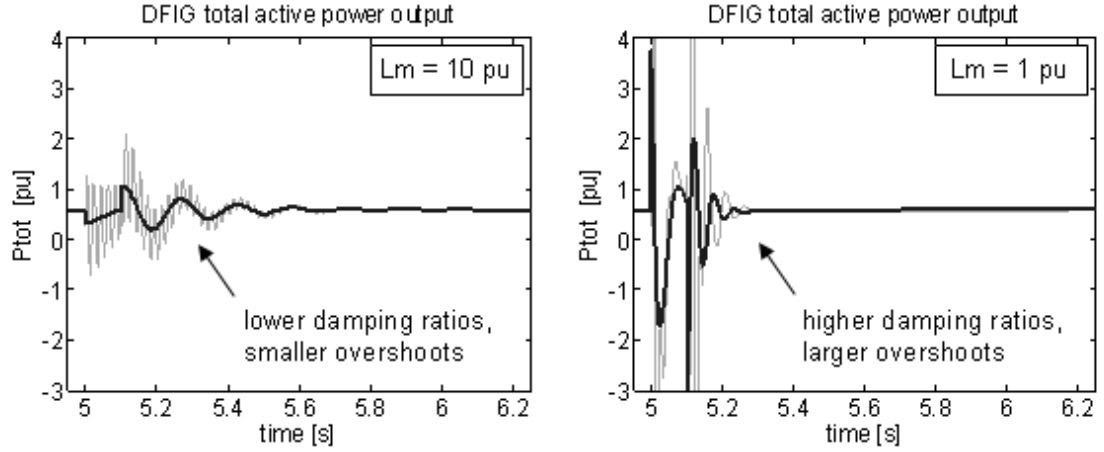


Figure 4.7: Open-loop DFIG response to 50% voltage drop during 100 ms with $L_m = 1$ and 10 pu. Thin light line / thick dark line = stator transients included / neglected.

4.4.2 Resistances

Varying the stator and rotor resistance while keeping all other parameters constant causes noticeable displacement in eigenvalues and change in participation factors. For the discussion, the ratio of the rotor to stator resistance is defined as $a_r = R_r/R_s$. Table 4.7 shows the eigenvalues of the open-loop DFIG at zero slip for different values of stator resistance R_s with $a_r > 1$ and < 1 .

Table 4.7: Effect of stator and rotor resistance on the modes of the open-loop DFIG at zero slip

R_s in [pu], $a_r = R_r/R_s$ ($L_m = 4$ pu, $a_{ss} = 1.01$, $a_{rr} = 1.015$)					
R_s	a_r	Eigenvalues			
0.0001	1.1	$-0.32 \pm j314.2$	$-2.14 \pm j63.79$	$-0.25 \pm j3.37$	-0.35
0.005	1.1	$-16.16 \pm j313.3$	$-9.99 \pm j63.80$	$-0.49 \pm j3.33$	-17.44
0.05	1.1	$-202.1 \pm j156.3$	$-112.6 \pm j156.2$	$-2.46 \pm j2.50$	-32.84
0.1	1.1	$-614.4 \pm j150.7$	$-39.88 \pm j162.8$	$-9.60 \pm j3.90$	-2.00
0.0001	0.9	$-0.32 \pm j314.2$	$-2.11 \pm j63.79$	$-0.25 \pm j3.37$	-0.28
0.005	0.9	$-16.16 \pm j313.5$	$-8.46 \pm j63.93$	$-0.45 \pm j3.34$	-14.26
0.05	0.9	$-182.4 \pm j222.2$	$-94.02 \pm j90.93$	$-2.01 \pm j2.79$	-47.29
0.1	0.9	$-546.8 \pm j170.0$	$-42.45 \pm j143.5$	$-3.48, -4.29, -17.51$	

For the tested range of parameters, the system is stable. For larger resistance values, the real part magnitude of complex conjugate modes tends to be larger (i.e. oscillating modes are further away from the imaginary axis when resistances are larger). Hence more

resistive machines have oscillatory dynamics with smaller time constants. For very resistive machines ($R_s \geq 0.1$), the real mode is the dominant mode (closest to the imaginary axis) and the system is referred to as over-damped.

Participation factors are also affected by resistance values. For more resistive machines, the electrical and mechanical dynamics are decoupled, as shown in Table 4.8, where for $R_s = 0.1$, λ_{HF1} and λ_{HF2} are electrical modes (significant participation from electrical states only), λ_{LF} and λ_{NO} are mechanical modes.

Fig. 4.8 shows the response of the open-loop DFIG to a 50% voltage drop during 100 ms with $R_s = 0.1$ and 0.0001 pu. The eigenvalues properties are shown in Table 4.8. As explained above, oscillations are damped out very rapidly when R_s is large.

Table 4.8: Participation factors of open-loop DFIG at zero slip for different resistances

$R_s = 0.1$ pu ($a_r = 1.1$, $L_m = 4$ pu, $a_{L_{ss}} = 1.01$, $a_{L_{rr}} = 1.015$)

	$\lambda = \sigma \pm j\omega$	f_{osc}	ζ	i_{qs}	i_{ds}	e'_{qs}	e'_{ds}	ω_r	θ_{tw}	ω_t	
λ_{MF1}	$-614.36 \pm j150.67$	23.98	.971	.40	.39	.11	.10	.00	.00	.00	E
λ_{MF2}	$-39.88 \pm j162.77$	25.91	.238	.10	.10	.38	.40	.02	.00	.00	E
λ_{LF}	$-9.60 \pm j3.90$	0.62	.927	.00	.00	.00	.03	.47	.47	.03	M
λ_{NO}	-2.00	0	1	.00	.00	.00	.00	.12	.22	.66	M

$R_s = 0.0001$ pu ($a_r = 1.1$, $L_m = 4$ pu, $a_{L_{ss}} = 1.01$, $a_{L_{rr}} = 1.015$)

	$\lambda = \sigma \pm j\omega$	f_{osc}	ζ	i_{qs}	i_{ds}	e'_{qs}	e'_{ds}	ω_r	θ_{tw}	ω_t	
λ_{HF}	$-0.32 \pm j314.16$	50.00	.001	.50	.48	.00	.02	.00	.00	.00	E
λ_{MF}	$-2.14 \pm j63.79$	10.15	.034	.02	.00	.00	.48	.47	.01	.00	EM
λ_{LF}	$-0.25 \pm j3.378$	0.54	.075	.00	.00	.00	.01	.00	.49	.50	M
λ_{NO}	-0.35	0	1	.00	.00	.99	.00	.00	.00	.00	E

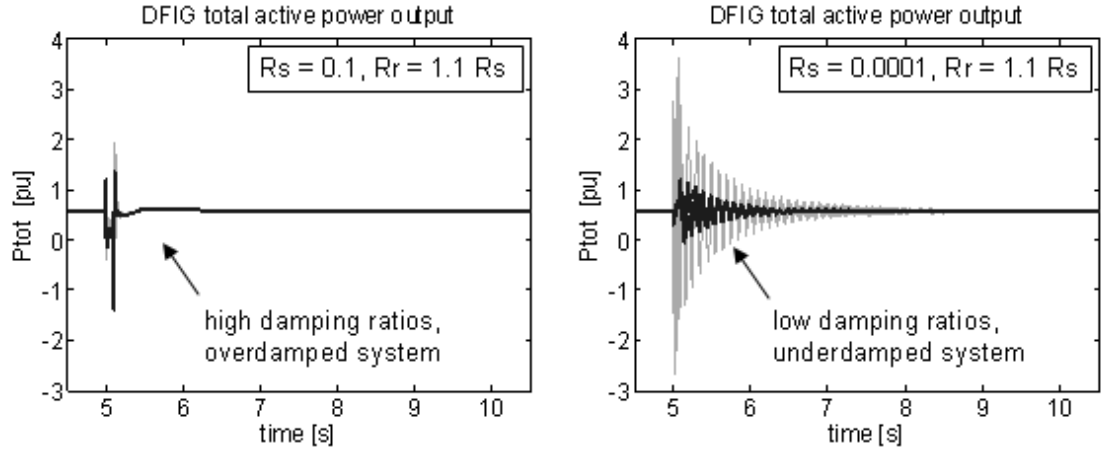


Figure 4.8: Open-loop DFIG response to 50% voltage drop during 100 ms with $R_s = 0.1$ and 0.0001 pu. Thin light / thick dark line = stator transients included / neglected.

4.4.3 Mechanical parameters

Table 4.9 shows the effect of varying inertias and stiffness on the open-loop DFIG eigenvalues. As expected, heavier machines (large H_t and H_g) present oscillations with lower frequencies, and drive trains that are stiffer (smaller gearbox ratio i.e. larger k) have oscillations with higher frequencies.

Table 4.9: Effect of drive train parameters on the modes of the open-loop DFIG at zero slip

H_t in [s], $H_g = 0.1H_t$, $k = 0.3$ pu/el.rad

H_t	λ_{HF}	λ_{MF} (f_{osc} [Hz], ζ)	λ_{LF} (f_{osc} [Hz], ζ)	λ_{NO}
12	$-15.92 \pm j313.3$	$-8.90 \pm j36.14$ (5.75, .239)	$-0.33 \pm j1.92$ (0.31, .168)	-17.44
8	$-15.98 \pm j313.3$	$-9.17 \pm j44.70$ (7.11, .201)	$-0.37 \pm j2.36$ (0.37, .155)	-17.44
4	$-16.16 \pm j313.3$	$-9.99 \pm j63.80$ (10.2, .155)	$-0.49 \pm j3.33$ (0.53, .146)	-17.44
2	$-16.53 \pm j313.3$	$-11.59 \pm j90.61$ (14.4, .123)	$-0.74 \pm j4.71$ (0.75, .155)	-17.44
1	$-17.39 \pm j313.2$	$-14.68 \pm j128.3$ (20.4, .114)	$-1.23 \pm j6.62$ (1.05, .182)	-17.44

k in [pu/el.rad], $H_t = 4$ s, $H_g = 0.1H_t$

k	λ_{HF}	λ_{MF} (f_{osc} [Hz], ζ)	λ_{LF} (f_{osc} [Hz], ζ)	λ_{NO}
30	$-16.20 \pm j313.3$	$-3.72 \pm j129.0$ (20.5, .029)	$-6.72 \pm j15.5$ (2.47, .398)	-17.42
3	$-16.16 \pm j313.3$	$-8.27 \pm j71.66$ (11.4, .115)	$-2.21 \pm j9.28$ (1.48, .231)	-17.43
.3	$-16.16 \pm j313.3$	$-9.99 \pm j63.80$ (10.2, .155)	$-0.49 \pm j3.33$ (0.53, .146)	-17.44
.03	$-16.16 \pm j313.3$	$-10.20 \pm j63.00$ (10.0, .160)	$-0.28 \pm j1.04$ (0.17, .260)	-17.44
.003	$-16.16 \pm j313.3$	$-10.22 \pm j62.91$ (10.0, .160)	$-0.26 \pm j0.22$ (0.04, .758)	-17.44

For the tested range of parameters, the machine dynamics remain stable. The electrical modes (high frequency and non-oscillating modes) are not significantly sensitive to mechanical parameters.

Participation factors are not significantly changed, except for very low inertia and high stiffness. For lower inertia, the medium frequency mode is more of an electrical nature. For higher stiffness, the low frequency mode becomes an electromechanical mode.

4.5 Sensitivity to grid strength

In the above discussion the stator voltage is assumed constant, i.e. the external grid is infinitely strong. If however the DFIG is connected to the infinite bus through a finite reactance, the terminal voltage is not constant and becomes an algebraic variable.

Fig. 4.9 shows the effect of the external series reactance $X_t + X_e$ (transformer and line series reactance) and series resistance R_e on the eigenvalues of the open-loop DFIG at zero slip. Considering the scaling of the axes, the stator mode (i_{qs} - i_{ds} mode) is the most sensitive to X_e and R_e (largest change in eigenvalue location). For the other modes, the sensitivity with respect to R_e is larger at small values of X_e . The observations of the root-loci can be summarized as follows.

- High frequency mode (= stator electrical mode): The effect of X_e and R_e are in opposite direction. Larger values of resistance R_e push the mode into the left half plane. Hence for more resistive external network, the high frequency electrical dynamics decay faster. Larger values of X_e push the mode into the right half plane. Hence for more inductive external network, closed-loop control or series compensation are required to reduce the effective value of X_e . The destabilizing effect X_e is also encountered in synchronous machines where the synchronizing torque decreases when X_e increases [127].
- Medium frequency mode (= rotor electro-mechanical mode, at zero slip): For non-zero line resistance ($R_e > 0$), when X_e is small the damping ratio is decreased for increasing X_e ; when X_e is large the damping ratio is increased for increasing X_e . For a given value of X_e , larger R_e makes the damping ratio smaller. This is

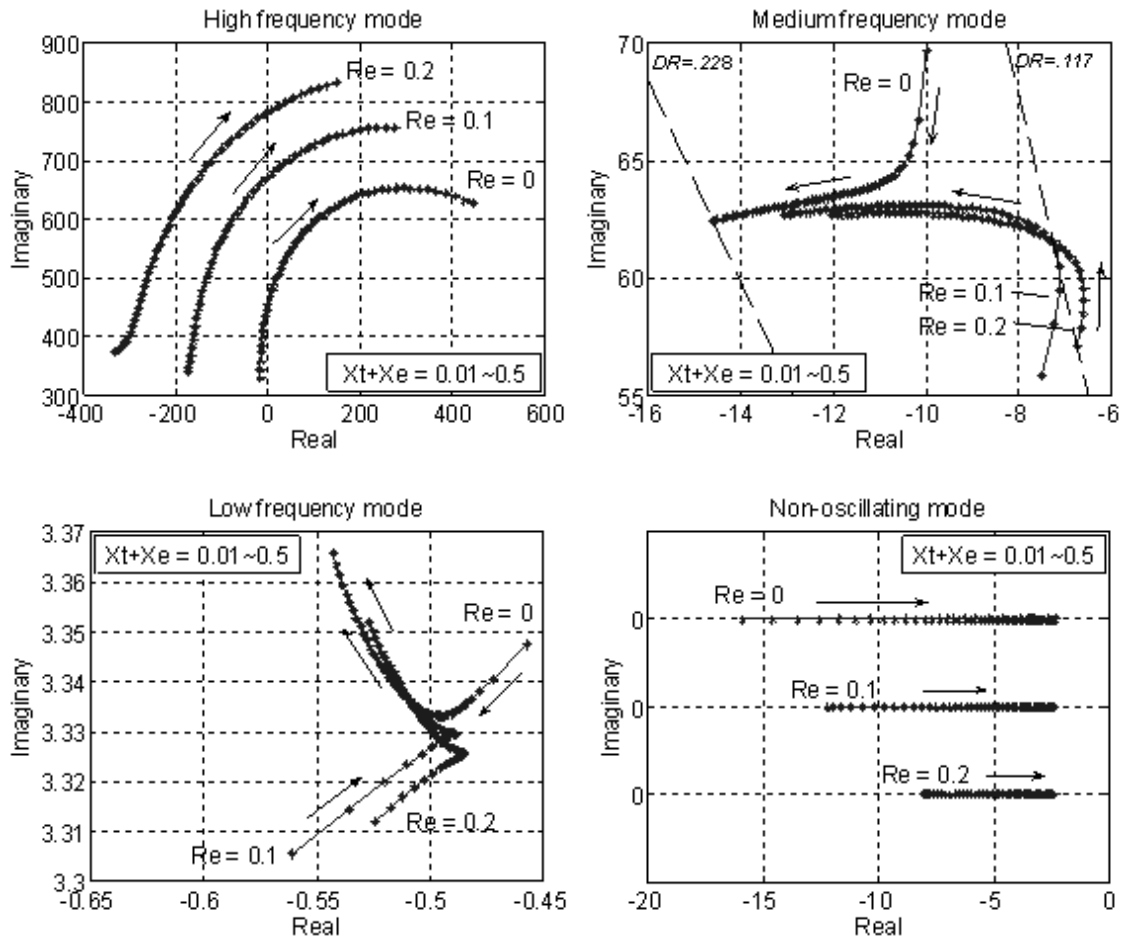


Figure 4.9: Root loci of open-loop DFIG at zero slip for different values of X_e and R_e ($X_t = 0.005$ pu = transo reactance, DR = damping ratio).

also encountered in synchronous machines where external line resistance introduce negative, though negligible, damping in certain condition [127]. Generally, the external resistance through which a synchronous machine is connected to the grid offers positive damping. However, a synchronous machine with no damper winding in a hydro power station may introduce negative damping when delivering light load over a long distance line having relatively higher resistance to reactance ratio [128]. Negative damping situation is also found when a machine is supplying a large local load partly and the other part is coming from the system [129]. The phenomenon of inadequate damping torque was initially referred to as hunting, and was observed for underloaded synchronous generators connected to the grid through long lines [127].

- Low frequency mode (= turbine mechanical mode): Considering the scaling of the axes, this mode is relatively less sensitive to external line parameters. This can be expected since it is an eigenvalue related mainly to turbine and drive train mechanical dynamics while X_e and R_e are electrical network parameters.
- Non-oscillating mode (= rotor electrical mode, at zero slip): This real eigenvalue is closer to the imaginary axis when X_e is larger. Hence for more inductive external network, the rotor electrical dynamics of the open-loop DFIG are slower. For the tested range of system parameters this mode remains in the left half plane.

Fig. 4.10 shows the effect of the external line shunt susceptance (line charging) B_e . The effect is not significant. This shows that DFIG dynamics are more sensitive to the line series impedance than shunt admittance.

Finally, grid strength does not affect significantly the participation factors. This is shown in Table 4.10 where the participation factors are given for a weak grid and can be compared with those of the base case (infinitely strong grid) in Table 4.2. As a result although frequency and damping ratio change, the stator mode remains decoupled from the other modes in both cases of strong and weak grids.

Table 4.10: Eigenvalues of open-loop DFIG at zero slip connected to a weak grid

$X_t + X_e = 0.5, R_e = 0.2, B_e = 0.2$ [pu on machine base]								
Eigenvalues		i_{qs}	i_{ds}	e'_{qs}	e'_{ds}	ω_r	θ_{tw}	ω_t
λ_{HF}	$+158.39 \pm j853.92$.50	.49	.00	.01	.00	.00	.00
λ_{MF}	$-12.02 \pm j62.33$.00	.01	.00	.48	.49	.01	.00
λ_{LF}	$-0.52 \pm j3.34$.00	.00	.00	.02	.00	.48	.49
λ_{NO}	-2.26	.00	.00	.97	.01	.00	.00	.01

4.6 Summary

Results of the open-loop analysis give a description of the system oscillatory dynamics in terms of range of oscillation frequencies, damping ratios, and time constants.

When the rotor voltage is constant (zero for the SCIG and non-zero for the DFIG), the typical small-signal behaviour of the machine is stable and consists of a superposition

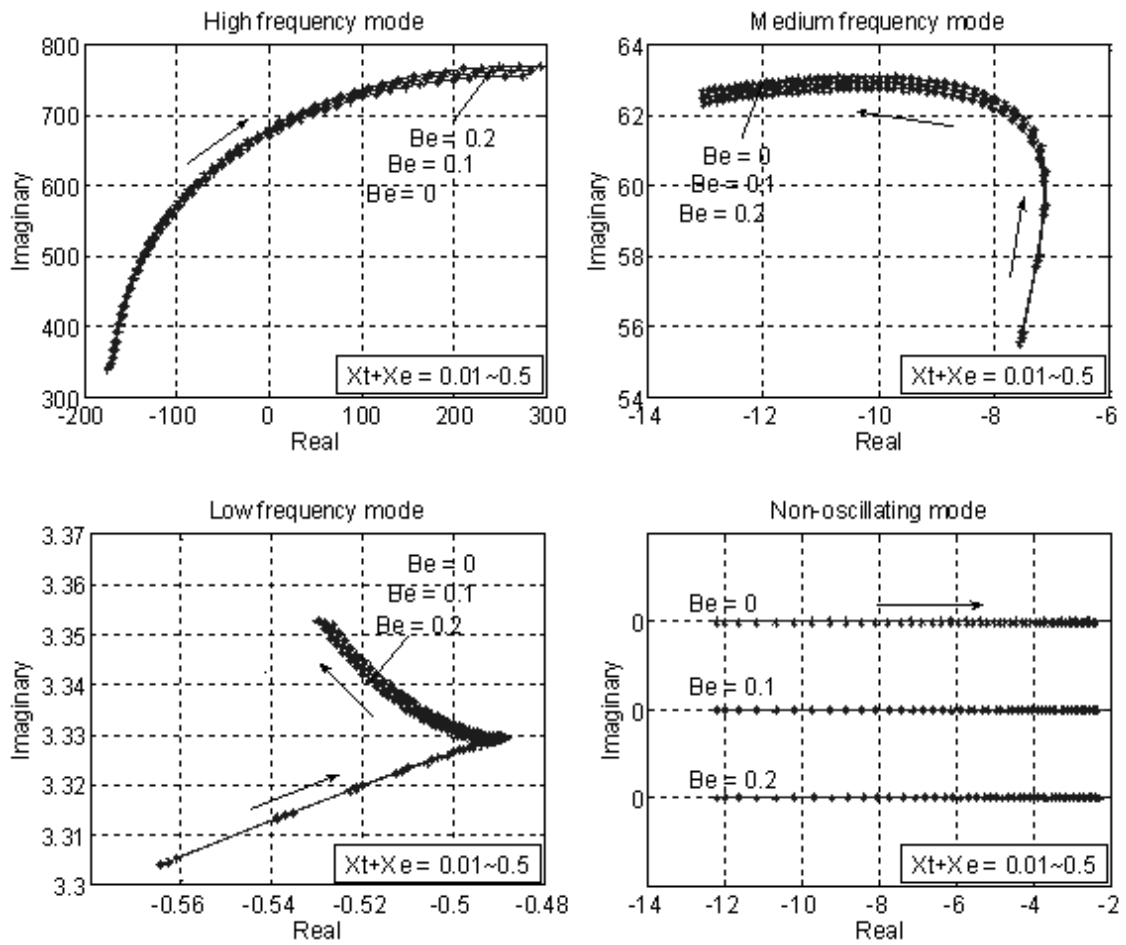


Figure 4.10: Root loci of open-loop DFIG at zero slip for different values of X_e and B_e ($X_t = 0.005$ pu = transo reactance).

of three types of oscillations: fast, medium and slow. The fast oscillations (~ 50 Hz) are associated with stator electrical dynamics. The medium oscillations ($5 \sim 25$ Hz) are due to rotor electrical and/or mechanical dynamics. The slow oscillations ($0.1 \sim 5$ Hz) are contributed by the shaft and turbine dynamics. Oscillations are damped faster when the rotor speed is subsynchronous, resistances are higher and inductances smaller.

In extreme situations where the machine is very resistive or where the leakage inductances are not positive, the oscillation frequencies may not be categorised as above and the induction generator may be unstable. At large negative slip (supersynchronous speed) with depressed voltage condition or when the external network is very inductive, the machine is unstable and closed-loop controls are required. For the open-loop DFIG and SCIG to be stable, the parameter L'_s must be larger than 0.01.

The sensitivity analysis to operating point shows that from a modal behaviour point of view (eigenvalues location and participation factors), the SCIG is similar to the open-loop DFIG at zero slip. The reason being that small-signal dynamics are mainly determined by rotor speed and terminal voltage rather than levels of active and reactive power.

Chapter 5

Analysis: Closed-loop behaviour

In this chapter, the closed-loop system is studied. One objective is to propose a tuning method for generic PI-controllers in the rotor-side converter and blade-pitch controller.

The proposed control design consists essentially of two parts. In the first part, the RSC controllers are tuned for subrated conditions (when output power is less than rated level). In the second part, the pitch controller is tuned (with the RSC gains obtained in part one) for rated conditions (when the output power is more than or equal to the rated level). In this work, the d-axis control loop of the rotor side converter controls the reactive power.

Modal analysis is used to derive analytical expressions which impose limits on the proportional gains of the RSC for stable operation. The robustness with respect to operating point, machine parameters and grid strength is verified.

A detailed explanation of the pitching activation and deactivation procedure is also given.

The effect of the controllers on the system dynamical behaviour are identified by comparing the small-signal properties of the closed-loop DFIG to those of the open-loop case.

5.1 Closed-loop DFIG eigenvalues

To facilitate the discussion, the typical eigenvalues of a closed-loop DFIG with properly tuned controls are first presented and compared with those of the open-loop case. The tuning method of the rotor-side converter PI controllers is discussed in detail subsequently.

Table 5.1 shows the variables and functions of the DAE for the closed-loop DFIG. Unlike in Table 4.1, the rotor voltages v_{qr} and v_{dr} are now algebraic variables that are

determined by the controllers of the RSC. As described in Chapter 2, the dynamics of the controllers are represented by the state variables Φ_{iq} , Φ_{id} , Φ_{Te} , Φ_{Qs} .

Table 5.1: DAE variables and functions for the closed-loop DFIG

$f(x, z, u)$	(2.135)-(2.141), (2.144), (2.145), (2.147), (2.148)
$g(x, z, u)$	(2.154)-(2.155), (2.146), (2.149)
x	$[i_{qs} \ i_{ds} \ e'_{qs} \ e'_{ds} \ \omega_r \ \theta_{tw} \ \omega_t \ \Phi_{iq} \ \Phi_{id} \ \Phi_{Te} \ \Phi_{Qs}]'$
z	$[v_{qs} \ \gamma_{Vs} \ v_{qr} \ v_{dr}]'$
$u = u_0$	$[v_w \ \beta]' = [v_{w0} \ \beta_0]'$

Table 5.2 shows the typical eigenvalues of a well tuned closed-loop DFIG. Details on the determination of the control parameters are given in the next subsections. The following eigenvalues can be distinguished:

- Stator modes ($\lambda_{i_{qs}}$, $\lambda_{i_{ds}}$)
- Rotor flux mode ($\lambda_{e'_{qs}e'_{ds}}$)
- Generator mechanical mode ($\lambda_{\omega_r\theta_{tw}}$)
- Turbine mechanical mode (λ_{ω_t})
- Controller modes ($\lambda_{\Phi_{iq}}$, $\lambda_{\Phi_{id}}$, $\lambda_{\Phi_{Te}}$, $\lambda_{\Phi_{Vs}}$)

Table 5.2: Eigenvalues of the DFIG with closed controls

q-axis gains: $K_{Te} = -1.5$, $T_{Te} = 0.025$, $K_{iq} = -1.0$, $T_{iq} = 0.0025$
d-axis gains: $K_{Qs} = +1.0$, $T_{Qs} = 0.050$, $K_{id} = -0.5$, $T_{id} = 0.0050$

$\lambda = \sigma \pm j\omega$	f [Hz]	ζ	τ [s]	Dominant states
-7452.2	0	1	0.00013	i_{qs}
-2942.3	0	1	0.00034	i_{ds}
$-8.64 \pm j309.6$	49.27	0.028	0.116	$e'_{qs} \ e'_{ds}$
$-2.79 \pm j11.16$	1.78	0.243	0.358	$\omega_r \ \theta_{tw}$
-0.189	0	1	5.29	ω_t
-422.3	0	1	0.0024	Φ_{iq}
-223.1	0	1	0.0045	Φ_{id}
-23.38	0	1	0.043	Φ_{Te}
-9.94	0	1	0.101	Φ_{Qs}

operating point: $v_{qs} = 1$ pu, $\omega_r = 0.955$ pu

The stator modes are real and have large magnitude. The location of the stator eigenvalues depend on machine parameters, operating point and indeed control parameters. As explained later, they are either far in the LHP or far in the RHP. The control parameters

can be chosen so that the stator modes are placed at some desired location. Limit values for the controller proportional gains can be determined to ensure that the stator modes are in the LHP (see next subsection). It is noted that large magnitudes for the stator eigenvalues are not a problem (the problem is a positive sign as it means instability). In fact, large negative real part is desirable since in such case the eigenvalue can be considered to be at $-\infty$ (relatively to the other eigenvalues) so that stator transients can be neglected i.e. so that stator variables can be approximated as algebraic variables instead of state variables (differential variables).

The rotor-flux mode is a high-frequency oscillating mode (40~55 Hz). It is sensitive to the model order (neglecting stator transients changes the location of this mode) and controller parameters. If the controllers are not tuned properly, this mode is in the RHP. Limit values for the proportional gains can also be determined to ensure that the rotor flux is stable (see next subsection). It is seen that the high frequency mode (~50 Hz) is due to the rotor electrical dynamics. This is in contrast with the familiar result for the synchronous generator, squirrel-cage induction generator and open-loop DFIG where the 50 Hz mode is associated with stator dynamics. For the closed-loop DFIG, neglecting stator transients does not remove the 50 Hz mode, though it increases slightly its damping.

The generator mechanical mode is an oscillating mode with frequency around 1~2 Hz. As shown below, this mode is not significantly sensitive to the DFIG model order, which means that a simplified model without the electrical transients (stator and rotor) exhibits correctly this mode. This mode is a well damped mode for a wide range of control parameters and operating points.

The turbine mechanical mode is a real eigenvalue in subrated condition (when pitch control is inactive). The location of this mode is mainly determined by the rotor speed and the torque control parameters. In rated condition (when pitch control is activated), the turbine speed dynamics interact with those of the blade pitch angle and give rise to a very low frequency mode whose damping depends on the pitch control parameters (see subsection 5.5).

The controller modes may be real or highly damped complex-conjugates depending on the control parameters. They may also be coupled with the generator or drive train

dynamics depending on the control parameters.

From the above observations, the closed-loop system differs from the open-loop configuration in several aspects. Apart from introducing controller modes and changing the coupling of the machine dynamics (no electro-mechanical mode for the closed-loop system), an important consequence of the converter controllers is that stator dynamics are associated with large real eigenvalues while the 50 Hz mode is associated with rotor electrical dynamics. As rotor electrical dynamics are not significantly coupled with the other dynamics, both stator and rotor electrical dynamics should be neglected if the point of interest is in low frequency oscillations as for power system stability studies (neglecting stator transients only does not remove the 50 Hz oscillations).

5.2 Tuning issues of rotor-side converter

For each PI controller in Fig. 2.12 (page 89), the parameters K and T (proportional gains and integral times) have to be selected for stability and desired performance. Root-loci plots show that stability of the closed-loop DFIG is mainly decided by the proportional gains (P-gains), while the integral times (I-times) influence mainly the speed of integral action. In this section, the particular issues relating to stability are examined, hence the discussion focusses on the P-gains. The effect of the I-times is reviewed in the next section.

Below, three DFIG models are considered:

- Full-order model (FOM)
- 5th order model (5thOM): stator transients neglected
- 3rd order model (3rdOM): stator and rotor electrical transients neglected

In the full-order model, all electrical dynamics (stator and rotor) change with a finite speed, and the DFIG has seven state variables (i_{qs} , i_{ds} , e'_{qs} , e'_{ds} , ω_r , θ_{tw} , ω_t). In the 5th order model, the stator variables are considered as algebraic, in other words they are assumed to change instantaneously; the DFIG has five state variables (e'_{qs} , e'_{ds} , ω_r , θ_{tw} , ω_t). In the 3rd order model, all electrical variables are considered as algebraic, and the DFIG has three state variables representing the mechanical dynamics (ω_r , θ_{tw} , ω_t). Since there are four controller states (Φ_{iq} , Φ_{id} , Φ_{Te} , Φ_{Qs}), the model order of the closed-loop

DFIG (number of DFIG states + number of controller states) is 11, 9 and 7 for the FOM, 5thOM and 3rdOM respectively.

5.2.1 Inappropriate tuning with simplified DFIG model

One particularity of the DFIG is that when tuning the controllers with the 5th or 3rdOM, one may obtain a set of PI-gains giving stable results for the reduced order models, but unstable for the full order model. This is shown in Table 5.3 where the gains were obtained by plotting the root-loci of the 5thOM and choosing the values for obtaining all the modes in the LHP.

Table 5.3: Example of inadequate PI-gains and corresponding eigenvalues

P gains: $K_{iq}=0.25, K_{Te}=2.5, K_{id}=5, K_{Qs}=10$			
I times: $T_{iq}=0.005, T_{Te}=0.05, T_{id}=0.0025, T_{Qs}=0.025$			
λ for FOM	λ for 5 th OM	λ for 3 rd OM	Domin. states
-919.7	—	—	i_{qs}
+1709.7	—	—	i_{ds}
+2.23 ± j312.4	-7.12 ± j286.5	—	$e'_{qs} \ e'_{ds}$
($\zeta = -0.007$)	($\zeta = 0.025$)		
($f = 49.72$)	($f = 45.60$)		
-2.74 ± j10.89	-2.74 ± j10.89	-2.74 ± j10.89	$\omega_r \ \theta_{tw}$
($\zeta = 0.244$)	($\zeta = 0.244$)	($\zeta = 0.244$)	
($f = 1.73$)	($f = 1.73$)	($f = 1.73$)	
-0.19	-0.19	-0.19	ω_t
-265.4	-228.9	-200.4	Φ_{iq}
-398.9	-399.9	-400.0	Φ_{id}
-33.53	-33.41	-33.74	Φ_{Te}
-36.32	-36.33	-36.32	Φ_{Qs}
operating point: $v_{qs} = 1, \omega_r = 0.955$			

In Table 5.3, the DFIG is stable if stator or both stator and rotor electrical transients are neglected (5th and 3rdOM). However, the DFIG is unstable if both stator and rotor electrical transients are considered (FOM) in which case there are two eigenvalues in the RHP. In other words, if stator variables change instantaneously, the DFIG is stable; if however, stator dynamics have a small but non-zero time constant (which is more likely to be the case in the real system), the DFIG is unstable. This is undesirable as stability is sensitive to model order and only guaranteed in the ideal case where stator or both stator

and rotor electrical variables change instantaneously.

The problem is due to the fast acting converter controls which make the electrical dynamics (stator and rotor) very sensitive to the controller gains. Hence, it suggests that PI-tuning should be done with the FOM. Simplifying the model should be done after ensuring stability of both stator and rotor electrical transients.

In the following, three aspects of the DFIG behaviour are examined to explain why the control parameters of Table 5.3 are not suitable. The first aspect relates to the relationship between inputs and outputs in the steady-state and indicates what sign the P-gains should have. The second aspect relates to the location of the stator modes and indicates limit values (maximum or minimum) of the P-gains. The third aspect relates to the location of the rotor electrical mode and indicates suitable range for the magnitude of the P-gains.

5.2.2 Steady-state behaviour: Sign of the P-gains

Steady-state characteristics of the DFIG were obtained in Chapter 3 where Fig. 3.13 (page 117) and 3.16 (page 119) showed the steady-state values of the controller inputs and outputs of the q-axis (T_e, i_{qr}, v_{qr}) and d-axis (Q_s, i_{dr}, v_{dr}) over the rotor slip range ± 0.5 .

Considering the q-axis variables in Fig. 3.16, for lower electrical torque ($T_{e1} > T_{e2} > T_{e3}$), the rotor q-axis current is higher ($i_{qr1} < i_{qr2} < i_{qr3}$). This means that the process gain from i_{qr} to T_e is negative and hence a negative proportional gain K_{T_e} should be used because when the torque is too low (positive error) the reference current should be decreased so that the torque eventually increases. Similarly, for higher rotor q-axis current ($i_{qr1} < i_{qr2} < i_{qr3}$), the rotor q-axis voltage is lower ($v_{qr1} > v_{qr2} > v_{qr3}$). Hence the proportional gain K_{i_q} should also be negative. A similar exercise for the d-axis indicates that K_{Q_s} should be positive and K_{i_d} negative.

In Fig. 3.13 and 3.16, the direct or reverse relationship between controller input and output holds over the whole slip range. Hence the conclusions regarding the sign of the P-gains hold for both sub- and supersynchronous speed.

5.2.3 Stator modes location: Limit value of the P-gains

The location of the stator modes can be evaluated analytically by applying Gershgorin theorem [130] on the state matrix of the closed-loop grid connected DFIG. Gershgorin theorem states that the eigenvalues of a matrix A are located in the union of the disks in the complex plane which have as centre the diagonal elements of A and as radius the sum of the off-diagonal elements (either row-wise or column-wise) [130]. Hence if all diagonal elements have negative real part, all disks are centered in the LHP and the eigenvalues are more likely to be in the LHP.

For the closed-loop DFIG full order model, the diagonal elements of the state matrix corresponding to the differential equations of the stator states (i_{qs} and i_{ds}) are:

$$a_{11} = \frac{\omega_{el}}{L'_s} \left(-R_1 + K_{mrr} K_{iq} (K_{mrr} - K_{Te} \frac{e'_{qs0}}{\omega_s}) - \left[\frac{\partial v_{qs}}{\partial i_{qs}} \right]_0 \right)$$

$$a_{22} = \frac{\omega_{el}}{L'_s} \left(-R_1 + K_{mrr} K_{id} (K_{mrr} - K_{Vs} \left[\frac{\partial v_{qs}}{\partial i_{ds}} \right]_0) - \left[\frac{\partial v_{ds}}{\partial i_{ds}} \right]_0 \right)$$

where $\partial v_{qs}/\partial i_{qs}$, $\partial v_{qs}/\partial i_{ds}$ and $\partial v_{ds}/\partial i_{ds}$ depend on the external network. Obtaining an analytical expression for these terms is not readily feasible. In a first step they can be ignored, which is the same as assuming constant terminal voltage (i.e. the DFIG is connected to an infinitely strong system). The effect of non-constant terminal voltage can be checked subsequently with numerical computation of the eigenvalues and time domain simulations. Hence:

$$a_{11} \approx \frac{\omega_{el}}{L'_s} \left(-R_1 + K_{mrr}^2 K_{iq} - K_{mrr} K_{iq} K_{Te} \frac{e'_{qs0}}{\omega_s} \right) \quad (5.1)$$

$$a_{22} \approx \frac{\omega_{el}}{L'_s} \left(-R_1 + K_{mrr}^2 K_{id} + K_{mrr} K_{id} K_{Qs} v_{qs0} \right) \quad (5.2)$$

It is seen that a_{11} and a_{22} depend on the operating point (v_{qs0} , e'_{qs0}), the machine parameters (R_1 , K_{mrr} , L'_s), and the P-gains (K_{iq} , K_{id} , K_{Te} , K_{Qs}). The dynamics of the DFIG are such that the stator eigenvalues are relatively closer to a_{11} and a_{22} than to the other diagonal elements of the state matrix. In Gershgorin framework, this is because a transformation can be applied to the state matrix so that the disks centered at a_{11} and a_{22} are disconnected from the remaining disks (see Appendix 7.2).

In other words, one can obtain a set of P-gains for some desired location of a_{11} and a_{22} , i.e. one can place the stator modes in some desired region of the left half plane around

a_{11} and a_{22} by choosing the P-gains appropriately. E.g. for the q-axis stator mode to be in the LHP around $-T_1$ where T_1 is real positive, i.e. for the condition $a_{11} \leq -T_1$ to be satisfied, the threshold value (minimum or maximum) of the proportional gain K_{Te} can be obtained using (5.1) as:

$$\begin{aligned} \text{if } K_{iq} > 0 \text{ and } e'_{qs0} > 0 &\rightarrow K_{Te} \geq K_{Te,th} \\ \text{if } K_{iq} > 0 \text{ and } e'_{qs0} < 0 &\rightarrow K_{Te} \leq K_{Te,th} \\ \text{if } K_{iq} < 0 \text{ and } e'_{qs0} > 0 &\rightarrow K_{Te} \leq K_{Te,th} \\ \text{if } K_{iq} < 0 \text{ and } e'_{qs0} < 0 &\rightarrow K_{Te} \geq K_{Te,th} \end{aligned} \quad (5.3)$$

$$\text{where } K_{Te,th} = \frac{\omega_s}{e'_{qs0}} \left(\frac{1}{K_{iq} K_{mrr}} \left(\frac{L'_s T_1}{\omega_{el}} - R_1 \right) + K_{mrr} \right) \quad (5.4)$$

Similarly, for the d-axis stator mode to be in the LHP around $-T_2$ where T_2 is real positive, i.e. for the condition $a_{22} \leq -T_2$ to be satisfied, one can obtain the threshold value of the proportional gain K_{Qs} using (5.2) as:

$$\begin{aligned} \text{if } K_{id} > 0 &\rightarrow K_{Qs} \leq K_{Qs,th} \\ \text{if } K_{id} < 0 &\rightarrow K_{Qs} \geq K_{Qs,th} \end{aligned} \quad (5.5)$$

$$\text{where } K_{Qs,th} = \frac{1}{v_{qs0}} \left(\frac{1}{K_{id} K_{mrr}} \left(\frac{L'_s T_2}{\omega_{el}} + R_1 \right) - K_{mrr} \right) \quad (5.6)$$

Equations (5.3)-(5.6) give restrictions on the outer loop P-gains for some T_1 and T_2 as function of inner loop P-gains and operating point. As the integral time of the current controllers is in the order of milliseconds [93], a consistent choice for T_1 and T_2 is $T_1 = T_2 = 10000$ which gives a time constant for the stator modes in the order of $1/10000 = 0.1$ ms i.e. ten times faster than the current controller integral action (stator transients should be faster so that they can be neglected).

Fig. 5.1 and 5.2 show the constraints on K_{Te} and K_{Qs} for positive and negative K_{iq} and K_{id} and for three operating points. The shaded areas show the values of proportional gains that satisfy (5.3)-(5.6). It is seen that for stable stator modes, the q-axis gains must have same sign, while the d-axis gains must have opposite sign. These conclusions hold for the different speed and voltage conditions. From the steady state analysis (see Subsection 3.3.2, 3.3.3), the correct combination is:

- $K_{iq} < 0$, $K_{Te} < 0$ for the q-axis, and
- $K_{id} < 0$, $K_{Qs} > 0$ for the d-axis.

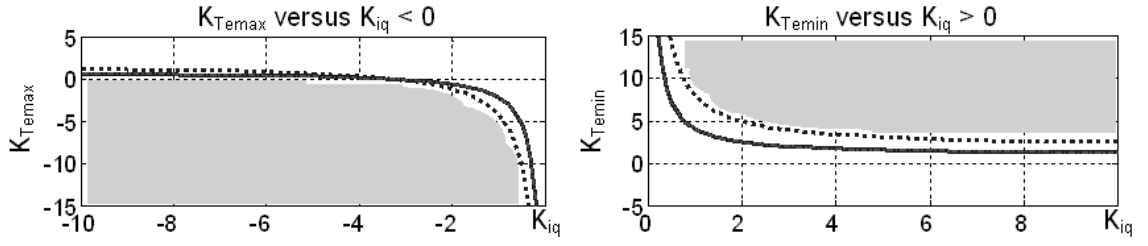


Figure 5.1: Max/min values of K_{Te} as function of K_{iq} for $T_1 = 10000$. Continuous: $v_{qs}=1, \omega_r=0.7$; dotted: $v_{qs}=0.5, \omega_r=0.7$; dash-dotted: $v_{qs}=1, \omega_r=1.1$. Shaded area = values that satisfy (5.3).

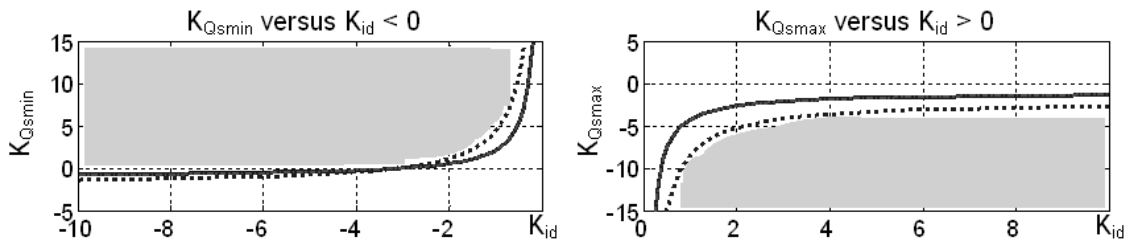


Figure 5.2: Max/min values of K_{Qs} as function of K_{id} for $T_2 = 10000$. Continuous: $v_{qs}=1, \omega_r=0.7$; dotted: $v_{qs}=0.5, \omega_r=0.7$; dash-dotted: $v_{qs}=1, \omega_r=1.1$. Shaded area = values that satisfy (5.5).

5.2.4 Rotor electrical mode location: Magnitude of the P-gains

Fig. 5.3 shows the root-loci of the rotor electrical mode for three sets of d-axis gains with negative q-axis gains varied over some range. It is seen that neglecting stator transients increases the sensitivity of the rotor electrical mode with respect to the P-gains (larger eigenvalue displacement), and more importantly, the stability of the system is mainly dependent on the d-axis gains, with smaller $|K_{id}|$, $|K_{Qs}|$ being required for stable rotor electrical dynamics (mode in the LHP).

The effect of model simplification depends on the control parameters. For larger d-axis gain magnitudes (set III), the 5thOM (simplified model where stator transients are neglected) gives more conservative location for the rotor electrical mode (more into the right half plane) with respect to the FOM (stator transients represented). For smaller d-axis gain magnitudes (set I), the opposite is true.

In addition, for the 5thOM, lower $|K_{Te}|$ (start of arrows) is better as it places the modes more into the LHP. Hence, the range of P-gains that give good location of the rotor

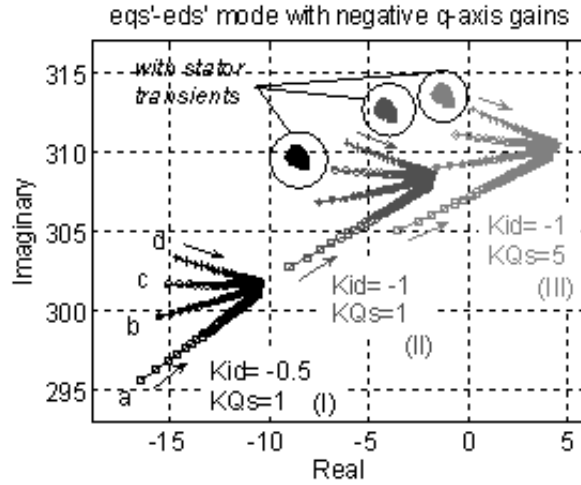


Figure 5.3: Root-loci of rotor electrical mode for FOM and 5th OM. Parameters varied are: d-axis gains (I, II, III); q-axis gains: $K_{Te} = -1 \sim -20$ (arrows), $K_{iq} = -0.5, -1, -2, -10$ (a, b, c, d). Operating point: $V_s = 1$, $P_{tot} = 0.5$, $\omega_r = 0.955$.

electrical mode can be determined as e.g.:

- d-axis gains: $K_{id} = -0.5 \sim -1$, $K_{Qs} = +0.5 \sim +1$
- q-axis gains: $K_{iq} = -0.5 \sim -2$, $K_{Te} = -0.5 \sim -2$

The choice of the P-gains within these ranges is discussed in the next section.

It is noted from Fig. 5.1 and 5.2 that for $|K_{iq}|, |K_{id}| = 0.5 \sim 1$, the values $|K_{Te}| = 1 \sim 2$ and $|K_{Qs}| \approx 1$ do not satisfy (5.3)-(5.6). The curves in Fig. 5.1 and 5.2 were obtained for $T_1 = T_2 = 10000$ (stator modes about 10 times faster than 1 ms). For a reduced value of T_1 and T_2 e.g. 3000 (stator modes about three times faster than 1 ms) the above lower magnitudes of K_{Te} and K_{Qs} are acceptable. This points out a trade-off between the time constants of the stator and rotor electrical dynamics. Using small magnitudes of P-gains is required for stable and fast decaying rotor electrical dynamics, however it makes the stator dynamics slower relative to the current controller. As stator modes are far in the LHP, it is more important to consider the location of the rotor electrical mode and hence select limited magnitude for the P-gains.

5.3 Proposed tuning procedure

From the issues discussed previously, the first steps of the DFIG PI-tuning procedure can be summarized as:

- 1) Determine the sign of the P-gains with steady state characteristics.
- 2) Obtain limit values of the P-gains for some desired region of the stator modes with (5.3)-(5.6).
- 3) Obtain ranges of the P-gains for stable rotor electrical mode with root-loci (possible trade off with step 2).

The present and following sections discuss the final steps:

- 4) Fine tune the P-gains and I-times to avoid oscillatory dq-coupling with eigenvalue and participation factors computation.
- 5) Check robustness to operating point and machine parameters with root-loci plots.
- 6) Check robustness to large disturbances with non-linear time-domain simulations.

The typical value of the integral times is in the order of 1 ms for the current controllers and 10 ms for the outer power/torque controllers [93]. Hence T_{iq} and T_{id} may be chosen within the range of e.g. 1~5 ms and T_{Te} and T_{Qs} within the range of e.g. 10~50 ms. The final choice of the PI-gains within the specified ranges is made with the following two considerations.

In cascaded control, stability is improved when the inner loop is faster than the outer loop [92]. Hence the gain magnitude of the inner loop controller should be smaller [92], i.e. $|K_{iq}|, |K_{id}| < |K_{Te}|, |K_{Qs}|$.

In addition, different gain magnitudes should be used in the d- and q-axis to avoid oscillatory coupling between d- and q-axis dynamics. This is shown in Table 5.4 for negative q-axis gains. Using $|K_{iq}| = |K_{id}|, |K_{Te}| = |K_{Qs}|$ (set (i)) gives dq-coupling for both stator and current controller dynamics. Using $|K_{iq}| \neq |K_{id}|, |K_{Te}| \neq |K_{Qs}|$ (set (ii)) separates the dq-dynamics in two real modes. Using different I-times (set (iii)) separates

Table 5.4: Oscillatory coupling between d- and q-axis dynamics

P-gains: (i)	$K_{iq} = -0.5, K_{Te} = -1.0, K_{id} = -0.5, K_{Qs} = +1$		
(ii), (iii)	$K_{iq} = -1.0, K_{Te} = -1.5, K_{id} = -0.5, K_{Qs} = +1$		
I-times: (i), (ii)	$T_{iq} = 0.0025, T_{Te} = 0.025, T_{id} = 0.0025, T_{Qs} = 0.025$		
(iii)	$T_{iq} = 0.0025, T_{Te} = 0.025, T_{id} = 0.0050, T_{Qs} = 0.050$		
λ for (i)	λ for (ii)	λ for (iii)	Dom. states
$-2686.9 \pm j80.0$	-7452.2	-7452.2	i_{qs}
	-2671.3	-2942.3	i_{ds}
$-3.79 \pm j308.8$	$-4.16 \pm j309.2$	$-8.64 \pm j309.6$	$e'_{qs} \ e'_{ds}$
$-2.77 \pm j11.22$	$-2.79 \pm j11.16$	$-2.79 \pm j11.16$	$\omega_r \ \theta_{tw}$
-0.19	-0.19	-0.19	ω_t
$-480.14 \pm j11.49$	-423.6	-422.3	Φ_{iq}
	-491.9	-223.1	Φ_{id}
-19.26	-23.38	-23.38	Φ_{Te}
-19.85	-19.87	-9.94	Φ_{Qs}
operating point: $ V_s =1, \omega_r=0.955$			

the controller modes further so that oscillatory dq-coupling may be avoided for changing operating conditions.

At this stage, a set of PI-gains satisfying the conditions of steps 1) to 4) of the proposed tuning procedure can be obtained. An example is given in Table 5.5. The effect of the integral times is shown in Table 5.6. The following observations can be made.

In Table 5.5, it is seen that simplifying the DFIG model influences significantly the electrical modes only ($i_{qs}, i_{ds}, e'_{qs}-e'_{ds}$). For power system studies where the focus is in frequencies below 10 Hz, the 3rdOM whereby both stator and rotor electrical dynamics are neglected, can be used as it preserves correctly the dynamics of interest. However, as discussed above, an appropriate set of PI-gains giving stable results for the full order model must be determined in the first place.

It is also seen that the high frequency mode (~ 50 Hz) is due to the rotor electrical dynamics. As seen from the dominant participation factors, this mode is associated with the dynamics of the transient voltage e'_{qs} and e'_{ds} which are a function of the rotor flux (equations (2.97) and (2.98) on page 85). In other words, the high frequency mode is due to the dynamics of the rotor flux which is determined by the interaction of the stator and rotor current flowing through the machine mutual inductance L_m and rotor inductance

Table 5.5: Example of Adequate PI-Gains and Corresponding Eigenvalues

P-gains: $K_{iq} = -1$, $K_{Te} = -1.5$, $K_{id} = -0.5$, $K_{Qs} = +1$
I-times: $T_{iq} = 0.0025$, $T_{Te} = 0.025$, $T_{id} = 0.005$, $T_{Qs} = 0.05$

λ for FOM	λ for 5 th OM	λ for 3 rd OM	Domin. states
-7452.2	—	—	i_{qs}
-2942.3	—	—	i_{ds}
$-8.64 \pm j309.6$ ($\zeta = 0.028$) ($f = 49.27$)	$-14.46 \pm j300.0$ ($\zeta = 0.048$) ($f = 47.75$)	—	e'_{qs} e'_{ds}
$-2.79 \pm j11.16$ ($\zeta = 0.243$) ($f = 1.78$)	$-2.79 \pm j11.16$ ($\zeta = 0.243$) ($f = 1.78$)	$-2.79 \pm j11.16$ ($\zeta = 0.243$) ($f = 1.78$)	ω_r θ_{tw}
-0.19	-0.19	-0.19	ω_t
-422.3	-403.4	-399.5	Φ_{iq}
-223.1	-216.8	-198.8	Φ_{id}
-23.38	-23.42	-23.39	Φ_{Te}
-9.94	-9.94	-9.94	Φ_{Qs}

operating point: $|V_s|=1$, $\omega_r=0.955$

Table 5.6: Effect of Integral Times on DFIG Modes

P-gains: $K_{iq} = -1$, $K_{Te} = -1.5$, $K_{id} = -0.5$, $K_{Qs} = +1$
I-times: (i) $T_{iq} = .0025$, $T_{Te} = .025$, $T_{id} = .005$, $T_{Qs} = .05$
(ii) $T_{iq} = .0050$, $T_{Te} = .050$, $T_{id} = .010$, $T_{Qs} = .10$
(iii) $T_{iq} = .0250$, $T_{Te} = .250$, $T_{id} = .050$, $T_{Qs} = .50$

λ for (i)	λ for (ii)	λ for (iii)	Dom. states
-7452.2	-7681.2	-7855.3	i_{qs}
-2942.3	-3059.7	-3147.5	i_{ds}
$-8.64 \pm j309.6$	$-11.15 \pm j311.8$	$-12.11 \pm j314.7$	e'_{qs} e'_{ds}
$-2.79 \pm j11.16$	$-2.70 \pm j11.22$	$-2.53 \pm j11.08$	ω_r θ_{tw}
-0.19	-0.19	-0.19	ω_t
-422.3	-205.5	-40.70	Φ_{iq}
-223.1	-105.5	-20.11	Φ_{id}
-23.38	-11.57	-2.31	Φ_{Te}
-9.94	-4.97	-0.99	Φ_{Qs}

operating point: $|V_s|=1$, $\omega_r=0.955$

L_{rr} (definitions on pages 75, 76, 79). This is in contrast with the familiar result for the synchronous generator, squirrel-cage induction generator and open-loop DFIG where the 50 Hz mode is associated with stator dynamics. For the closed-loop DFIG, neglecting stator transients does not remove the 50 Hz mode, though it increases slightly its damping.

In Table 5.6, the controller modes (Φ_{iq} , Φ_{id} , Φ_{Te} , Φ_{Qs}) are most affected. For I-times twice/ten times bigger the magnitude of the controller modes are about twice/ten times smaller i.e. the speed of the integrator action is twice/ten times slower. The other modes are not significantly changed (relatively to their magnitude). Hence, integral times do not affect stability.

5.4 Robustness verification

The above analysis describes the dynamics around a particular operating point for some machine parameters and small disturbances. In this section, the effect of changing parameters and conditions on the eigenvalues of the closed-loop DFIG is examined.

5.4.1 Robustness to operating point

Table 5.7 shows the DFIG eigenvalues with the gains of Table 5.5 for different rotor speeds. It is seen that for the wide range of operating conditions considered, the dynamical characteristics of the system are preserved.

Table 5.7: Effect of rotor speed on the closed-loop DFIG Modes

Control parameters of Table 5.5 are used

ω_r	λ_{iqs}	λ_{ids}	$\lambda_{e'_{qs}e'_{ds}} (\zeta, f)$	$\lambda_{\omega_r\theta_{tw}} (\zeta, f)$	λ_{ω_t}
0.7	-7436.1	-2961.3	$-6.49 \pm j311.3$ (.021,49.55)	$-2.62 \pm j11.17$ (.228,1.78)	-0.138
0.8	-7444.4	-2953.5	$-7.34 \pm j310.7$ (.024,49.44)	$-2.69 \pm j11.16$ (.234,1.78)	-0.158
0.9	-7450.3	-2946.1	$-8.18 \pm j310.0$ (.026,49.33)	$-2.75 \pm j11.16$ (.240,1.78)	-0.178
1.0	-7453.7	-2939.4	$-9.02 \pm j309.3$ (.029,49.23)	$-2.16 \pm j11.18$ (.190,1.78)	-0.066
1.1	-7451.7	-2933.3	$-9.86 \pm j308.6$ (.032,49.12)	$-2.16 \pm j11.18$ (.190,1.78)	-0.072
1.2	-7443.6	-2928.2	$-10.7 \pm j308.0$ (.035,49.02)	$-2.16 \pm j11.18$ (.190,1.78)	-0.079

ω_r	$\lambda_{\Phi_{iq}}$	$\lambda_{\Phi_{id}}$	$\lambda_{\Phi_{Te}}$	$\lambda_{\Phi_{Qs}}$
0.7	-420.8	-220.4	-23.51	-9.95
0.8	-421.4	-221.4	-23.46	-9.94
0.9	-422.0	-222.5	-23.41	-9.94
1.0	-422.5	-223.6	-23.95	-9.93
1.1	-423.0	-224.9	-23.96	-9.93
1.2	-423.4	-226.2	-23.97	-9.93

For different rotor speeds, the only noticeable variation is in the mechanical turbine

mode, which is closer to the imaginary axis for synchronous and super-synchronous speed but remains stable. This means that for $\omega_r \geq 1$ the rotational speed takes longer to reach a new steady state value.

Table 5.8 and 5.9 show the effect of the terminal voltage and reactive power level on the closed-loop DFIG modes. Again, the dynamical characteristics of the system are preserved over the wide range of tested conditions.

Table 5.8: Effect of terminal voltage on closed-loop DFIG modes

Control parameters of Table 5.5 are used

V_s	$\lambda_{i_{qs}}$	$\lambda_{i_{ds}}$	$\lambda_{e'_{qs}e'_{ds}}(\zeta, f)$	$\lambda_{\omega_r\theta_{tw}}(\zeta, f)$	λ_{ω_t}
1.1	-7920.5	-3099.9	$-8.23 \pm j309.8$ (.027,49.30)	$-2.79 \pm j11.15$ (.243,1.77)	-0.189
1.0	-7452.2	-2942.3	$-8.64 \pm j309.6$ (.028,49.27)	$-2.79 \pm j11.16$ (.243,1.78)	-0.189
0.9	-6982.4	-2784.5	$-9.10 \pm j309.4$ (.029,49.25)	$-2.79 \pm j11.17$ (.242,1.78)	-0.189
0.75	-6271.2	-2547.6	$-9.90 \pm j309.2$ (.032,49.21)	$-2.78 \pm j11.20$ (.241,1.78)	-0.189
0.5	-5002.7	-2154.4	$-11.8 \pm j310.1$ (.038,49.36)	$-2.75 \pm j11.27$ (.237,1.79)	-0.191

V_s	$\lambda_{\Phi_{iq}}$	$\lambda_{\Phi_{id}}$	$\lambda_{\Phi_{Te}}$	$\lambda_{\Phi_{Qs}}$
1.1	-421.1	-221.9	-24.30	-10.41
1.0	-422.3	-223.1	-23.38	-9.94
0.9	-423.8	-224.5	-22.35	-9.42
0.75	-426.6	-227.0	-20.53	-8.54
0.5	-434.7	-232.6	-16.41	-6.70

Table 5.9: Effect of reactive power level on the closed-loop DFIG modes

Control parameters of Table 5.5 are used

Q_s	$\lambda_{i_{qs}}$	$\lambda_{i_{ds}}$	$\lambda_{e'_{qs}e'_{ds}}(\zeta, f)$	$\lambda_{\omega_r\theta_{tw}}(\zeta, f)$	λ_{ω_t}
-0.5	-7453.2	-2852.3	$-9.26 \pm j309.4$ (.030,49.23)	$-2.79 \pm j11.16$ (.243,1.77)	-0.189
-0.25	-7452.8	-2883.7	$-9.03 \pm j309.4$ (.030,49.25)	$-2.79 \pm j11.16$ (.243,1.77)	-0.189
0	-7452.4	-2915.4	$-8.82 \pm j309.5$ (.029,49.26)	$-2.79 \pm j11.16$ (.243,1.78)	-0.189
+0.25	-7452.1	-2947.5	$-8.61 \pm j309.6$ (.028,49.28)	$-2.79 \pm j11.16$ (.243,1.78)	-0.189
+0.5	-7451.8	-2979.7	$-8.40 \pm j309.7$ (.027,49.29)	$-2.79 \pm j11.16$ (.243,1.78)	-0.189

Q_s	$\lambda_{\Phi_{iq}}$	$\lambda_{\Phi_{id}}$	$\lambda_{\Phi_{Te}}$	$\lambda_{\Phi_{Qs}}$
-0.5	-422.2	-224.1	-23.38	-9.64
-0.25	-422.3	-223.8	-23.38	-9.75
0	-422.3	-223.4	-23.38	-9.85
+0.25	-422.3	-223.1	-23.38	-9.95
+0.5	-422.4	-222.8	-23.38	-10.05

For different terminal voltage levels, the major variation is in the stator modes. Although for depressed voltage their magnitude is reduced, they remain far in the LHP and far from the current controller modes (i.e. they remain sufficiently faster).

For different reactive power outputs, all eigenvalues are virtually unchanged. For a given terminal voltage, network parameters (series inductance and line charging) influence mainly the power factor of the DFIG. Hence, grid strength does not affect the small-signal behaviour of the DFIG with reactive power control in the d-axis.

From the above observations, using fixed PI-gains in the rotor side converter is acceptable over the normal range of operating slip, terminal voltage and power factor in subrated regime. In rated regime, the mechanical modes and controller modes are different due to the pitching mechanism. The pitch controller has to be tuned appropriately to ensure stability. This topic is discussed in the next section.

5.4.2 Robustness to machine parameters

Table 5.10 and 5.11 give the closed-loop DFIG eigenvalues with the gains of Table 5.5 for different machine inductances and resistances.

Table 5.10: Effect of inductances on the closed-loop DFIG modes

Control parameters of Table 5.5 are used; $L_{ss}=1.01L_m$; $L_{rr}=1.005L_{ss}$

L_m	$\lambda_{i_{qs}}$	$\lambda_{i_{ds}}$	$\lambda_{e'_{qs}e'_{ds}}(\zeta, f)$	$\lambda_{\omega_r\theta_{tw}}(\zeta, f)$	λ_{ω_t}
8	-3471.1	-1320.6	$-9.24 \pm j309.2$ (.030,49.22)	$-2.79 \pm j11.16$ (.243,1.78)	-0.189
6	-4804.5	-1866.7	$-8.90 \pm j309.3$ (.029,49.22)	$-2.79 \pm j11.16$ (.243,1.78)	-0.189
4	-7452.2	-2942.3	$-8.64 \pm j309.6$ (.028,49.27)	$-2.79 \pm j11.16$ (.243,1.78)	-0.189
2	-15364.4	-6144.7	$-8.72 \pm j311.0$ (.028,49.49)	$-2.79 \pm j11.16$ (.243,1.78)	-0.189
1	-31170.0	-12535.3	$-9.51 \pm j313.9$ (.030,49.96)	$-2.79 \pm j11.16$ (.243,1.78)	-0.190

L_m	$\lambda_{\Phi_{iq}}$	$\lambda_{\Phi_{id}}$	$\lambda_{\Phi_{Te}}$	$\lambda_{\Phi_{Qs}}$
8	-452.7	-248.3	-23.38	-9.98
6	-436.5	-234.3	-23.38	-9.97
4	-422.3	-223.1	-23.38	-9.94
2	-409.8	-213.8	-23.38	-9.84
1	-404.0	-209.6	-23.39	-9.66

It is seen that for the wide range of values considered, the dynamical characteristics of the system are preserved. The electrical modes are sensitive to the variation of inductances

Table 5.11: Effect of resistances on the closed-loop DFIG modes

Control parameters of Table 5.5 are used; $R_r=1.1R_s$

R_s	$\lambda_{i_{qs}}$	$\lambda_{i_{ds}}$	$\lambda_{e'_{qs}e'_{ds}}(\zeta, f)$	$\lambda_{\omega_r\theta_{tw}}(\zeta, f)$	λ_{ω_t}
.0001	-7405.4	-2907.0	-9.13 $\pm j309.9$ (.029,49.32)	-2.79 $\pm j11.16$ (.243,1.78)	-0.189
.001	-7414.0	-2913.7	-9.02 $\pm j309.9$ (.029,49.32)	-2.79 $\pm j11.16$ (.243,1.78)	-0.189
.01	-7499.9	-2978.1	-8.18 $\pm j309.2$ (.026,49.22)	-2.79 $\pm j11.16$ (.243,1.78)	-0.189
.05	-7876.7	-3263.4	-4.66 $\pm j306.7$ (.015,48.81)	-2.79 $\pm j11.15$ (.243,1.77)	-0.189
.1	-8339.5	-3615.3	-1.07 $\pm j303.5$ (.004,48.30)	-2.79 $\pm j11.15$ (.243,1.77)	-0.189

R_s	$\lambda_{\Phi_{iq}}$	$\lambda_{\Phi_{id}}$	$\lambda_{\Phi_{Te}}$	$\lambda_{\Phi_{Qs}}$
.0001	-424.2	-225.2	-23.33	-9.93
.001	-423.9	-224.8	-23.34	-9.93
.01	-420.5	-221.1	-23.44	-9.94
.05	-406.4	-206.2	-23.86	-9.97
.1	-390.9	-190.9	-24.33	-10.01

and resistances. For high inductances, the magnitude of the stator modes are reduced but they remain far from the current controller modes in the LHP. For different resistances, the DFIG modes are virtually unchanged when resistances are small. In very resistive machine, the 50 Hz mode (rotor flux mode) has a lower damping ratio. Retuning of the controllers may be required to keep the damping ratio at an acceptable levels.

Table 5.12 gives the closed-loop DFIG modes for different inertias. The mechanical modes are sensitive to the variation of inertias. For heavier machines, the mechanical dynamics are slower (smaller real part magnitude) as expected but remain stable.

5.4.3 Robustness to disturbance severity

Fig. 5.4 and 5.5 show the time domain response to a network disturbance (0.5 pu voltage drop at the infinite bus during 100 ms) and wind speed variations (random disturbances with increasing and decreasing mean values).

The responses were obtained by simulating the non-linear DFIG model (2.135)-(2.149) in Simulink using the variable step solver ode23s. Results for both 5thOM and 3rdOM are shown. A zoomed view of the active power and rotor speed under network disturbance is given in Fig. 5.6, where the FOM response is also shown.

It is seen that linear analysis gives a good description of the DFIG dynamical behav-

Table 5.12: Effect of inertias on the closed-loop DFIG modes

Control parameters of Table 5.5 are used; $H_g=0.1H_t$

H_t	$\lambda_{i_{qs}}$	$\lambda_{i_{ds}}$	$\lambda_{e'_{qs}e'_{ds}} (\zeta, f)$	$\lambda_{\omega_r\theta_{tw}} (\zeta, f)$	λ_{ω_t}
12	-7453.1	-2942.3	$-8.64 \pm j309.6$ (.028,49.27)	$-\mathbf{0.93} \pm j\mathbf{6.53}$ (.141,1.04)	$-\mathbf{0.063}$
8	-7452.9	-2942.3	$-8.64 \pm j309.6$ (.028,49.27)	$-\mathbf{1.40} \pm j\mathbf{7.97}$ (.173,1.27)	$-\mathbf{0.094}$
6	-7452.7	-2942.3	$-8.64 \pm j309.6$ (.028,49.27)	$-\mathbf{1.86} \pm j\mathbf{9.17}$ (.199,1.46)	$-\mathbf{0.126}$
3	-7451.7	-2942.3	$-8.64 \pm j309.6$ (.028,49.27)	$-\mathbf{3.72} \pm j\mathbf{12.8}$ (.279,2.04)	$-\mathbf{0.252}$
1	-7447.8	-2942.3	$-8.64 \pm j309.6$ (.028,49.27)	$-\mathbf{11.1} \pm j\mathbf{21.0}$ (.468,3.34)	$-\mathbf{0.764}$

H_t	$\lambda_{\Phi_{iq}}$	$\lambda_{\Phi_{id}}$	$\lambda_{\Phi_{Te}}$	$\lambda_{\Phi_{Qs}}$
12	-421.9	-223.1	-23.78	-9.94
8	-422.0	-223.1	-23.68	-9.94
6	-422.1	-223.1	-23.58	-9.94
3	-422.6	-223.1	-23.19	-9.94
1	-424.4	-223.1	-21.68	-9.94

ious. The 50 Hz and 1.75 Hz modes are most visible under network disturbance on the electrical and mechanical variables respectively. For the different types of disturbance and initial conditions, the system is stable, the stability is not model order dependent, and the high frequency oscillations are damped out very quickly. Hence for power system studies where fast electrical transients are not of interest, the 3rdOM can be used.

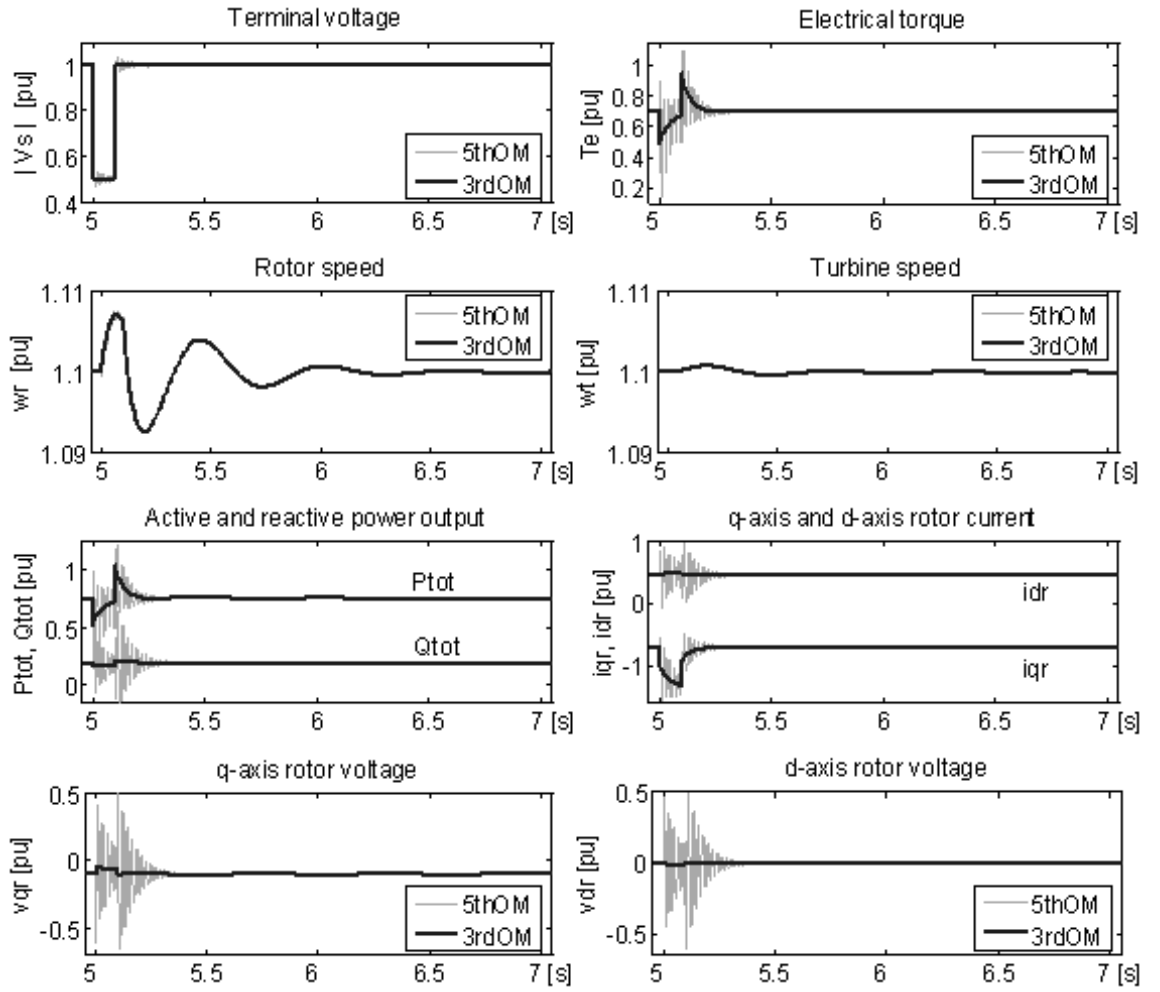


Figure 5.4: DFIG response to network disturbance (0.5 pu voltage drop at infinite bus) with the control parameters of Table 5.5 and constant wind speed.

5.5 Pitch control tuning

In the previous section, PI-gains of the rotor-side converter controllers were obtained for suitable performance in subrated condition when pitch control is inactive (Table 5.5). In the following, the pitch controller is tuned for operation in rated condition when the pitch control is active.

5.5.1 Choosing PI-gains

For the generic control scheme described in Section 2.5, the control parameters of the pitch controller are K_{ω_r} and T_{ω_r} where K_{ω_r} is the proportional gain and T_{ω_r} is the in-

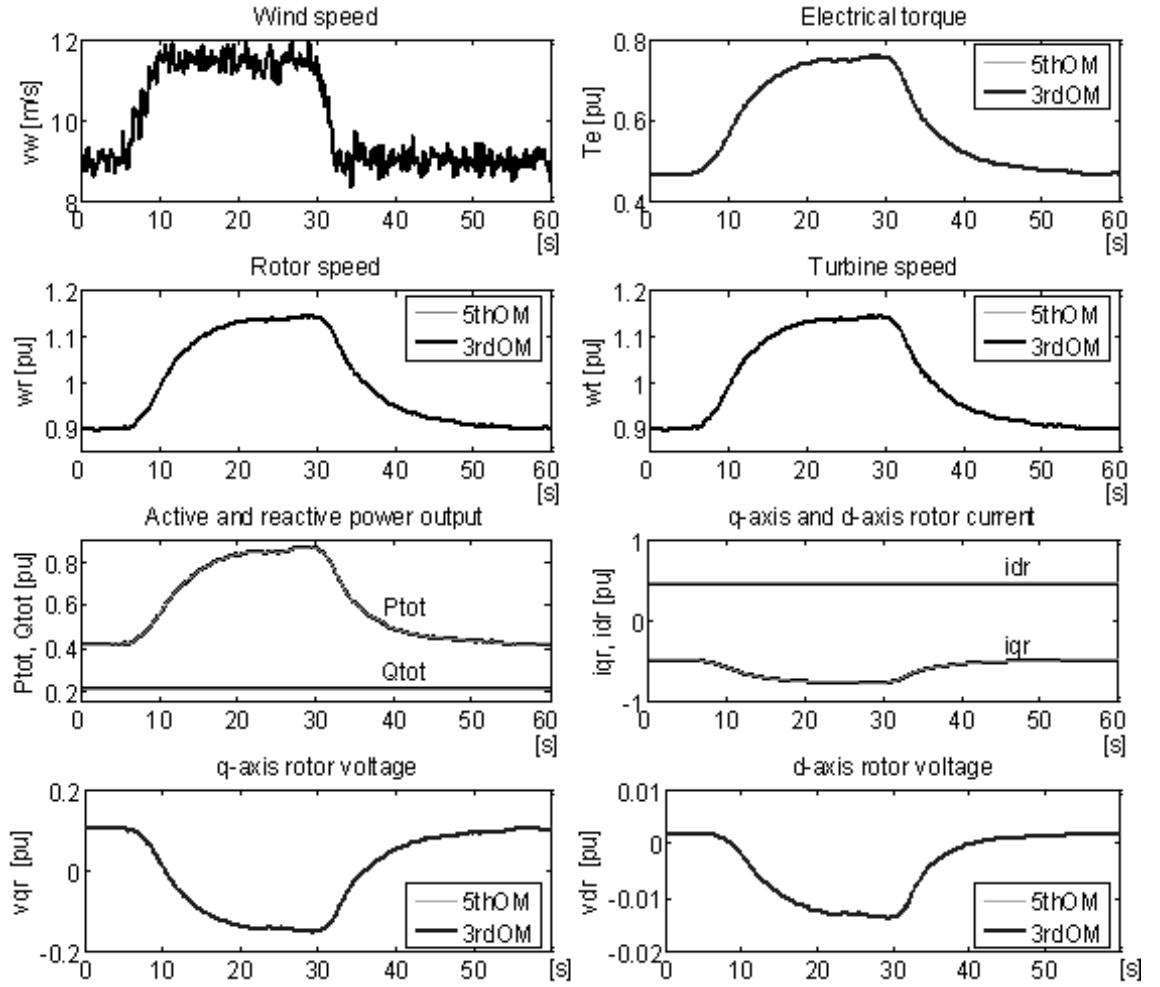


Figure 5.5: DFIG response to random wind speed variation with the control parameters of Table 5.5 and constant infinite bus voltage.

tegral time ($K_{\omega_r}/T_{\omega_r}$ is the integral gain) of the speed controller. In subrated condition, desired pole location can be specified and the rotor-side converter control parameters are determined accordingly. In rated conditions, K_{ω_r} and T_{ω_r} are tuned for the chosen set of RSC PI-gains. When selecting the pitch control parameters, there is a trade-off between minimizing blade pitching actions versus minimizing active power output variations as shown below.

Before discussing how K_{ω_r} and T_{ω_r} are chosen, the typical eigenvalues of a well-tuned DFIG in rated regime are described and compared to those of the subrated case. Table 5.13 gives an example of typical modes of the closed-loop DFIG with pitch control activated. Compared to Table 5.5 where eigenvalues are given for the closed-loop DFIG

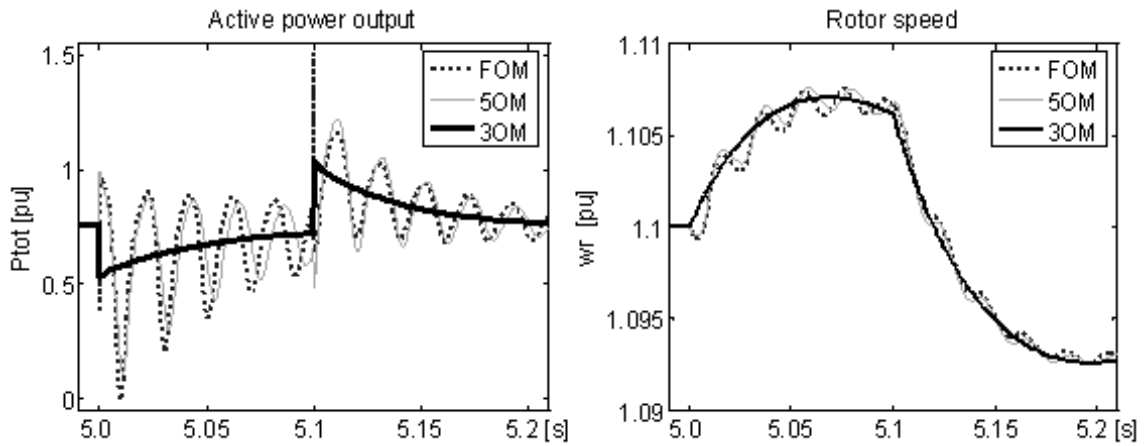


Figure 5.6: Zoomed view of Fig. 5.4

in subrated conditions, pitch control dynamics only affect the turbine mechanical mode. In rated regime, the turbine dynamics (ω_t) interact with the pitching mechanism (β) and speed controller dynamics (Φ_{ω_r}). In Table 5.13, turbine and pitch dynamics interaction results in a pair of complex conjugate eigenvalues, while speed controller dynamics give an additional real mode.

The particular coupling between turbine, pitching and speed control dynamics (ω_t , β , Φ_{ω_r}) changes according to operating point and control parameters, however the resulting eigenvalues are always one pair of complex conjugate and one real mode. Table 5.14 shows the participation factors of the dominant states of the eigenvalues related to ω_t , β and Φ_{ω_r} for different operating points. The coupling between the state variables changes, but overall the complex conjugate mode is more related to the turbine and pitch actuator dynamics (larger participation factors of ω_t and β) while the real mode is more related to the speed controller dynamics (larger participation of Φ_{ω_r}). In the remainder of this text, these two modes are referred to as turbine-pitch modes.

In Table 5.13 above, the eigenvalues are given for $K_{\omega_r} = -150$ and $T_{\omega_r} = 3$. The following paragraphs explain how these values are chosen with root-loci plots and time-domain simulations. It is noted that the proportional gain K_{ω_r} is negative. As explained in Subsection 5.2.2, this is because the process gain from pitch angle to rotor speed is reverse acting (speed decreases when pitch angle increases).

Fig. 5.7 shows the root-loci of the turbine-pitch modes for $K_{\omega_r} = -10 \sim -300$ with

Table 5.13: Example of closed-loop DFIG eigenvalues in rated regime

RSC q-axis gains: $K_{Te} = -1.5$, $T_{Te} = 0.025$, $K_{iq} = -1.0$, $T_{iq} = 0.0025$
RSC d-axis gains: $K_{Qs} = +1.0$, $T_{Qs} = 0.050$, $K_{id} = -0.5$, $T_{id} = 0.0050$
Pitch controller gains: $K_{\omega_r} = -150$, $T_{\omega_r} = 3$

FOM $\lambda = \sigma \pm j\omega$	5 th OM $\lambda = \sigma \pm j\omega$	3 rd OM $\lambda = \sigma \pm j\omega$	Dominant states
-7443.2	—	—	i_{qs}
-2928.2	—	—	i_{ds}
-10.7 ± j308.0 ($f = 49.02$ Hz) ($\zeta = 0.035$)	-16.2 ± j295.8 ($f = 47.08$ Hz) ($\zeta = 0.055$)	—	e'_{qs} e'_{ds}
-2.16 ± j11.14 ($f = 1.77$ Hz) ($\zeta = 0.190$)	-2.16 ± j11.14 ($f = 1.77$ Hz) ($\zeta = 0.190$)	-2.16 ± j11.14 ($f = 1.77$ Hz) ($\zeta = 0.190$)	ω_r θ_{tw}
-0.34 ± j0.73 ($f = 0.117$ Hz) ($\zeta = 0.423$)	-0.34 ± j0.73 ($f = 0.117$ Hz) ($\zeta = 0.423$)	-0.34 ± j0.73 ($f = 0.117$ Hz) ($\zeta = 0.423$)	ω_t β (Φ_{ω_r})
-423.4	-406.5	-399.6	Φ_{iq}
-226.2	-222.2	-199.3	Φ_{id}
-23.97	-24.03	-23.97	Φ_{Te}
-9.93	-9.93	-9.93	Φ_{Qs}
-0.43	-0.43	-0.43	Φ_{ω_r} (ω_t β)

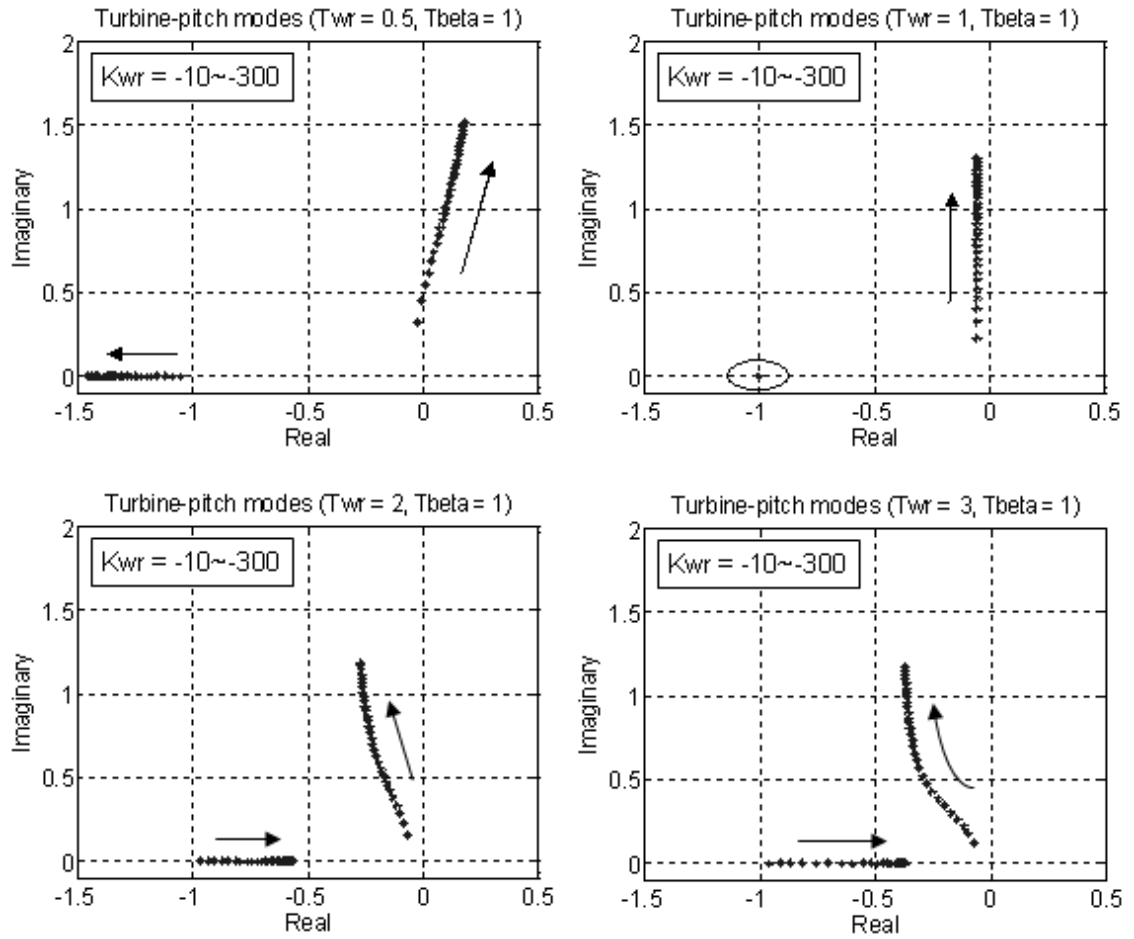
operating point: $v_{qs}=1$ pu, $\omega_r=1.2$ pu, $P_{tot}=1$ pu, $v_w=15$ m/s, $\beta=14.9^\circ$

Table 5.14: Participation factors of the turbine-pitch modes for different operating points

Operating point				Turb.-pitch modes $\lambda = \sigma \pm j\omega$	Participation factors		
v_w	P_{tot}	β	ω_r		ω_t	Φ_{ω_r}	β
13	1	4.7	1.2	-0.19 ± j0.42	.41	.33	.22
				-0.67	.24	.25	.49
15	1	14.9	1.2	-0.34 ± j0.73	.41	.19	.35
				-0.43	.22	.63	.13
17	1	21.1	1.2	-0.40 ± j1.03	.41	.14	.40
				-0.37	.14	.80	.05
19	1.08	23.9	1.3	-0.43 ± j1.28	.42	.11	.43
				-0.35	.10	.87	.02

v_w [m/s], P_{tot} [pu], β [°], ω_r [pu]

$T_{\omega_r} = 0.5, 1, 2$ and 3 . For stable operation (all eigenvalues in the left half plane), the speed controller integral time constant T_{ω_r} must be larger than the pitch actuator time constant T_β . Larger magnitudes for the proportional gain K_{ω_r} give slightly higher oscillation frequencies. To decide which range of K_{ω_r} and T_{ω_r} is more appropriate, time



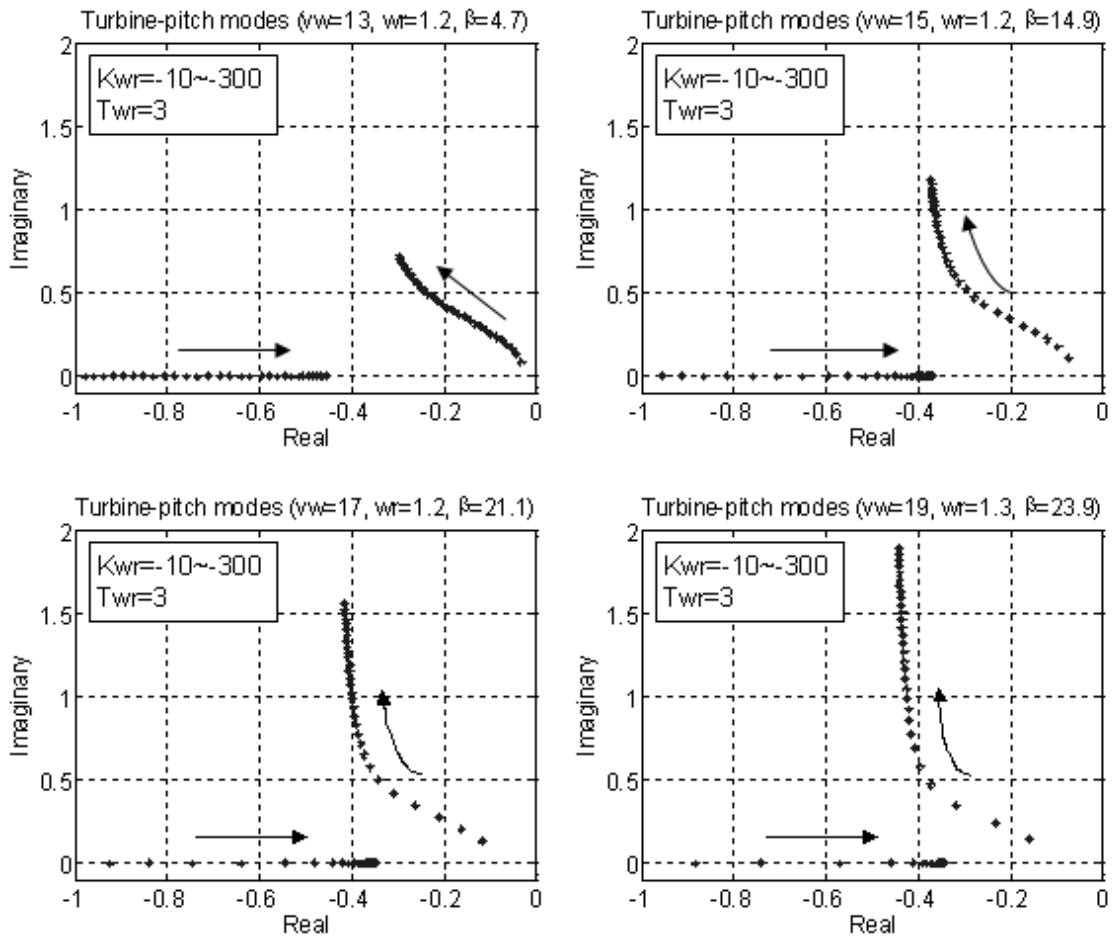
$T_{\beta} = 1 \text{ s} = \text{pitching actuator time constant}$

operating point: $v_w = 15 \text{ m/s}$, $\beta = 14.9^\circ$, $\omega_r = 1.2 \text{ pu}$, $P_{tot} = 1 \text{ pu}$

Figure 5.7: Root loci of turbine-pitch modes for different values of pitch control parameters K_{ω_r} and T_{ω_r} .

domain responses to wind speed disturbances have to be examined in order to assess the magnitude and duration of power output deviations (see below).

Fig. 5.8 shows the root-loci of the turbine-pitch modes for different wind speeds and corresponding pitch angles. Considering the scaling of the axes, the modes are moderately, but not considerably, sensitive to the initial wind speed. In the following, results of eigenvalue computations are only shown for $v_w = 15$ m/s. It can be expected that for other initial wind speed conditions the eigenvalues will not be significantly different.



$$v_w \text{ [m/s]}, \omega_r \text{ [pu]}, \beta \text{ [deg]}, \text{pitch controller parameters: } T_{\omega_r} = 3 \text{ s}, T_{\beta} = 1 \text{ s}$$

Figure 5.8: Root loci of turbine-pitch modes for different values of wind speed v_w and pitch angle β .

Fig. 5.9 shows the response of the blade pitch angle and total active power output to a wind speed step increase from $v_w = 15$ to 16 m/s at $t = 5$ s (rated wind speed is 12 m/s), for different proportional gain magnitudes. Larger $|K_{\omega_r}|$ values give shorter settling time and less overshoot in active power response. However, as predicted by the eigenvalues shown in Table 5.15, the associated oscillation frequency is higher and damping ratio lower. This means that there are more pitching direction changes, which is undesirable from a mechanical fatigue viewpoint. A value of $|K_{\omega_r}| = 150$ gives good compromise.

Table 5.15: Turbine-pitch modes for different values of K_{ω_r}

K_{ω_r}	T_{ω_r}	Turb.-pitch modes	f [Hz]	ζ	τ [s]
-50	3	$-0.17 \pm j0.30$	0.048	0.498	5.74
		-0.76	0	1	1.31
-150	3	$-0.34 \pm j0.73$	0.117	0.423	2.91
		-0.43	0	1	2.34
-300	3	$-0.37 \pm j1.78$	0.187	0.303	2.67
		-0.37	0	1	2.70

operating point: $v_{qs}=1$ pu, $\omega_r=1.2$ pu, $P_{tot}=1$ pu, $v_w=15$ m/s, $\beta=14.9^\circ$

Fig. 5.10 shows the response of the pitch angle and active power output to a wind speed step increase from 15 to 16 m/s, for different integral time constants. For a given $|K_{\omega_r}|$, larger T_{ω_r} (i.e. smaller integral gain) gives higher damping ratio for the oscillations, as predicted by the eigenvalues shown in Table 5.16. However too large T_{ω_r} gives a longer rising time. This is due to the real mode coming closer to the imaginary axis. A value of $T_{\omega_r} = 3$ gives good compromise.

Table 5.16: Turbine-pitch modes for different values of T_{ω_r}

K_{ω_r}	T_{ω_r}	Turb.-pitch modes	f [Hz]	ζ	τ [s]
-150	2	$-0.23 \pm j0.77$	0.123	0.288	4.31
		-0.65	0	1	1.54
-150	3	$-0.34 \pm j0.73$	0.117	0.423	2.91
		-0.43	0	1	2.34
-150	5	$-0.44 \pm j0.74$	0.118	0.514	2.25
		-0.22	0	1	4.46

operating point: $v_{qs}=1$ pu, $\omega_r=1.2$ pu, $P_{tot}=1$ pu, $v_w=15$ m/s, $\beta=14.9^\circ$

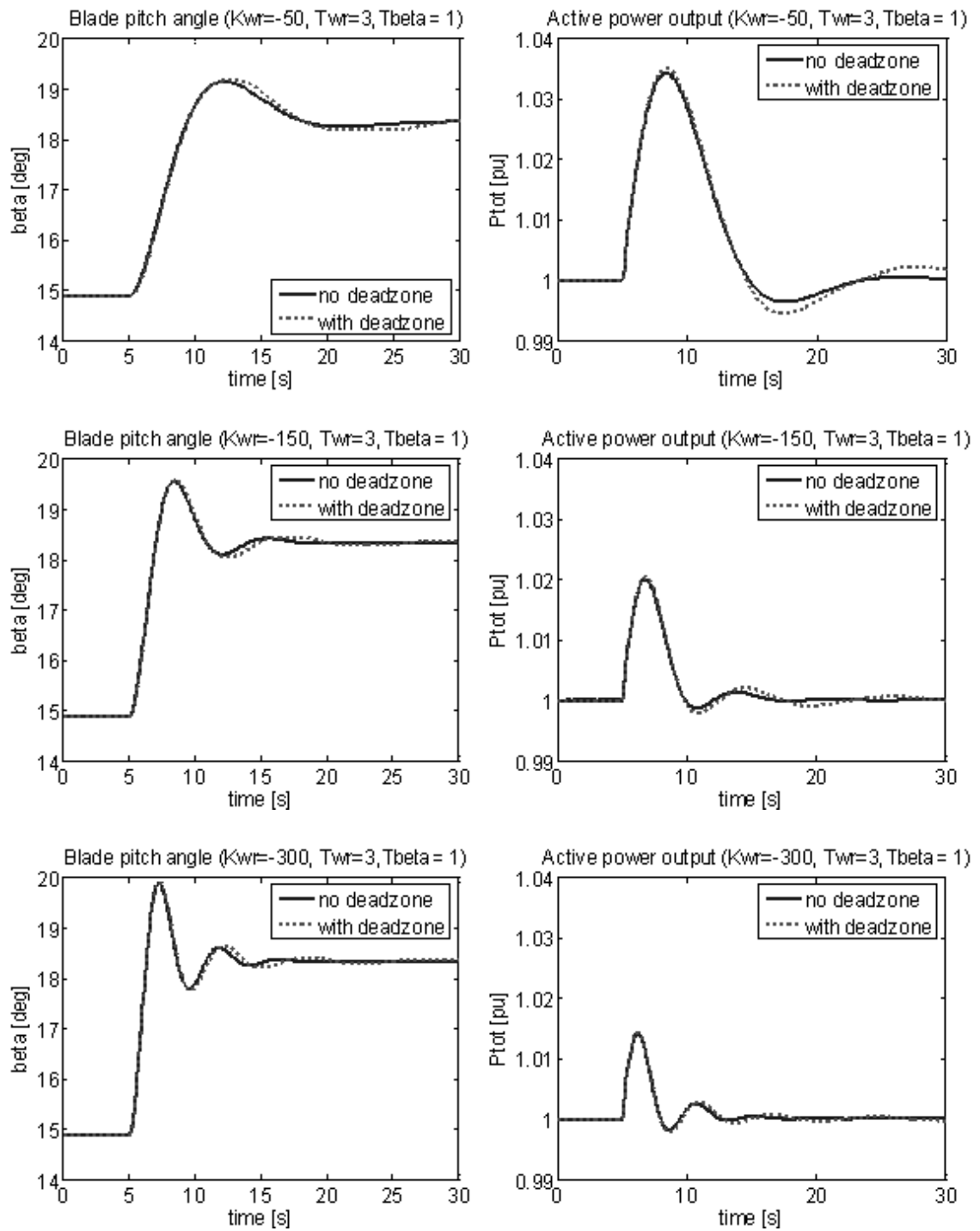


Figure 5.9: Closed-loop DFIG response to wind speed step increase from $v_w = 15$ to 16 m/s at $t = 5$ s for different values of K_{ω_r} .

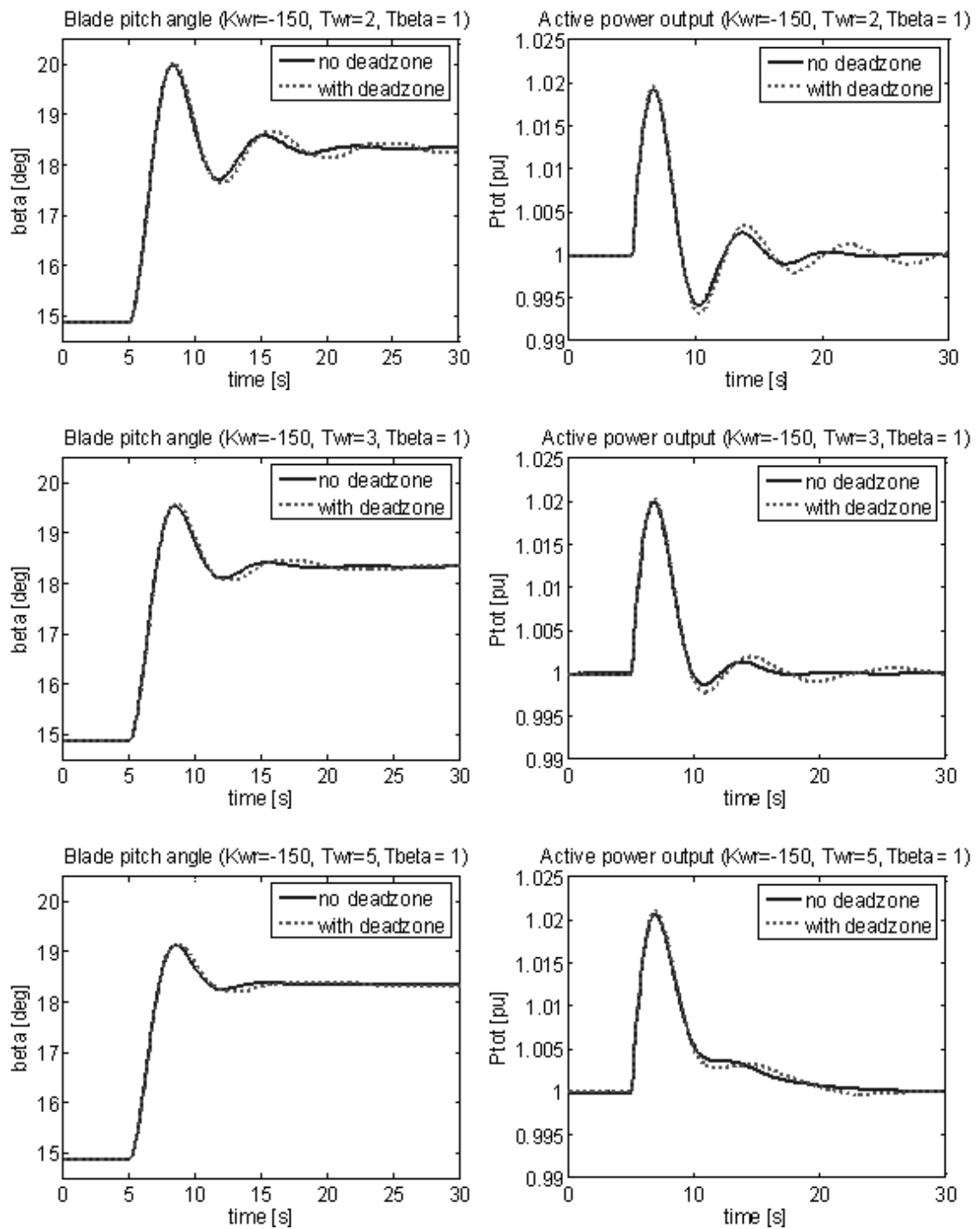


Figure 5.10: Closed-loop DFIG response to wind speed step increase from $v_w = 15$ to 16 m/s at $t = 5$ s for different values of T_{ω_r} .

In the above figures, time domain responses are observed for a step increase in wind speed. Below, responses to randomly varying wind speeds are examined. It is seen that the conclusions regarding the gains K_{ω_r} and T_{ω_r} are maintained.

Fig. 5.11 shows the DFIG response to randomly varying wind speed for different values of proportional gain K_{ω_r} . Smaller magnitudes of the gain ($K_{\omega_r} = -50$) gives less

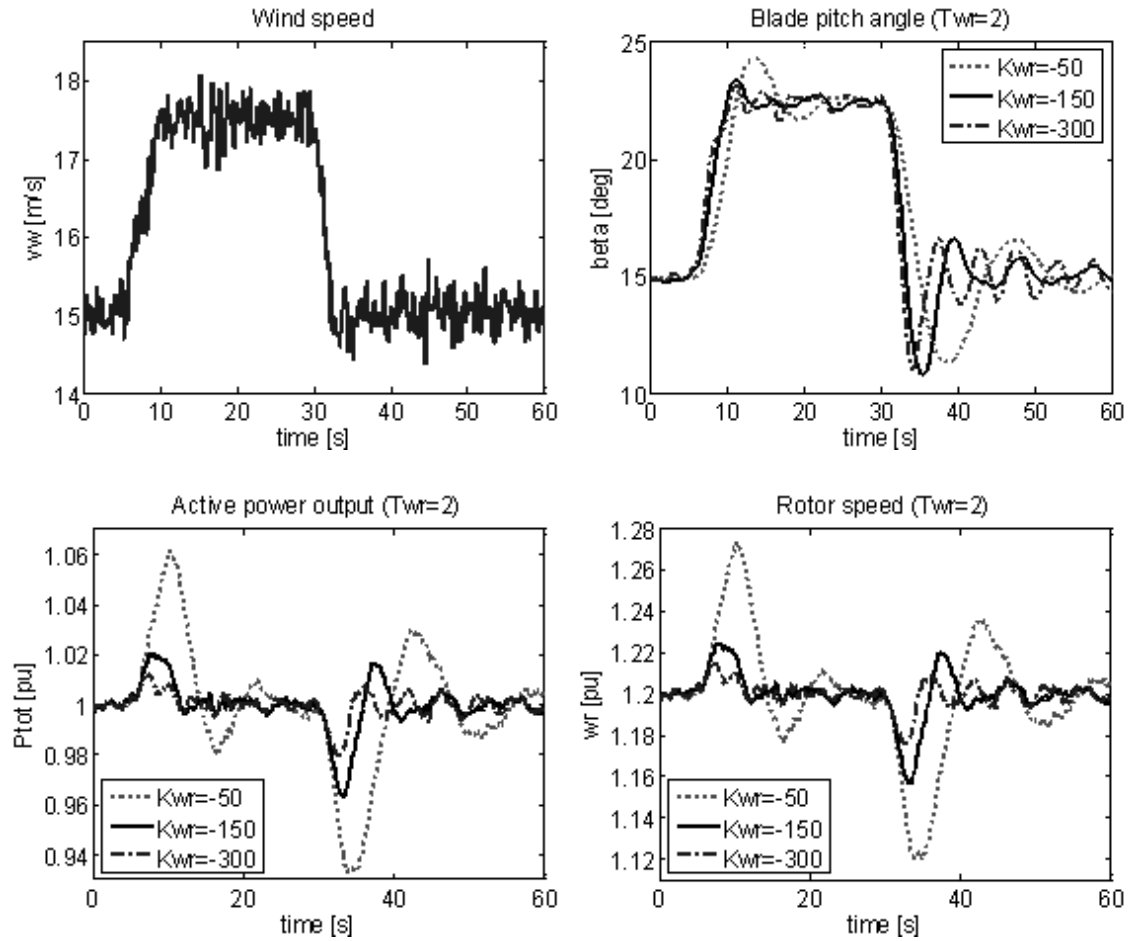


Figure 5.11: Closed-loop DFIG response (with deadzone) to randomly varying wind speed for different values of proportional gain K_{ω_r} .

pitching direction changes but larger active power and speed deviations. The opposite happens for larger magnitudes of the gain ($K_{\omega_r} = -300$). As for the step response, $K_{\omega_r} = -150$ gives a good compromise.

Fig. 5.12 shows the DFIG response to randomly varying wind speed for different values of integral time constant T_{ω_r} . It is seen that $T_{\omega_r} = 3$ gives a good compromise

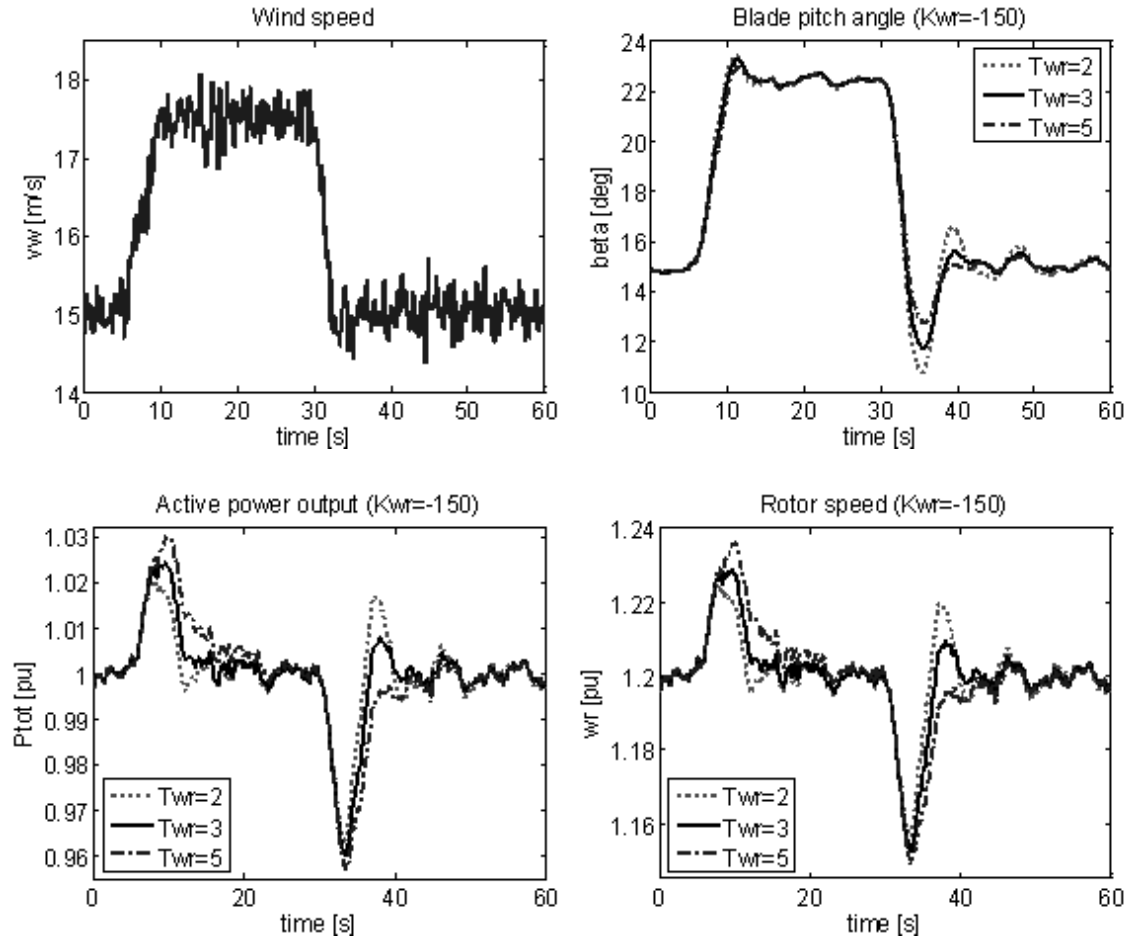


Figure 5.12: Closed-loop DFIG response (with deadzone) to randomly varying wind speed for different values of integral time constant T_{ω_r} .

between speed of power recovery and limitation of power overshoot.

From the above analysis, $K_{\omega_r} = -150$ and $T_{\omega_r} = 3$ are appropriate pitch controller parameters as they give good performance for different operating conditions and different types of disturbances. Since the pitching mechanism influences mainly the mechanical modes (Table 5.13) and negligibly the electrical modes, it can be expected that the result of this section will not be significantly sensitive to the values of the RSC control gains.

5.5.2 Activation and deactivation conditions

For smooth operation, transition conditions between subrated and rated regimes (i.e. pitch control activation and deactivation conditions) have to be specified appropriately. In the following, the procedure used in this work is described.

The conditions are formulated with two main objectives: 1) unnecessary pitching direction changes (which wear the components) should be minimized, and 2) wind speed measurements (which may not be accurate enough for on-line control purpose [55], p. 69) should not be used. To comply with the first objective, a deadzone and ‘up-pitch angle’ limits (β_{dz} and β_{up}) are used; more explanations are given below. To comply with the second objective, the transition decisions are formulated as function of the initial pitch angle and rotor speed measurements (β and ω_r).

The initial pitch angle can fall in one of the following three status:

- A) Pitch control is initially inactive ($\beta = 0^\circ$)
- B) Pitch control is initially active, around rated wind speed ($0 < \beta \leq \beta_{up}$)
- C) Pitch control is initially active, well above rated wind speed ($\beta > \beta_{up}$)

Depending on the initial pitch angle status, the measurement of the rotor speed gives the final transition decision. For the above status, the decisions are as follows:

- A) Activate pitching if rotor speed becomes larger than rated speed ($\omega_r > \omega_{rated}$)
- B) Deactivate pitching if rotor speed becomes lower than rated speed ($\omega_r < \omega_{rated}$)
- C) Maintain pitch active irrespective of the rotor speed

The parameter β_{up} is the value of pitch angle above which the pitch control remains active irrespective of the rotor speed. This condition is specified to avoid unnecessary transition between on/off status of the pitch controller after a decrease in wind speed in rated conditions.

Fig. 5.13 gives the DFIG response to a wind speed decrease (with random disturbances) in rated regime and high wind speed conditions (i.e. wind speed is well above its rated value, which is 12 m/s in the case study). Without the condition on β_{up} the pitch controller is activated and deactivated successively as the rotor speed reaches its reference value (which is the rated speed i.e. 1.2 pu in the case study). From a mechanical fatigue viewpoint the large number of on/off switchings (and hence pitching direction changes) is undesirable. In addition, since the wind speed remains quite high, the pitch controller should not be deactivated. These problems can be solved by specifying the condition on β_{up} , which gives a smoothed pitch angle variation.

The trade-off between minimizing pitching actions and power deviation during tran-

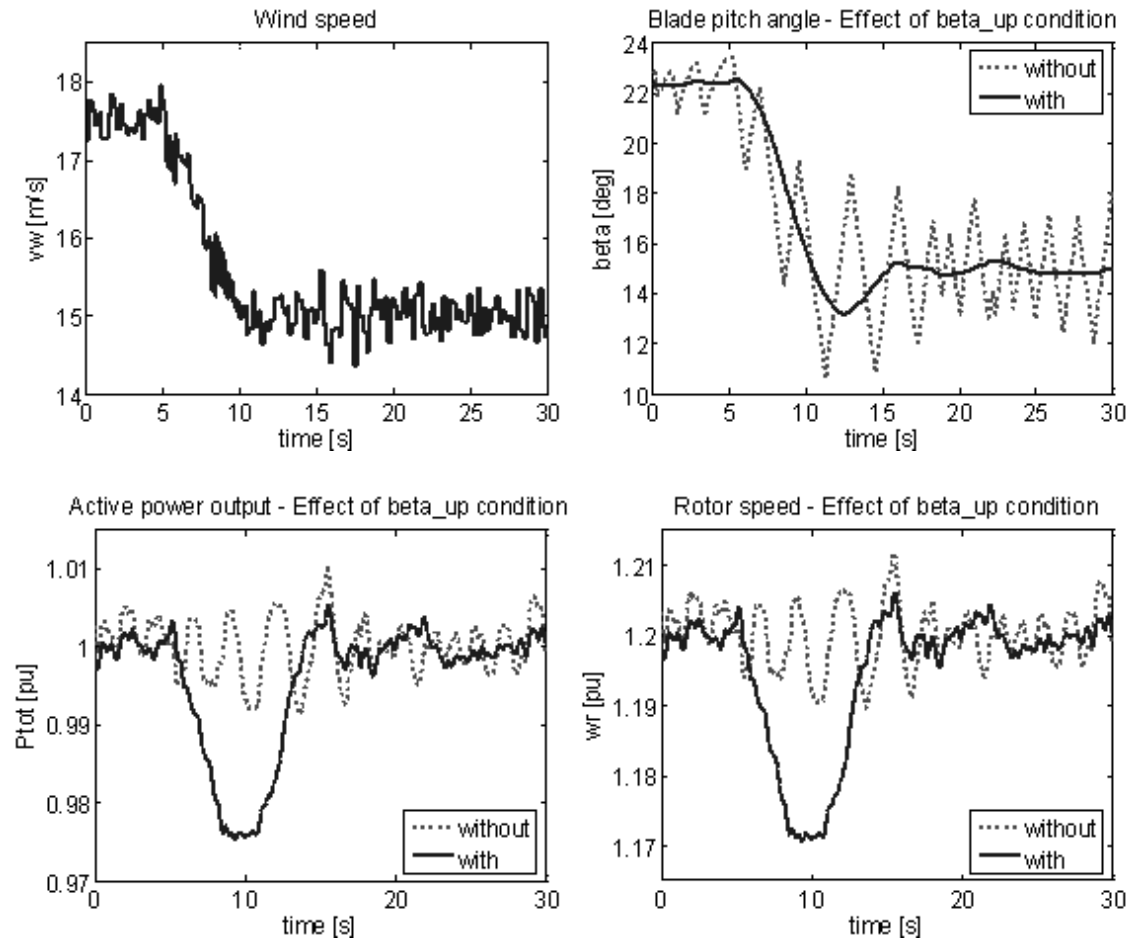


Figure 5.13: Closed-loop DFIG response to wind speed decrease in rated regime with/without condition on β_{up} .

sients can also be observed in Fig. 5.13. With the condition on β_{up} , the variation in power output is more important. However for the rather severe disturbance (drop in wind speed of about 2.5 m/s within 5 seconds) the associated power deviation is limited to about $-2.5\% \sim +0.5\%$, which is a reasonable performance. It is noted that active power output and rotor speed have virtually the same behaviour as the torque is controlled (by the rotor-side converter) to be constant in rated condition.

The value of β_{up} has to be chosen according to the deadzone. Since the deadzone is by definition the amount of pitch angle error that is ignored, β_{up} has to be larger or equal to the deadzone value (in other words, if the pitch control is active, the actual pitch angle must be above or equal to the deadzone). In addition, β_{up} should not be too large either because it gives more transition between on/off status when the wind generator is operating near rated wind speed. This is shown in Fig. 5.14 where it is seen that for the different values of β_{up} , active power output is not significantly different but more on/off transitions are required for $\beta_{up} = 0.5^\circ$. In the remainder of this work, β_{up} is equal to the deadzone, i.e. $\beta_{up} = \beta_{dz} = 0.1^\circ$.

5.5.3 Coordination of torque control

To avoid unnecessary power shedding in rated condition when the rotor speed drops below rated value (e.g. due to wind speed disturbances and corresponding transients), the electrical torque control of the rotor side converter has to be coordinated with the pitch control.

In Subsection 2.4.1, it was explained that the torque reference is obtained as $T_{e,ref} = T_{e,ref}(\omega_r)$ (Fig. 2.13). If no additional condition is specified, the torque reference is smaller than the rated torque if the rotor speed is below rated value ($T_{e,ref} = K_{opt}\omega_r^2 < T_{e,rated}$ if $\omega_r < \omega_{r,rated}$). Hence in rated regime, if the rotor speed drops below $\omega_{r,rated}$, the electrical torque reference (and hence output power) will be decreased accordingly.

To avoid the problem, it suffices to take into account the initial pitch angle value. If the pitch angle is initially larger than a threshold value i.e. if $\beta > \beta_{th,Teref}$, the electrical torque reference is maintained at $T_{e,ref} = T_{e,rated}$ regardless of the rotor speed. It is noted that the threshold $\beta_{th,Teref}$ used in the RSC controller (to coordinate the reference

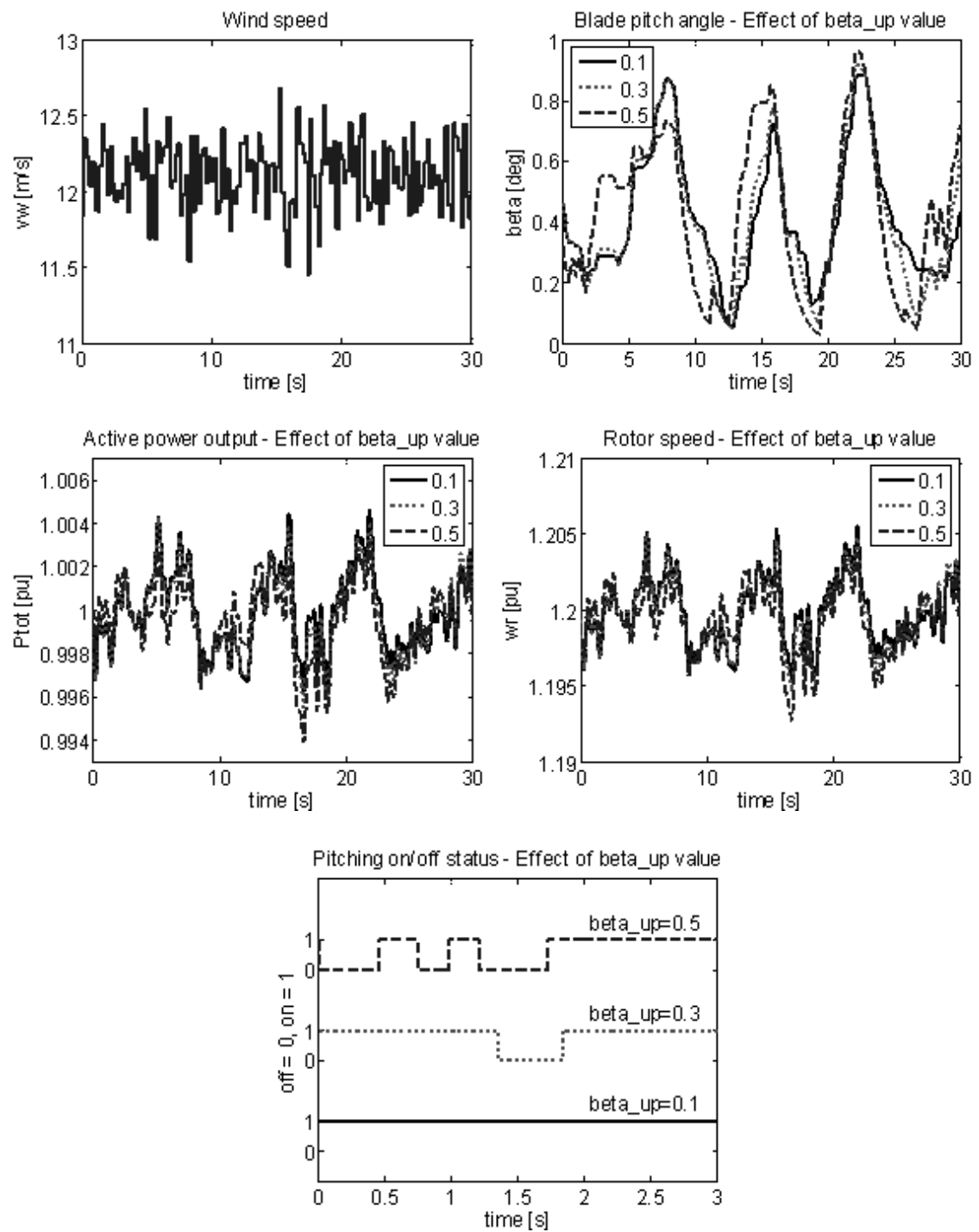


Figure 5.14: Closed-loop DFIG response to varying wind speed around rated value with $\beta_{up} = 0.1, 0.3, 0.5$.

electrical torque) is not the same as the limit β_{up} used in the pitch controller (to determine the initial pitch angle status).

When choosing the value of $\beta_{th,Teref}$, there is a trade off between smooth deactivation in low wind speed and smooth deactivation around rated wind speed. This is shown in Fig. 5.15 and 5.16. In the former case, larger value of $\beta_{th,Teref}$ gives a less abrupt change in output power. In the latter case, a smaller value gives smaller drops in output power. A good compromise for both cases is to choose $\beta_{th,Teref} = 0.001^\circ$.

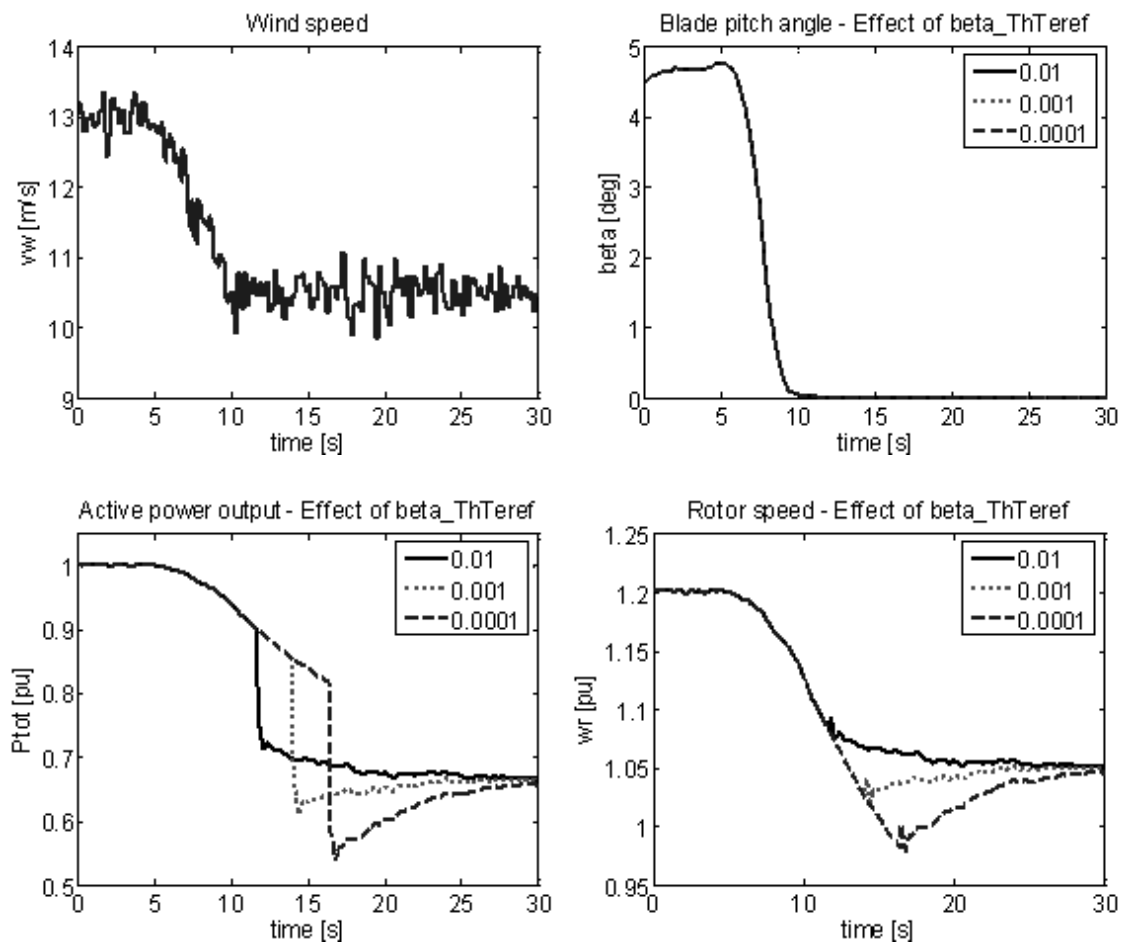


Figure 5.15: Deactivation of pitch control with final wind speed below rated value for $\beta_{th,Teref} = 0.01, 0.001, 0.0001$.

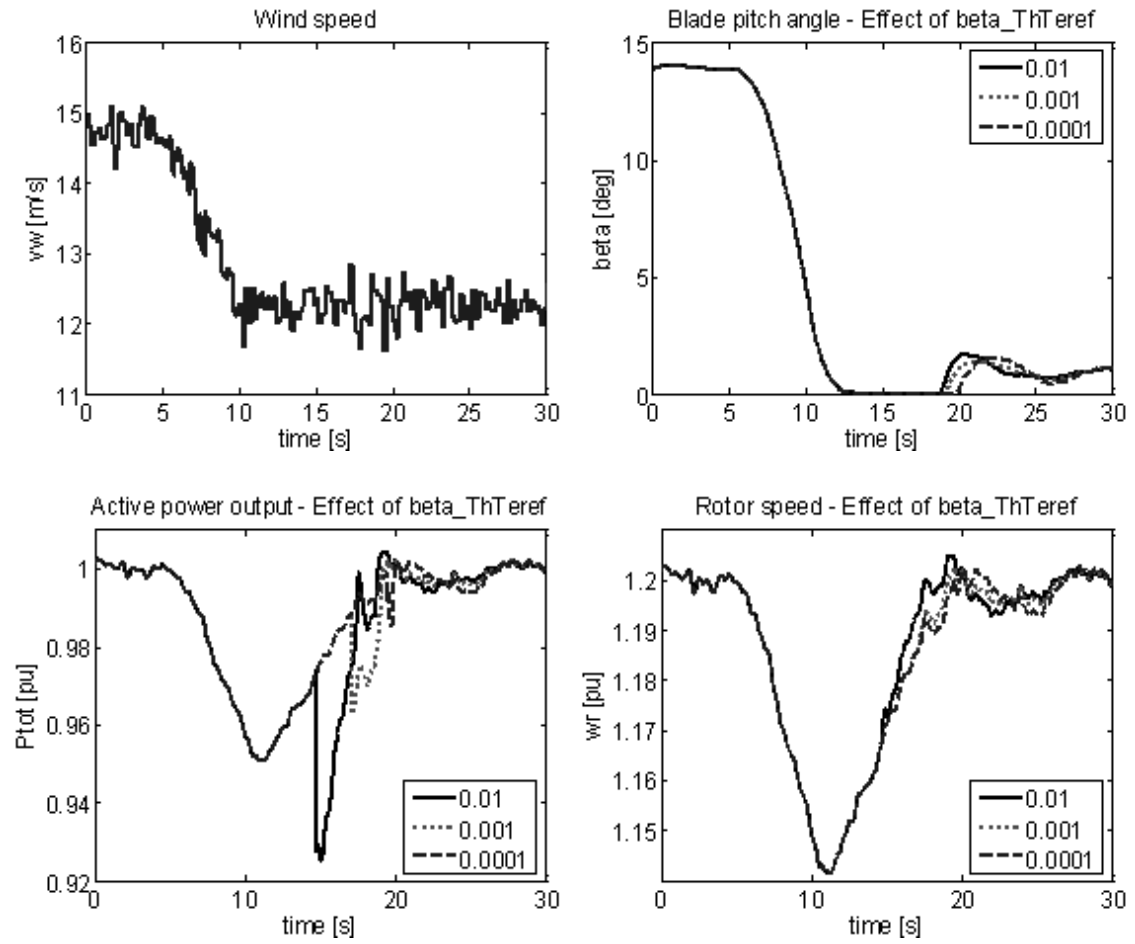


Figure 5.16: Deactivation of pitch control with final wind speed around rated value for $\beta_{th,Teref} = 0.01, 0.001, 0.0001$.

As a summary Fig. 5.17 and 5.18 show the flow charts for the pitch transition conditions and the reference torque coordination.

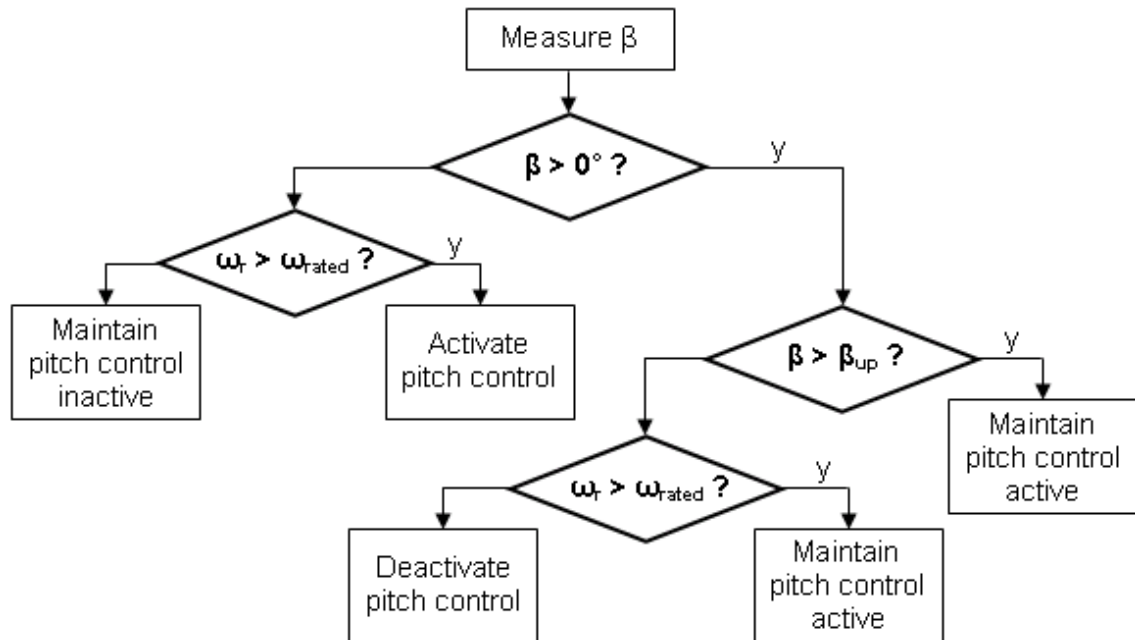
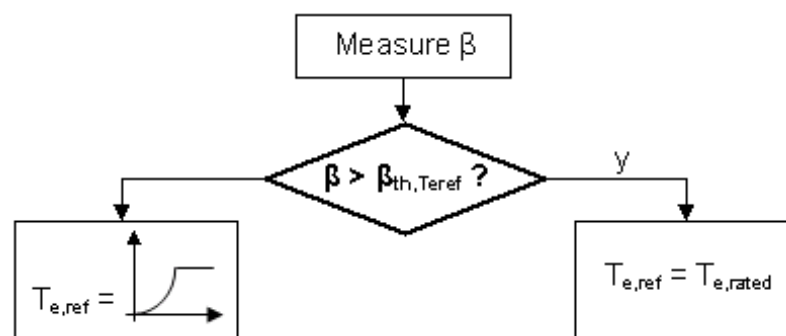


Figure 5.17: Activation and deactivation conditions for the pitch controller.



5.6 Summary

When tuning the RSC controllers, stator transients should be considered and model simplification for stability studies should be done only once a set of appropriate control gains has been obtained. The reason is that when neglecting stator transients, one may find PI-gains giving stable result for simplified DFIG models, but unstable for the full order model (where stator and rotor electrical transients are represented) which reflects more realistic situations.

To address the issue, a tuning procedure of the RSC can be formulated to ensure stable stator and rotor electrical dynamics. Firstly, the physics of the system (steady-state gains) are examined to determine the correct sign of the controller gains for a given definition of positive rotor current. Secondly, analytical expressions can be derived using Gershgorin theorem to obtain limit values of the gains so that stator modes are placed at some desired location. Thirdly, root-loci are observed to determine the allowed magnitude of the controller gains for stable rotor electrical dynamics. Additional criteria on the PI-gains to avoid oscillatory coupling between d- and q-axis dynamics can also be identified. For properly tuned control parameters, the dynamical performance of the closed-loop DFIG are preserved over a wide range of machine parameters and operating points.

For the pitch control tuning, there is a stability criterion that requires the speed controller time constant to be larger than the actuators time constant ($T_{\omega_r} > T_\beta$). Eigenvalue computations and time-domain responses can be used to determine the final values of pitch control gains. The exercise consists essentially in weighting trade offs between smoother power output and less pitching activities.

Finally, two important practical issues in DFIG control are the transition between subrated and rated regimes, and the coordination of the RSC and pitch controllers. A suitable procedure for pitching activation and deactivation must be in place to ensure smooth operation and avoid unnecessary on/off transitions due to disturbances. A suitable coordination of the electrical torque reference must be in place to avoid unnecessary power output drops in rated conditions due to disturbances.

Chapter 6

Analysis: Multi-machine power system

The previous chapters discussed the behaviour, stability, and control of the DFIG. Small-signal analysis was performed on a single-machine infinite bus system and the eigenvalues of the DFIG were observed. In this chapter, the interest is in examining how replacing synchronous generators by doubly-fed induction generators influences the oscillatory stability of a power system. The interest is now in the low frequency oscillations of the synchronous generators. In particular, the discussion focuses on the eigenvalue corresponding to the inter-area mode (IAM). The IAM is the eigenvalue that relates to the speed-angle oscillation of the generators in an area against those in another area.

Fig. 6.1 [49] shows the considered study system. It is the two-area power system model proposed in [131] to study the small-signal stability of power systems with remotely connected synchronous machines. The long lines between bus 5, 8 and 6 divide the system in two areas. Within each area, generators are grouped together and modelled by two equivalent machines.

To observe the effect of the generation mix on the oscillatory stability of the power system, two scenarios are considered. In the first scenario, all generators are synchronous machines. In the second scenario, the SG at bus 2 in Area I is replaced by a DFIG with terminal reactive power control. For each of these two cases, the effect of the following factors on the IAM is observed:

- (a) the power generation sharing among the generators,
- (b) the amount of active power transferred in the inter-tie lines.

The results show that with a DFIG at bus 2 instead of an SG can both improve or deterio-

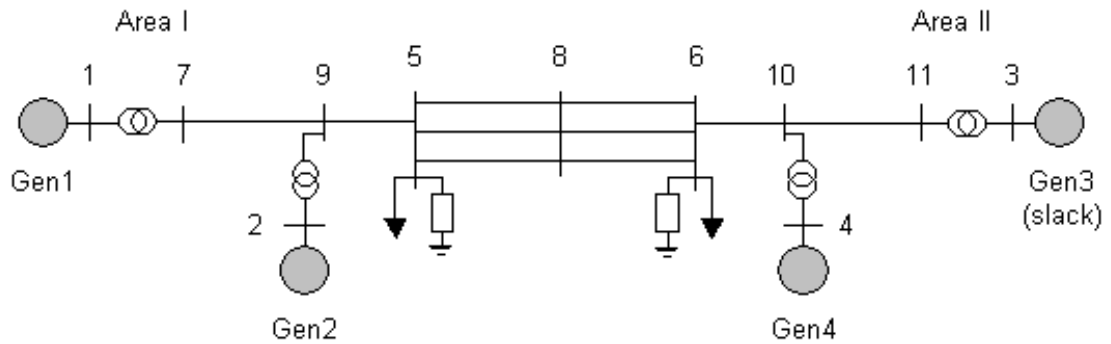


Figure 6.1: Two-area power system model

rate the IAM damping ratio depending on the operating point.

To facilitate the analysis, the small-signal properties (eigenvalues and participation factors) of the study system is first discussed for a base case.

6.1 Small-signal properties of the study system

Table 6.2 to 6.5 show the complex eigenvalues (oscillating modes) of the study system in Fig. 6.1 for the base case loadflow solution given in Table 6.1. In Table 6.2 the synchronous machines are equipped with DC1A self-excited excitation systems (slow with low gain). In Table 6.3 the synchronous machines are equipped with DC1A separately-excited excitation systems (slow with low gain). In Table 6.4 the synchronous machines are equipped with DC2A type excitation systems (slow with high gain). In Table 6.5 the synchronous machines are equipped with ST1A type excitation systems (static and fast). In the present work, there is no load compensation and no supplementary power system stabiliser control loop. Parameters of the SGs and excitation systems are given in Appendix 3. In each table, the eigenvalues are given for the case where all four generators are synchronous machines, and for the case where the generator at bus 2 is replaced by a DFIG. The DFIG has the same MW and MVar output as Gen 2 and hence the system voltage profile, MW and MVar outputs of the remaining SGs remain unaltered. For each load, the model used is the constant power model since the interest here is to compare study results where the same load model is used.

When all generators are synchronous machines the low frequency dynamics consist of

speed-angle and exciter-field oscillations. These oscillations can be classified into intra-area modes (oscillations within Area I and II) and inter-area modes (oscillations between Area I and II).

Table 6.1: Base case loadflow solution

Bus nb	V_{mag}	V_{ang}	P_{gen}	Q_{gen}	P_{load}	Q_{load}
1	1.0100	-0.0103	490	38	0	0
2	1.0100	-0.1177	210	10	0	-35
3	1.0100	0	492	39	0	0
4	1.0100	-0.1020	230	12	0	-35
5	0.9913	-0.2501	0	0	700	35
6	0.9910	-0.2427	0	0	700	35
7	1.0070	-0.0827	0	0	0	0
8	1.0008	-0.2475	0	0	0	0
9	1.0100	-0.0103	0	0	0	0
10	0.9985	-0.1802	0	0	0	0
11	0.9983	-0.1705	0	0	0	0

V_{mag} [pu], V_{ang} [rad], P [MVA], Q [MVA]

Replacing an SG by a DFIG changes the dynamics of the area where the generation mix is modified (the DFIG adds a mechanical mode contributed by its mechanical variables, and the intra-area SG oscillations are removed since there is just one equivalent SG left), but the low-frequency dynamic properties of the overall system are essentially unchanged. They are still composed of speed-angle and exciter-field oscillations within and between areas. In particular, the inter-area speed-angle mode whose frequency and damping ratio are slightly modified is still contributed by the synchronous generators only. The latter observation means effectively that the change in the IAM location is more related to the removal of the SG at bus 2 (removal of its synchronous inertia and damping torque contribution) rather than to the addition of the DFIG.

In other words, in multi-machine studies where the focus is on the impact of the generation mix (synchronous and non-synchronous) on the oscillating stability, the conclusions are more related to removal of synchronous dynamics rather than to the introduction of asynchronous dynamics. This underlines the fact that low frequency speed-angle oscillations are inherent to synchronous machines.

Fig. 6.2 shows the change in inter-area speed-angle oscillating mode for the 4 types of SG excitation systems. For the considered operating point, removal of an SG (and

replacement by a DFIG) leads to virtually unchanged damping ratio and slightly higher frequency. The higher frequency can be explained by the removal of synchronous inertia i.e. the equivalent generator in Area I is lighter and hence the resulting oscillation frequency is higher. The negligible change in damping can be explained by the small change in damping torque of the equivalent generator. In the following, it is shown that the magnitude and direction of the change depend on the type of SG excitation system and the operating point.

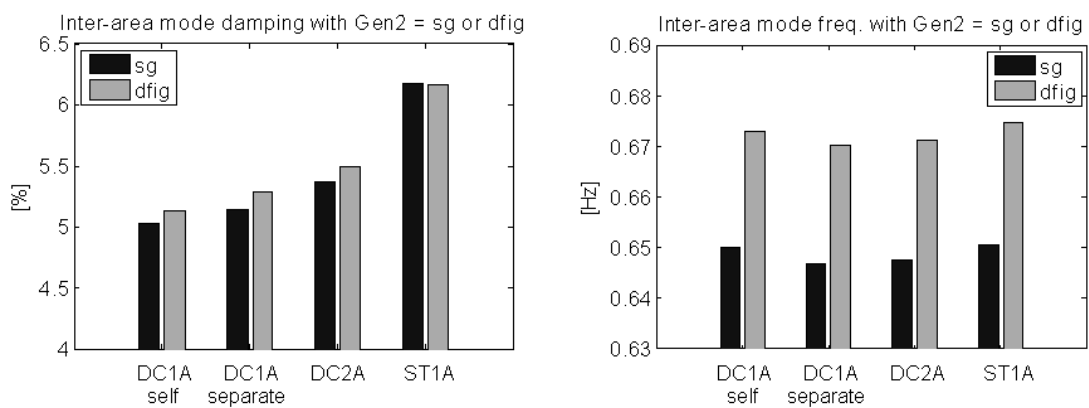


Figure 6.2: Base case inter-area mode damping ratio and frequency

Table 6.2: Base case complex modes: SG with DC1A self exciter

Study system with 4 SG*Oscillating modes in Area I*

$\lambda = \sigma \pm j\omega$	ζ	f_{osc} [Hz]	Name	Dominant states
$-0.64 \pm j5.72$.112	0.91	Speed-angle	$\omega_{r1}, \delta_1, \omega_{r2}, \delta_2$
$-0.30 \pm j0.37$.633	0.06	Exciter-field	$E'_{q1}, R_{f1}, E'_{q2}, R_{f2}$
$-5.52 \pm j0.89$.987	0.14	Exciter-field	$E'_{d1}, E_{fd1}, E'_{d2}, E_{fd2}$

Oscillating modes in Area II

$\lambda = \sigma \pm j\omega$	ζ	f_{osc} [Hz]	Name	Dominant states
$-0.62 \pm j5.82$.107	0.93	Speed-angle	$\omega_{r3}, \delta_3, \omega_{r4}, \delta_4$
$-0.29 \pm j0.36$.629	0.06	Exciter-field	$E'_{q3}, R_{f3}, E'_{q4}, R_{f4}$
$-5.58 \pm j0.89$.987	0.14	Exciter-field	$E'_{d3}, E_{fd3}, E'_{d4}, E_{fd4}$

Inter-area oscillating modes

$\lambda = \sigma \pm j\omega$	ζ	f_{osc} [Hz]	Name	Dominant states
$-0.21 \pm j4.08$.050	0.65	Speed-angle	$\omega_{r1}, \delta_1, \omega_{r3}, \delta_3$
$-0.55 \pm j0.56$.706	0.09	Exciter-field	$E'_{q1}, R_{f1}, E'_{q3}, R_{f3}$
$-1.40 \pm j0.49$.945	0.08	Exciter-field	$E'_{q1}, R_{f1}, E'_{q3}, R_{f3}$
$-4.53 \pm j0.77$.986	0.12	Exciter-field	$E'_{d1}, E_{fd1}, E'_{d3}, E_{fd3}$

Study system with 1 DFIG and 3 SG*Oscillating modes in Area I*

$\lambda = \sigma \pm j\omega$	ζ	f_{osc} [Hz]	Name	Dominant states
$-2.75 \pm j11.16$.240	1.78	DFIG mech. mode	$\omega_{r2}, \theta_{tw2}$

Oscillating modes in Area II

$\lambda = \sigma \pm j\omega$	ζ	f_{osc} [Hz]	Name	Dominant states
$-0.61 \pm j5.80$.105	0.92	SG speed-angle	$\omega_{r3}, \delta_3, \omega_{r4}, \delta_4$
$-0.29 \pm j0.37$.625	0.06	SG exciter-field	$E'_{q3}, R_{f3}, E'_{q4}, R_{f4}$
$-5.57 \pm j0.90$.987	0.14	SG exciter-field	$E'_{d3}, E_{fd3}, E'_{d4}, E_{fd4}$

Inter-area oscillating modes

$\lambda = \sigma \pm j\omega$	ζ	f_{osc} [Hz]	Name	Dominant states
$-0.22 \pm j4.23$.051	0.67	SG speed-angle	$\omega_{r1}, \delta_1, \omega_{r3}, \delta_3$
$-0.53 \pm j0.55$.696	0.09	SG exciter-field	$E'_{q1}, R_{f1}, E'_{q3}, R_{f3}$
$-1.73 \pm j0.96$.875	0.15	SG exciter-field	$E'_{q1}, R_{f1}, E'_{q3}, R_{f3}$
$-4.60 \pm j0.78$.986	0.12	SG exciter-field	$E'_{d1}, E_{fd1}, E'_{d3}, E_{fd3}$

Table 6.3: Base case complex modes: SG with DC1A separate exciter

Study system with 4 SG*Oscillating modes in Area I*

$\lambda = \sigma \pm j\omega$	ζ	f_{osc} [Hz]	Name	Dominant states
$-0.65 \pm j5.71$.114	0.91	Speed-angle	$\omega_{r1}, \delta_1, \omega_{r2}, \delta_2$
$-5.28 \pm j7.93$.554	1.26	Exciter-field	$E_{fd1}, V_{R1}, E_{fd2}, V_{R2}$
$-0.41 \pm j0.49$.642	0.08	Exciter-field	$E'_{q1}, R_{f1}, E'_{q2}, R_{f2}$

Oscillating modes in Area II

$\lambda = \sigma \pm j\omega$	ζ	f_{osc} [Hz]	Name	Dominant states
$-0.63 \pm j5.80$.108	0.92	Speed-angle	$\omega_{r3}, \delta_3, \omega_{r4}, \delta_4$
$-5.29 \pm j7.93$.555	1.26	Exciter-field	$E_{fd3}, V_{R3}, E_{fd4}, V_{R4}$
$-0.41 \pm j0.48$.649	0.08	Exciter-field	$E'_{q3}, R_{f3}, E'_{q4}, R_{f4}$

Inter-area oscillating modes

$\lambda = \sigma \pm j\omega$	ζ	f_{osc} [Hz]	Name	Dominant states
$-0.21 \pm j4.06$.051	0.65	Speed-angle	$\omega_{r1}, \delta_1, \omega_{r3}, \delta_3$
$-0.41 \pm j1.07$.356	0.17	Exciter-field	$E'_{q1}, R_{f1}, E'_{q3}, R_{f3}$
$-0.42 \pm j0.78$.471	0.12	Exciter-field	$E'_{q1}, R_{f1}, E'_{q3}, R_{f3}$
$-5.18 \pm j7.81$.553	1.24	Exciter-field	$E_{fd1}, V_{R1}, E_{fd3}, V_{R3}$
$-5.24 \pm j7.88$.554	1.25	Exciter-field	$E_{fd1}, V_{R1}, E_{fd3}, V_{R3}$

Study system with 1 DFIG and 3 SG*Oscillating modes in Area I*

$\lambda = \sigma \pm j\omega$	ζ	f_{osc} [Hz]	Name	Dominant states
$-2.75 \pm j11.16$.240	1.78	DFIG mech. mode	$\omega_{r2}, \theta_{tw2}$

Oscillating modes in Area II

$\lambda = \sigma \pm j\omega$	ζ	f_{osc} [Hz]	Name	Dominant states
$-0.62 \pm j5.79$.107	0.92	SG speed-angle	$\omega_{r3}, \delta_3, \omega_{r4}, \delta_4$
$-5.29 \pm j7.93$.555	1.26	SG exciter-field	$E_{fd3}, V_{R3}, E_{fd4}, V_{R4}$
$-0.41 \pm j0.49$.645	0.08	SG exciter-field	$E'_{q3}, R_{f3}, E'_{q4}, R_{f4}$

Inter-area oscillating modes

$\lambda = \sigma \pm j\omega$	ζ	f_{osc} [Hz]	Name	Dominant states
$-0.22 \pm j4.21$.053	0.67	SG speed-angle	$\omega_{r1}, \delta_1, \omega_{r3}, \delta_3$
$-0.40 \pm j1.10$.342	0.18	SG exciter-field	$E'_{q1}, R_{f1}, E'_{q3}, R_{f3}$
$-0.42 \pm j0.77$.477	0.12	SG exciter-field	$E'_{q1}, R_{f1}, E'_{q3}, R_{f3}$
$-5.18 \pm j7.80$.553	1.24	SG exciter-field	$E_{fd1}, V_{R1}, E_{fd3}, V_{R3}$
$-5.24 \pm j7.88$.554	1.25	SG exciter-field	$E_{fd1}, V_{R1}, E_{fd3}, V_{R3}$

Table 6.4: Base case complex modes: SG with DC2A exciter

Study system with 4 SG*Oscillating modes in Area I*

$\lambda = \sigma \pm j\omega$	ζ	f_{osc} [Hz]	Name	Dominant states
$-0.67 \pm j5.71$.116	0.91	Speed-angle	$\omega_{r1}, \delta_1, \omega_{r2}, \delta_2$
$-0.23 \pm j0.49$.418	0.08	Exciter-field	$E'_{q1}, R_{f1}, E'_{q2}, R_{f2}$
$-51.04 \pm j30.74$.857	4.89	Exciter-field	$E_{fd1}, V_{R1}, E_{fd2}, V_{R2}$

Oscillating modes in Area II

$\lambda = \sigma \pm j\omega$	ζ	f_{osc} [Hz]	Name	Dominant states
$-0.65 \pm j5.81$.111	0.92	Speed-angle	$\omega_{r3}, \delta_3, \omega_{r4}, \delta_4$
$-0.22 \pm j0.48$.420	0.08	Exciter-field	$E'_{q3}, R_{f3}, E'_{q4}, R_{f4}$
$-51.04 \pm j30.74$.857	4.89	Exciter-field	$E_{fd3}, V_{R3}, E_{fd4}, V_{R4}$

Inter-area oscillating modes

$\lambda = \sigma \pm j\omega$	ζ	f_{osc} [Hz]	Name	Dominant states
$-0.22 \pm j4.07$.054	0.65	Speed-angle	$\omega_{r1}, \delta_1, \omega_{r3}, \delta_3$
$-0.40 \pm j1.04$.359	0.16	Exciter-field	$E'_{q1}, R_{f1}, E'_{q3}, R_{f3}$
$-0.30 \pm j0.77$.366	0.12	Exciter-field	$E'_{q1}, R_{f1}, E'_{q3}, R_{f3}$
$-50.79 \pm j30.31$.859	4.82	Exciter-field	$E_{fd1}, V_{R1}, E_{fd3}, V_{R3}$
$-50.24 \pm j30.55$.858	4.86	Exciter-field	$E_{fd1}, V_{R1}, E_{fd3}, V_{R3}$

Study system with 1 DFIG and 3 SG*Oscillating modes in Area I*

$\lambda = \sigma \pm j\omega$	ζ	f_{osc} [Hz]	Name	Dominant states
$-2.75 \pm j11.16$.240	1.78	DFIG mech. mode	$\omega_{r2}, \theta_{tw2}$

Oscillating modes in Area II

$\lambda = \sigma \pm j\omega$	ζ	f_{osc} [Hz]	Name	Dominant states
$-0.64 \pm j5.79$.110	0.92	SG speed-angle	$\omega_{r3}, \delta_3, \omega_{r4}, \delta_4$
$-0.22 \pm j0.49$.414	0.08	SG exciter-field	$E'_{q3}, R_{f3}, E'_{q4}, R_{f4}$
$-51.04 \pm j30.75$.857	4.89	SG exciter-field	$E_{fd3}, V_{R3}, E_{fd4}, V_{R4}$

Inter-area oscillating modes

$\lambda = \sigma \pm j\omega$	ζ	f_{osc} [Hz]	Name	Dominant states
$-0.23 \pm j4.22$.055	0.67	SG speed-angle	$\omega_{r1}, \delta_1, \omega_{r3}, \delta_3$
$-0.40 \pm j1.06$.355	0.17	SG exciter-field	$E'_{q1}, R_{f1}, E'_{q3}, R_{f3}$
$-0.30 \pm j0.75$.366	0.12	SG exciter-field	$E'_{q1}, R_{f1}, E'_{q3}, R_{f3}$
$-50.78 \pm j30.30$.859	4.82	SG exciter-field	$E_{fd1}, V_{R1}, E_{fd3}, V_{R3}$
$-50.94 \pm j30.57$.858	4.86	SG exciter-field	$E_{fd1}, V_{R1}, E_{fd3}, V_{R3}$

Table 6.5: Base case complex modes: SG with ST1A static exciter

Study system with 4 SG*Oscillating modes in Area I*

$\lambda = \sigma \pm j\omega$	ζ	f_{osc} [Hz]	Name	Dominant states
$-0.71 \pm j5.74$.123	0.91	Speed-angle	$\omega_{r1}, \delta_1, \omega_{r2}, \delta_2$
$-0.47 \pm j0.63$.597	0.10	Exciter-field	$E'_{q1}, V_{R1}, E'_{q2}, V_{R2}$

Oscillating modes in Area II

$\lambda = \sigma \pm j\omega$	ζ	f_{osc} [Hz]	Name	Dominant states
$-0.69 \pm j5.83$.118	0.93	Speed-angle	$\omega_{r3}, \delta_3, \omega_{r4}, \delta_4$
$-0.45 \pm j0.62$.592	0.10	Exciter-field	$E'_{q3}, V_{R3}, E'_{q4}, V_{R4}$

Inter-area oscillating modes

$\lambda = \sigma \pm j\omega$	ζ	f_{osc} [Hz]	Name	Dominant states
$-0.25 \pm j4.09$.062	0.65	Speed-angle	$\omega_{r1}, \delta_1, \omega_{r3}, \delta_3$
$-0.81 \pm j0.85$.689	0.14	Exciter-field	$E'_{q1}, V_{R1}, E'_{q3}, V_{R3}$
$-1.33 \pm j0.92$.824	0.15	Exciter-field	$E'_{q1}, V_{R1}, E'_{q3}, V_{R3}$

Study system with 1 DFIG and 3 SG*Oscillating modes in Area I*

$\lambda = \sigma \pm j\omega$	ζ	f_{osc} [Hz]	Name	Dominant states
$-2.75 \pm j11.16$.240	1.78	DFIG mech. mode	$\omega_{r2}, \theta_{tw2}$

Oscillating modes in Area II

$\lambda = \sigma \pm j\omega$	ζ	f_{osc} [Hz]	Name	Dominant states
$-0.68 \pm j5.82$.116	0.93	SG speed-angle	$\omega_{r3}, \delta_3, \omega_{r4}, \delta_4$
$-0.46 \pm j0.62$.591	0.10	SG exciter-field	$E'_{q3}, V_{R3}, E'_{q4}, V_{R4}$

Inter-area oscillating modes

$\lambda = \sigma \pm j\omega$	ζ	f_{osc} [Hz]	Name	Dominant states
$-0.26 \pm j4.24$.062	0.67	Speed-angle	$\omega_{r1}, \delta_1, \omega_{r3}, \delta_3$
$-0.79 \pm j0.85$.682	0.13	Exciter-field	$E'_{q1}, V_{R1}, E'_{q3}, V_{R3}$
$-1.41 \pm j0.92$.837	0.15	Exciter-field	$E'_{q1}, V_{R1}, E'_{q3}, V_{R3}$

6.2 Impact of power generation dispatch

Fig. 6.3 and 6.4 show how the oscillation frequency and damping ratio of the IAM are affected by the generation dispatch in area I between generators at bus 1 and 2 supplying a constant level of loads at bus 5 and 6. Table 6.6 and 6.7 give the active power generation, load and transfer values for each case.

When the power transferred between the areas is low (Table 6.6 and Fig. 6.3), removal of the SG at bus 2 (and replacement by a DFIG) gives less or more damping depending on the generation sharing within Area I. For lower contribution of Generator 2 (Case 1) the damping ratio is deteriorated. For larger contribution of Generation 2 (Case 5) the damping ratio is improved. From the participation factor analysis in the previous section it was established that the IAM is characterised by the synchronous machines on the system. Hence the deterioration or improvement is explained by the difference between the equivalent synchronous machine in Area I (equivalent single synchronous machine that would give the same dynamical behaviour seen from bus 5) before and after replacement of the generator at bus 2. Before replacement, the equivalent synchronous machine of area I is made of both SG1 and SG2, after replacement it is made of SG1 only. For lower contribution of Generator 2 (Case 1), the equivalent SG of Area I operates closer to its limits after replacement of the generator at bus 2. For higher contribution of Generator 2 (Case 5), the equivalent SG of Area I operates closer to its limits before replacement of the generator at bus 2. As the damping torque is diminished for machines operating close to their limits, the damping ratio is deteriorated for Case 1 and improved for Case 5 as the SG is being replaced by a DFIG.

When the power transferred between the areas is high (Table 6.7 and Fig. 6.4), the same qualitative observations and explanations can be made.

The sensitivity of IAM to the operating point is greater when the SG are equipped with static fast exciters. Again this is explained by the sensitivity of the resulting equivalent SG of Area I which is greater when ST1A-type exciters are used as the resulting damping torque is more sensitive to the operating point due to the higher forcing capability (larger gain) and faster response (smaller time constant).

Table 6.6: Active power generation, load and transfer for Fig. 6.3

Case	Generation				Load		Transfer II to I
	Area I =	Gen1 + Gen2	Area II =	Gen3 + Gen4	Total =	Load5 + Load6	
1	700 =	630 + 70	726 =	496 + 230	1400 =	700 + 700	15
2	700 =	560 + 140	724 =	494 + 230	1400 =	700 + 700	13
3	700 =	490 + 210	722 =	492 + 230	1400 =	700 + 700	11
4	700 =	420 + 280	720 =	490 + 230	1400 =	700 + 700	9
5	700 =	350 + 350	719 =	489 + 230	1400 =	700 + 700	8

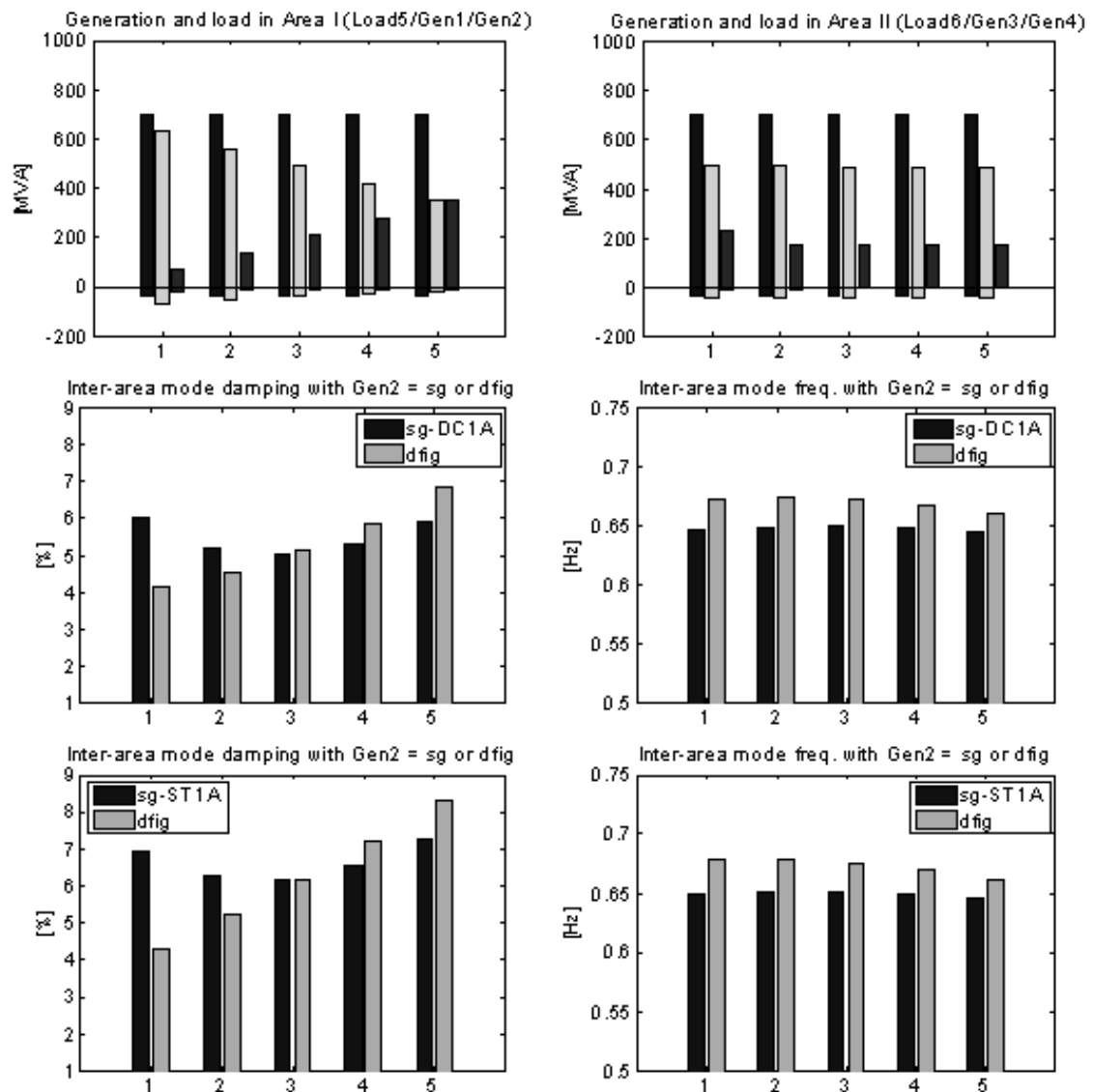


Figure 6.3: Effect of power generation sharing with low power transfer

Table 6.7: Active power generation, load and transfer for Fig. 6.4

Case	Generation				Load		Transfer I to II
	Area I =	Gen1 + Gen2	Area II =	Gen3 + Gen4	Total =	Load5 + Load6	
1	900 =	810 + 90	533 =	363 + 170	1400 =	700 + 700	175
2	900 =	720 + 180	530 =	360 + 170	1400 =	700 + 700	179
3	900 =	630 + 270	526 =	356 + 170	1400 =	700 + 700	182
4	900 =	540 + 360	524 =	354 + 170	1400 =	700 + 700	185
5	900 =	450 + 450	522 =	352 + 170	1400 =	700 + 700	187

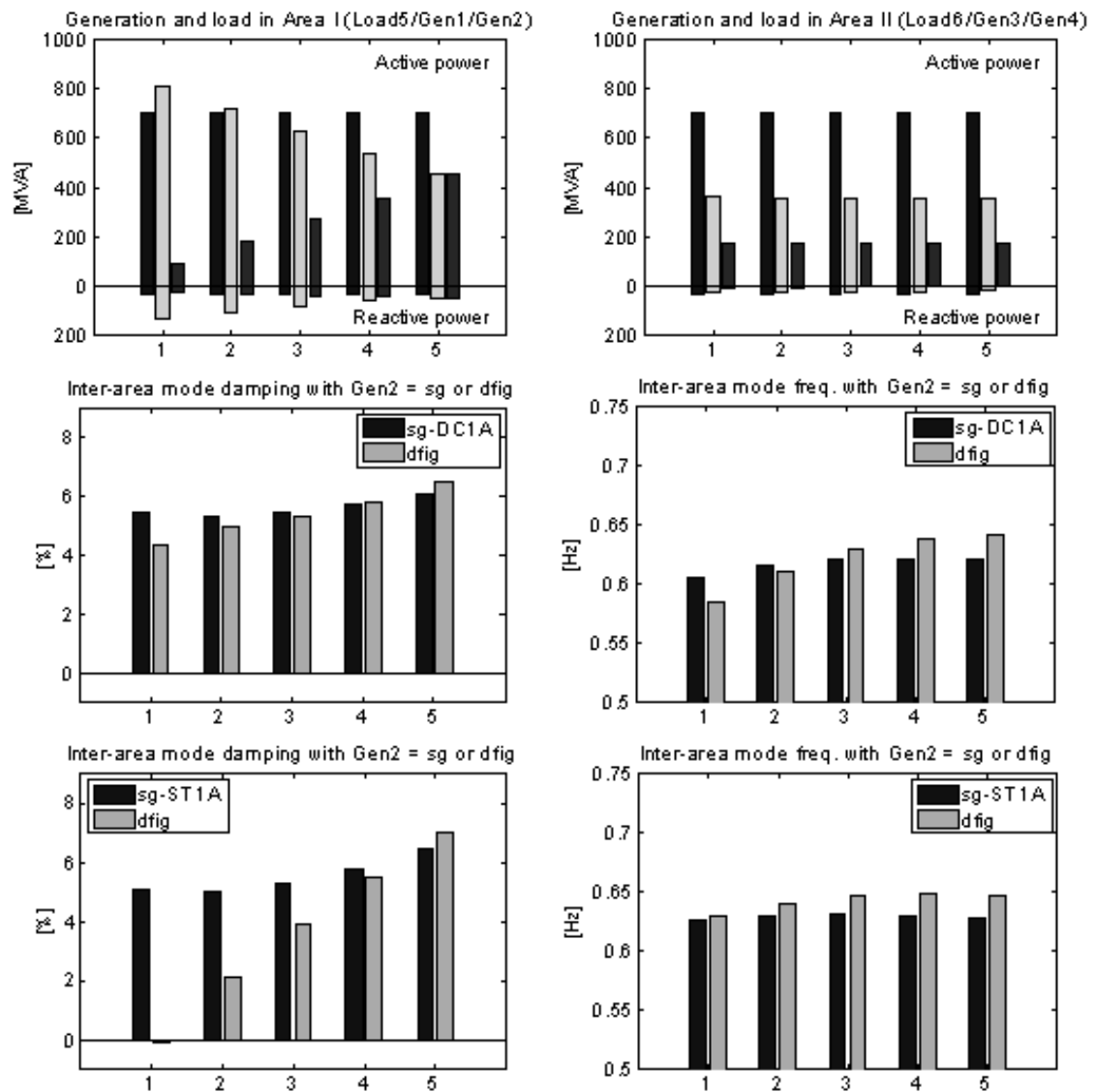


Figure 6.4: Effect of power generation sharing with high power transfer

The fact that the IAM damping ratio improves with the generation share of the DFIG has also been observed in [74]. It is noted that in Fig. 6.3 and 6.4, the total load of the system is the same. The only difference is in the amount of power transferred between the areas. The fact that the IAM sensitiveness to power generation sharing does not change qualitatively for different level of inter-tie power flows has also been observed in [100].

6.3 Impact of power transfer

Fig. 6.5 and 6.6 show how the oscillation frequency and damping ratio of the IAM are affected by the level of intertie power transfer. Table 6.8 and 6.9 give the active power generation, load and transfer values for each case.

The results confirm the observation made in the previous section. For lower generation share of Generator 2 (Table 6.8 and Fig. 6.5), the damping ratio is deteriorated regardless of the level of power transfer. This is explained by the fact that the equivalent SG in Area I is operating closer to its limit after replacement of the generator at bus 2, reducing the damping torque. For higher generation share of Generator 2 (Table 6.9 and Fig. 6.6), the damping ratio is improved regardless of the level of power transfer. The reason being that the equivalent SG in Area I is operating closer to its limit before replacement of the generator at bus 2. The larger sensitivity for SG with ST1A-type exciters can also be observed.

The studies in Table 6.8/Fig. 6.5 and Table 6.9/Tab. 6.6 show the effect of inter-area power flow on the damping ratio for low and high power generation sharing of Gen2, whereby outputs of Gen 1 and Gen 2 are simultaneously changed. Table 6.10/Tab. 6.7 and Table 6.11/Tab. 6.8 show the effect of inter-area power flow with constant output of either Gen 1 or Gen 2. Again it is seen that improvement or deterioration of the damping factor is mainly determined by power dispatch between Gen 1 and Gen 2. In Table 6.10/Tab. 6.7 the power sharing of Gen 2 is low in all cases and the damping ratio is deteriorated when replacing synchronous generation by non-synchronous generation. In Table 6.11/Tab. 6.8 the power sharing of Gen 2 is sufficiently high in case 1 and 2 to give a favorable change in damping ratio. It is also seen that in Table 6.11/Tab. 6.8 the damping ratio is on overall higher than in Table 6.10/Tab. 6.7 because the generators in Area I are operating at a lower

capacity factor i.e. their operating point is less close to their limits.

Table 6.8: Active power generation, load and transfer for Fig. 6.5

Case	Generation				Load		Transfer I to II
	Area I =	Gen1 + Gen2	Area II =	Gen3 + Gen4	Total =	Load5 + Load6	
1	700 =	560 + 140	724 =	494 + 230	1400 =	700 + 700	-13
2	750 =	600 + 150	674 =	454 + 220	1400 =	700 + 700	36
3	800 =	640 + 160	625 =	415 + 210	1400 =	700 + 700	83
4	850 =	680 + 170	577 =	377 + 200	1400 =	700 + 700	131
5	900 =	720 + 180	529 =	339 + 190	1400 =	700 + 700	179

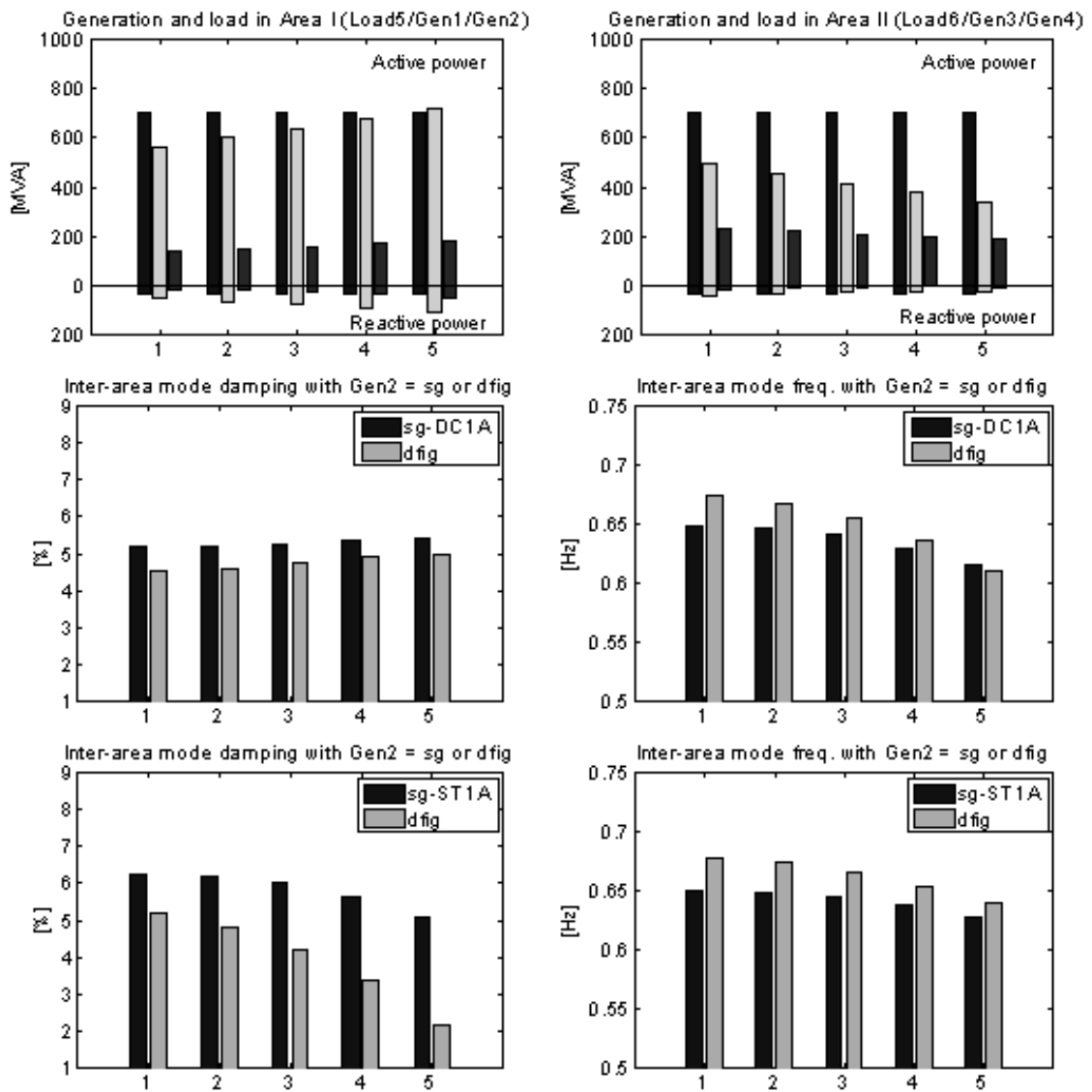


Figure 6.5: Effect of power transfer with low sharing of Gen2

Table 6.9: Active power generation, load and transfer for Fig. 6.6

Case	Generation				Load		Transfer I to II
	Area I =	Gen1 + Gen2	Area II =	Gen3 + Gen4	Total =	Load5 + Load6	
1	700 =	350 + 350	719 =	489 + 230	1400 =	700 + 700	-8
2	750 =	375 + 375	669 =	449 + 220	1400 =	700 + 700	41
3	800 =	400 + 400	619 =	409 + 210	1400 =	700 + 700	90
4	850 =	425 + 425	570 =	370 + 200	1400 =	700 + 700	138
5	900 =	450 + 450	521 =	331 + 190	1400 =	700 + 700	187

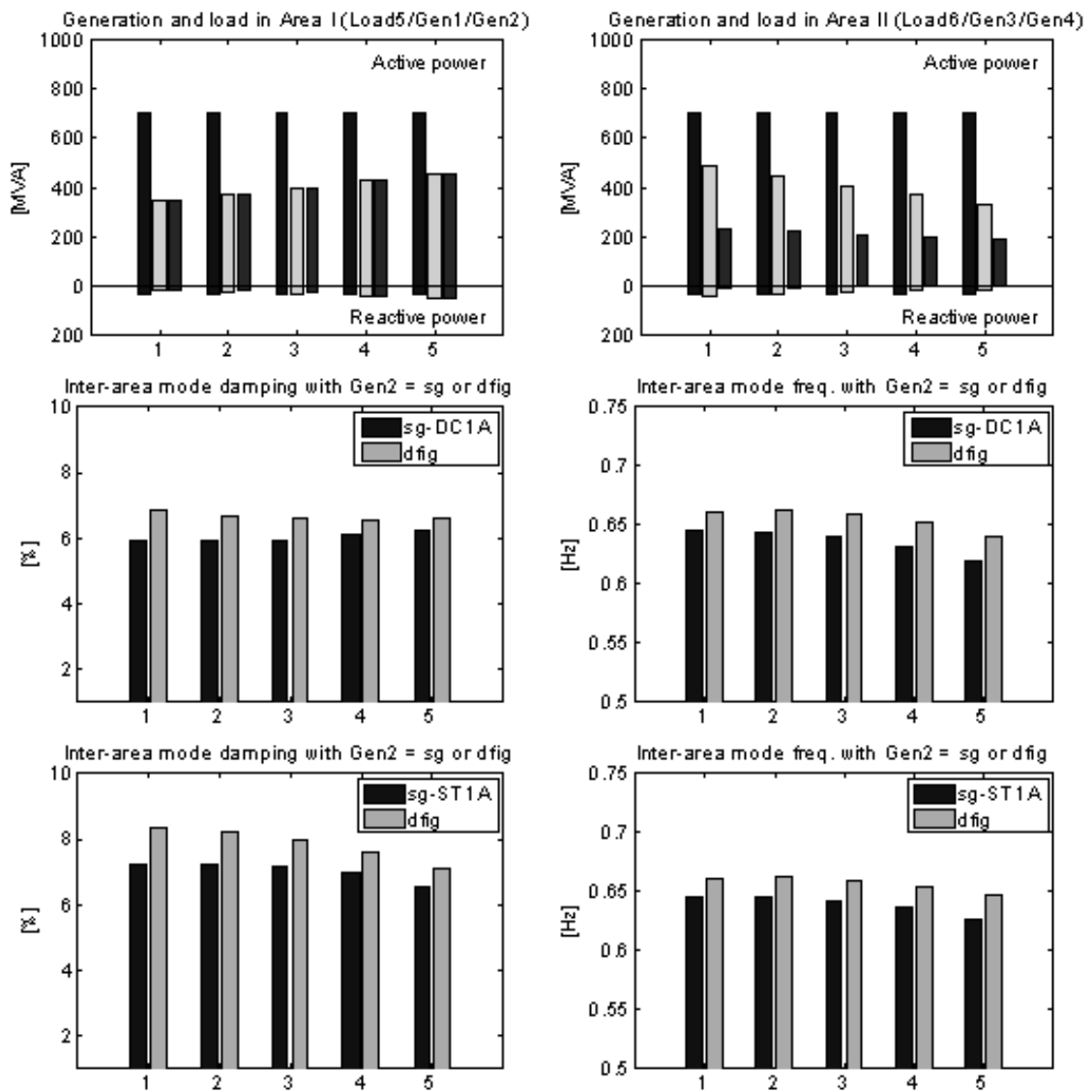


Figure 6.6: Effect of power transfer with high sharing of Gen2

Table 6.10: Active power generation, load and transfer for Fig. 6.7

Case	Generation				Load		Transfer I to II
	Area I =	Gen1 + Gen2	Area II =	Gen3 + Gen4	Total =	Load5 + Load6	
1	700 =	600 + 100	722 =	322 + 400	1400 =	700 + 700	-14
2	750 =	600 + 150	672 =	347 + 325	1400 =	700 + 700	36
3	800 =	600 + 200	623 =	373 + 250	1400 =	700 + 700	85
4	850 =	600 + 250	575 =	400 + 175	1400 =	700 + 700	134
5	900 =	600 + 300	527 =	427 + 100	1400 =	700 + 700	183

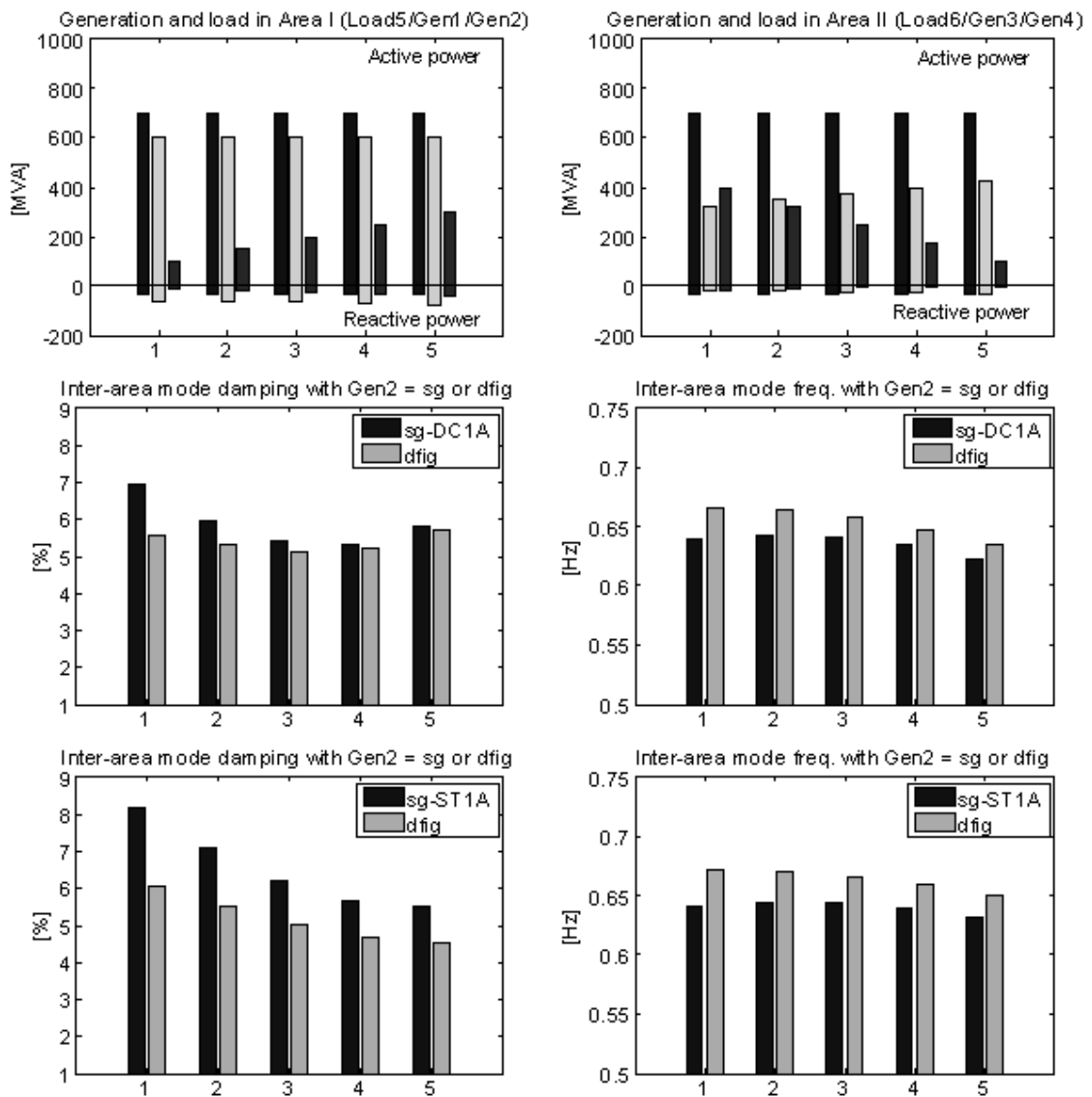


Figure 6.7: Effect of power transfer with constant Gen1 output

Table 6.11: Active power generation, load and transfer for Fig. 6.8

Case	Generation				Load		Transfer I to II
	Area I =	Gen1 + Gen2	Area II =	Gen3 + Gen4	Total =	Load5 + Load6	
1	700 =	400 + 300	716 =	316 + 400	1400 =	700 + 700	-9
2	750 =	450 + 300	668 =	343 + 325	1400 =	700 + 700	39
3	800 =	500 + 300	620 =	370 + 250	1400 =	700 + 700	87
4	850 =	550 + 300	573 =	398 + 175	1400 =	700 + 700	135
5	900 =	600 + 300	527 =	427 + 100	1400 =	700 + 700	183

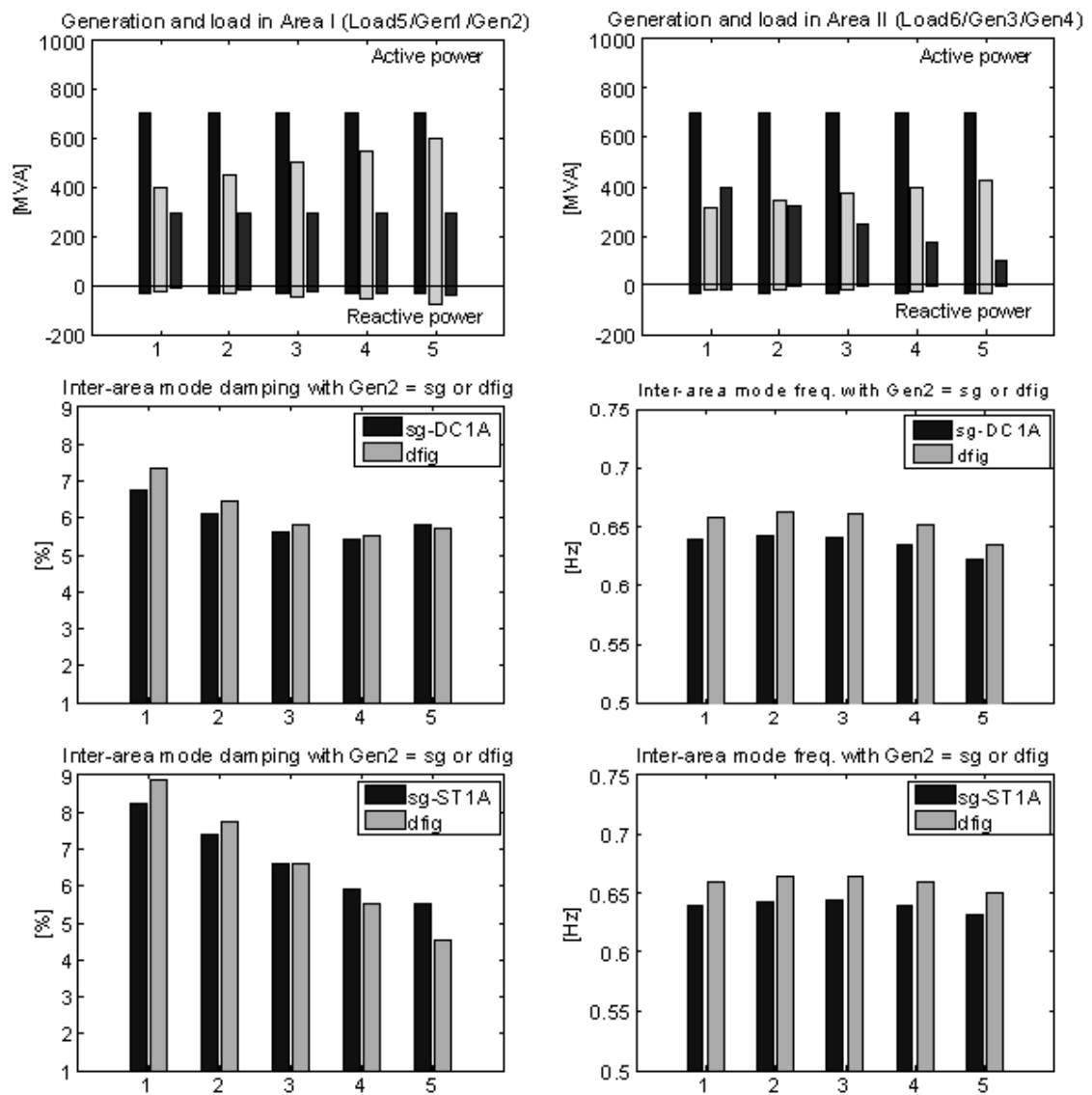


Figure 6.8: Effect of power transfer with constant Gen2 output

6.4 Summary

In this chapter, the effect of replacing an SG by a DFIG on the inter-area mode of a simple power system has been investigated.

Participation factor analysis confirmed that the inter-area mode is contributed by the state variables of the synchronous machines only. Hence, the change in damping is more to do with the removal of the synchronous machines than with the introduction of the DFIG.

Different test cases showed that the damping ratio is either improved or deteriorated depending on the operating point of the area-equivalent SG before and after replacing one of the SG within that area by a DFIG. The change in dynamics can be explained in terms of change in damping torque of the area-equivalent SG before and after replacement. If the area-equivalent SG is operated closer to its limits after replacement, the damping ratio will be less.

Chapter 7

Conclusion and future work

7.1 Conclusion

In this work, the dynamical behaviour of the DFIG has been analysed. Eigenvalue analysis was chosen as the study method to obtain an analytical interpretation of observations reported in the literature from experimental studies and time domain simulations studies.

The first part of the thesis reviewed in detail the modelling of the DFIG components relevant for the power system dynamics. The second part presented the analysis of the DFIG behaviour. Four contexts were considered:

- Steady-state behaviour
- Open-loop behaviour
- Closed-loop behaviour
- Interaction with synchronous machines

The results of the analysis provided insight regarding the modelling adequacy of the DFIG, the control tuning of the controllers and its impact on the oscillatory stability of the power system.

The effects of the closed-loop controls on the modelling adequacy were investigated by comparing the eigenvalues of the SCIG and DFIG. From the observations it was concluded that for the SCIG which operates at very small positive slip, a simplified electro-mechanical model whereby stator dynamics are neglected was adequate. For the closed-loop controlled DFIG, the controllers effectively separate the mechanical frequencies

from electrical ones and there is no electro-mechanical mode. As opposed to the open-loop control case, the oscillatory properties of the DFIG with closed-loop controls are not significantly sensitive to the rotor speed. From the eigenvalue analysis, stator transients are associated with real eigenvalues far away from the imaginary axis in the left half plane, whereas the high frequency electrical mode is associated with the rotor electrical transients. As a result the model of the DFIG with closed-loop controls can be further simplified by neglecting both stator and rotor electrical transients. The response of the simplified DFIG model is thus determined by the dynamics of the controllers and mechanical parts. For power system stability studies where the interest is in lower frequency oscillations this was shown to be adequate.

Speed variability is possible due to the ac-dc-ac converter in the rotor circuit required to produce rotor voltage at slip frequency. Using a back-to-back converter allows bidirectional power flows and hence operation at both sub- and supersynchronous speed. Formulating the control algorithm of the converters in a synchronously rotating frame allows decoupled control of the generator speed (or active power) and terminal voltage (or reactive power). When tuning the RSC controllers, stator transients should be considered and model simplification for stability studies should be done only once a set of appropriate control gains has been obtained. The reason was shown to be the fact that when neglecting stator transients, it is possible to find PI-gains giving stable result for simplified DFIG models, but unstable for the full order model (where stator and rotor electrical transients are represented) which reflects more realistic situations. To address the issue, a tuning procedure of the RSC was formulated to ensure stable stator and rotor electrical dynamics.

The effect of replacing SGs by DFIGs on the oscillatory stability of the power system, was investigated by observing the low frequency mode of the synchronous machines in a generic two area power system model. The results showed that the oscillatory dynamics of the power system depend significantly on the operating point of the SGs. Using a DFIG instead of an SG may improve or deteriorate the inter-area mode damping ratio depending on the operating point of the equivalent SG before and after replacement. If the area-equivalent SG is operated closer to its limits after replacement, the damping ratio

will be reduced. In addition participation factor analysis confirmed that the inter-area mode is contributed by the state variables of the synchronous machines only. Hence, the change in the IAM location is more related to the removal of the SG (removal of its synchronous inertia, damping and synchronizing torque contribution) rather than to the addition of the DFIG.

7.2 Future work

The following points are identified as potential future work based on the results of the present thesis:

- Analysis of the dynamical behaviour of a multi-DFIG wind farm: The interests would be to identify the dynamics that determine the overall behaviour at the common point of coupling, the effect of unequal wind speed distribution on the mechanical and electrical power variation within the wind farm, the cases in which these dynamics would be relevant (e.g. voltage control, power extraction optimisation) and when they would need to be controlled.
- Control design with advanced control algorithm: In this thesis linear PI-controllers were assumed and simulation results showed satisfactory response. One could investigate how non-linear control algorithm improve the behaviour of the DFIG and whether the increase in complexity leads to much improved behaviour.
- Laboratory or field validation: this would be more relevant for testing complex control algorithm to show the feasibility and validate the benefit with respect to simpler alternatives.
- Control design with additional objectives e.g. to take into account the effects of intra-wind farm phenomena, PSS functionality, Q/V-droop feature.

Further analysis of power system oscillatory stability was not mentioned as it was shown that for such studies the dynamics of the DFIG are not essential, i.e. in such studies the focus would be on the SGs instead. Other areas of power system stability such as

voltage stability requiring fault-ride through capabilities from the DFIG and fault studies are indeed very topical. In such studies, the focus would be on the control design.

Appendix 1: DFIG parameters

System base values:

f_B base frequency = 50 [Hz]
 ω_{el} electrical base speed = $2\pi f_B$ [rad/s]
 S_{Bwt} wind turbine base power = 5 [MVA]

Initial condition for loadflow (in [pu] on machine base):

Bus 1 (DFIG) = PV bus $V_1 = 1$ or 0.9, $P_1 = 0.34$ or 0.9
 Bus 3 = infinite bus $V_3 = 0.98$ or 0.88, $\theta_3 = 0$
 Line 1-2 = transfo $X = 0.05$
 Line 2-3 = line $R = .0075$, $X = .03$, $y_{ch} = .0145833$

DFIG parameters ([pu] on machine base):

ω_s synchronous speed = 1 [pu]
 L_m mutual inductance = 4 [pu]
 L_{ss} stator inductance = $1.01 L_m$
 L_{rr} rotor inductance = $1.005 L_{ss}$
 R_s stator resistance = 0.005 [pu]
 R_r rotor resistance = $1.1 R_s$
 $R_1 = R_s + R_2$
 $R_2 = K_{mrr}^2 R_r$
 $K_{mrr} = L_m / L_{rr}$
 $L'_s = L_{ss} - L_m K_{mrr}$
 $T_r = L_{rr} / R_r$
 H_t turbine inertia = 4 [s]
 H_g generator inertia = $0.1 H_t$
 k_{sh} drive train shaft stiffness = 0.3 [pu/el.rad]
 c_{sh} drive train damping coefficient = 0.01 [pu.s/el.rad]

Turbine variables:

$\lambda = (\omega_t [\text{rad/s}] R [\text{m}]) / (v_w [\text{m/s}])$ = tip speed ratio
 β blade pitch angle [deg], = 0 deg in subrated conditions
 v_w wind speed [m/s]

Turbine parameters:

P_{rated}	turbine rated power = 5 [MW]
v_{wrated}	rated wind speed = 15 [m/s]
$C_p(\lambda, \beta)$	performance coefficient $= c_1 \left(\frac{c_2}{\lambda + c_8\beta} - \frac{c_2 c_9}{\beta^3 + 1} - c_3\beta - c_4\beta^{c_5} - c_6 \right) \dots$ $\dots \exp \left(\frac{-c_7}{\lambda + c_8\beta} + \frac{c_7 c_9}{\beta^3 + 1} \right) + c_{10}\lambda$ $c_1 = 0.5176, c_2 = 116, c_3 = 0.4, c_4 = c_5 = 0, c_6 = 5,$ $c_7 = 21, c_8 = 0.08, c_9 = 0.035, c_{10} = 0.0068, \text{ see [108]}$
C_{pmax}	maximum value of C_p when β is 0 deg, = 0.48
λ_{opt}	tip speed ratio when C_p is C_{pmax} , = 8.10
R	blade length [m] $= \sqrt{P_{rated}[\text{W}] / (0.5\rho\pi C_{pmax} v_{wrated}^3)} = 40.05 \text{ [m]}$
ρ	air density = 1.225 [kg/m ³]

The rated rotor speed is chosen as the synchronous speed, hence:

n_{pp}	generator pole pairs number = 2
ω_{rrated}	generator rated speed (mechanical) [rad/s] = ω_{el}/n_{pp}
ω_{trated}	turbine rated speed [rad/s] = $v_{wrated}\lambda_{opt}/R$
n_{gb}	gearbox ratio = $\omega_{rrated}/\omega_{trated} = 51.78$
T_{mB}	turbine base torque = $n_{gb}P_{rated}/\omega_{rrated}$
K_{opt}	$= 0.5\rho\pi R^5 C_{pmax} \omega_{trated}^3 / (\lambda_{opt}^3 P_{rated})$

Appendix 2: Gershgorin Theorem

Gershgorin theorem states that the eigenvalues of a complex matrix A will be located in the regions of the complex plane defined by a set of disks [130]. The disks have as center the diagonal elements of A and as radius the sum of the magnitude of the off-diagonal elements in a same row (or same column). If the disks form two disconnected sets, the number of eigenvalues in each set is the number of disks in the set. As an example, the following 2x2 matrix is considered:

$$A = \begin{pmatrix} a_{11} & a_{12} \\ a_{21} & a_{22} \end{pmatrix} \quad (7.1)$$

The eigenvalues of A are in the union of the disks D_{row1} (center a_{11} , radius $|a_{12}|$) and D_{row2} (center a_{22} , radius $|a_{21}|$), or equivalently in the union of the disks D_{col1} (center a_{11} , radius $|a_{21}|$) and D_{col2} (center a_{22} , radius $|a_{12}|$). If A is transformed to $B = T^{-1}AT$, where

$$T = \begin{pmatrix} \sqrt{\left|\frac{a_{21}}{a_{22}}\right|} & 0 \\ 0 & 1 \end{pmatrix}, B = \begin{pmatrix} a_{11} & a_{12}\sqrt{\left|\frac{a_{21}}{a_{12}}\right|} \\ a_{21}\sqrt{\left|\frac{a_{12}}{a_{21}}\right|} & a_{22} \end{pmatrix}$$

the eigenvalues are the same and the Gershgorin disks are identical row-wise and column-wise (same radius): D_1 has center a_{11} and radius $\sqrt{|a_{12}a_{21}|}$, D_2 has center a_{22} and radius $\sqrt{|a_{21}a_{12}|}$. If the distance between the disks centers is sufficiently large, i.e. if $|a_{11} - a_{22}| > 2\sqrt{|a_{12}a_{21}|}$, D_1 and D_2 are disconnected. If in addition a_{11} is large and negative, D_1 is completely in the LHP as illustrated in Fig. 7.1.

For the closed-loop DFIG full-order model the elements in the first two rows of A_c (corresponding to the differential equations of i_{qs} and i_{ds}) have larger magnitudes than the elements of the remaining rows (due to the factor ω_{el}/L'_s where $L'_s = L_{ss}^2 - L_m^2/L_{rr}$ is very small). This means that the Gershgorin disk centers a_{11} and a_{22} (corresponding

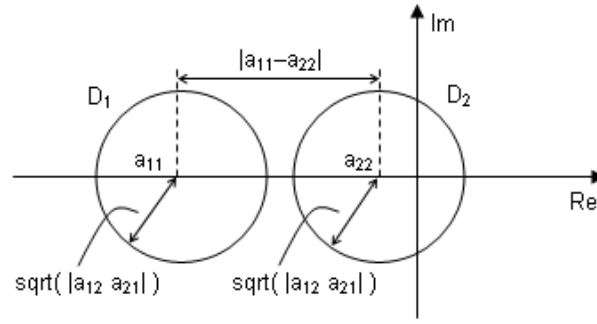


Figure 7.1: Gershgorin disks of the 2x2 matrix $B = T^{-1}AT$

to the rows and columns of i_{qs} and i_{ds}) are far from the remaining centers. They can be in the LHP or RHP depending on the control parameters. By imposing $a_{11} < -T_1$ and $a_{22} < -T_2$ (i.e. by imposing the disk centers to be far in the LHP), a transformation T can be found so that the Gershgorin disks of $B = T^{-1}AT$ is made of two disconnected sets, one of which contains a_{11} and a_{22} and is completely in the LHP. This ensures that stator dynamics are stable. The other set of disks is closer to the imaginary axis and covers partially the RHP. The corresponding eigenvalues are the mechanical modes of the DFIG which are stable and hence in the LHP.

Appendix 3: Two-area power system parameters

System base values:

f_B	base frequency = 50 [Hz]
ω_{el}	electrical base speed = $2\pi f_B$ [rad/s]
S_{Bsys}	system base power = 100 [MVA]
S_{Bgen1}	base power of generator at bus 1 = 1000 [MVA]
S_{Bgen2}	base power of generator at bus 1 = 500 [MVA]
S_{Bgen3}	base power of generator at bus 1 = 1000 [MVA]
S_{Bgen4}	base power of generator at bus 1 = 500 [MVA]

Transformer parameters in [pu] on machine base:

Line 1-7 = transfo	$X = 0.15$
Line 3-11 = transfo	$X = 0.15$
Line 2-9 = transfo	$X = 0.15$
Line 4-10 = transfo	$X = 0.15$

Line parameters in [pu] on system base:

Line 7-9 = line	$R = .0025, X = .02, y_{ch} = .04375$
Line 10-11 = line	$R = .0025, X = .02, y_{ch} = .04375$
Line 9-5 = line	$R = .001, X = .01, y_{ch} = .0175$
Line 6-10 = line	$R = .001, X = .01, y_{ch} = .0175$
Line 5-8 = line	$R = .011, X = .11, y_{ch} = .1925$
Line 5-8 = line	$R = .011, X = .11, y_{ch} = .1925$
Line 5-8 = line	$R = .011, X = .11, y_{ch} = .1925$
Line 8-6 = line	$R = .011, X = .11, y_{ch} = .1925$
Line 8-6 = line	$R = .011, X = .11, y_{ch} = .1925$
Line 8-6 = line	$R = .011, X = .11, y_{ch} = .1925$

SG parameters in [pu] on machine base [49]:

R_s	0
X_d	1.8
X'_d	0.3
X_q	1.7
X'_q	0.55
T'_{do}	8
T'_{qo}	0.4
H	6.5

SG exciter in [pu] on machine base:

	K_E	T_E	a_{sat}	b_{sat}	K_A	T_A	K_F	T_F	T_B	T_C
DC1A self [49]	*	0.36	.0056	1.075	20	0.055	0.125	1.8	-	-
DC1A sep [121]	1	0.314	.0039	1.555	20	0.2	0.063	0.35	-	-
DC2A [132]	1	1.33	.0373	1.1435	300	0.01	0.1	0.675	-	-
ST1A [132]	-	-	-	-	200	-	-	-	10	1

1. DC-Exciters

DC-excitors are nowadays rarely employed. In Great Britain, the last one was decommissioned in the early 70s. In the US and the rest of the world, a large number were still in use in the early 90s [132]. DC-excitors are classified into three categories according to the type of regulator they use [132]:

- DC1A: continuous regulation with mechanical and rotating amplifiers (self or separate).
- DC2A: continuous regulation with solid-state amplifiers (most advanced)
- DC3A: discontinuous regulation (most archaic)

The oldest DC-excitors had non-continuous regulators (DC3A). Then with the development of mechanical and rotating amplifier equipment, continuous regulators appeared (DC1A). Finally, solid-state devices allowed a third generation of DC excitors with larger regulator limits (DC2A). A typical model of DC-excitation system with automatic voltage regulator is shown in Fig. 7.2 [132]. The main components are:

- Exciter: rotating DC-machine with iron saturation (K_E, T_E, S_E)

- Regulator: amplifies the voltage error signal (K_A, T_A)
- Exciter system stabiliser: seldom used when transient gain reduction is used [133] (K_F, T_F)
- Transient gain reductor: normally the lead time constant (T_C) is smaller than the lag time constant (T_B) so that the effect is to reduce high frequency gain [133]; otherwise T_B and T_C represent equivalent time constants inherent to the voltage regulator [132]
- Transducer: senses the terminal voltage (T_R)

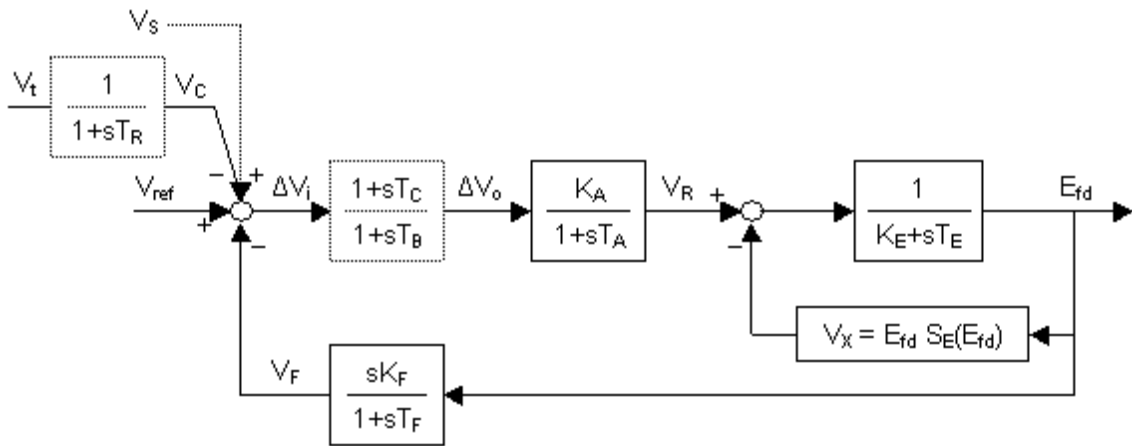


Figure 7.2: Slow exciter: DC-type exciter model

The output of the system is the field voltage E_{fd} . The inputs are the terminal voltage V_t , the PSS signal V_S if applicable, and the reference set point V_{ref} . The system in Fig. 7.2 has 5 states variables:

E_{fd} = DC-machine state

V_R = regulator state

$R_f = (K_F/T_F)E_{fd} - V_F$ = exciter system stabiliser state referred to as rate feedback

$x_{TGR} = \Delta V_o - (T_C/T_B)\Delta V_i$ = transient gain reductor state

V_C = voltage transducer and/or load compensator (not shown) state

The corresponding differential equations are:

$$\begin{aligned}
dE_{fd}/dt &= (1/T_E)(-E_{fd} + K_E(V_R - V_x)) \\
dV_R/dt &= (1/T_A)(-V_R + K_A\Delta V_o) \\
dR_f/dt &= -R_f/T_F + (K_F/T_F^2)E_{fd} \\
dx_{TRG}/dt &= -x_{TRG}/T_B + (1/T_B)(1 - T_C/T_B)\Delta V_i \\
dV_C/dt &= (1/T_R)(-V_C + V_t)
\end{aligned}$$

In steady-state, V_F and V_S (outputs of the exciter system stabiliser and PSS respectively) are zero. The TGR time constants T_B , T_C are usually small enough to be neglected [132]. The exciter gain is $K_E = 1$ when the exciter system is separately excited. For self-excited excitation system, K_E is computed so that $V_R = 0$; however if K_E is given, a fixed shunt field rheostat is assumed and K_E should not be recomputed [132]. Self-excited exciters are more common [49]. In the present work, the delays of the voltage transducer are considered as negligible, there is no load compensation, and no PSS.

2. Static exciters

In static-type exciters, the excitation voltage (and sometimes current) is rectified by controlled or non-controlled rectifiers. Static-type exciters are classified into three categories according to the type of rectifier they use [132]:

- ST1A: potential-source controlled rectifier
- ST2A: compound-source (V and I) rectifier
- ST3A: potential or compound-source rectifier with voltage control loop (field voltage control linearises exciter control and makes output independent of system disturbances)

Fig. 7.3 shows a typical model of fast excitation systems with transient gain reduction (TGR) [132]. The main components are:

- Automatic voltage regulator (K_A , T_A)
- Filter for transient gain reduction (T_C , T_B)

- Filter for transient gain increase (T_{C1}, T_{B1}) - more rarely employed
- Transducer for terminal voltage measurement and/or compensation (T_R)
- Transient feedback stabilizer (K_F, T_F) - seldom used when TGR is used
- Field current limiter (K_{LR}) - optional

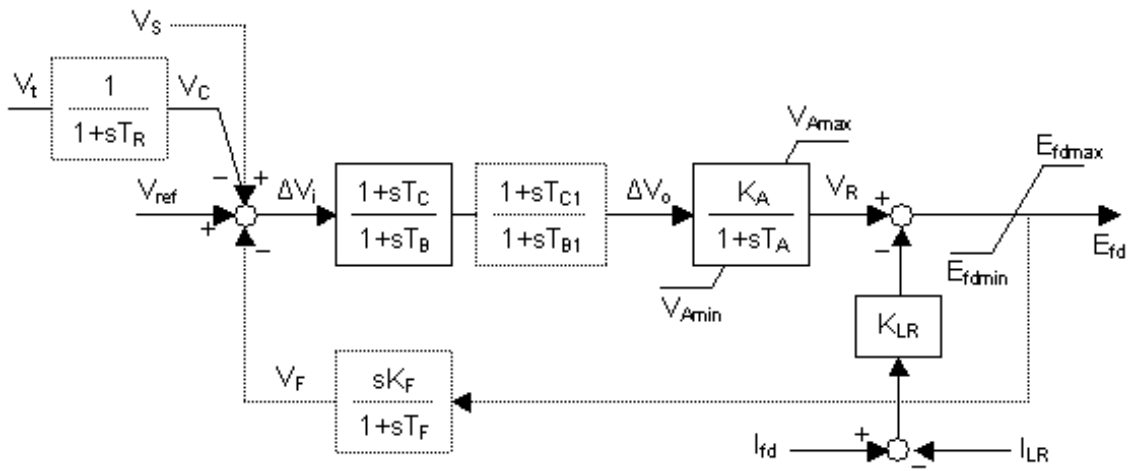


Figure 7.3: Fast exciter: Static-type exciter model

In static excitation systems, the excitation power comes from the generator terminal or auxiliaries through transformers and regulated by rectifiers. The maximum excitation voltage ($E_{fd,max}$) depends directly on the generator terminal voltage and also on the field current. When limits are modelled, the positive limit can be represented as a linear function of I_{fd} . For the negative limit, the I_{fd} term would not be included. The exciter time constant T_A is very small, so that exciter stabilizer may not be needed. Usually, TGR is used in either forward path (T_C, T_B) or feedback path (K_F, T_F). For most systems, the way the firing angle is derived results in a linear input output relationship for the voltage regulator (K_A). Static-type exciters have very high forcing capability with high ceiling voltage. An additional field current limiter may be required to protect the exciter and generator rotor.

Bibliography

- [1] Global Wind Energy Council. Global wind 2006 report. [Online]. Available: <http://www.gwec.net>
- [2] Earth Policy. World wind electricity-generating capacity 1980-2005. [Online]. Available: http://www.earth-policy.org/Indicators/Wind/2006_data.htm#fig1
- [3] BTM Consult Aps. Ten year review 1995-2004: 10 years review of the wind power industry, forecast and scenarios 2005 through 2025. [Online]. Available: <http://www.btm.dk/ten-index.htm>
- [4] Union for the Co-ordination of Transmission of Electricity. National electricity consumption 2006 and peak load. [Online]. Available: http://www.ucte.org/statistics/consumption/e_default.asp
- [5] Wind-Works. Wind penetration update Denmark 2007. [Online]. Available: <http://www.wind-works.org/articles/WindPenetrationUpdateDenmark2007.html>
- [6] Sustainable Development Commission. Wind power in the UK. [Online]. Available: <http://www.sd-commission.org.uk>
- [7] British Wind Energy Association. (2004) Wind and the uk's 10% target. [Online]. Available: <http://www.bwea.com/energy/briefing-sheets.html>
- [8] A. Johnson and N. Tleis, "The development of grid code requirements for new and renewable forms of generation in great britain," *Wind Engineering*, vol. 29, no. 3, pp. 201–216, May 2005.
- [9] The Crown Estate. Offshore wind energy. [Online]. Available: http://www.thecrownestate.co.uk/offshore_wind_energy
- [10] British Wind Energy Association. (2007) Wind farms in the UK. [Online]. Available: <http://www.bwea.com/statistics>
- [11] ——. (2007) Uk wind power portfolio reaches new milestone. [Online]. Available: <http://www.bwea.com/media/news/070209.html>
- [12] American Wind Energy Association. Wind web tutorial: Wind energy basics. [Online]. Available: http://www.awea.org/faq/wwt_basics.html#top

- [13] British Wind Energy Association. (2006) BWEA briefing on UK wind capacity factors. [Online]. Available: <http://www.bwea.com/ref/capacityfactors.html>
- [14] The Royal Academy of Engineering. The cost of generating electricity: A commentary. [Online]. Available: http://www.raeng.org.uk/news/publications/list/reports/Cost_Generation_Commentary.pdf
- [15] European Process Engineer. Debating the true cost of wind power electricity. [Online]. Available: <http://www.engineerlive.com/european-process-engineer/environmental-solutions/2113/debating-the-true-cost-of-wind-power-electricity.thtml>
- [16] G. Boyle, *Renewable Energy*. The Open University, Oxford, 1996.
- [17] Iowa Energy Center. Wind energy manual. [Online]. Available: <http://www.energy.iastate.edu/renewable/wind/cs-index.html>
- [18] J. Manwell, J. McGowan, and A. Rogers, *Wind Energy Explained*. John Wiley & Sons, 2002.
- [19] Danish Wind Industry Association. Know how: Guided tour. [Online]. Available: <http://www.windpower.org>
- [20] T. Ackermann, *Wind Power in Power Systems*. John Wiley & sons, 2005.
- [21] W. Grainger and N. Jenkins. Offshore windfarm electrical connections. Proc. of British Wind Energy Association Conf. [Online]. Available: http://www.owen.eru.rl.ac.uk/documents/bwea20_46.pdf
- [22] S. Heier, *Grid Integration of Wind Energy Conversion Systems*. Wiley, 1998.
- [23] P. Gipe, "Pitch versus stall: The numbers are in," *Renewable Energy World*, vol. 6, no. 4, Aug. 2003.
- [24] T. Thiringer, A. Petersson, and T. Petru, "Grid disturbance response of wind turbines equipped with induction generator and doubly-fed induction generator," in *Proc. of IEEE Power Eng. Soc. General Meeting*, vol. 3, July 2003, pp. 1542–1547.
- [25] J. G. Slootweg, H. Polinder, and W. L. Kling, "Representing wind turbine electrical generating systems in fundamental frequency simulations," *IEEE Trans. Energy Conversion*, vol. 18, no. 4, pp. 516–524, Dec. 2003.
- [26] A. D. Hansen, L. Helle, F. Blaabjerg, E. Ritchie, S. Munk-Nielsen, H. Bindner, P. Srensen, and B. Bak-Jensen, "Conceptual survey of generators and power electronics for wind turbines," RISO National Laboratory, Roskilde, Denmark, Tech. Rep. Ris-R-1205(EN), ISBN 87-550-2743-1, Dec. 2001.
- [27] R. Pena, J. C. Clare, and G. M. Asher, "Doubly fed induction generator using back-to-back PWM converters and its application to variable-speed wind-energy generation," *IEE Proc. on Electric Power Appl.*, vol. 143, no. 3, pp. 231–241, May 1996.

- [28] S. Muller, M. Deicke, and R. W. D. Doncker, "Adjustable speed generators for wind turbines based on doubly-fed induction machines and 4-quadrant IGBT converters linked to the rotor," in *Proc. of IEEE Ind. Applicat. Conf.*, vol. 4, Oct. 2000, pp. 2249–2254.
- [29] J. Ekanayake, L. Holdsworth, and N. Jenkins, "Comparison of 5th order and 3rd order machine models for doubly fed induction generator (dfig) wind turbines," *Electric Power Systems Research*, vol. 67, no. 3, pp. 207–215, Dec. 2003.
- [30] Y. Tang and L. Xu, "A flexible active and reactive power control strategy for a variable speed constant frequency generating system," *IEEE Trans. Power Electron.*, vol. 10, no. 4, pp. 472–478, July 1995.
- [31] F. M. Hughes, O. Anaya-Lara, N. Jenkins, and G. Strbac, "Control of DFIG-based wind generation for power network support," *IEEE Trans. Power Syst.*, vol. 20, no. 4, pp. 1958–1966, Nov. 2005.
- [32] R. G. de Almeida, E. D. Castronuovo, and J. A. P. Lopes, "Optimum generation control in wind parks when carrying out system operator requests," *IEEE Trans. Power Syst.*, vol. 21, no. 2, pp. 718–725, May 1996.
- [33] A. D. Hansen and L. H. Hansen, "Wind turbine concept market penetration over 10 years (1995–2004)," *Wind Energy*, vol. 10, no. 1, pp. 81–97, Nov. 2006.
- [34] D. Schreiber, "Power electronics for wind turbines (semikron)," in *Proc. of European Center for Power Electronics, Seminar Renewable Energies, Kassel, Germany*, vol. 1, Feb. 2006.
- [35] GE Energy. 3.6 MW series wind turbine. [Online]. Available: http://www.gepower.com/prod_serv/products/wind_turbines/en/36mw/index.htm
- [36] Vestas. V90-3MW wind turbine. [Online]. Available: http://www.vestas.com/vestas/global/en/Products/Wind_turbines/V90_3_0.htm
- [37] M. V. A. Nunes, J. A. P. Lopes, H. H. Zurn, U. H. Bezerra, and R. G. Almeida, "Influence of the variable-speed wind generators in transient stability margin of the conventional generators integrated in electrical grids," *IEEE Trans. Energy Conversion*, vol. 19, no. 4, pp. 692–701, Dec. 2004.
- [38] European Commission, Energy, Renewable sources. Wind turbine grid connection and interaction. [Online]. Available: http://ec.europa.eu/energy/res/sectors/doc/wind_energy/maxibrochure_final_version.pdf
- [39] T. Petru and T. Thiringer, "Modeling of wind turbines for power system studies," *IEEE Trans. Power Syst.*, vol. 17, no. 4, pp. 1132–1139, Nov. 2002.
- [40] J. L. Rodriguez-Amenedo, S. Arnalte, and J. C. Burgos, "Automatic generation control of a wind farm with variable speed wind turbines," *IEEE Trans. Energy Conversion*, vol. 17, no. 2, pp. 279–284, 2002.

- [41] W. Janssen, H. Luetze, A. Buecker, T. Hoffmann, and R. Hagedorn, "Low voltage ride through for wind turbine generators," U.S. Patent US 6,921,985 B2, 2005.
- [42] S. A. Papathanassiou and M. P. Papadopoulos, "State-space modelling and eigenvalue analysis of the slip energy recovery drive," *IEE Proc. on Electric Power Appl.*, vol. 144, no. 1, pp. 27–36, Jan. 1997.
- [43] E. Akpinar, R. E. Trahan, and A. D. Nguyen, "Modeling and analysis of closed-loop slip energy recovery induction motor drive using a linearization technique," *IEEE Trans. Energy Conversion*, vol. 8, no. 4, pp. 688–697, Dec. 1993.
- [44] Y. Lei, A. Mullane, G. Lightbody, and R. Yacamini, "Modeling of the wind turbine with a doubly fed induction generator for grid integration studies," *IEEE Trans. Energy Conversion*, vol. 21, no. 1, pp. 257–264, Mar. 2006.
- [45] L. Xu and W. Cheng, "Torque and reactive power control of a doubly fed induction machine by position sensorless scheme," *IEEE Trans. Ind. Applicat.*, vol. 31, no. 3, pp. 636–642, May 1995.
- [46] A. Petersson, T. Thiringer, L. Harnefors, and T. Petru, "Modeling and experimental verification of grid interaction of a dfig wind turbine," *IEEE Trans. Energy Conversion*, vol. 20, no. 4, pp. 878–886, Dec. 2005.
- [47] S. Seman, J. Niiranen, S. Kanerva, A. Arkkio, and J. Saitz, "Performance study of a doubly fed wind-power induction generator under network disturbances," *IEEE Trans. Energy Conversion*, vol. 21, no. 4, pp. 883–890, Dec. 2006.
- [48] J. G. Slootweg, S. W. H. de Haan, H. Polinder, and W. L. Kling, "General model for representing variable speed wind turbines in power system dynamics simulations," *IEEE Trans. Power Syst.*, vol. 18, no. 1, pp. 144–151, Feb. 2003.
- [49] P. Kundur, *Power System Stability and Control*. McGraw-Hill, 1994.
- [50] V. Akhmatov, "Variable-speed wind turbines with doubly-fed induction generators, part I: Modelling in dynamic simulation tools," *Wind Engineering*, vol. 26, no. 2, pp. 85–108, Mar. 2002.
- [51] N. W. Miller, J. J. Sanchez-Gasca, W. W. Price, and R. W. Delmerico, "Dynamic modeling of GE 1.5 and 3.6 MW wind turbine-generators for stability simulations," in *Proc. of IEEE Power Eng. Soc. General Meeting*, vol. 3, 2003, pp. 1977–1983.
- [52] P. Ledesma and J. Usaola, "Doubly fed induction generator model for transient stability analysis," *IEEE Trans. Energy Conversion*, vol. 20, no. 2, pp. 388–397, June 2005.
- [53] M. A. Poller, "Doubly-fed induction machine models for stability assessment of wind farms," in *Proc. of Power Tech. Conf.*, vol. 3, June 2003, pp. 1–6.
- [54] H. Snel, "Review of aerodynamics for wind turbines," *Wind Energy*, vol. 6, no. 3, pp. 203–211, June 2003.

- [55] A. D. Hansen, C. Jauch, P. Srensen, F. Iov, and F. Blaabjerg, "Dynamic wind turbine models in power system simulation tool Digsilent," RISO National Laboratory, Roskilde, Denmark, Tech. Rep. Ris-R-1400(EN), ISBN 87-550-3198-6, Dec. 2003.
- [56] P. Sorensen, A. D. Hansen, and P. A. C. Rosas, "Wind models for simulation of power fluctuations from wind farms," *Journal of Wind Engineering and Industrial Aerodynamics*, vol. 90, no. 12, pp. 1381–1402, Dec. 2002.
- [57] J. M. Rodriguez, J. L. Fernandez, D. Beato, R. Iturbe, J. Usaola, P. Ledesma, and J. R. Wilhelmi, "Incidence on power system dynamics of high penetration of fixed speed and doubly fed wind energy systems: study of the spanish case," *IEEE Trans. Power Syst.*, vol. 17, no. 4, pp. 1089–1095, Nov. 2002.
- [58] C. Eping, J. Stenzel, M. Poller, and H. Muller, "Impact of large scale wind power on power system stability," in *Proc. of Large-Scale Integr. of Wind Power and Transm. Networks for Offsh. Wind farms Int. Worksh.*, vol. 1, Apr. 2005, pp. 1–9.
- [59] E. Muljadi, C. P. Butterfield, B. Parsons, and A. Ellis, "Effect of variable speed wind turbine generator on stability of a weak grid," *IEEE Trans. Energy Conversion*, vol. 22, no. 1, pp. 29–36, Mar. 2007.
- [60] E. Muljadi and C. P. Butterfield, "Pitch-controlled variable-speed wind turbine generation," *IEEE Trans. Ind. Applicat.*, vol. 37, no. 1, pp. 240–246, Jan. 2001.
- [61] J. G. Slootweg, H. Polinder, and W. L. Kling, "Dynamic modelling of a wind turbine with doubly fed induction generator," in *Proc. of IEEE Power Eng. Soc. Summer Meeting*, vol. 1, July 2001, pp. 644–649.
- [62] A. D. Hansen, P. Srensen, F. Iov, and F. Blaabjerg, "Control of variable speed wind turbines with doubly-fed induction generators," *Wind Engineering*, vol. 28, no. 4, pp. 411–432, 2004.
- [63] M. M. Hand, "Variable-speed wind turbine controller systematic design methodology: A comparison of non-linear and linear model-based designs," National Renewable Energy Laboratory, Colorado, Tech. Rep. NREL/TP-500-25540, 1999.
- [64] M. Poller and S. Achilles, "Aggregated wind park models for analyzing power system dynamics," in *Proc. of Large-Scale Integr. of Wind Power and Transm. Networks for Offsh. Wind farms Int. Worksh.*, vol. 1, Apr. 2003, pp. 1–10.
- [65] E. van der Hooft, P. Schaak, and T. van Engelen, "Wind turbine control algorithms," Tech. Rep.
- [66] G. Tapia, A. Tapia, and J. X. Ostolaza, "Two alternative modeling approaches for the evaluation of wind farm active and reactive power performances," *IEEE Trans. Energy Conversion*, vol. 21, no. 4, pp. 909–920, Dec. 2006.

- [67] F. W. Koch, I. Erlich, F. Shewarega, and U. Bachmann, "Dynamic interaction of large offshore wind farms with the electric power system," in *Proc. of Power Tech. Conf.*, vol. 3, June 2003, p. 7.
- [68] J. Ekanayake, L. Holdsworth, X. G. Wu, and N. Jenkins, "Dynamic modeling of doubly fed induction generator wind turbines," *IEEE Trans. Power Syst.*, vol. 18, no. 2, pp. 803–809, May 2003.
- [69] L. Holdsworth, X. G. Wu, J. B. Ekanayake, and N. Jenkins, "Comparison of fixed speed and doubly-fed induction wind turbines during power system disturbances," *IEE Proc. on Gen., Transm. and Distr.*, vol. 150, no. 3, pp. 343–352, May 2003.
- [70] R. G. de Almeida, J. A. P. Lopes, , and J. A. L. Barreiros, "Improving power system dynamic behavior through doubly fed induction machines controlled by static converter using fuzzy control," *IEEE Trans. Power Syst.*, vol. 19, no. 4, pp. 1942–1950, Nov. 2004.
- [71] E. N. Hinrichsen and P. J. Nolan, "Dynamics and stability of wind turbine generators," *IEEE Trans. Power App. Syst.*, vol. PAS-101, no. 8, pp. 2640–2648, Aug. 1982.
- [72] S. K. Salman, A. L. J. Teo, and I. M. Rida, "The effect of shaft modelling on the assessment of fault CCT and the power quality of a wind farm," in *Proc. of Harmonics and Quality of Power Int. Conf.*, vol. 3, Oct. 2000, pp. 994–998.
- [73] S. K. Salman and A. L. J. Teo, "Windmill modeling consideration and factors influencing the stability of a grid-connected wind power-based embedded generator," *IEEE Trans. Power Syst.*, vol. 18, no. 2, pp. 793–802, May 2003.
- [74] J. J. Sanchez-Gasca, N. W. Miller, and W. W. Price, "A modal analysis of a two-area system with significant wind power penetration," in *Proc. of IEEE Power Eng. Soc. General Meeting*, vol. 2, Oct. 2004, pp. 1148–1152.
- [75] A. Feijoo, J. Cidras, and C. Carrillo, "A third order model for the doubly-fed induction machine," *Electric Power Systems Research*, vol. 56, no. 2, pp. 121–127, Nov. 2000.
- [76] A. Tapia, G. Tapia, J. X. Ostolaza, and J. R. Saenz, "Modeling and control of a wind turbine driven doubly fed induction generator," *IEEE Trans. Energy Conversion*, vol. 18, no. 2, pp. 194–204, June 2003.
- [77] J. Usaola and P. Ledesma, "Dynamic incidence of wind turbines in networks with high wind penetration," in *Proc. of IEEE Power Eng. Soc. Summer Meeting*, vol. 2, July 2001, pp. 755–760.
- [78] V. Akhmatov, H. Knudsen, and A. Nielsen, "Advanced simulation of windmills in the electric power supply," *Electric Power Systems Research*, vol. 22, no. 6, pp. 421–434, Aug. 2000.

- [79] T. Thiringer and J. Luomi, "Comparison of reduced-order dynamic models of induction machines," *IEEE Trans. Power Syst.*, vol. 16, no. 1, pp. 119–126, Feb. 2001.
- [80] P. Srensen, A. D. Hansen, P. Christensen, M. Mieritz, J. Bech, B. Bak-Jensen, and H. Nielsen, "Verification of transient events in large wind power installations," RISO National Laboratory, Roskilde, Denmark, Tech. Rep. Ris-R-1331(EN), Dec. 2003.
- [81] J. G. Slootweg, S. W. H. de Haan, H. Polinder, and W. L. Kling, "Modeling wind turbines in power system dynamics simulations," in *Proc. of IEEE Power Eng. Soc. Summer Meeting*, vol. 1, July 2001, pp. 22–26.
- [82] V. Akhmatov, "Variable-speed wind turbines with doubly-fed induction generators, part III: Model with the back-to-back converters," *Wind Engineering*, vol. 27, no. 2, pp. 79–91, Mar. 2003.
- [83] ———, "Variable-speed wind turbines with doubly-fed induction generators, part IV: Uninterrupted operation features at grid faults with converter control coordination," *Wind Engineering*, vol. 27, no. 6, pp. 519–529, Dec. 2003.
- [84] F. M. Hughes, O. Anaya-Lara, N. Jenkins, and G. Strbac, "A power system stabilizer for DFIG-based wind generation," *IEEE Trans. Power Syst.*, vol. 21, no. 2, pp. 763–772, May 2006.
- [85] M. R. Rathi and N. Mohan, "A novel robust low voltage and fault ride through for wind turbine application operating in weak grids," in *Proc. of IEEE Industrial Electronics Soc. Conf.*, vol. 1, Nov. 2005, pp. 1–6.
- [86] A. Mullane, G. Lightbody, and R. Yacamini, "Wind-turbine fault ride-through enhancement," *IEEE Trans. Power Syst.*, vol. 20, no. 4, pp. 1929–1937, Nov. 2005.
- [87] C. Abbey, W. Li, L. Owatta, and G. Joos, "Power electronic converter control techniques for improved low voltage ride through performance in wtgs," in *Proc. of IEEE Power Electronics Specialists Conf.*, vol. 1, June 2006, pp. 1–6.
- [88] R. Narayanan, D. Platt, and S. Perera, "Improvements to voltage sag ride-through performance of ac variable speed drives," in *Proc. of Australasian Universities Power Engineering Conf.*, vol. 1, Sept. 1999, pp. 1–7.
- [89] L. Holdsworth, I. Charalambous, J. Ekanayake, and N. Jenkins, "Power system fault ride through capabilities of induction generator based wind turbines," *Wind Engineering*, vol. 28, no. 4, pp. 399–409, 2004.
- [90] E. Muljadi and C. Butterfield, "Wind farm power system model development," National Renewable Energy Laboratory, Colorado, Tech. Rep. NREL/CP-500-36199, 2004.

- [91] V. Akhmatov, "An aggregated model of a large wind farm with variable-speed wind turbines equipped with doubly-fed induction generators," *Wind Engineering*, vol. 28, no. 4, pp. 479–486, 2004.
- [92] D. A. M. D. E. Seborg, T. F. Edgar, *Process dynamics and control, 2nd edition*. John Wiley and Sons, 2004.
- [93] P. Sorensen, A. D. Hansen, T. Lund, and H. Bindner, "Reduced models of doubly fed induction generator system for wind turbine simulations," *Wind Energy*, vol. 9, no. 4, pp. 299–311, Oct. 2005.
- [94] E. A. Bossanyi, "The design of closed loop controllers for wind turbines," *Wind Energy*, vol. 3, no. 3, pp. 149–163, July 2000.
- [95] J. Morren, S. W. H. de Haan, W. L. Kling, and J. A. Ferreira, "Wind turbines emulating inertia and supporting primary frequency control," *IEEE Trans. Power Syst.*, vol. 21, no. 1, pp. 433–434, Feb. 2006.
- [96] V. Akhmatov, "Variable-speed wind turbines with doubly-fed induction generators, part II: Power system stability," *Wind Engineering*, vol. 26, no. 3, pp. 171–188, May 2002.
- [97] P. Cartwright, L. Holdsworth, J. B. Ekanayake, and N. Jenkins, "Co-ordinated voltage control strategy for a doubly-fed induction generator (DFIG)-based wind farm," *IEE Proc. on Gen., Transm. and Distr.*, vol. 151, no. 4, pp. 495–502, July 2004.
- [98] M. G. Ioannides, "Doubly fed induction machine state variables model and dynamic response," *IEEE Trans. Energy Conversion*, vol. 6, no. 1, pp. 55–61, Mar. 1991.
- [99] P. Sorensen, A. D. Hansen, K. Thomsen, H. Madsen, H. A. Nielsen, N. K. Poulsen, F. Iov, F. Blaabjerg, and M. H. Donovan, "Wind farm controllers with grid support," in *Proc. of Large-Scale Integr. of Wind Power and Transm. Networks for Offsh. Wind farms Int. Worksh.*, vol. 1, Apr. 2005, pp. 1–6.
- [100] J. G. Slootweg and W. L. Kling, "The impact of large scale wind power generation on power system oscillations," *Electric Power Systems Research*, vol. 67, no. 1, pp. 9–20, Oct. 2003.
- [101] A. Mendonca and J. A. P. Lopes, "Impact of large scale wind power integration on small signal stability," *Proc. of Future Power Systems Int. Conf.*, vol. 1, no. 1, pp. 1–5, Nov. 2005.
- [102] J. G. Leishman, "Challenges in modelling the unsteady aerodynamics of wind turbines," *Wind Energy*, vol. 5, no. 2-3, pp. 85–132, Apr. 2002.
- [103] H. Snel, "Review of the present status of rotor aerodynamics," *Wind Energy*, vol. 1, no. 1, pp. 46–69, Jan. 1999.

- [104] H. Snel and J. G. Schepers, "Engineering models for dynamic inflow phenomena," *Journal of Wind Engineering and Industrial Aerodynamics*, vol. 39, no. 2, pp. 267–281, Mar. 1992.
- [105] D. Simms, S. Schreck, M. Hand, and L. J. Fingersh, "NREL unsteady aerodynamics experiment in the NASA-Ames wind tunnel: a comparison of predictions to measurements," National Renewable Energy Laboratory, Colorado, Tech. Rep. NREL/TP-500-29494, 2001.
- [106] A. D. Hansen, P. Sørensen, F. Iov, and F. Blaabjerg, "Initialisation of grid-connected wind turbine models in power-system simulations," *Wind Engineering*, vol. 27, no. 1, pp. 21–38, Feb. 2003.
- [107] T. G. van Engelen and E. L. van der Hooft, "Dynamic inflow compensation for pitch controlled wind turbines," Proc. of European Wind Energy Conf., Nov. 2004, presented as a poster.
- [108] Matlab. Wind turbine model of simpowersystem. [Online]. Available: <http://www.mathworks.com/access/helpdesk/help/toolbox/phymod/powersys/windturbine.html>
- [109] R. K. Vierck, *Vibration Analysis*. Harper and Row, 1979.
- [110] I. committee report, "Recommended phasor diagram for synchronous machines," *IEEE Trans. Power App. Syst.*, vol. PAS-88, no. 11, pp. 1593–1610, Nov. 1969.
- [111] D. Novotny and T. A. Lipo, *Vector Control and Dynamics of AC Drives*. Oxford University Press, 1996.
- [112] P. M. Anderson and A. A. Fouad, *Power system control and stability*. Wiley-Interscience, 2003.
- [113] V. Akhmatov, "Analysis of dynamic behaviour of electric power systems with large amount of wind power," Ph.D. dissertation, Technical University of Denmark, Apr. 2003.
- [114] P. Ledesma, J. Usaola, J. L. Rodriguez, and J. C. Burgos, "Comparison between control systems in a doubly fed induction generator when connected to an electric grid," in *Proc. of European Wind Energy Conf.*, vol. 1, Apr. 1999.
- [115] P. Van Meirhaeghe. (2003) Double fed induction machine: an Eurostag model. [Online]. Available: <http://www.eurostag.be>
- [116] J. Jung, S. Lim, and K. Nam, "A feedback linearizing scheme for a pwm converter-inverter having a very small dc-link capacitor," *IEEE Trans. Ind. Applicat.*, vol. 35, no. 5, pp. 1124–1131, Sept. 1999.
- [117] H. Hur, J. Jung, and K. Nam, "A fast dynamics dc-link power-balancing scheme for a pwm converter-inverter system," *IEEE Trans. Ind. Electron.*, vol. 48, no. 4, pp. 794–803, Aug. 2001.

- [118] N. J. Wheeler, H. Zhang, and D. A. Grant, "Minimisation of reactive component values in back-to-back converters," in *Proc. of Power Electronics and Variable-Speed Drives Int. Conf.*, Oct. 1994, pp. 240–245.
- [119] L. Malesani, L. Rossetto, P. Tenti, and P. Tomasin, "Ac/dc/ac power converter with reduced energy storage in the dc link," *IEEE Trans. Ind. Applicat.*, vol. 31, no. 2, pp. 287–292, Mar. 1995.
- [120] W. G. . of Study Committee C4, "Modeling and dynamic behavior of wind generation as it relates to power system control and dynamic performance," CIGRE, Tech. Rep. CIGRE-WG-601.C4, Jan. 2007.
- [121] P. W. Sauer and M. A. Pai, *Power System Dynamics and Stability*. Prentice Hall, 1998.
- [122] R. Grunbaum, P. Halvarsson, D. Larsson, and P. R. Jones, "Conditioning of power grids serving offshore wind farms based on asynchronous generators," in *Proc. of Power Electronics, Machines and Drives Int. Conf.*, vol. 1, Apr. 2004, pp. 34–39.
- [123] P. W. Sauer and M. A. Pai, "Power system steady-state and the load-flow jacobian," *IEEE Trans. Power Syst.*, vol. 5, no. 4, pp. 1374–1383, Nov. 1990.
- [124] J. G. Slootweg, H. Polinder, and W. L. Kling, "Initialization of wind turbine models in power system dynamics simulations," in *Proc. of Power Tech. Conf.*, vol. 4, Sept. 2001, pp. 1–6.
- [125] L. Holdsworth, X. G. Wu, J. B. Ekanayake, and N. Jenkins, "Direct solution method for initialising doubly-fed induction wind turbines in power system dynamic models," *IEE Proc. on Gen., Transm. and Distr.*, vol. 150, no. 3, pp. 334–342, May 2003.
- [126] J. Machowski, J. W. Bialek, and J. R. Bumby, *Power system dynamics and stability*. John Wiley & Sons, 1997.
- [127] M. A. Pai, D. P. S. Gupta, and K. R. Padiyar, *Topics in Small Signal Analysis of Power Systems*. manuscript (published book: *Small Signal Analysis of Power Systems*, Alpha Science International, 2004), 2003.
- [128] S. B. Crary, *Power System Stability Vol II*. John Wiley & Sons, 1955.
- [129] F. P. D. Mello and L. T. Laskowski, "Concepts of power system dynamic stability," *IEEE Trans. Power App. Syst.*, vol. PAS-94, no. 1, pp. 827–833, May 1975.
- [130] R. A. Brualdi and S. Mellendorf, "Regions in the complex plane containing the eigenvalues of a matrix," *The American Mathematical Monthly*, vol. 101, no. 10, pp. 975–985, Dec. 1994.
- [131] M. Klein, G. Rogers, and P. Kundur, "A fundamental study of inter-area oscillations in power systems," *IEEE Trans. Power Syst.*, vol. 6, no. 3, pp. 914–921, Aug. 1991.

-
- [132] “Recommended practice for excitation system models for power system stability studies,” *IEEE Standard*, vol. 421, no. 5, Mar. 1992.
- [133] G. Rogers, *Power System Oscillations*. Kluwer Academic Publishers, 2000.